

**TRANSITIONING FROM A DIPOLE TO A RELATIVISTIC
RESPONSE IN ATOMS AND MOLECULES**

by

Patrick D. Grugan

A dissertation submitted to the Faculty of the University of Delaware in partial fulfillment of the requirements for the degree of Doctor of Philosophy in Physics

Fall 2017

© 2017 Patrick D. Grugan
All Rights Reserved

**TRANSITIONING FROM A DIPOLE TO A RELATIVISTIC
RESPONSE IN ATOMS AND MOLECULES**

by

Patrick D. Grugan

Approved: _____

Edmund R. Nowak, Ph.D.

Chair of the Department of Physics and Astronomy

Approved: _____

George H. Watson, Ph.D.

Dean of the College of Arts and Sciences

Approved: _____

Ann L. Ardis, Ph.D.

Senior Vice Provost for Graduate and Professional Education

I certify that I have read this dissertation and that in my opinion it meets the academic and professional standard required by the University as a dissertation for the degree of Doctor of Philosophy.

Signed: _____
Barry C. Walker, Ph.D.
Professor in charge of dissertation

I certify that I have read this dissertation and that in my opinion it meets the academic and professional standard required by the University as a dissertation for the degree of Doctor of Philosophy.

Signed: _____
Krzysztof Szalewicz, Ph.D.
Member of dissertation committee

I certify that I have read this dissertation and that in my opinion it meets the academic and professional standard required by the University as a dissertation for the degree of Doctor of Philosophy.

Signed: _____
Yi Ji, Ph.D.
Member of dissertation committee

I certify that I have read this dissertation and that in my opinion it meets the academic and professional standard required by the University as a dissertation for the degree of Doctor of Philosophy.

Signed: _____
Lars Gundlach, Ph.D.
Member of dissertation committee

ACKNOWLEDGEMENTS

The production of this work has been perhaps a little too long in the making, but I have learned quite a bit on my journey and would like to take the time to thank a few people for all their help, support, and encouragement.

I would like to thank Dr. Barry Walker. His herculean strength of patience with me for a student is something I would not envy. Working with him during my time producing this work has been exceptional for me. He has shown me how to be a better scientist with his wealth of knowledge of both experiment and theory. My gratitude for this and all the work he has put in teaching me cannot be stated enough.

Science is not a solitary pursuit and in this, I too was not an exception. I would like to thank my colleagues. Nagitha Ekanayake for teaching me about the laser system and that if everything is working, it soon will not be. Sui Luo for his help on coding projects. Siyu Luo for his help with data collections and discussions on theoretical models. The friendship of these gentlemen was greatly appreciated. I would also like to thank the undergraduates that have helped through the years.

None of this would be possible without the help of my thesis committee Dr. Krzysztof Szalewicz, Dr. Yi Ji, and Dr. Lars Gundlach. They have taken the time to read this work and make comments to help guide me to producing something that I hope will be a contribution to the study of light matter interaction.

Finally, I would like to thank my father Thomas E. Grugan. Without him I would not be here and would not have completed this work. He may not have understood my every explanation, but he understood my passion. Thanks dad.

TABLE OF CONTENTS

LIST OF TABLES	viii
LIST OF FIGURES	ix
ABSTRACT	xviii
 Chapter	
1 INTRODUCTION	1
1.1 Motivation	1
1.2 Atomic Response with Increasing Intensity	2
1.3 Molecular Response with Increasing Intensity	8
1.4 Experimental Considerations	10
1.5 Arrangement of Topics	12
BIBLIOGRAPHY	14
2 EXPERIMENTAL APPARATUS: TERAWATT LASER SYSTEM AND ION SPECTROMETER	16
2.1 Terawatt Laser System	16
2.1.1 Mode-locked Oscillator	16
2.1.2 Pulse Stretcher, Regenerative Amplifier, Multipass Amplifier & Pulse Compression	23
2.2 Time of Flight Ion Spectrometry	23
2.2.1 Second Iteration: Inclusion of Magnetic Field	26
2.2.2 Third Iteration: Truncated Flight Tube	32
BIBLIOGRAPHY	42
3 CLASSICAL STUDY OF ULTRA-STRONG, NONPERTURBATIVE FIELD INTERACTIONS WITH A	

ONE-ELECTRON ATOM: VALIDITY OF THE DIPOLE APPROXIMATION FOR THE BOUND STATE INTERACTION	43
3.1 Introduction	43
3.2 Method	45
3.3 Results	47
3.3.1 Trajectories and Ensemble Distributions	47
3.3.2 Ionization rates	50
3.3.3 Angular distributions	55
3.4 Conclusion	56
3.5 Afterward	59
BIBLIOGRAPHY	62
4 SUBSTITUTION EFFECTS ON STRONG AND ULTRA-STRONG FIELD MOLECULAR IONIZATION	67
4.1 Introduction	67
4.2 Experimental Setup	68
4.3 Experimental Results	70
4.3.1 TOF Spectra	70
4.3.2 Ion Fragment Energy	71
4.3.3 Coincidence Measurements	73
4.3.4 Energy Spectra	78
4.3.5 Ion Count Rates	81
4.4 Understanding the Interaction	84
4.5 Conclusion	91
BIBLIOGRAPHY	93
5 LIMITS OF STRONG FIELD RESCATTERING IN THE RELATIVISTIC REGIME	96
5.1 Introduction	96
5.2 Theoretical Considerations	98
5.2.1 Quantum Mechanical Treatment	99

5.2.2	Semi-Classical Treatment	101
5.3	Results	101
5.4	Further Considerations	103
5.5	Influence on Above Threshold Ionization	104
5.6	Conclusion	106
5.7	Afterward	106
5.7.1	Analytic estimate of nonrelativistic recollision flux	106
5.7.2	Relativistic recollision cutoff and flux	107
BIBLIOGRAPHY		112
6	CONCLUSIONS	116
6.1	Bound State Dynamics: Validity of the Dipole Approximation	116
6.2	Molecular Ionization in the Strong and Ultrastrong field	117
6.3	Limits of Strong Field Rescattering	118
6.4	Outlook for Future Work	119
BIBLIOGRAPHY		120
Appendix		
A	SOURCE CODE FOR CLASSICAL IONIZATION STUDY	121
B	SOURCE CODE FOR COINCIDENCE MAPPING	185
C	SOURCE CODE SPECTROMETER CHARACTERIZATION	190

LIST OF TABLES

2.1	Values for varied parameters in code to calculate time of flight for ions in UHV chamber	37
4.1	Values for Kinetic Energy of Release of carbon ions from chloromethane	73
4.2	Values for Ionization Potentials	86
4.3	Values for ΔIP , the change in energy of carbon and chlorine ion's ionization potentials in chloromethane	87

LIST OF FIGURES

1.1	Schematic drawing of the photoelectric effect. The absorption of a photon (colored in orange) will allow the ionization of an electron with ionization potential IP_1 as long as $E_\gamma = IP_1$	3
1.2	(a) Schematic drawing of the multiphoton ionization. The absorption of photons (colored in orange) will allow the ionization of an electron with ionization potential IP_1 as long as $nE_\gamma = IP_1$, where n is the number of photons absorbed. (b) Example of multiphoton ionization of argon. The number of Ar^{9+} vs intensity has a slope of 6, indicative of 6 photon absorption of 800 nm photons.	4
1.3	Schematic drawing of the Tunneling Ionization. The external electromagnetic field has a sufficiently low enough frequency and high enough magnitude (colored in orange) that the ionic potential will deform enough to allow the ionization of an electron with ionization potential IP_1 by tunneling through the depressed barrier.	5
1.4	Schematic drawing of the rescattering process. The external electromagnetic field tunnel ionizes an electron (coloured in red) that can be driven back towards the parent ion when the direction of the field reverses.	7
1.5	Experimental example of non-sequential ionization of Helium. The production of He^{2+} up to 3×10^{15} W/cm ² is the result of an electron from the ionization of He rescattering with the parent He^+ ion and producing He^{2+} as reported in [9].	8
1.6	Schematic drawing of enhanced ionization. The external laser field drops the potential energy barrier on one side of the molecular ion. When the separation between the ions is at some critical distance R_c , the barrier between the two atomic ions will allow the electron, with ionization potential (blue triangles), to ionize.	10

1.7	Time of flight spectrum from the ionization of chloromethane. Pictured specifically are the ions $^{35}\text{Cl}^+$ and $^{37}\text{Cl}^+$, and indicated are there respective centroid times and FWHM time spans.	11
2.1	Schematic diagram of the CPA terawatt laser system	17
2.2	Schematic diagram of the Kerr-lens Mode-locked oscillator	18
2.3	Spectrum of the output pulse from the mode-locked oscillator. The black line gives the spectrum for a separation distance between the two prisms of 400 mm, the red line gives the spectrum for a separation distance of 401 mm and the blue line gives the spectrum for a separation distance of 399 mm.	19
2.4	Comparison of spectra for the output pulse from the mode-locked oscillator at optimized mode-locking position for three different positions of the folding mirror. Graphical shifting to match central wavelengths and peak intensities has been done.	21
2.5	Estimates for the amount of glass for each prism at optimized folding mirror positions L_0 , L_1 , and L_2	23
2.6	Diagram of beam waist in the $x - z$ plane. At $z = 0$ the minimum diameter of the beam, $2w_0$ is shown.	25
2.7	Diagram of the rectangular aperture in stainless steel top plate. . .	26
2.8	Schematic diagram of horizontal and vertical polarizations. These are the orientation of the pulse's electric field in relation to the drift tube and the detector.	27
2.9	Top down view of spectrometer detailing beam focus and off-axis gold parabolic mirror.	28
2.10	Side view of spectrometer detailing the length of the drift tube along with home-built solenoid magnets.	29
2.11	Magnetic field measurements in (a) the region just inside the drift tube, and (b) an inch above the drift tube.	31
2.12	Time of flight traces for a C^{4+} ion with horizontal and vertical polarization.	31

2.13	Third iteration of TOF spectrometer with truncated flight tube. . .	33
2.14	Time of flight trace for $^{13}\text{CH}_4$ collected at an intensity of $I \sim 1 \times 10^{16}$ W/cm 2 . Indicated are the fragmental ions of $\text{C}^+ - \text{C}^{4+}$, $\text{O}^+ - \text{O}^{3+}$, N_2^+ and O_2^+	35
2.15	(a) The residual, $S = \left(\frac{t_{exp} - t_{calc}}{t_{exp}}\right)^2$, for three different values of parameters. (b) the time difference, $\Delta t = t_{exp} - t_{calc} $, with the values of the parameters in part (a).	37
2.16	(a) TOF spectrum for CH_3Cl taken at an intensity of 1×10^{16} W/cm 2 . (b) Transform of TOF into spectrum of mass to charge ratio.	38
2.17	TOF spectrum for CH_4 and CH_3Cl taken at an intensity of 1×10^{16} W/cm 2 as a function of mass to charge ratio in vertical polarization. Isotope carbon-13 is used in the gasses.	39
2.18	TOF spectrum for CH_3Cl taken at an intensity of 1×10^{16} W/cm 2 as a function of mass to charge ratio in (a) horizontal polarization, and (b) vertical polarization.	40
3.1	Trajectories in precession for a $Z = 1, n = 18$ Rydberg state in a 4×10^{-7} a.u. constant E_{laser} field (a, red, solid) and the full E_{laser}, B_{laser} fields (b, blue, dash) as well as for a tightly bound state $Z = 8, n = 1$ in a constant 23 a.u. E_{laser} field (a, red, solid) and the full E_{laser}, B_{laser} fields (b, blue, dash). Approximately 10 orbits are plotted for each case. Rescaled coordinates, $xt = x\sqrt{E}$, are shown along with atomic units.	48

- 3.2 Configuration space distributions for $Z = 4$ (a,c,e,g,i) and $Z = 20$ (b,d,f,h,j). The configuration space with no external laser field is shown in (a,b). A line out of the classical configuration space compared with the quantum wave function probability, $P(x)$, is in (c,d). The differences between the configuration space with no external field and an external E_{laser} field with a peak value of 9.8 a.u. for $Z=4$ and 710 a.u. for $Z=20$ are shown in (e,f). The difference between the configuration space with the full E_{laser}, B_{laser} fields (9.8 a.u. for $Z=4$, 710 a.u. for $Z=20$) and the dipole approximation are in (g,h). An estimate of numerical fluctuations within the configuration space plots is shown in (i,j) as determined by subtracting two ensembles that differ only in the trajectory initial conditions for the 10^5 trajectories. The color assignment shown at the bottom of the figure ranges from 0 (black) to 1 (red) for (a,b). The range for the other plots is -0.16 (black) to +0.16 (red) for (e,f) and -0.016 (black) to +0.016 (red) for (g,h,i,j). 51
- 3.3 Fraction of electrons ionized vs. field strength for $Z = 1$ (blue, open circle), 4 (green, open square), and 20 (red, open triangle). Solid lines, which are through the data points, represent the dipole approximation, i.e. E_{laser} only. Open symbols are used for the results when E_{laser} and B_{laser} is are fully included. 52
- 3.4 $E E_{1/2}$ (red, solid triangle) and $E_B E_{1/2}$ (blue, open circle) as a function of intensity for multiple Z states (a). A trendline (solid, black) is shown to compare the results expected from a nonrelativistic $E_{critical}$ dependence. Frequency dependence of ionization for $Z=4, 12, 20$ plotted as a ratio of $E_B E_{1/2} / E E_{1/2}$ (b) from the low frequency limit, i.e. 0.0001 times the Kepler frequency, up to 0.05 times the Kepler frequency for the ionizing state. For reference, the Kepler frequencies (Z state, binding energy) are: 2.5 a.u. (4, 8 a.u.), 23 a.u. (12, 72 a.u.), and 63.6 a.u. (20, 200 a.u.). 54
- 3.5 Polar plot of the electron position at ‘birth’, i.e. ionization in the full field case E_{laser}, B_{laser} (a). The plot is for $Z=1$ (black, solid x, intensity = 0.16 a.u.), $Z=5$ (red, solid square, intensity = 2200 a.u.), $Z=10$ (green, open circle, intensity = 110,000 a.u.), $Z=20$ (blue, inverted solid triangle, intensity = 4,100,000 a.u.). The difference between this emission and that for the dipole approximation (E_{laser}) is shown in (b) where the distributions with the full field (E_{laser}, B_{laser}) minus dipole case (E_{laser}) only are shown in an angle, Z charge state contour plot. 57

3.6	Combined Coulomb and Electric field ($F_C + F_{E_{laser}}$,red) and magnetic field ($F_{B_{laser}}$,blue) forces on the electron for (a) $Z = 20, n = 1, l = 0.5$, (b) $Z = 4, n = 1, l = 0.5$ and (c) $Z = 1, n = 1, l = 0.5$. The magnitude of the field in each case is $E_{critical}$: $E_{critical}^{Z=1} = 0.0625a.u.$; $E_{critical}^{Z=4} = 4a.u.$; $E_{critical}^{Z=20} = 500a.u.$	58
3.7	Configuration space distributions for $Z = 4$ (a,c,e) and $Z = 20$ (b,d,f). The differences between the configuration space with no external field and an external E_{laser} field with a peak value of $E = 9.1$ a.u. and frequency $f = 0.07$ a.u. for $Z = 4$ and $E = 680$ a.u., $f = 1.8$ a.u. for $Z = 20$ are shown in (a,b). The difference between the configuration space with the full E_{laser}, B_{laser} fields (9.12 a.u. for $Z = 4$, 680 a.u. for $Z = 20$) and the dipole approximation are in (c,d). An estimate of numerical fluctuations within the configuration space plots is shown in (e,f). The color assignment is the same as Fig. 2.(a,b) -0.16(black) to 0.16(red), (c,d,e,f) -0.016(black) to 0.016(red)	60
4.1	Time of flight spectra gathered at 5×10^{18} W/cm ² for the molecules methane (black)(CH ₄), chloromethane (red)(CH ₃ Cl) as a function of mass to charge ratio, m/q . Indicated in the figure are some of the relevant ions studied.	70
4.2	Time of flight spectra for carbon ions from methane (black) and chloromethane (red) (a) C ⁺ , (b) C ²⁺ , (c) C ³⁺ and (d) C ⁴⁺ gathered at saturation intensities for each ion. The chloromethane spectra have been offset to allow for easier distinction of the spectra. Blue dashed guidelines have been added to show the time span of each ion used in the energy analysis. Contaminates of known ions have also been indicated.	72
4.3	Covariance map for chloromethane taken at C ²⁺ saturation intensity of 5.7×10^{14} W/cm ² . TOF spectra has a 10 ns bin size. Scale of contours are divided by 10^{-4}	74
4.4	Time slices of the covariance map for chloromethane taken at C ²⁺ saturation intensity of 5.7×10^{14} W/cm ² corresponding to the times around (a) C ⁺ and (b) C ²⁺ arrival times. Plotted below is (c) the normal TOF spectrum used to create the covariance map. Indicated in the figure are peaks for Cl ⁺ , Cl ²⁺ , and Cl ³⁺ . Circled in magenta are portions of the map where there is correlation between C ⁺ and Cl ⁺ and C ⁺ and Cl ²⁺ . Circled in blue are portions of the map where there is correlation between C ²⁺ and Cl ²⁺ and C ²⁺ and Cl ³⁺	75

4.5	(Top) Sum over the C^+ portion of the covariance map versus time. (Black line) is the raw sum over a time range of $0.995 \mu s - 1.155 \mu s$, (Blue line) a weighted average smoothing function to highlight correlations. (Bottom) time of flight spectrum for the collected coincidence measurement. (Black) TOF data with 39 ps bins, (Red) TOF data with 10 ns bins.	76
4.6	(a) Sum over the C^{2+} portion of the covariance map versus time with (c) the corresponding time of flight spectrum for the collected coincidence measurement taken at an intensity of $1.05 \times 10^{16} \text{ W/cm}^2$. (b) Sum over the C^{3+} portion of the covariance map versus time with (d) the corresponding time of flight spectrum for the collected coincidence measurement taken at an intensity of $2.25 \times 10^{16} \text{ W/cm}^2$	77
4.7	Schematic diagram of the spectrometer with parameters to be varied. These include the extraction voltage ΔV_1 , the flight tube length D , the initial ion position y_0 , the length of the interaction with the MCP voltage ΔV_2 , and the time offset t_0 (not indicated).	78
4.8	Experimental, t_{exp} , and calculated, t_{calc} , times for our TOF spectrometer. The values of the chamber parameters for this particular configuration are: $V_1=2995 \text{ V}$, $D=0.1195 \text{ m}$, $y_0=-5 \times 10^{-4} \text{ m}$, $d=3.25 \times 10^{-3} \text{ m}$, $t_0=1.425 \times 10^{-7} \text{ s}$. These values give a residue $S=3.8404 \times 10^{-6}$	79
4.9	Energy spectrum of carbon ions C^+ (black), C^{2+} (blue), C^{3+} (green), C^{4+} (red) from CH_3Cl with laser polarization parallel to the flight tube axis and an intensity in the interaction region at the saturation intensity for the carbon ion yield of each species: $4.4 \times 10^{14} \text{ W/cm}^2$ for C^+ , $5.7 \times 10^{14} \text{ W/cm}^2$ for C^{2+} , $1.3 \times 10^{15} \text{ W/cm}^2$ for C^{3+} , $6.5 \times 10^{15} \text{ W/cm}^2$ for C^{4+}	80
4.10	Energy spectrum of carbon ions C^+ (top), C^{2+} (second), C^{3+} (third), C^{4+} (bottom) from CH_3Cl with laser polarization parallel to the flight tube axis and rectangular aperture collected at the saturation intensities for each species from C^+ $4.4 \times 10^{14} \text{ W/cm}^2$ (black), C^{2+} $5.7 \times 10^{14} \text{ W/cm}^2$ (blue), C^{3+} $1.3 \times 10^{15} \text{ W/cm}^2$ (green), C^{4+} $6.5 \times 10^{15} \text{ W/cm}^2$ (red). The ion yields have been adjusted to give a normalized (unity) yield when integrated over energy. Half of the maximum energy observed for the fragments is highlighted in the figure.	82

4.11	(a) Ion count rates for C^+ (black), C^{2+} (blue), C^{3+} (green), C^{4+} (red) as a function of laser power. The calibration to intensity is 10^{-3} in power corresponds to 3.54×10^{13} W/cm ²	83
4.12	(a) Ion count rates for Cl^+ (black triangles), Cl^{2+} (blue circles), Cl^{3+} (green circles), Cl^{4+} (red squares), Cl^{6+} (light blue squares), Cl^{7+} (orange squares) as a function of laser power. The calibration to intensity is 10^{-3} in power corresponds to 3.54×10^{13} W/cm ²	83
4.13	(a)-(c) Ionization of parent molecule CH_3Cl at 4.8×10^{13} W/cm ² where the separation of the carbon and chlorine, $r = 1.0R_{eq}$. Also plotted is the ionization energy of the parent ion CH_3Cl^+ . The zero of the plot is at the center of mass of the system. Solid lines represent the potential where the charge distribution on the carbon and chlorine atoms takes into account the dipole moment and polarizability of the molecule. Dashed lines represent the potential when the charge is evenly distributed.	85
4.14	(a)-(c) Ionization of C neutral at 4.4×10^{14} W/cm ² where the separation of the carbon and chlorine, $r = 1.14R_{eq}$. (d)-(f) Ionization of Cl^+ at 4.4×10^{14} W/cm ² where $r = 1.4R_{eq}$. (g)-(i) Ionization of C^+ at 5.6×10^{14} W/cm ² where $r = 1.75R_{eq}$	88
4.15	(a)-(c) Ionization of Cl^{2+} at 8.3×10^{14} W/cm ² where $r = 1.94R_{eq}$. (d)-(f) Ionization of C^{2+} at 1.2×10^{15} W/cm ² where $r = 2.0R_{eq}$. (g)-(i) Ionization of Cl^{3+} at 1.7×10^{15} W/cm ² where $r = 2.3R_{eq}$. . .	90
4.16	(a)-(c) Ionization of C^{3+} at 7.12×10^{15} W/cm ² where $r = 2.4R_{eq}$. (d)-(f) Ionization of Cl^{5+} at 8.4×10^{15} W/cm ² where $r = 2.65R_{eq}$. (g)-(i) Ionization of Cl^{6+} at 1.2×10^{16} W/cm ² where $r = 2.8R_{eq}$. . .	91
5.1	(a) Trajectory (solid-red) for photoelectron born (η_B) and returning to the parent ion (η_R) in an oscillating electric field (dashed-blue) for the peak “ $3.2U_p$ ” recollision. Corresponding ionization probability current $\mathbf{j}(\mathbf{r}, \eta_B)$ for Ar^{4+} ionization at 4.6×10^{15} W/cm ² , 2400 nm (b); and Ar^{9+} , 1.6×10^{18} W/cm ² , 200 nm (c). In (b,c) the initial localized $\mathbf{j}(0, \eta_B)$ magnitude is divided by ten.	97

- 5.2 Normalized differential rescattering flux (a) via RCCSFA (line) and SCMC (symbol) for the laser wavelength $\lambda = 800$ nm. Line color scales with Γ_R : Ar⁵⁺ at 5.8×10^{15} W/cm² ($\Gamma_R = 0.06$, square); Ar⁷⁺ at 2.7×10^{16} W/cm² ($\Gamma_R = 0.7$, circle); Ar⁸⁺ at 5.6×10^{16} W/cm² ($\Gamma_R = 3.8$, triangle); Ar⁸⁺ at 1.3×10^{17} W/cm² ($\Gamma_R = 13$, diamond); Ar⁸⁺ at 6×10^{17} W/cm² ($\Gamma_R = 140$, square); Ar⁹⁺ at 1×10^{18} W/cm² ($\Gamma_R = 320$, circle); Ar¹¹⁺ at 2.8×10^{18} W/cm² ($\Gamma_R = 1,700$, triangle); Ar¹³⁺ at 6.3×10^{18} W/cm² ($\Gamma_R = 6,100$, diamond); Ar¹⁴⁺ at 1.3×10^{19} W/cm² ($\Gamma_R = 20,000$, square). In (a) the change from traditional rescattering (blue) to the relativistic cutoff region (orange) is highlighted in the background and a shadow line gives the typical highest possible $d\bar{F}_R/d\varepsilon$ at optical frequencies. For clarity, long and short contributions to $d\bar{F}_R/d\varepsilon$ are summed in the nonrelativistic limit $\Gamma_R < 1$. For RCCSFA with argon HCI (see Afterward), $d\bar{F}_R/d\varepsilon$ at cutoff as a function of U_p is shown in (b) and the relationship between U_p and the recollision cutoff energy is given (c) for laser wavelengths 80 nm (blue), 800 nm (red), and 8000 nm (black) with shading to aid the eye. 100
- 5.3 ATI as a function of laser intensity and wavelength for photoelectron energies near $10U_p$. Blue lines indicate $U_p = 10, 100, 1000$ a.u. The dashed line corresponds to $\Gamma_R = 1$. The color scale for ATI spans from 10^{-30} to 10^{-6} a.u. 105
- 5.4 Normalized differential rescattering flux (a) via RCCSFA (line) and SCMC (symbol) with a 8000 nm laser wavelength for: Ar⁺ at 4.8×10^{13} W/cm² ($\Gamma_R = 0.25$, square); Ar²⁺ at 2.3×10^{14} W/cm² ($\Gamma_R = 3.0$, circle); Ar³⁺ at 1×10^{15} W/cm² ($\Gamma_R = 37$, triangle); Ar⁴⁺ at 2.6×10^{15} W/cm² ($\Gamma_R = 160$, diamond); Ar⁵⁺ at 5.8×10^{15} W/cm² ($\Gamma_R = 590$, square); Ar⁶⁺ at 1.5×10^{16} W/cm² ($\Gamma_R = 2900$, circle); Ar⁷⁺ at 2.7×10^{16} W/cm² ($\Gamma_R = 7400$, triangle). The cutoff energy (b) and flux at cutoff (c) are summarized from RCCSFA (a) and plotted as a function of U_p . The points in (b,c) from low to high U_p correspond to the Ar⁺ to Ar⁷⁺ charge state progression. The Eq. (5) cutoff (b) and Eq. (6) flux are shown by highlighted orange dashed lines. Energies possible with a $3.2 U_p$ rule are indicated by shading in (b). 108

- 5.5 Normalized differential rescattering flux (a) via RCCSFA (line) and SCMC (symbol) with a laser wavelength of 80 nm for: Ar⁹⁺ at 1×10^{18} W/cm² ($\Gamma_R=0.03$, square); Ar¹¹⁺ 2.8×10^{18} W/cm² ($\Gamma_R=0.17$, circle); Ar¹³⁺ 6.3×10^{18} W/cm² ($\Gamma_R=0.61$, triangle); Ar¹⁴⁺ 1.3×10^{19} W/cm² ($\Gamma_R=2.1$, diamond); Ar¹⁵⁺ 1.8×10^{19} W/cm² ($\Gamma_R=3.3$, square); Ar¹⁶⁺ 1.5×10^{21} W/cm² ($\Gamma_R=5300$, circle); Ar¹⁷⁺ 2×10^{21} W/cm² ($\Gamma_R=7700$, triangle). The cutoff energy (b) and flux at cutoff (c) are summarized from RCCSFA (a) and plotted as a function of U_p . The points in (b,c) from low to high U_p have a correspond to the Ar⁹⁺ to Ar¹⁷⁺ charge state progression. The Eq. (5) cutoff (b) and Eq. (6) flux are shown by highlighted orange dashed lines. Energies possible with a $3.2 U_p$ rule are indicated by shading in (b). 109
- 5.6 The cutoff energy (a) and flux at cutoff (b) are summarized from Fig. 5.2(a) and plotted as a function of U_p . The points in (a,b) from low to high U_p (also Ar⁵⁺ to Ar¹⁴⁺) have a corresponding $\Gamma_R=0.058, 0.74, 140, 319, 1674, 6091$. The Eq. (5) cutoff (b) and Eq. (6) flux are shown by highlighted orange dashed lines. Energies possible with a $3.2 U_p$ rule are indicated by shading in (a). 110
- 5.7 Normalized differential rescattering flux (a) via RCCSFA with Ar⁸⁺ at 5.9×10^{17} W/cm² for the laser wavelengths: 100 nm ($\Gamma_R = 0.034$), 200 nm ($\Gamma_R = 0.55$), 400 nm ($\Gamma_R = 8.8$), 800 nm ($\Gamma_R = 140$), 1000 nm ($\Gamma_R = 341$), 2000 nm ($\Gamma_R = 5000$), 3000 nm ($\Gamma_R = 3 \times 10^4$). The cutoff energy (b) and flux at cutoff (c) are summarized from (a) and plotted as a function of U_p . The points in (b,c) from low to high U_p (also short 100 nm to long 3000 nm wavelength) have a corresponding $\Gamma_R=0.034, 0.55, 8.8, 140, 341, 5000, \text{ and } 3 \times 10^4$. The Eq. (5) cutoff (b) and Eq. (6) flux are shown by highlighted orange dashed lines. Energies possible with a $3.2 U_p$ rule are indicated by shading in (b). 111

ABSTRACT

Light-matter interaction has been a major avenue of study for decades. With the advent of the laser, precise control, manipulation and study of atoms and molecules has been possible, and as the power output of lasers has increased, so has our understanding of the interaction of light with matter. As the peak power of lasers increase from the terawatt to petawatt and soon the exawatt, our comprehension of the interaction with atoms and molecules with these intense light fields must grow. Our understanding of ionization processes such as tunneling ionization, dissociative ionization and enhanced ionization have guided us through intensities of up to 10^{19} W/cm², but as the intensity of light reaches farther into the relativistic regime, these ideas must be extended. The work in this thesis presents both theoretical and experimental results that try to extend the process of ionization into this province.

We present a classical, relativistic Monte Carlo calculation investigating the role of the magnetic field on bound state dynamics and ionization for atoms in ultrastrong external radiation fields. Atoms with atomic numbers $1 \leq Z \leq 20$ in external fields from 0.01 a.u. to 10^3 a.u. are studied. We show that in calculations of ionization rates, the dipole approximation of the field yields accurate values compared to a full treatment of classical electromagnetic laser field for intensities up to 10^{23} W/cm². The calculations indicate the quasi-static approximation is valid for external field frequencies less than one-twentieth of the Kepler orbit time for the ionizing state. For ionization at fields above 100 a.u., the magnetic field affects the atom by altering the portion of the bound state that ionizes and deflecting the mean emission angle of the photoelectron angular distributions, though no change in the width of the final state angular emission about this mean occurs. The photoelectron distribution and change in the ionizing bound

state are seen as a first indication of nonperturbative, magnetic field effects for atoms in ultrastrong radiation fields.

The ionization of chlorinated methane molecules (CH_3Cl) in strong and ultrastrong (10^{14} - 10^{18} W/cm²) laser fields is experimentally investigated. The charge states of carbon (C^{m+} , $1 \leq m \leq 4$) exhibit characteristics of molecular ionization, such as Coulomb explosion, and kinetic energies of release have been determined. The energy spectra of the ions show no dependence on the intensity, indicating that the energy comes entirely from a dissociation process. The charge states of chlorine show similar results, with a some correlation between the charge states of carbon and chlorine. A simple 1D classical model of an aligned CCl ion is used to model the interaction and shows that enhanced ionization is a driving influence for lower charge states of carbon and chlorine, but as the intensity grows the response becomes more atomic in nature.

Recollision of an electron with a parent ion for a laser driven atomic system is investigated in the relativistic regime via a strong field quantum description and Monte-Carlo semi-classical approach. We find the relativistic recollision energy cutoff is independent of the ponderomotive potential U_p , in contrast to the well-known $3.2U_p$ -scaling. The relativistic recollision energy cutoff is determined by the ionization potential of the atomic system and achievable with non-negligible recollision flux before entering a “rescattering free” interaction. The ultimate energy cutoff is limited by the available intensities of short wavelength lasers and cannot exceed a few thousand Hartree, setting a boundary for recollision based attosecond physics.

Chapter 1

INTRODUCTION

1.1 Motivation

The study of light-matter interaction has had a long and broad history. Near the beginning, Ptolemy was considering the angles that light made when passing through transparent objects, and this was later codified with Snell's Law involving the refractive index of materials. Later, Isaac Newton was able to show the make-up of white light broken down into its constituent colors due to dispersion considerations. These processes considered the bulk response of a medium to light, whether that light be made up of waves or particles.

Beginning with Planck's considerations for blackbodies, we get the notion of quanta of energy, or photons, and how they interact with matter. Several years after Planck's work, Einstein used them to put forward a theory of the photoelectric effect where a photon of light is absorbed by a material. If the energy of the photon, $\hbar\omega$, is greater than or equal to the work function, W , of the material (later determined as the ionization potential) then an electron will be released. Any energy of the photon that is above the work function will be carried away as kinetic energy in the electron.

The photoelectric effect is an example of an ionization process, and with the advent of the ruby laser by T.H. Maiman in 1960 the intensity at which light can interact with matter has significantly increased. Lasers have allowed many identical photons to impinge on a material and has given rise to the idea of multiphoton ionization. As the intensity of light grew, so did the number of photons in a given volume. This led to tunneling ionization, where there are so many photons, it is impractical to think of individual photon-matter interaction and start to model the light more classically as a wave.

As the intensity of light grows with the next generation of chirped pulse amplification type lasers and the arrival of attosecond (10^{-18} s) pulses, the processes that have thus been explored must be extended in order to understand this next step in light-matter interaction. At these new intensities we can no longer ignore the magnetic field component of light and must understand how it influences the motion of electrons, both bound and unbound. We must be able to determine the outcome of the interaction of ultrastrong laser pulses with different molecules.

This work will explore the response of both atoms and molecules that goes beyond the simple dipole approximation to see the influence of the magnetic field component of light. These investigations are done both theoretically and experimentally.

1.2 Atomic Response with Increasing Intensity

At low intensities ($< 10^{12}$ W/cm²) the response of an atom to the incident light can be characterized by the photoelectric effect. First proposed by Einstein in 1905 [1] the photoelectric effect is associated with the absorption of a single photon by a metal and the subsequent release of an electron that may carry excess kinetic energy. This was later understood as the photon, which has energy $\hbar\omega$, being absorbed by a bound electron that has an ionization potential, IP , that is less than or equal to the photon energy. If the photon has energy in excess of IP then the electron will leave the atom with a kinetic energy, $E_K = \hbar\omega - IP$. This is shown schematically in figure 1.1. The photoelectric effect is the result of the absorption of a single photon, but is it possible to absorb more than one photon?

At intensities larger than those where the photoelectric effect occurs (10^{12} - 10^{14} W/cm²) there is the possibility of the atom to absorb more than one photon in the ionization process. Multiphoton ionization [2, 3] (MPI) is understood as the absorption of a number of low energy photons of energy, $E_\gamma = \hbar\omega$, being absorbed by an electron during the ionization process. This necessarily means that the ionization potential of the electron must be $IP \leq nE_\gamma = n\hbar\omega$, where n is the number of photons absorbed.

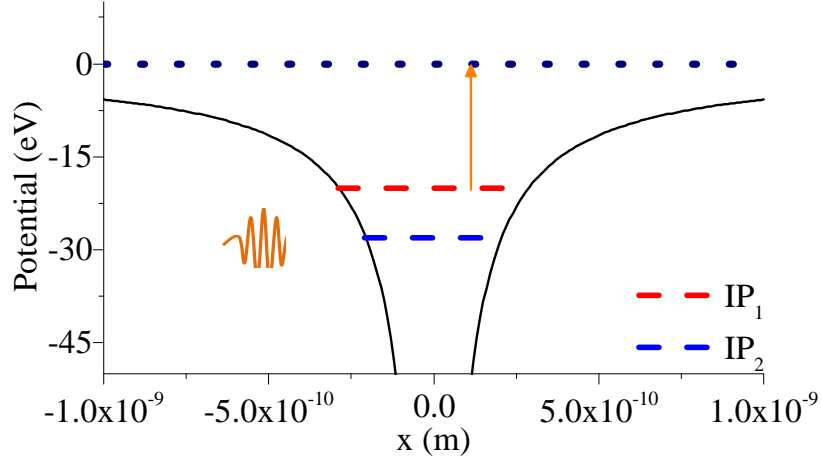


Figure 1.1: Schematic drawing of the photoelectric effect. The absorption of a photon (colored in orange) will allow the ionization of an electron with ionization potential IP_1 as long as $E_\gamma = IP_1$.

This type of ionization is supported theoretically by lowest order perturbation theory (LOPT).

This process can be seen experimentally in the dependence of the number of ions produced versus the number of photons, or intensity, of the incident light and has a relationship that corresponds to $N_{ions} = I^n$. Multiphoton ionization is shown schematically in figure 1.2(a) and an example of ion count versus intensity for argon, starting from neutral argon atoms, is shown in figure 1.2(b). For the argon data, this is the number of Ar^{9+} ions in the intensity range of $\sim 8 \times 10^{17}$ to 5×10^{18} W/cm^2 .

On a log-log scale the slope of the curve changes at 2.0×10^{18} W/cm^2 from roughly 6 to a slope of $\frac{3}{2}$, where nearly all argon atoms are ionized to Ar^{9+} ions, which indicates that from 8×10^{17} to 2×10^{18} W/cm^2 Ar^{8+} requires $n = 6$ photons to ionize an electron and produce Ar^{9+} . This data was collected using laser pulses centered at 800 nm. The energy of these photons would thus be $E_\gamma = 1.55$ eV and the total energy absorbed by the electron would be ~ 9.3 eV.

For the intensities in the regime of MPI and above ($> 10^{14}$ W/cm^2) there is another mechanism that allows the ionization of electrons. Keldysh [2] was able to

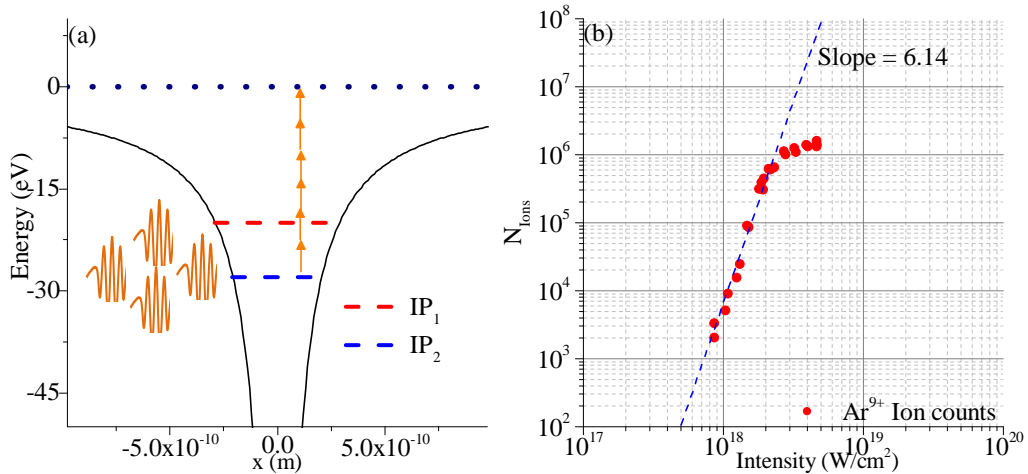


Figure 1.2: (a) Schematic drawing of the multiphoton ionization. The absorption of photons (colored in orange) will allow the ionization of an electron with ionization potential IP_1 as long as $nE_\gamma = IP_1$, where n is the number of photons absorbed. (b) Example of multiphoton ionization of argon. The number of Ar^{9+} vs intensity has a slope of 6, indicative of 6 photon absorption of 800 nm photons.

show that the frequency of the incident radiation was an important consideration. He showed that if the the frequency of the incoming radiation was large enough, the response of the ionic potential and that of the electron would be much slower than that change in the external electromagnetic field, and would result in multiphoton ionization.

However, if the frequency of the electromagnetic field is large enough the atomic potential and the electrons have enough time to respond to its influence and this can result in tunneling ionization. In tunneling ionization the external light field is no longer thought of as individual photons to be absorbed by the electron, it is now considered as a wave that can deform the binding ionic potential. This is drawn schematically in figure 1.3. We can see from the figure that due to considering only the external electric field \vec{E}_{ext} , the ionic potential is reduced enough that an electron with ionization potential IP_1 could tunnel through the depressed barrier.

The rate at which an electron will tunnel through this depressed barrier was first

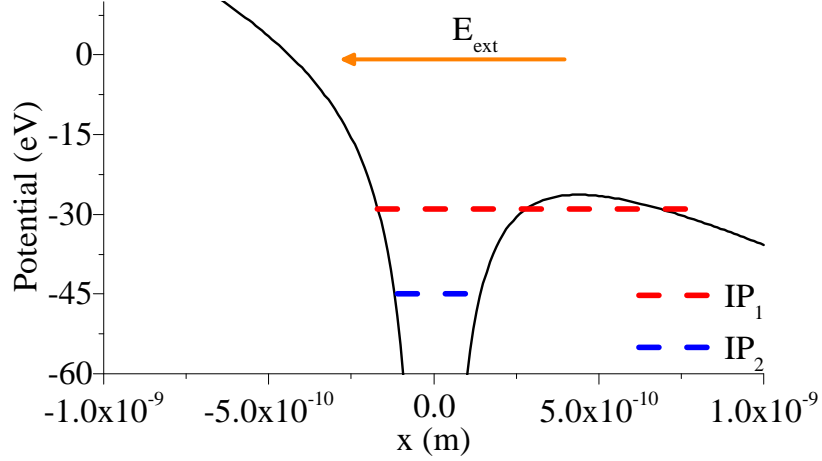


Figure 1.3: Schematic drawing of the Tunneling Ionization. The external electromagnetic field has a sufficiently low enough frequency and high enough magnitude (colored in orange) that the ionic potential will deform enough to allow the ionization of an electron with ionization potential IP_1 by tunneling through the depressed barrier.

calculated by Landau and Lifshitz in the case of a hydrogen atom [4] in a static electric field and was later extended to hydrogen like states in an alternating electric field by Perelomov, Popov, and Terent'ev [5]. After this Ammosov, Delone, and Krainov [6] generalized this to complex atoms in an arbitrary state. All of the relationships derived for tunneling ionization have similar relationships of the rate to the strength of the external field given by,

$$W \propto e^{-\frac{2}{3E_{ext}}} \quad (1.1)$$

where W is the rate of ionization for an electron and E_{ext} is the magnitude of the external electromagnetic field.

The transition from multiphoton ionization to tunneling ionization was first first proposed by Keldysh [2] by considering the time it takes an electron to tunnel through a barrier of width

$$l = \frac{IP}{eE_{ext}} \quad (1.2)$$

where IP is the ionization potential of the electron, e is the charge of an electron, and E_{ext} is the strength of the external field. Considering the average speed of the electron

to be on the order of $\sim (IP/m)^{1/2}$, the frequency, or the inverse of the tunneling time of the electron, can be shown to be,

$$\omega_t = \frac{eE_{ext}}{\sqrt{2mIP}} \quad (1.3)$$

and only relies on the ionization energy and the instantaneous magnitude of the external field.

This frequency is then compared to the frequency of the external field to determine when MPI or tunneling ionization occurs. When the frequency of the external field ω is much smaller than the tunneling rate, ω_t , ($\omega \ll \omega_t$) the main mechanism of ionization is tunneling. In the opposite case, $\omega \gg \omega_t$, multiphoton ionization is the major mechanism for ionization.

These cases are easily summarized by implementation of the Keldysh parameter,

$$\gamma = \frac{\omega}{\omega_t} = \sqrt{\frac{IP}{2U_p}} \quad (1.4)$$

where U_p is the ponderomotive energy, the cycle averaged kinetic energy an electron in an alternating electric field. The ponderomotive energy is given by the relationship,

$$U_p = \frac{e^2 E_{ext}^2}{4m\omega^2} \quad (1.5)$$

The Keldysh parameter easily shows the regime, multiphoton or tunneling ionization, that one can expect by just considering the properties of the external field and the atom or ion in question.

One consideration that must be taken into account with tunneling ionization that relates to the frequency of the external field is the motion of the electron once ionization has occurred. It has been shown [7] that an electron will ionize near the peak of the external field. Once it has ionized, it is influenced mainly by that external field and as the field changes direction, the electron can be directed back towards its parent ion. This is shown schematically in figure 1.4.

There are several possible outcomes to the interaction of the rescattering electron and the parent ion. One possibility is recombination, where the electron is recaptured

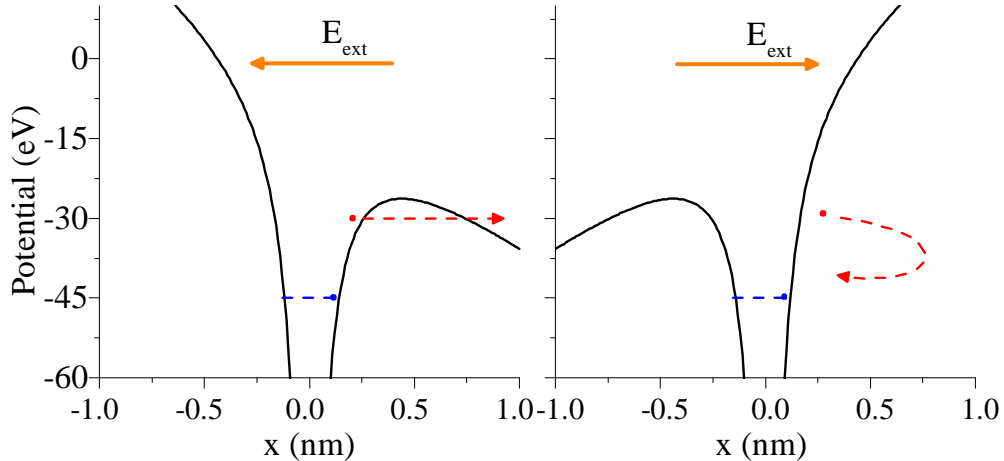


Figure 1.4: Schematic drawing of the rescattering process. The external electromagnetic field tunnel ionizes an electron (coloured in red) that can be driven back towards the parent ion when the direction of the field reverses.

by the ion and emits a photon. This is the basis for high harmonic generation (HHG)[8] where the emitted photon is some number multiple of the ionizing laser frequency. The multiple of the ionizing laser frequency is dependent on the ionization potential of the exiting electron and the amount of energy gained by the electron in the continuum. The relationship that describes the maximum number for the harmonic is given by [8],

$$N_{max} \cong \frac{IP + 3U_p}{\omega} \quad (1.6)$$

where IP and U_p have been defined earlier, and ω is the external field's frequency.

Another possibility is an inelastic collision that imparts part of the ionized electron's energy to the remaining bound electrons, leaving them in an excited state, or there is the possibility of giving one or more of the remaining electrons enough energy to ionize. This result is known as non-sequential ionization (NSI) and was first seen experimentally in [9] as shown in Fig. 1.5.

One defining feature of all the above relationships about the interaction of light with matter is the assumption of the dipole approximation. In this approximation, the laser magnetic field is ignored and the electric field component is the main driving force of electron dynamics. Moreover, this field is approximated by the dipole term only. As

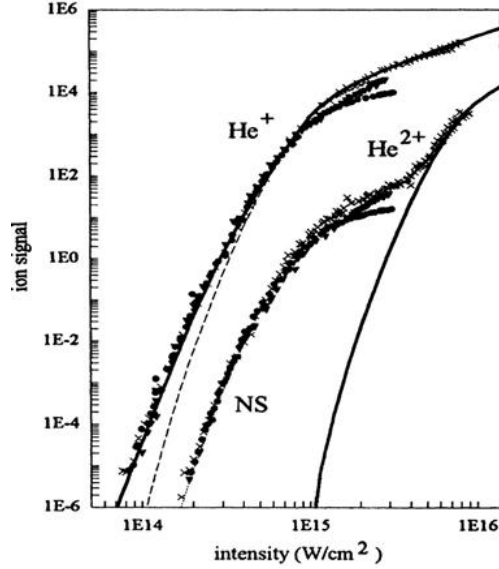


Figure 1.5: Experimental example of non-sequential ionization of Helium. The production of He^{2+} up to $3 \times 10^{15} \text{ W/cm}^2$ is the result of an electron from the ionization of He rescattering with the parent He^+ ion and producing He^{2+} as reported in [9].

the intensity of the light grows ($> 10^{16} \text{ W/cm}^2$) the speed of the electron increases and relativistic effects ($v/c \approx 0$) start to take effect.

Once the external magnetic field can no longer be ignored, one effect that can take place, once the electron is in the continuum, is the deflection of the electron's trajectory along the laser propagation direction. The amount of this deflection is measured by the Lorentz deflection parameter [10] given by,

$$\Gamma_R = \frac{\sqrt{U_p^3 I P}}{3c^2 \omega} \quad (1.7)$$

where c is the speed of light and ω is defined earlier. With rescattering probability being proportional to $e^{-\Gamma_R}$, deflection due to the external magnetic field becomes significant when $\Gamma_R > 1$.

1.3 Molecular Response with Increasing Intensity

The molecular response to light fields follows a similar path as that of atoms. Starting at lower intensities, the photoelectric effect is a large contributor to ionization,

and then multiphoton ionization [11] as the intensity increases.

One must also consider the role that the laser frequency has to play, just as in atomic ionization. With this in mind a theory for molecular tunneling [12] was introduced that expanded the ideas of tunneling ionization to molecules.

Once a molecule has been ionized, there are several outcomes that can occur. The time-scales for electron motion are much smaller than those for atomic motion and the motions of the two can be separated i.e.; one can use the Born-Oppenheimer approximation. This leads to the Franck-Condon condition that states that electronic transitions will occur on much faster time-scale than the time it takes the nuclei to transfer to the new equilibrium position. This new electronic configuration can lead to excited states of the molecule or dissociative states.

When a molecule transitions to a dissociative states the atoms inside will start to move apart with a certain amount of energy. The charge states of the individual atoms will determine the amount of energy that each atomic fragment has. If each atomic fragment has a positive charge, the process of Coulomb explosion [13] can occur, where the positive ions quickly repel each other.

With the molecular ion fragments still under the influence of the laser field, the ionization process can still occur. How does it proceed in this case? One possibility is the enhanced ionization (EI) [14]. This process is understood as that of charge localization on one of the atomic ions that has a deformed potential due to the external field and the neighbouring ion. With the deformed potential, the localized electron can now tunnel through or pass over the middle portion of the potential. This is shown schematically in figure 1.6 where the two ions are separated by some distance R_c [15] that allows the middle barrier to be low enough for ionization from either ion.

By measuring the energies of the atomic ion fragments and knowing their respective charges, one can determine the critical separation of the ions through [15],

$$R_c = \frac{1}{4\pi\epsilon_0} \frac{q_1 q_2}{E_K^{q_1} + E_K^{q_2}} \quad (1.8)$$

where E_K refers to the kinetic energy of the particle and q is the charge of the fragment.

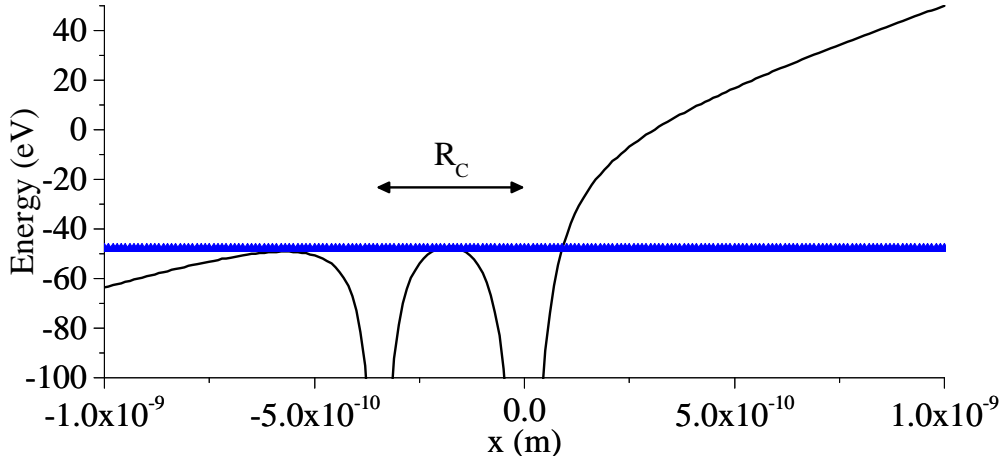


Figure 1.6: Schematic drawing of enhanced ionization. The external laser field drops the potential energy barrier on one side of the molecular ion. When the separation between the ions is at some critical distance R_c , the barrier between the two atomic ions will allow the electron, with ionization potential (blue triangles), to ionize.

Most of the work done on molecular ionization has been done at lower intensities ($\leq 10^{16}$ W/cm²), but what path does molecular ionization follow when the intensity is increased? Some work [16] shows that the production of highly charged ions becomes more atomic-like as intensity increases, and molecular effects can be ignored.

Understanding molecular ionization dynamics in the ultrastrong field can lead to exciting new possibilities including quantum chemical reaction control [17], attosecond resolution of molecular dynamics [18], and molecular orbital tomography [19].

1.4 Experimental Considerations

The detection of ions in the case of atomic ionization is done relatively easy through time of flight mass spectrometry (TOFMS)[20]. For the case of atoms in intense laser fields, the ions have little or no initial momentum and can be easily extracted out of the interaction region. Molecular ionization on the other hand can impart a large amount of energy to ion fragments. In this case, it is conceivable that ions with large initial momentum may not be detected, depending on the geometry of

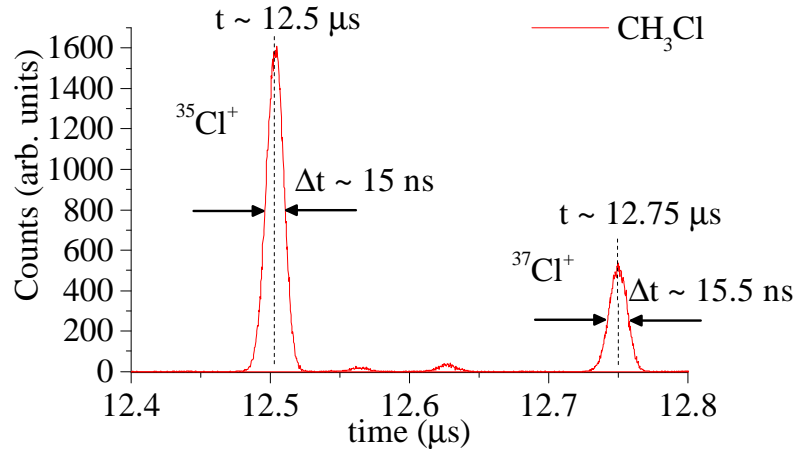


Figure 1.7: Time of flight spectrum from the ionization of chloromethane. Pictured specifically are the ions $^{35}\text{Cl}^+$ and $^{37}\text{Cl}^+$, and indicated are their respective centroid times and FWHM time spans.

the spectrometer.

Some more modern techniques, such as cold target recoil ion momentum spectroscopy (COLTRIMS) [21], make detecting all available ions relatively simple. With traditional TOFMS, the choices for ensuring complete ion detection are limited. One possibility is to shrink the length of the drift region that the ions encounter before detection. Two disadvantages to this approach are the possibility of the initial energy of the ions is so large, the length of the drift region would become negligible. The other disadvantage is the fact that the shorter the drift region the less resolution the spectrometer has.

The mass resolution of a spectrometer is given by the relationship,

$$\frac{m}{\Delta m} = \frac{t}{2\Delta t} \quad (1.9)$$

where Δm and Δt are the full width at half maximum (FWHM) mass and time of a particular peak respectively and t is the centroid of the peak. An example for t and δt are shown for a spectrum of $^{35}\text{Cl}^+$ and $^{37}\text{Cl}^+$ produced from the ionization of chloromethane in figure 1.7.

This means that the resolution of a spectrometer is dependent on the time it takes an ion to reach the detector, and this is controlled through the length of the drift region. With a shorter drift region, the time of flight is reduced and so is the mass resolution of the spectrometer.

The above relation for the mass resolution makes the assumption that the initial energy of the ions is zero, and if this is not true, the mass resolution can also suffer. This is a problem for molecular ionization.

One possible way to clarify the mass resolution for an initial energy is to model the TOF for ions. This can easily be done by solving Newton's equations and these results can be compared to known ion times of flight. This allows the modelling of the TOF for an ion with initial energy and the extent to which an ion spectrum will spread out can be taken into account.

However, it will not allow the distinction of ions that are extremely close together. An example of this from chloromethane are the ions of $^{35}\text{Cl}^{3+}$ and $^{12}\text{C}^+$, which have mass to charge ratios of 11.667 and 12 respectively. For a short drift region, these ions may take only around 1 ms to reach the detector but have a time span of tens of nanoseconds. This will decrease the resolution and make it more difficult to tell one ion from another.

1.5 Arrangement of Topics

The goal of this dissertation is to quantify and clarify the subject of light matter interaction as the intensity of light increases from strong fields (10^{13} - 10^{16} W/cm²) to ultrastrong fields (10^{16} - 10^{20} W/cm²) and to address specifically the influence of the laser magnetic field on bound state dynamics, the ionization process of molecules to ultrastrong fields, and the limits of rescattering in the relativistic regime.

To address these problems, chapter 2 discusses a homebuilt terrawatt laser system that allows us to generate transform-limited 35 fs pulses with hundreds of millijoules worth of energy which can reach intensities of up to 10^{19} W/cm². Also in this

chapter are the details of our time of flight spectrometer that has a short (~ 12 cm) drift tube and how we modelled this to account for ions with initial momentum.

Chapter 3 theoretically discusses the influence of the laser magnetic field on bound state dynamics of a single electron around an ion of varying atomic number Z . Specifically it looks at the difference between the dynamics that are brought upon by solving Hamilton's equations with the full electromagnetic field and those by solving those equations using the dipole approximation.

Chapter 4 details the experiments carried out for molecular ionization in strong and ultrastrong fields. Specifically it looks at how substituting a chlorine atom for a hydrogen atom in methane (changing it to chloromethane) changes the ionization dynamics and the yields of similar ions, namely carbon ions.

Chapter 5 discusses the rescattering process in the relativistic regime, where the influence of the laser magnetic field can no longer be ignored. Specifically the results of two different models for rescattering are investigated. One model is a strong field quantum description of rescattering and the other is a classical Monte-Carlo approach. The agreement between the two models points to an ultimate cutoff in relativistic rescattering energy that is independent of the ponderomotive energy of the electron. This is in contrast with the non-relativistic rescattering energy that scales as $3.2U_p$.

Finally, in chapter 6 we will discuss the possibilities of future work in molecular strong and ultrastrong field ionization, with the possibility of changing from a simple TOFMS setup to a velocity map imaging (VMI) system.

BIBLIOGRAPHY

- [1] A. Einstein. *Ann. Phys. LPZ* **17**, 132–148 (1905).
- [2] L.V. Keldysh. *Sov. Phys. JETP* **20**(5), 1307 (1965).
- [3] G.S. Voronov and N.B. Delone. *Sov. Phys. JETP* **23**(1), 54 (1966).
- [4] L.D. Landau and E.M. Lifshitz. *Quantum Mechanics*. Pergamon Press, New York, NY, 2nd ed. edition, 1965.
- [5] A.M. Perelomov, V.S. Popov, and M.V. Terent'ev. *Sov. Phys. JETP* **23**(5), 926 (1966).
- [6] M. V. Ammosov, N. B. Delone, and V. P. Krainov. *Zh. Eksp. Teor. Fiz.* **91**, 2008–2013 (1986).
- [7] P. B. Corkum. *Phys. Rev. Lett.* **71**, 1994–1997 (1993).
- [8] M. Lewenstein, Ph. Balcou, M. Yu. Ivanov, Anne L'Huillier, and P. B. Corkum. *Phys. Rev. A* **49**, 2117–2132 (1994).
- [9] B. Walker, B. Sheehy, L. F. DiMauro, P. Agostini, K. J. Schafer, and K. C. Kulander. *Phys. Rev. Lett.* **73**, 1227–1230 (1994).
- [10] S. Palaniyappan, I. Ghebregziabher, A. DiChiara, J. MacDonald, and B. C. Walker. *Phys. Rev. A* **74**, 033403 (2006).
- [11] Philip M. Johnson, Michael R. Berman, and David Zakheim. *J. Chem. Phys.* **62**(6), 2500–2502 (1975).
- [12] X. M. Tong, Z. X. Zhao, and C. D. Lin. *Phys. Rev. A* **66**, 033402 (2002).
- [13] T. Ditmire, T. Donnelly, A. M. Rubenchik, R. W. Falcone, and M. D. Perry. *Phys. Rev. A* **53**, 3379–3402 (1996).
- [14] D. M. Villeneuve, M. Yu. Ivanov, and P. B. Corkum. *Phys. Rev. A* **54**, 736–741 (1996).
- [15] J H Posthumus, L J Frasiniski, A J Giles, and K Codling. *J. Phys. B* **28**(10), L349 (1995).

- [16] Sasi Palaniyappan, Rob Mitchell, Rob Sauer, Isaac Ghebregziabher, Samantha L. White, M. F. Decamp, and B. C. Walker. *Phys. Rev. Lett.* **100**, 183001 (2008).
- [17] Robert J. Levis, Getahun M. Menkir, and Herschel Rabitz. *Science* **292**(5517), 709–713 (2001).
- [18] S. Baker, J. S. Robinson, C. A. Haworth, H. Teng, R. A. Smith, C. C. Chirila, M. Lein, J. W. G. Tisch, and J. P. Marangos. *Science* **312**(5772), 424–427 (2006).
- [19] Y Mairesse, N Dudovich, J Levesque, M Yu Ivanov, P B Corkum, and D M Villeneuve. *New J. Phys.* **10**(2), 025015 (2008).
- [20] W. C. Wiley and I. H. McLaren. *Review of Scientific Instruments* **26**(12), 1150–1157 (1955).
- [21] R. Drner, V. Mergel, O. Jagutzki, L. Spielberger, J. Ullrich, R. Moshhammer, and H. Schmidt-Bcking. *Phys. Rep.* **330**(2), 95 – 192 (2000).

Chapter 2

EXPERIMENTAL APPARATUS: TERAWATT LASER SYSTEM AND ION SPECTROMETER

The experimental data collected for this thesis would not have been possible without a homebuilt ultrafast chirped pulse amplification terawatt laser system [1], and its modifications throughout the years [2, 3]. Also utilized are a series of high precision time-of-flight (TOF) mass spectrometers with mass resolutions ranging from $280 \leq m/\Delta m \leq 300$. The following sections will go into greater detail about each portion of the laser system and mass spectrometers.

2.1 Terawatt Laser System

The Chirped Pulse Amplification (CPA) laser system is composed of several subsystems, outlined schematically in figure 2.1. The pulses start from a mode-locked oscillator which are then chirped, or stretched, in time by the pulse stretcher. From the stretcher the pulses are then passed to the regenerative amplifier that increases the energy of the pulses by six orders of magnitude. One more stage of amplification in the multipass amplifier which boosts the energy of the pulses by another two orders of magnitude. After the multipass, the pulses travel to the compressor that removes the chirp produced in the stretcher. These pulses are then used in experiments. The laser system is capable of producing 35 fs pulses with 150 mJ of energy at a 10 Hz repetition rate. Pulses with these characteristics are capable of reaching intensities of 10^{19} W/cm².

2.1.1 Mode-locked Oscillator

Our CPA terawatt laser system begins with a Kerr-lens mode-locked Ti:Saph oscillator. The oscillator produces 2 nJ 35 fs pulses at 76 MHz. It is pumped with a 532

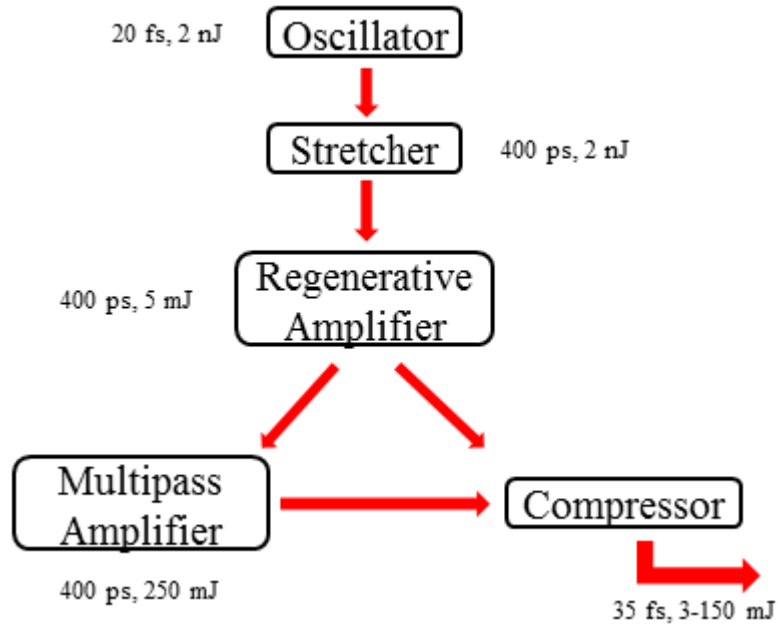


Figure 2.1: Schematic diagram of the CPA terawatt laser system

nm continuous wave, CW, laser running with 1.85-2.25 W of power. The mode-locked power of the oscillator is around 150 mW, this gives an efficiency of around 8%. The alignment of the oscillator is the most important step in the functioning of the laser. A detailed schematic of the oscillator is given in figure 2.2, and the various components will be discussed.

In order to produce the pulses that have been described, the oscillator must meet three requirements [1].

- i)* Operation in multi-longitudinal frequency modes
- ii)* Favoring of mode-locked operation with spatial modes
- iii)* Phase differences group delay between frequency modes minimized

The first requirement is satisfied by the use of Ti:Saph as the gain medium. This gain medium has a broadband range of possible modes, from <720 nm to >840 nm [4]. The second requirement is fulfilled by the geometry of the cavity, the Kerr-lens effect in the gain medium, and by use of a mechanical slit near the output coupler. The

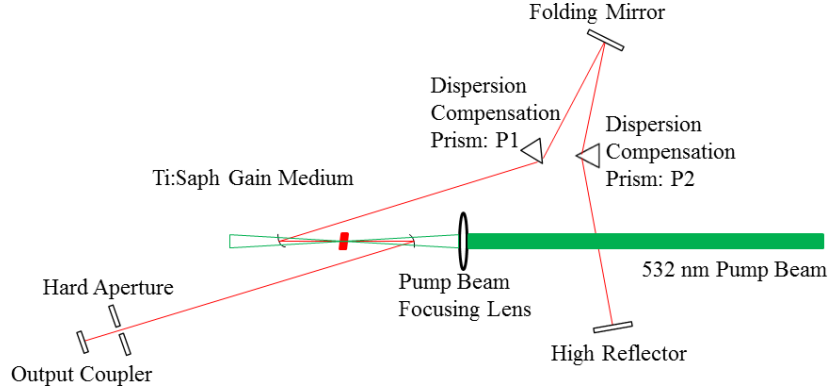


Figure 2.2: Schematic diagram of the Kerr-lens Mode-locked oscillator

third requirement, control of dispersion inside the cavity, is done through the use of a pair of Brewster-angle fused silica prisms. It is this requirement that greatly affects the broadness and stability of the outgoing pulses.

The dispersion of the cavity comes from propagation through material which adds positive dispersion to the pulse and causes pulse broadening and larger phase difference in the frequency modes. This positive dispersion is compensated for by the inclusion of the prism pair. The angular dispersion of a prism pair, for a double pass set-up, is given approximately by the relation [5],

$$-\frac{2\lambda_0^3}{\pi c} L \left(\frac{\partial n}{\partial \lambda_0} \right)^2 \quad (2.1)$$

where λ_0 is the wavelength of the light, n is the index of refraction for the prism material and L is the separation distance between the two prisms. This relationship gives a negative definite relationship for the amount of angular dispersion and is controlled mainly through the separation between the prisms.

With the gain medium having such a broad range of possible modes with a central wavelength between 790 nm and 800 nm, the dispersion must be compensated in such a way as to allow the excitation of most or all of the modes above and below this central wavelength.

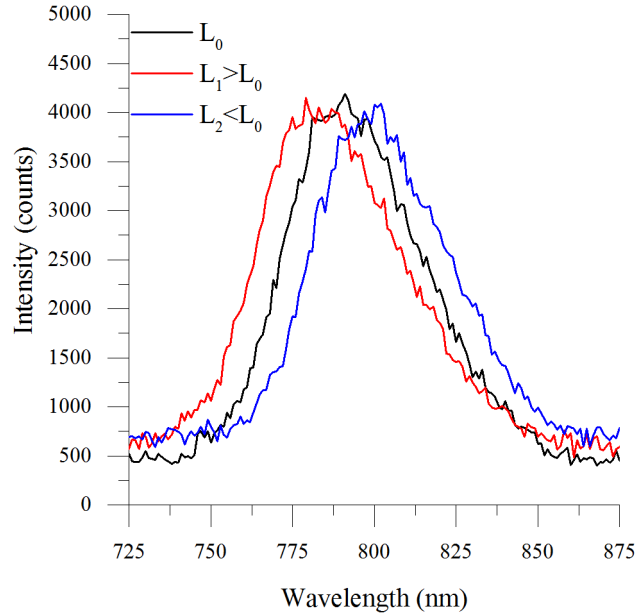


Figure 2.3: Spectrum of the output pulse from the mode-locked oscillator. The black line gives the spectrum for a separation distance between the two prisms of 400 mm, the red line gives the spectrum for a separation distance of 401 mm and the blue line gives the spectrum for a separation distance of 399 mm.

Figure 2.3 gives the spectrum of the output pulse at three different values of the separation distance of the prisms and shows how the central wavelength of the pulse changes. For a separation of the prisms of $L_0 \approx 400$ mm, the central wavelength of the output pulse is in 790 - 800 nm range and the bandwidth of the pulse is around 53 nm. For a separation distance of $L_1 \approx 401$ mm, the central wavelength has shifted to shorter wavelengths to the 780 - 790 nm range and the bandwidth is unchanged. Lastly for a separation of $L_2 \approx 399$ mm the central wavelength has shifted to longer wavelengths to the 800 - 810 nm range and again the bandwidth is unchanged. What we can see from the figure is that when the separation distance between the prisms is increased we get more input from the blue end of the gain medium's spectrum and when the separation distance is decreased we get more input from the red end of the medium's spectrum.

These results are consistent with what we should see from increasing or decreasing the amount of negative dispersion inside the cavity. For a medium with positive dispersion, the longer wavelengths in a pulse's spectrum should travel faster than the shorter, and the opposite would be true for a medium with purely negative dispersion. This would mean that with positive dispersion, redder wavelengths have little phase difference and with negative dispersion bluer wavelengths have little phase difference. Thus by adding more negative dispersion to our pulse and increasing the separation distance between the prisms, we should see a greater contribution of shorter wavelengths which is what is seen. Also, by decreasing the amount of negative dispersion, we should see a greater contribution of longer wavelengths and again this is supported by our data.

The procedure to optimize the bandwidth of our pulse first requires determining qualitatively how much positive or negative dispersion the oscillator has initially. This qualitative determination can be done by examining the characteristics of the output pulse. When there is too much negative dispersion, or too much angular dispersion, a stable output pulse that has a central wavelength shifted more towards the blue end of the spectrum. In the opposite case, too little negative dispersion, the central wavelength is shifted towards the red end of the spectrum and the spectrum narrows. Also, the output pulse becomes more unstable when there is not enough negative dispersion present in the cavity.

In order to optimize the negative dispersion, mode-locking must first be attained. After this, the position of the folding mirror has to be changed. The position of prism P2 must be adjusted to let the central wavelength of the output pulse to be in the 790 - 800 nm range. Prism P1 then is inserted more into the beam path until the power reaches a maximum or there is mode breakthrough. The prism can then be taken slightly out of the beam path so that the power drops to roughly 5% of its maximum.

The slight removal of P1 also serves another purpose. Due to the Kerr-lens effect the mode-locked spatial mode of the laser is smaller than the CW spatial mode of the laser. By slightly removing P1 the CW spatial mode of the laser will be clipped,

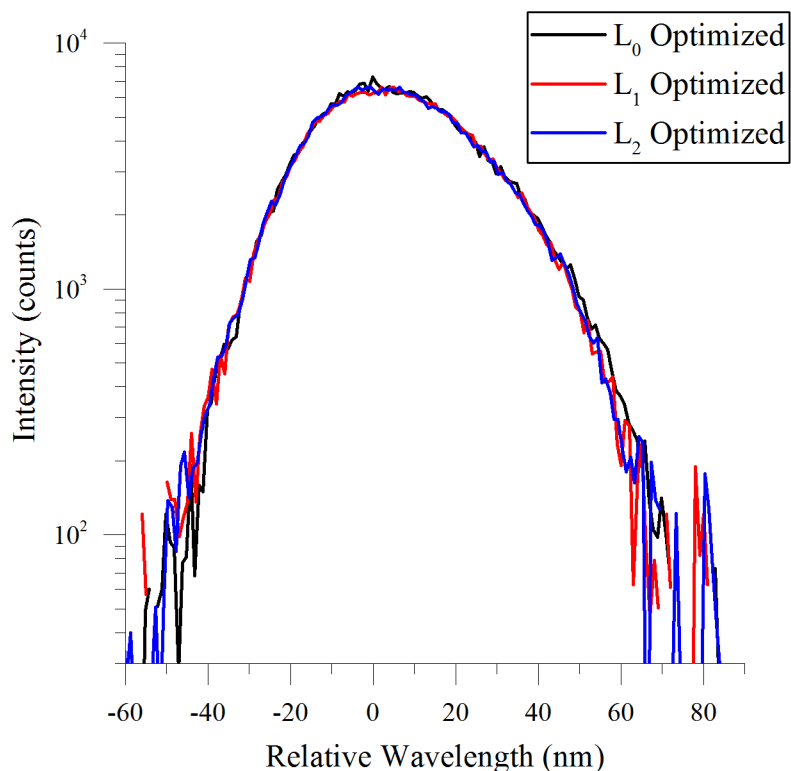


Figure 2.4: Comparison of spectra for the output pulse from the mode-locked oscillator at optimized mode-locking position for three different positions of the folding mirror. Graphical shifting to match central wavelengths and peak intensities has been done.

thus allowing our laser to favour the mode-locking mode helping to satisfy the second requirement.

After removing P1, mode-locking is then optimized by adjusting the positions of the pumping lens and Ti:Saph crystal in order to maximize output power. After mode-locking has been optimized, the position of prism P2 can then be changed to adjust the output spectrum. Little adjustments to the position of prism P1 can be made to ensure no mode breakthrough occurs, but most of the control in the output spectrum is in the position of prism P2.

Figure 2.4 gives the optimized spectrum of the output pulse for three different folding mirror positions. The spectra have been shifted graphically so that the central

wavelengths and peak intensities match. It can be seen that the change in output pulse bandwidth is very small for each of the mirror positions. For position $L_0 \cong 400$ mm the Full Width at Half-Maximum (FWHM) bandwidth is 48 nm, as is the bandwidth for position $L_1 \cong 399$ mm. For position $L_2 \cong 401$ mm the FWHM bandwidth is 47 nm. The largest change can be seen in the wings of the spectra on the level of 10^{-2} of the maximum. This gives the indication that the for these mirror positions the second order dispersion of the pulse is very small and that any phase distortion would come from higher order effects.

The amount of glass that the beam passes through in each of the cases for optimized mode-locking in each of the mirror positions, which determines the amount of third order dispersion (TOD), is estimated in figure 2.5. The estimates show that the total amount of glass that the pulses passes through changes with changing mirror position. The amount of material for an optimized mirror position L_0 is almost 2.1 mm, for mirror position L_1 is almost 2.0 mm and for mirror position L_2 is roughly 1.7 mm. The amount of material for the prisms only changes by a few hundreds of microns from one optimized mirror position to another. This will slightly change the amount of TOD in the pulse, which is reflected in our output spectra.

The last characteristic of the oscillator that must be considered is the output power. The output power of the oscillator should be around 150 mW, but can be ± 50 mW from that value. If the output power of oscillator is too large, there can be mode breakthrough and the pulse can be unstable. These problems can be rectified by dropping the power of the pump laser until the pulse is stable and the output power is in the correct range. If the power is too low, there is a process that can be taken to correct this as well.

An iterative process of adjusting the output coupler and the high reflector to optimize the mode-locked power. This allows the pulse to overlap with the pump beam inside the gain crystal. Most of the adjustments made to the two end mirrors will be in the vertical direction, but slight movement in the horizontal direction can also be made, but the bandwidth and central wavelength of the output will have to be closely

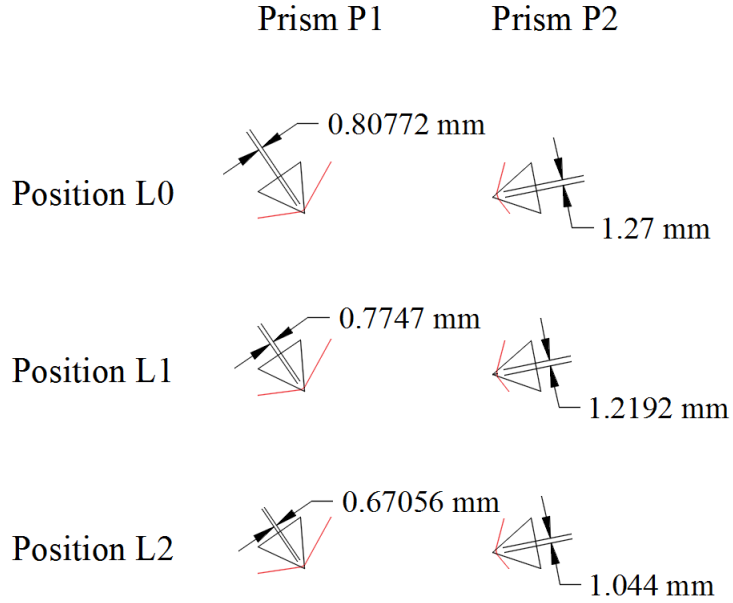


Figure 2.5: Estimates for the amount of glass for each prism at optimized folding mirror positions L_0 , L_1 , and L_2 .

watched since there can be changes to them with horizontal adjustments. Once the power has been optimized the pump power can be raised or lowered as needed.

2.1.2 Pulse Stretcher, Regenerative Amplifier, Multipass Amplifier & Pulse Compression

Once the stable broadband pulses are out of the oscillator they travel through the rest of the laser system as described above. The details of each subsystem of the laser can be found in [1, 2, 3, 6, 7].

2.2 Time of Flight Ion Spectrometry

We use the laser pulses generated in the system described above in our experiments. The experiments conducted in our work rely on time of flight mass spectroscopy (TOFMS). TOFMS relies on creating ions, extracting them from the interaction region using a potential difference, letting them drift for a certain distance and determining the time it takes for their arrival at the detector.

In our experiments, the ions are created by focusing the laser pulses, using an off-axis gold plated parabolic mirror, between two stainless steel plates. The focus of the laser is directed into an effusive gas jet of atoms or molecules. Once the atoms or molecules have been ionized, they are extracted from this interaction region by a potential difference on the stainless steel plates. This potential difference can range anywhere from 500 V to 3000 V. Once the ions pass through the plates they enter a field free region where they drift with a constant velocity until they reach the detector. Our detector is composed of two chevron style micro-channel plates (MCP) biased with a negative potential. The signal from the MCP detector is sent through a pre-amplifier and discriminator. From here the signal is analysed by a picosecond time analyser (PTA) which outputs NIM pulses for collection on a desktop computer or oscilloscope. More details of our ultra high vacuum (UHV) spectrometer can be found in [3].

The spectrometer detailed in [3] extracts the ions from the interaction region using a potential difference on the stainless steel plates. The top plate has a small circular hole in the center ranging anywhere from $100\mu\text{m}$ to $1000\mu\text{m}$. The purpose of this hole being small is that it limits the volume of the focus from which the ions will appear.

The focal volume of the beam can be estimated by assuming a Gaussian spatial mode for the incoming beam. This will give a focal spot radius of,

$$w_0 = \frac{4}{\pi} \frac{f\lambda}{D} \quad (2.2)$$

where f/D is the inverse of the f-number for the optics, and λ is the wavelength of the incoming beam. If the beam is travelling along the \hat{z} direction, then the distance from the focal spot in which the beam's cross sectional area is increased by a factor of two is known as the Rayleigh range z_R and is given by,

$$z_R = \frac{\pi w_0^2}{\lambda} \quad (2.3)$$

These relationships allow us to define the beam waist as a function of z as,

$$w(z) = w_0 \sqrt{1 + \left(\frac{z}{z_R}\right)^2} \quad (2.4)$$

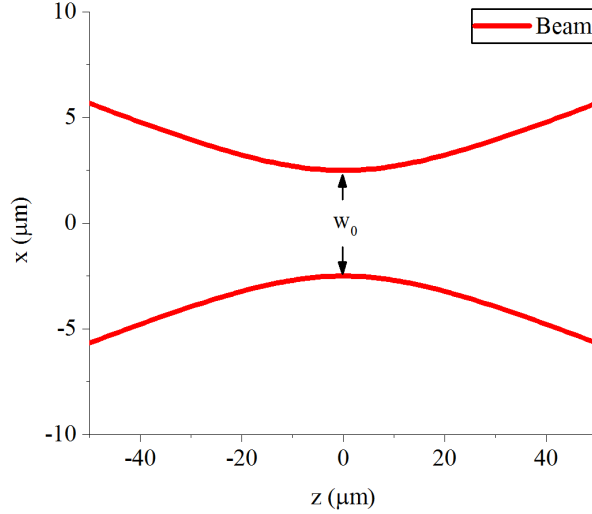


Figure 2.6: Diagram of beam waist in the $x - z$ plane. At $z = 0$ the minimum diameter of the beam, $2w_0$ is shown.

Figure 2.6 shows the beam waist as a in the $x - z$ plane as a function of z .

Switching to cylindrical coordinates it is easy to define the intensity profile for the beam as a function of the z coordinate,

$$I(r, z) = \frac{2P}{\pi w_0^2(z)} \exp\left(\frac{-2r^2}{w_0^2(z)}\right) \quad (2.5)$$

where P is the power in the beam and r is the transverse distance from the \hat{z} axis. From this we can see that the intensity can drop from its peak to a value that is roughly two orders of magnitude lower within the Rayleigh range. This will still allow for a large number of ions to be created outside of the focus. By limiting the size of the hole in the top plate, we can limit the ions coming to the detector only to those coming from the highest intensity parts of the focal volume.

The problem with using a circular hole in our top plate is that it will not only limit ions coming from the highest intensities but it will also limit those ions to having very little, close to zero, initial energy.

For a hole of $1000\mu m$, the initial energy that ions can have in a direction perpendicular to the direction of the detector is less than 5 eV. This limiting of initial

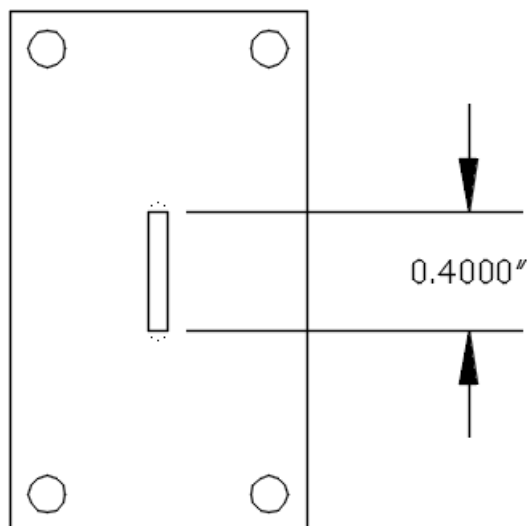


Figure 2.7: Diagram of the rectangular aperture in stainless steel top plate.

energy can be overcome by enlarging the size of the hole in the top plate, however the shape must also be changed. In order to still limit the intensity region from which ions are originating the aperture in the top plate must be small in the propagation direction, \hat{z} . In order to allow a larger initial energy of ions to be collected the aperture must be large in the transverse direction. This is accomplished by making the aperture rectangular. Figure 2.7 shows the dimensions of the top plate that have replaced those with a small circular aperture.

2.2.1 Second Iteration: Inclusion of Magnetic Field

Using our original spectrometer and conducting experiments on molecules detailed in chapter 4 we observed a difference in the amount of ions detected when the polarization of the laser pulses was parallel to the drift region as compared to perpendicular to it, termed vertical polarization (VP) and horizontal polarization (HP) respectively and diagrammed in figure 2.8.

This difference comes from the ions having an initial momentum that is along the polarization of the laser pulses. The initial momentum of these ions changes the time of flight if the momentum is towards or away from the detector. For those ions

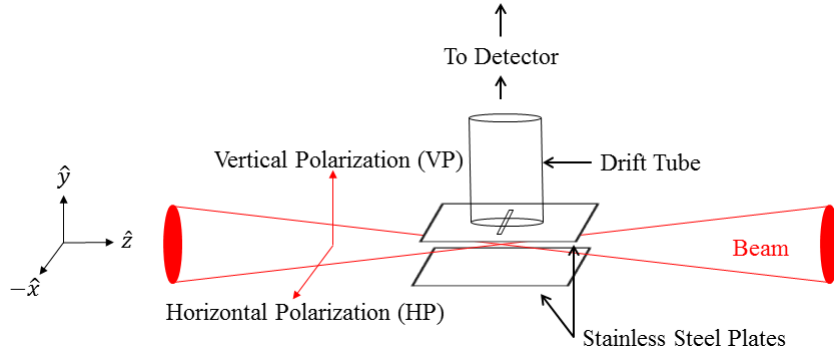


Figure 2.8: Schematic diagram of horizontal and vertical polarizations. These are the orientation of the pulse’s electric field in relation to the drift tube and the detector.

that come off with an initial momentum perpendicular to the direction of the detector, it is possible, depending on the value of the initial momentum, that the ions will not make it the detector based on the geometry of our spectrometer.

To overcome this possible systematic error in our data, we built a new ion spectrometer that was similar to the one described, but this one included a magnetic field parallel to the direction of ion drift in the spectrometer. In this spectrometer the laser would again be focused into an effusive gas jet between stainless steel plates by an off axis gold plated parabolic mirror as depicted in figure 2.9. This figure gives a top-down view of the spectrometer with the focal point of the mirror visible in the center of our stainless steel plates

Figure 2.10 gives a side view of the spectrometer with the flight tube clearly visible. From the figure, we can see that the total drift region is around 46 cm allowing for a large mass discrimination of roughly $m/\Delta m = 180$. The magnetic field generated in the flight tube is produced by four solenoid type magnets that fit over the flight tube. Each magnet is made up of size 18 American wire gauge magnet wire that is wrapped around a base that is roughly three inches in length and two inches in diameter. This allows for roughly 68 loops and 12 layers of wire on each magnet. With this amount of wire, each magnet has a resistance of roughly 8Ω .

The power supplied to our magnets is generated by two HP/Agilent 6264B DC

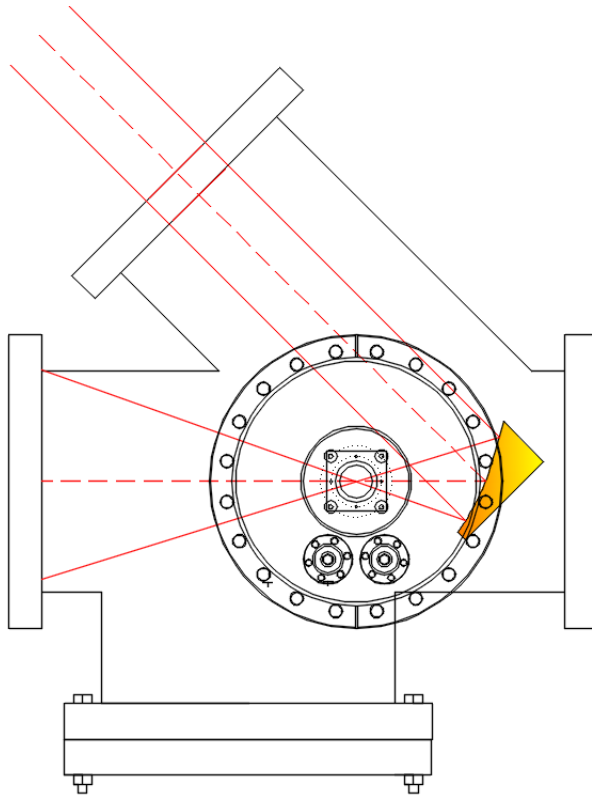


Figure 2.9: Top down view of spectrometer detailing beam focus and off-axis gold parabolic mirror.

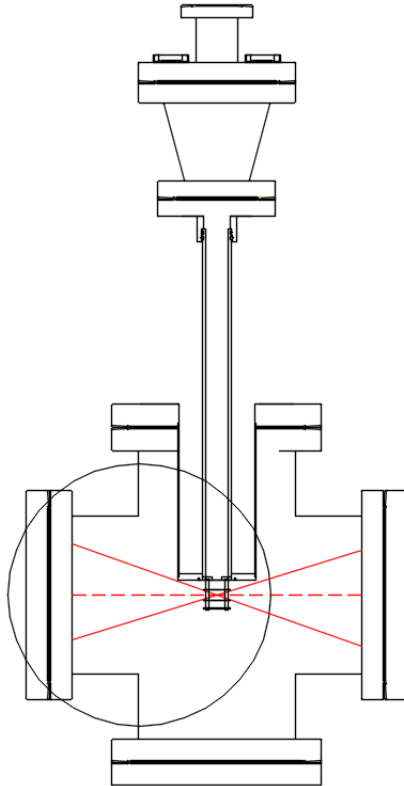


Figure 2.10: Side view of spectrometer detailing the length of the drift tube along with home-built solenoid magnets.

variable power supply (0-20 V/0-20 A) units connected in parallel. With these power supplies and our solenoids connected in parallel the total current in our magnets should be around 10 Amperes at maximum voltage. Measurements of the magnetic field in regions A and B (shown in Fig. 2.10) are shown in fig. 2.11. We can see from Fig. 2.11(b) that at a power supply voltage of 20 V, the magnetic field has a value of 102 Gauss, which is very close to a calculated value of 112 Gauss for a 10 Amp current running through a 2 Ω resistor.

With these values for the magnetic field, we can estimate the energy that ions can have in order to be confined to the flight tube and be detected. With the assumption that the ions come out of the interaction region perpendicular to the flight tube axis and the magnetic field is parallel with the flight tube axis, we can use the Lorentz force law,

$$m\vec{a} = q\vec{v} \times \vec{B} \quad (2.6)$$

$$m\frac{v^2}{r} = qvB \quad (2.7)$$

$$p = qrB \quad (2.8)$$

$$\sqrt{2mE} = qrB \quad (2.9)$$

$$E = \frac{(qrB)^2}{2m} \quad (2.10)$$

Where r is the radius of the circular path that the ion will follow, E is the energy of the ion, B is the value of the magnetic field, m is the mass of the ion, and q is the charge of the ion. For a typical ion that we will look at, C^{4+} , and using the magnetic field measured and a value of r being half the diameter of the flight tube, being 1 inch, the value of the energy that a C^{4+} ion can have in order to be detected is, $E \approx 1.0$ eV.

We can compare this to the energy we see from the ions in our TOF spectra. When the polarization of the laser is parallel to drift tube axis, any initial momentum the ions have will show up in the spectra as a time difference in the ions that come off in a direction towards the detector showing up at an earlier time and those that come off in a direction away from the detector showing up at a later time, as seen in figure 2.12.

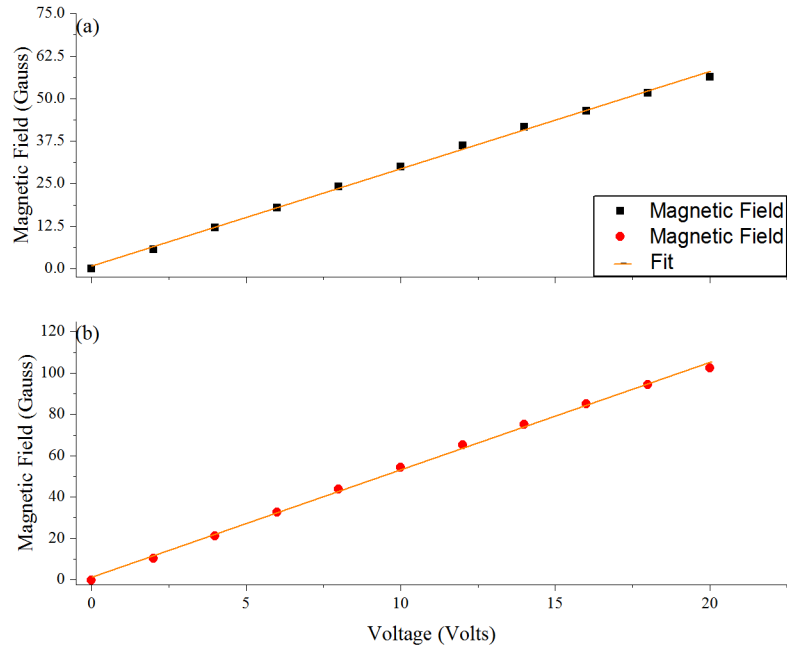


Figure 2.11: Magnetic field measurements in (a) the region just inside the drift tube, and (b) an inch above the drift tube.

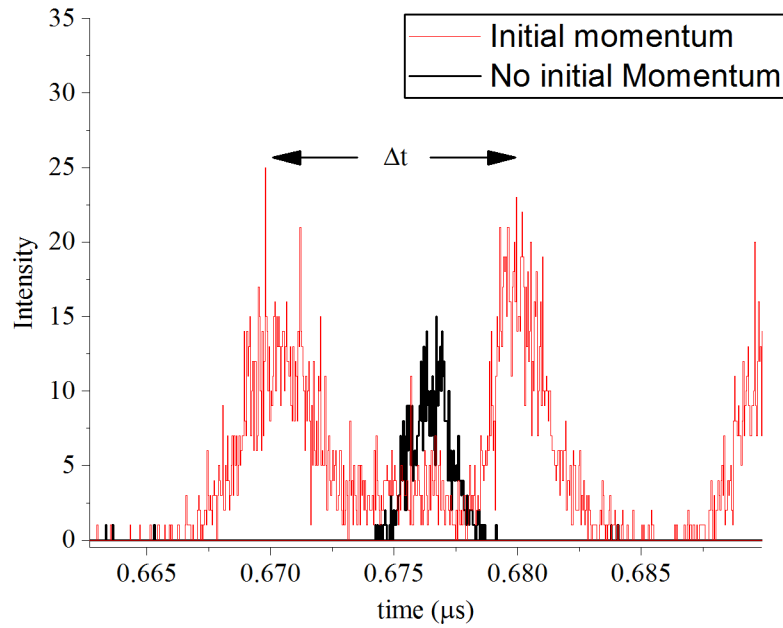


Figure 2.12: Time of flight traces for a C^{4+} ion with horizontal and vertical polarization.

We can estimate the initial energy of the ions by knowing a few details about the spectrometer, the ion itself, and information from the spectrum. If the mass to charge ratio of the ion is determined and we know the repelling voltage on the stainless steel plates, along with their separation are, and we measure the time difference, Δt , of the fast and slow ions in the spectrum, the energy can be estimated by [8]

$$E_k = \frac{1}{8m} \left(q \left(\frac{\Delta V}{l} \right) \Delta t \right)^2 \quad (2.11)$$

where m is the mass of the ion, q is the charge, Δt is the measured time difference, ΔV is the voltage difference on the stainless steel extraction plates, and l is their separation distance.

From this relationship and measuring the time difference for particular ions, we find that the typical kinetic energies range from 5 eV to 35 eV for C^+ to C^{4+} , respectively.

In order to contain ions with these types of energies, the magnetic field would need to be a lot stronger. This might be possible with better designed or constructed magnets or a better power supply. However, there is another solution in order to detect ions with large initial energies.

2.2.2 Third Iteration: Truncated Flight Tube

With large initial energies, the strength of a magnetic field required to detect ions with initial momentum perpendicular to the axis of the drift tube would need to be on the order of 500 T. One other possibility to ensure ion detection is to shorten the distance that the ions have to travel. This can be accomplished by shortening the length of the drift region that the ions are in before being detected.

The length of the flight tube will be constrained by the size of the detector and the voltage difference on the extractor plates. Simply using Newton's equations and assuming that the ions start in the middle of the extractor plates, we can show that the total distance of the drift tube should be

$$D = \sqrt{\frac{q\Delta V}{2E}} \left(\frac{d}{2} \right) - l \quad (2.12)$$

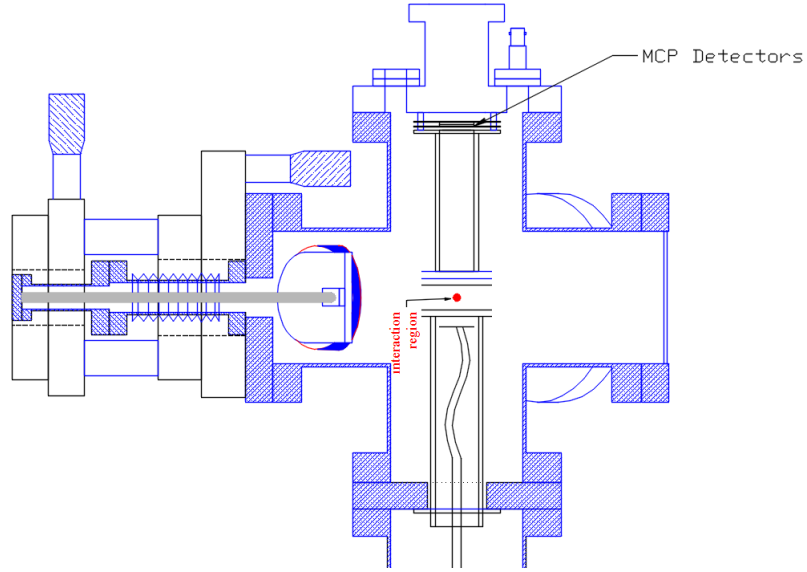


Figure 2.13: Third iteration of TOF spectrometer with truncated flight tube.

Where q is the charge on the ion, ΔV is the voltage difference on the extractor plates, E is the initial energy of the ion, d is the diameter of the detector, and l is the separation distance of the extractor plates. For our spectrometer, the values of the above variables are: $l = 1.778 \times 10^{-2}$ m; $d = 2.54 \times 10^{-2}$ m. The value of the potential difference should be as large as possible so that the ions have little time to travel in the direction perpendicular to the direction of the detector, thus $\Delta V = 3000$ V. We will assume that the ions have an initial energy, $E = 50$ eV. Using these values, we estimate a value of $D \approx 12$ cm.

The new chamber that was build is shown in figure 2.13 and has a drift tube of roughly 15 cm. This is slightly longer than that calculated to contain ions with an initial energy of 50 eV, but will allow ions with an initial energy of roughly 35 eV to be detected.

The advantage of a shorter drift region is apparent, allowing the collection of ions with large initial energies, but the disadvantage of a shorter drift region is that the mass discrimination, $m/\Delta m$, decreases. With a smaller mass discrimination the ability to determine where in the spectrum a particular ion shows up or the span of

time that the ion covers becomes more difficult.

To overcome the smaller mass discrimination, a computer program was written, shown in Appendix C, that calculates the time an ion with a particular mass to charge ratio takes to reach the detector. This time will change depending on several parameters that are varied between certain limits. Once the time is calculated it is compared to a measured time for that ion and the residual, $S = \left(\frac{t_{exp}-t_{calc}}{t_{exp}}\right)^2$, where t_{exp} is the measured time of the ion's arrival at the detector and t_{calc} is the calculated time of arrival, is computed and minimized until optimal values for the parameters are attained.

With the smaller mass resolution, how are the experimental times for a given ion determined?

Figure 2.14 shows an experimental trace of the TOF spectrum gathered in the third iteration of our ion spectrometer of methane. The methane that was used utilized the ^{13}C isotope of carbon which minimizes possible degeneracies with other ions with the same mass to charge ratio as ^{12}C . In the figure, there are peaks that are labelled, specifically the ion fragments of carbon, oxygen and a couple of homonuclear ions of nitrogen and oxygen.

The identity of individual peaks was first determined by relying on the fact that the time an ion arrives at the detector is dependant on the mass to charge ratio of the ion, which can be written as,

$$t \propto \sqrt{\frac{m}{q}} \quad (2.13)$$

This does not help unless more information about the chamber is available, but a ratio of two arrival times can be taken and times or mass to charge ratios can be determined. This method allows the determination of times or mass to charge ratios if the mass to charge ratio and time of one of these ions is known. The known ion can be as simple as H^+ or as complex as H_2O^+ . Once the time for one of these ions is known, the time for any ion can be determined through,

$$t_1 = t_2 \sqrt{\left(\frac{m_1 q_2}{m_2 q_1}\right)} \quad (2.14)$$

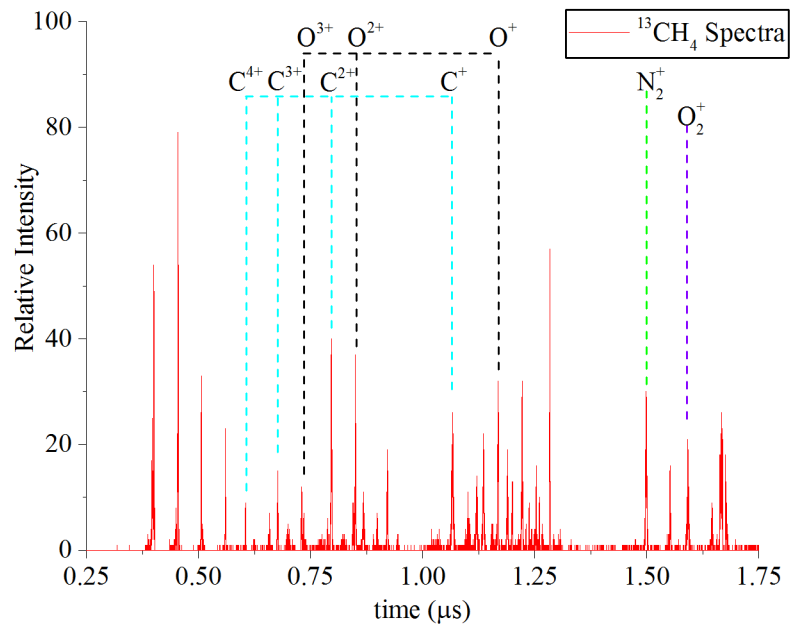


Figure 2.14: Time of flight trace for $^{13}\text{CH}_4$ collected at an intensity of $I \sim 1 \times 10^{16}$ W/cm^2 . Indicated are the fragmental ions of $\text{C}^+ - \text{C}^{4+}$, $\text{O}^+ - \text{O}^{3+}$, N_2^+ and O_2^+ .

We use this method by first collecting a spectrum with no gas present in the chamber. Even though the spectrometer is a UHV setting, it is impossible to get a true vacuum. This means that there is some background gas inside the chamber. This background gas is atmosphere which is composed mostly of nitrogen, oxygen, and water vapour. Once a spectrum is collected with the background gas it is easy to identify certain peaks.

Since hydrogen has the smallest mass to charge ratio, the H^+ ion should arrive first to the detector. Water vapour and the time interval around it has a unique form. With the intensities that are used in our experiments a spectrum collected with background gas should have peaks produced by H_2O^+ , OH^+ and O^+ which have mass to charge ratios of 18, 17 and 16 amu/C respectively. The O^+ ions come from the oxygen in the background gas as well from the water vapour. The OH^+ could only come from the water vapour. We can use the times for these ions to determine the time for ions that we are interested in for a particular experiment.

Once individual peaks are identified and experimental times are determined, the code is run and parameters for the chamber are optimized. The parameters that are varied in this code are the voltage difference across the extraction region, the length of the drift region, the starting position of the ions in the extraction region, the length of a region near the detector where the ions are accelerated toward the detector, and a time offset. Each of these parameters have a set of limits that can be determined by measurements, in the case of the drift region, or approximated, in the case of the time offset this was seen from the TOF for hydrogen ions in our spectra. Once the parameters are allowed to vary, the code calculates the time for a particular ion and the residual is calculated. Shown in figure 2.15(a) are values for the residual from three different values for the given parameters. The values for each trial are shown in table 2.1.

With the code we are able to model the TOF for ions with a precision on the picosecond level as shown in figure 2.15(b). The plot shows the absolute value of the difference in the calculated times with three different sets of optimized parameters from

Table 2.1: Values for varied parameters in code to calculate time of flight for ions in UHV chamber where, V is the potential difference across the extraction region; D is the length of the drift region; y_0 is the starting position of the ions in the extraction region; d is the length of a region near the detector where the ions are accelerated toward the detector; t_0 is the time offset

Trial	V (V)	D (m)	y_0 (m)	d (m)	t_0 (s)
0	2995	0.11975	-5×10^{-4}	3.25×10^{-3}	1.425×10^{-7}
1	2993	0.12175	-1×10^{-3}	3.88×10^{-3}	1.425×10^{-7}
2	3024	0.121	-2.5×10^{-4}	3.5×10^{-3}	1.35×10^{-7}

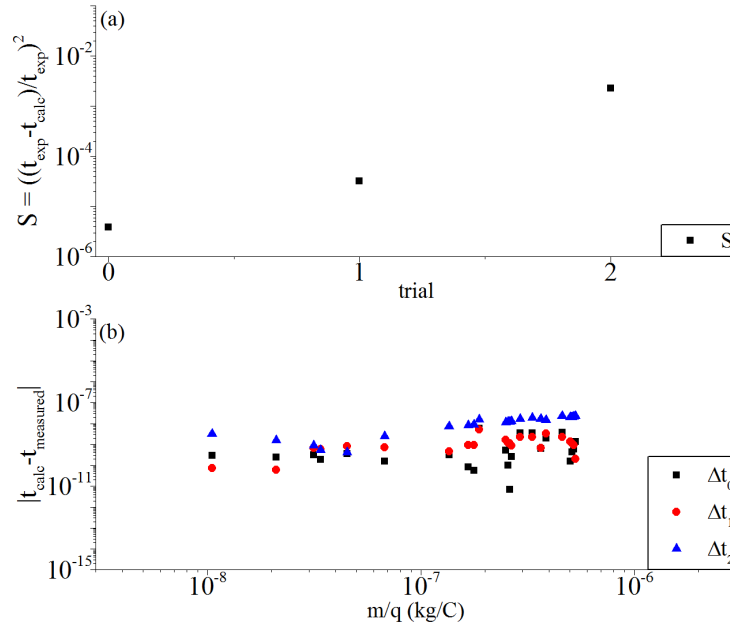


Figure 2.15: (a) The residual, $S = \left(\frac{t_{exp} - t_{calc}}{t_{exp}}\right)^2$, for three different values of parameters. (b) the time difference, $\Delta t = |t_{exp} - t_{calc}|$, with the values of the parameters in part (a).

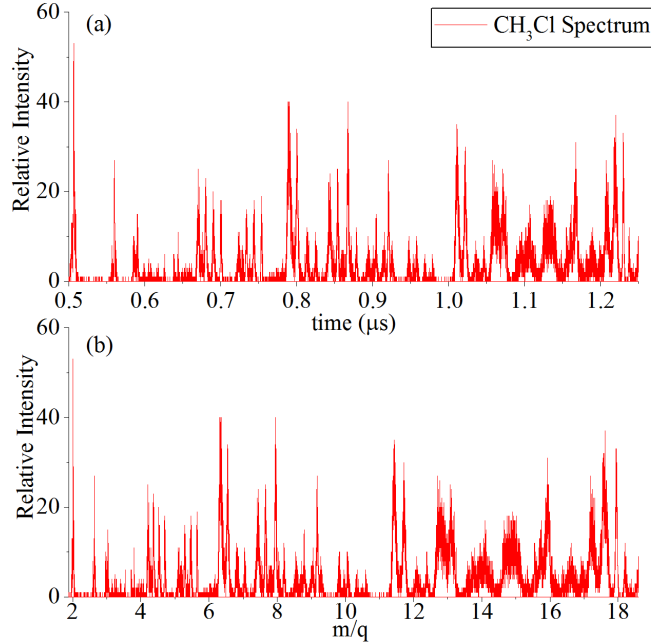


Figure 2.16: (a) TOF spectrum for CH₃Cl taken at an intensity of 1×10^{16} W/cm².
 (b) Transform of TOF into spectrum of mass to charge ratio.

table 2.1 and the measured times for the ions.

Using our model of the spectrometer, we are able to extract from the time arrival of ions the mass to charge ratio for those ions. In figure 2.16(a), we see that the time of flight for CH₃Cl is quite complicated, and determining which ion peak is which can be difficult. However, using our model of the spectrometer, we can turn this TOF spectrum into a spectrum of mass to charge ratios. This will allow us to determine what peak is associated with which ion since there are only certain ions that will be available inside the chamber.

Figure 2.17 shows the spectrum for two different gasses, methane and chloromethane. We can see from the figure that for methane the spectrum is very clear with clean narrow peaks. Chloromethane, on the other hand, has many peaks that sometimes run together.

Closer inspection of a mass to charge ratio equal to 4.33 shows that methane has a single peak that corresponds to C³⁺, whereas chloromethane has three distinct peaks.

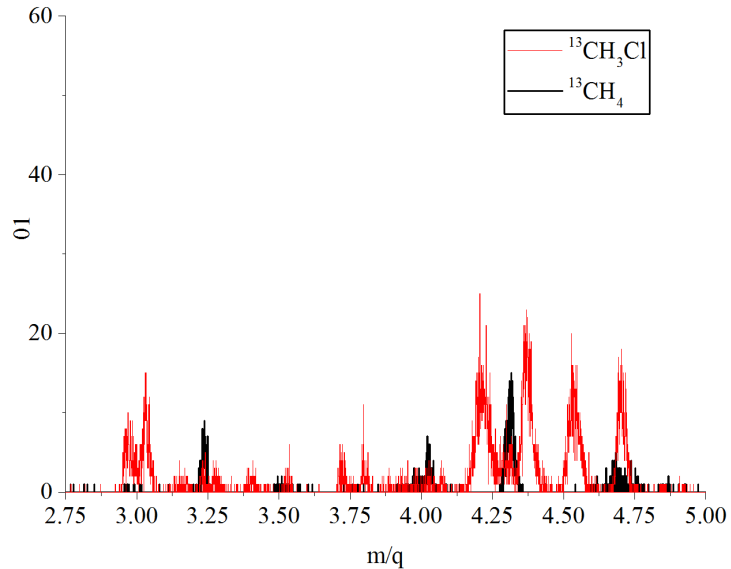


Figure 2.17: TOF spectrum for CH_4 and CH_3Cl taken at an intensity of 1×10^{16} W/cm^2 as a function of mass to charge ratio in vertical polarization. Isotope carbon-13 is used in the gasses.

If this spectrum was in units of time, it would be difficult to determine if the three peaks near 4.33 were separate ions or the same ion with different initial energies. The two large peaks on either side of the smaller one at a value of 4.33 have mass to charge ratios of 4.2 and 4.37. These values of mass to charge do not have a corresponding mass that fits into a known mass that could be in our spectrometer.

The purpose of this spectrometer is to ensure that ions with large initial energies will be detected irrespective of laser polarization. With a truncated drift tube identifying ions in the TOF spectrum can be difficult which is solved with our model of the spectrometer. We can now compare spectra of ions with large initial energies for any differences for vertical versus horizontal laser polarization.

Figure 2.18(a) gives the spectra for CH_3Cl with horizontal polarization and 2.18(b) with vertical polarization. Specifically shown are the C^{4+} ions and a structure in the spectra can be seen to be quite different. For vertical polarization, three distinct peaks are present. The peak with smaller values of m/q are those that have initial

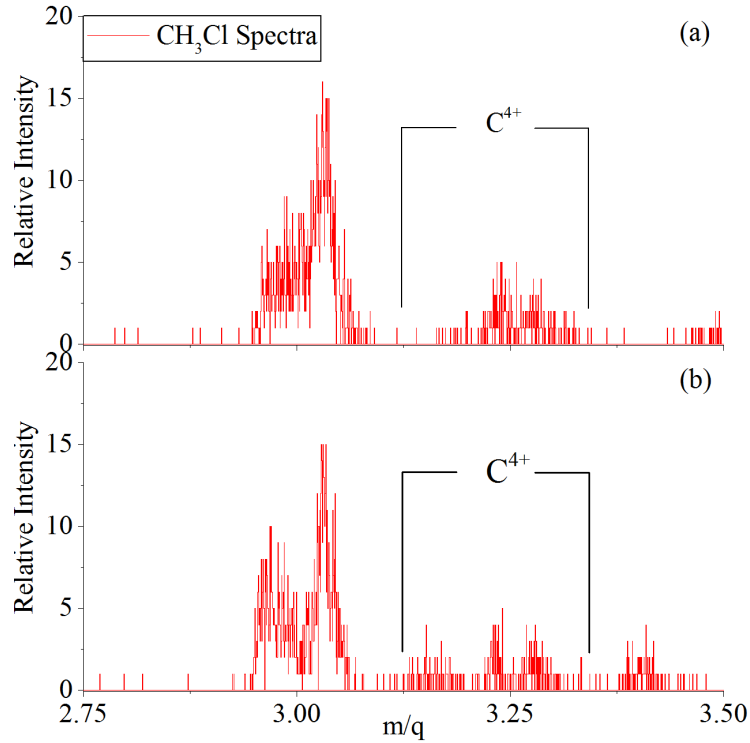


Figure 2.18: TOF spectrum for CH_3Cl taken at an intensity of $1 \times 10^{16} \text{ W/cm}^2$ as a function of mass to charge ratio in (a) horizontal polarization, and (b) vertical polarization.

momentum in the direction of our detector and those with larger m/q with initial momentum away from the detector. The central peak at $m/q = 3.25$ are the ions with zero momentum towards or away from the detector. This could be ions with no initial momentum at all or those that come out of the interaction with horizontal momentum. In horizontal polarization, the central peak is broadened and the smaller m/q peak is almost non-existent.

The total number of C^{4+} ions in each polarization in figure 2.18 is 342 and 362 for horizontal and vertical polarization respectively. This is within the \sqrt{N} noise for the total number of counts, which indicates that there is no difference in the total number of ions we collect at either polarization.

Multiple collections at varying lengths of time and pressure allow us to get an idea of the energies that the C^{4+} ions have due to the interaction. The initial energy

of these ions is 34.6 ± 5.79 eV. With little difference in the number of ions collected, the truncated drift tube has given us a detection method that is independent of laser polarization for up to 35 eV of initial energy.

BIBLIOGRAPHY

- [1] Zhao hui Yang. *Development of a University-Scale Tera-Watt Laser System*. PhD Thesis, University of Delaware, 2001.
- [2] Anthony DiChiara. *Ionization Measurements of Argon, Krypton and Xenon Atoms with Petawatt to Exawatt cm^{-2} Laser Fields*. PhD Thesis, University of Delaware, 2007.
- [3] Enam Chowdhury. *Atomic Response in Ultra-Intense Fields*. PhD Thesis, University of Delaware, 2004.
- [4] Milton Birnbaum and Alexander J. Pertica. *J. Opt. Soc. Am. B* **4**(9), 1434–1436 (1987).
- [5] J. P. Gordon and R. L. Fork. *Opt. Lett.* **9**(5), 153–155 (1984).
- [6] Sasikumar Palaniyappan. *Relativistic Rescattering and Multi-electron Ionization of Atoms and Molecules in Ultra-strong Laser Fields*. PhD Thesis, University of Delaware, 2008.
- [7] Nagitha Ekanayake. *Photoionization of Highly Charged Ions from Ultra-intense, Ultraviolet and Near-infrared Radiation Fields*. PhD Thesis, University of Delaware, 2013.
- [8] Kennosuke Hoshina, Yusuke Furukawa, Tomoya Okino, and Kaoru Yamanouchi. *J. Chem. Phys.* **129**(10), 104302 (2008).

Chapter 3

CLASSICAL STUDY OF ULTRA-STRONG, NONPERTURBATIVE FIELD INTERACTIONS WITH A ONE-ELECTRON ATOM: VALIDITY OF THE DIPOLE APPROXIMATION FOR THE BOUND STATE INTERACTION

3.1 Introduction

Ionization is an essential response of the atom to a strong external field. It is an interaction that spans from Rydberg atoms [1, 2, 3, 4, 5] in microwave radiation to multielectron excitation in strong [6, 7, 8, 9, 10, 11, 12, 13, 14, 15, 16, 17] and ultrastrong [18, 19, 20, 21, 22] optical frequency fields. Advances in laser technology continue to push the boundaries of this interaction in frequency and intensity with the emergence of 4th generation free electron lasers [23, 24, 25], high peak power terawatt [26, 27, 28, 29, 30] and petawatt lasers [31, 32, 33, 34].

Many strong field models that address the interaction of these sources with atoms and molecules [35, 36, 37, 38, 39, 40] capitalize on the dipole approximation, where the laser magnetic field is assumed to be zero ($B_{laser} = 0$) and the physics is dominated by the external electric field (E_{laser}). As the external field and velocity of the interacting atomic or molecular states increase, this approximation will breakdown [41]. The new frontier in ultrastrong radiation-matter interactions has attracted significant theoretical interest [42, 43, 44, 45, 46, 47, 48, 49]. Yet precision experimental results up to intensities as high as 10^{19} W/cm² [50, 51, 52] have not observed any affect of B_{laser} on the one-electron ionization yield. Recent experiments and models have included B_{laser} in their treatment of phenomena and address primarily photoelectron final states [53, 54, 55] and rescattering [56, 57, 58]. Photoelectron final state measurements verified the forward deflection of the photoelectron in the continuum due to the large momentum

transfer from the photons to the electron and also revealed the angular distributions of these photoelectrons [59]. Ultrastrong field rescattering models address the continuum electron and its deflection by the B_{laser} Lorentz force as it is being accelerated by E_{laser} . In the rescattering process, B_{laser} is believed to have an influence above intensities of 3×10^{16} W/cm² for optical fields and more generally when the relativistic rescattering parameter $\gamma_R > 1$ [41, 60] where $\gamma_R = \sqrt{U_p^3 V_{IP}} / (3c^2 \omega)$ for a radiation field with a peak magnitude of E_0 , speed of light c , carrier frequency of ω , ponderomotive energy of $U_p = E_0^2 / 4\omega^2$, and V_{IP} ionization potential.

Rescattering and photoelectron final state research deal with the result of the ultrastrong external magnetic field interaction after the electron ionizes. There are still fundamental questions on how the ultrastrong field affects the bound state dynamics and ‘birth’ of the photoelectron. It has been reported that even in the intensity range of 10^{17} W/cm² to 10^{18} W/cm² for quasistatic as well as high frequency, stabilization fields, the magnetic field can influence ionization [61, 62]. A clear understanding of the ionization mechanism is crucial insight into the physics behind the ultrastrong field interaction [63]. Conceivably, it is possible ultrastrong magnetic fields and the electron cyclotron frequency in the bound state can create dynamics, such as is the case for ‘cycloatoms’ [64]. Because the strong field is comparable to the Coulomb field, these interactions are beyond the traditional, perturbative response.

A detailed classical study on the effects of B_{laser} in the ionization process is undertaken here with the objective to determine the validity of the dipole approximation for the bound state interaction in a regime well known to be relativistic and require a full E_{laser} and B_{laser} treatment for the continuum. This study addresses when the magnetic field begins to affect the bound state and to what extent in the ultrastrong field interaction a dipole interaction can be used to calculate the ionization probability. By studying classical electron dynamics, a physical model of strong field ionization has been gained for a number of phenomena including harmonic generation and complex multielectron phenomena [65, 66]. Furthermore, as the fields and energy

of the electron increase, there is an indication strong external field interactions will become more classical [67]. We present here calculations describing the influence of B_{laser} on the bound state and ionization for an atom at ‘relativistic, ultrastrong intensities. First, we address bound state dynamics of the electron by inspecting electron ensemble trajectories in configuration space during the interaction. Second, we calculate B_{laser} induced changes in the ionization rate as a function of field strength. Last, we inspect angular distributions for the photoelectrons when they first appear, or are ‘born’ in the continuum.

3.2 Method

In our calculations, the atom is treated as a single electron, hydrogen-like system. This is motivated by the success of the single active electron approximation in strong fields where the ‘outer’, least-tightly bound electron (typically in the ground state) directly interacts with the external field and the ‘inner’, core electrons do not [68]. With the 10^3 eV to 10^6 eV electron energies in ultrastrong fields, multielectron processes are significant [69] but single electron processes remain a primary mechanism. Our second approximation is the classical description of the electron and field, following the dynamics with trajectories. The classical treatment of strong fields is a well established technique [70, 71] and allows the investigation of full three-dimensional dynamics currently intractable with relativistic quantum calculations [49].

For correspondence to the quantum case, we use bound state energies $E_n = -Z^2/2n^2$ [72] where n is the principle quantum number and Z is the atomic number. The angular momentum of the electron is varied between 0 and \hbar . The choice of angular momentum in this range does not change the results presented here. Quantum uncertainty and probability is mimicked [73] in our classical system by giving position and momentum distributions to the microcanonical Monte Carlo ensembles consistent with the uncertainty principle. In determining the initial position and momentum of the electrons we follow the method given in [73]. The Kepler orbits are defined by a set of five parameters: inclination of the orbit (i); ascending node longitude (Ω);

mean anomaly (α); orbit eccentricity (e); and an argument of pericenter (ω_A). These parameters are generated randomly to create 3D ensembles for the electron and can take on the values,

$$0 \leq \alpha \leq 2\pi, 0 \leq e^2 \leq 1, -1 \leq \cos i \leq 1,$$

$$0 \leq \Omega \leq 2\pi, 0 \leq \omega_A \leq 2\pi$$

The values of position and momenta as functions of time are generated by integrating Hamilton's equations of motion for the electron in a soft core potential [67].

$$\frac{dp_x}{dt} = -\frac{Ze^2x}{(r^2 + \delta)^{3/2}} - eE_{laser}(\vec{r}, t)\left[1 - \frac{p_z}{\sqrt{p^2 + m_0^2c^2}}\right] \quad (3.1)$$

$$\frac{dp_y}{dt} = -\frac{Ze^2y}{(r^2 + \delta)^{3/2}} \quad (3.2)$$

$$\frac{dp_z}{dt} = -\frac{Ze^2x}{(r^2 + \delta)^{3/2}} - eE_{laser}(\vec{r}, t)\frac{p_x}{\sqrt{p^2 + m_0^2c^2}} \quad (3.3)$$

$$\frac{dx}{dt} = \frac{p_xc}{\sqrt{p^2 + m_0^2c^2}} \quad (3.4)$$

$$\frac{dy}{dt} = \frac{p_yc}{\sqrt{p^2 + m_0^2c^2}} \quad (3.5)$$

$$\frac{dz}{dt} = \frac{p_zc}{\sqrt{p^2 + m_0^2c^2}} \quad (3.6)$$

Where c is the speed of light, δ is our soft core parameter, Z is the atomic number, e is the charge, m_0 is the rest mass, $r = \sqrt{x^2 + y^2 + z^2}$ and $p = \sqrt{p_x^2 + p_y^2 + p_z^2}$. When the dipole approximation is considered, the Lorentz force term from B_{laser} is dropped, i.e. the $eE_{laser}(\vec{r}, t)p_z/\sqrt{p^2 + m_0^2c^2}$ in eq. 1 and $eE_{laser}(\vec{r}, t)p_x/\sqrt{p^2 + m_0^2c^2}$ term in eq. 3. The value of δ is chosen to keep the energy of the electron less than 5 MeV at $r = 0$. We also verified using a Coulomb potential with an $r = 0$ exit condition (e.g. excluding results for trajectories that come close enough to $r = 0$ so their energy would exceed 5 MeV) does not change the outcome. Spin is neglected as it does not affect ionization at the level of 5% until $Z = 60$ [74]. The accuracy of the solutions can be gauged by the conservation of energy in the absence of the external radiation field. In this case,

the energy deviates by less than 10^{-9} after 200 Kepler orbits for any state used in the calculation.

Our field is a linearly polarized plane wave propagating in \hat{z} with E_{laser} in the \hat{x} direction. We linearly increase the field over many Kepler orbits, $\tau_K = 2\pi(n^3/Z^2)$, of the state being ionized and then hold the field constant at a maximum value. The ramp rate of $50 \tau_K$ from zero to the maximum is safely in the adiabatic limit, which begins to breakdown in our calculations for ramps faster than $5\tau_K$. After the ramp, the field is held constant at the maximum value for an additional $50\tau_K$. To calculate angular distributions we employ a \sin^2 pulse shape with a full-width-at-half-maximum of $200\tau_K$. Similar results are achieved with the ramped field pulse shape. The calculations are done in the quasistatic limit with carrier frequencies from zero to one-twentieth of the Kepler orbit frequency.

3.3 Results

3.3.1 Trajectories and Ensemble Distributions

Figure 1 presents a selection of individual trajectories. For a connection to strong field studies with Rydberg atoms, we show the $(Z,n) = (1,18)$ state bound by 0.0015 Hartree as well as the $(Z,n)=(8,1)$ state bound by 32 Hartree. The trajectories start as a closed Kepler orbit [72] with a given angular momentum in the calculation for Fig. 1 of $\hbar/2$. As the field is introduced the trajectories change to open orbits with an orbital precession whose period is the inverse of the Stark frequency [75]. Figure 1 shows trajectories without (a,c) and with B_{laser} (b,d) for the (1,18) Rydberg state, dipole interaction at a field of 4×10^{-7} a.u. (a,b) and (8,1) state interacting with an ultrastrong field of 23 a.u (c, d).

Despite the change in the field by 10^7 the systems show similarities with each other. Both sets of orbits are, for example, in precession staying within an area described by two parabolas [76]. There is an apparent lack of dependence on B_{laser} when comparing the trajectories calculated using only E_{laser} (Fig. 1(a,c)) and with the full

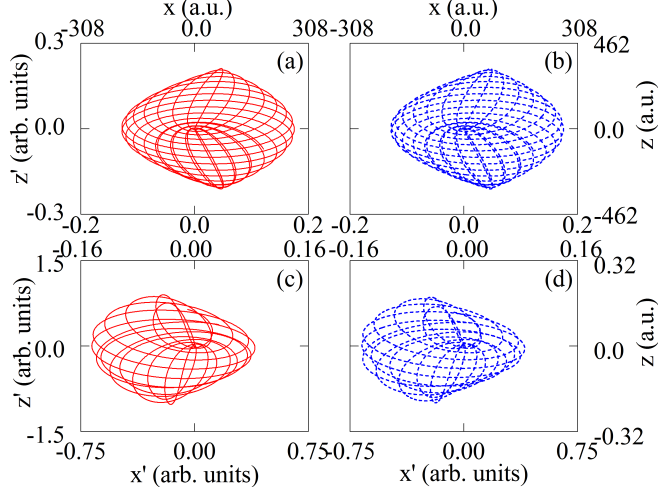


Figure 3.1: Trajectories in precession for a $Z = 1, n = 18$ Rydberg state in a 4×10^{-7} a.u. constant E_{laser} field (a, red, solid) and the full E_{laser}, B_{laser} fields (b, blue, dash) as well as for a tightly bound state $Z = 8, n = 1$ in a constant 23 a.u. E_{laser} field (a, red, solid) and the full E_{laser}, B_{laser} fields (b, blue, dash). Approximately 10 orbits are plotted for each case. Rescaled coordinates, $x' = x\sqrt{E}$, are shown along with atomic units.

E_{laser} and B_{laser} field Fig. 1 (b,d). One can say the role of B_{laser} does not, at first glance, change electron trajectories in an obvious way.

To examine full ensembles of 10^4 to 10^5 trajectories, we turn to probabilities within configuration space. The probability distributions presented are a time average over a 1000 by 1000 spatial grid. For the 2D, x-z plot we integrate over the y coordinate. The $(Z,n) = (4,1)$ and $(20,1)$ states for the figure are for the strong field and ultrastrong field interaction, respectively. We have chosen to show these results for a low frequency field which polarizes the atom in one direction. The results in the figure as shown are indistinguishable for fields with a carrier frequency from d.c. to 0.007 a.u. for $Z=4$ and frequencies from d.c. to 0.18 a.u. for $Z=20$. The choice of the low frequency presentation was to allow any dynamics from the field polarization to be clearly seen. Results for frequencies that are still quasistatic but approaching the Kepler frequency are shown in the Afterward for frequencies of 0.07 a.u. ($Z=4$) and 1.8 a.u. ($Z=20$).

To begin we show the bound state configuration spaces with no external field

in Fig. 2(a,b). For comparison, the electron probability is compared in Fig. 2(c,d) to the quantum wave function probability calculated using the Schrodinger equation. Next we plot the configuration space with an E_{laser} only external field ($B_{laser} = 0$) ramped up to a value where roughly one-third of the trajectories ionize by the end of the interaction in Fig. 2(e,f). For the (4,1) state this is an external field of 10 a.u. and for the (20,1) case the ultrastrong field is 710 a.u. The results are shown with the bound state configuration space (Fig. 2(a,b)) subtracted. The probability magnitude range for these differences in Fig. 2(e,f) is 16% of the range shown for the field free distributions in Fig. 2(a,b).

Polarization, aligned orbitals, and ionization effects are all visible in Fig. 2(e,f). The polarization response is visible by the elongation of the probability along E_{laser} and a slight shift of the probability along $-\hat{x}$, i.e. a deficiency for $x > 0$ and overall increase for $x < 0$. Alignment effects are evident by the preservation of certain orbits in configuration space. The alignment effect [77, 78] corresponds to the the quantum case where m states aligned along E_{laser} have different ionization rates. The highest ionization rates are for $m=0$ (no magnetic moment along E_{laser}) since the electron passes by the tunneling region in the potential on each orbit. States orbiting with a magnetic moment aligned with or against E_{laser} are less likely to ionize and the two lobes from the projection of this orbit in the x-z plane are most clearly seen at $x = 0$, $z = \pm 0.4$ a.u. in Fig. 2(e).

Finally we give the configuration space with the full E_{laser} , B_{laser} field. To highlight any difference we show this result in Fig. 2(g,h) after subtracting the E_{laser} only configuration space used in Fig. 2(e,f). The resulting range in Fig. 2(g,h) is 1.6% of that shown for the field free distributions in Fig. 2(a,b). The calculated noise floor (Fig. 2(i,j)) is obtained from the subtraction of configuration spaces for full E_{laser} and B_{laser} external field calculations with two different random number trajectory ensemble launches and the same 1.6% range as in Fig. 2(g,h).

Figure 2(h) shows including B_{laser} alters the most stable trajectory regions in configuration space, i.e. trajectories that are more stable against ionization. These

B_{laser} induced shifts are not present in the nonrelativistic case Fig. 2(g) but are clearly visible features in Fig. 2(h) that result from the interaction of B_{laser} on the bound state. The changes in Fig. 2(h) are at the few percent level in the configuration space for an intensity of 10^{23} W/cm². One may speculate for the quantum case these shifts would be manifested by a change in the distribution of the ionization among the m-states.

3.3.2 Ionization rates

Classical ionization of the bound state begins as the external field increases to the critical field $E_{critical} = \frac{Z^3}{16n^4}$ [79], where at the critical radius the external field magnitude equals the Coulomb field for a bound state with energy $-\frac{Z^2}{2n^2}$. The values of $E_{critical}$ and $r_{critical} = \frac{4n^2}{Z}$ can be calculated for an effective 1-D, hydrogen system [79]. The threshold, critical 1-D values are applicable for infinitely long interactions with the external field and ionization through a singular point on the effective potential directly along E_{laser} . Since the electron only visits the ionization region on the barrier once per Kepler orbit, to achieve significant ionization probabilities with short pulse fields and 3D electron distributions a larger ionization region in the potential and E_{laser} values greater than $E_{critical}$ are required.

As the electron moves toward the point of ionization at $r_{critical}$, the total electric field is near zero and yet B_{laser} is unopposed at full magnitude. Hence, near $r_{critical}$ it could be argued the magnetic field should have the greatest influence on the ionization process by causing the electron to deflect away from the region in the barrier where ionization is most likely. To show the impact of any such dynamic we calculate the percentage of the electron ensemble that ionizes as a function of the laser field strength. Ionization in these calculations is classical and defined as an electron trajectory that traverses over the effective barrier, i.e. $r > r_{critical}$. This criteria is the same as the requirement that the total energy be positive at the end of the pulse when the electron is accelerated in the field beyond $r_{critical}$ to an energy greater than the binding energy. For the high fields used in these studies, the time this takes is approximately $8/Zc$,

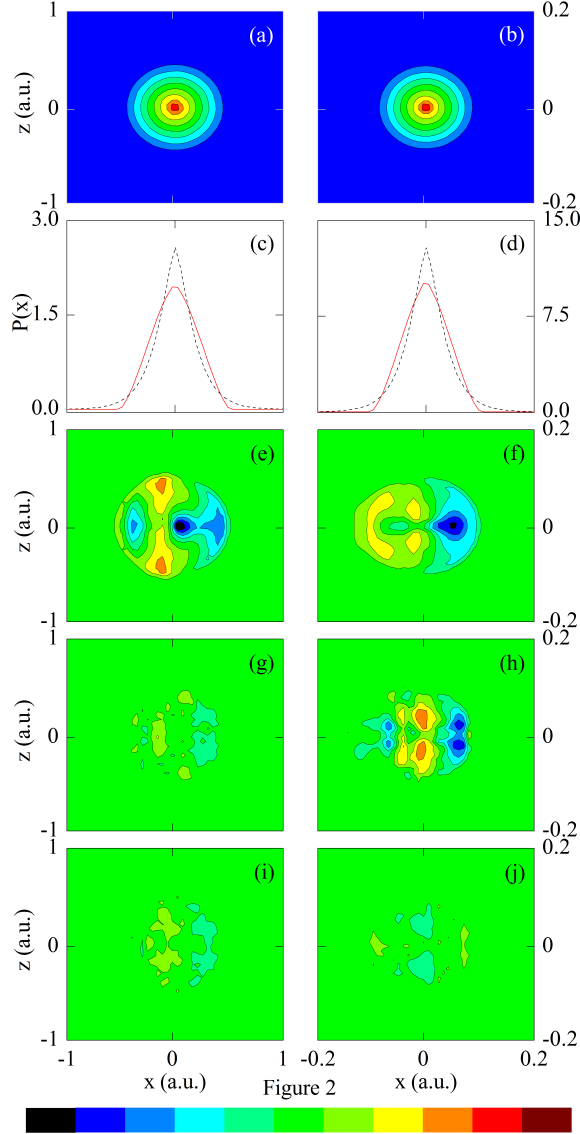


Figure 3.2: Configuration space distributions for $Z = 4$ (a,c,e,g,i) and $Z = 20$ (b,d,f,h,j). The configuration space with no external laser field is shown in (a,b). A line out of the classical configuration space compared with the quantum wave function probability, $P(x)$, is in (c,d). The differences between the configuration space with no external field and an external E_{laser} field with a peak value of 9.8 a.u. for $Z=4$ and 710 a.u. for $Z=20$ are shown in (e,f). The difference between the configuration space with the full E_{laser}, B_{laser} fields (9.8 a.u. for $Z=4$, 710 a.u. for $Z=20$) and the dipole approximation are in (g,h). An estimate of numerical fluctuations within the configuration space plots is shown in (i,j) as determined by subtracting two ensembles that differ only in the trajectory initial conditions for the 10^5 trajectories. The color assignment shown at the bottom of the figure ranges from 0 (black) to 1 (red) for (a,b). The range for the other plots is -0.16 (black) to +0.16 (red) for (e,f) and -0.016 (black) to +0.016 (red) for (g,h,i,j). 51

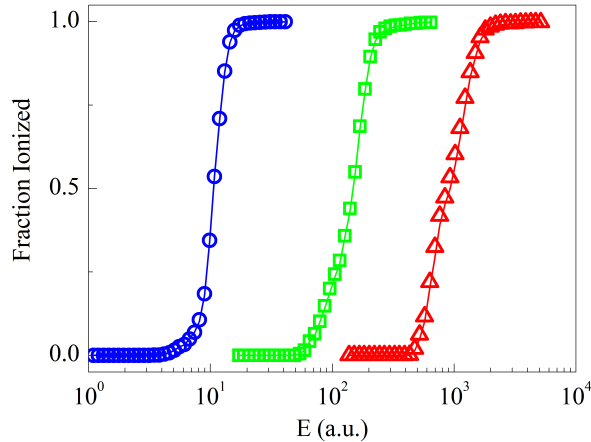


Figure 3.3: Fraction of electrons ionized vs. field strength for $Z = 1$ (blue, open circle), 4 (green, open square), and 20 (red, open triangle). Solid lines, which are through the data points, represent the dipole approximation, i.e. E_{laser} only. Open symbols are used for the results when E_{laser} and B_{laser} is are fully included.

which is essentially instantaneously in the quasistatic fields used for these studies. This spatial criteria was used to speed up the calculations since propagation in the continuum is numerically intensive and often not critical, e.g. when calculating the ionization rate. Reinteraction of the ionized electron with the parent ion in the case of alternating laser fields, where the electron may recollide [65, 66] with the parent ion on subsequent cycles of the laser field, is neglected.

Figure 3 gives the ionization curves for three selected (Z,n) states $(4,1)$, $(10,1)$, and $(20,1)$. The ionization onset is at $E_{critical}$ and ionization increases with the field until eventually 100% ionization occurs. For the pulse durations used in this study, 50% ionization occurs near two- to three-times $E_{critical}$ and 100% ionization by the end of the pulse is in the range of six $E_{critical}$. The figure displays the ionization when the laser field is treated within the dipole approximation and when B_{laser} is included. The results for the two cases essentially overlay each other on the figure as rendered.

Figure 4(a) shows the field required to achieve 50% ionization of the trajectory ensemble without the magnetic field. The field value that gives an ionization level

of 50% in the dipole approximation is denoted as ${}_E E_{1/2}$ and with the full calculation using the laser electric and magnetic field, the field value resulting in 50% ionization is denoted by ${}_{EB} E_{1/2}$. In the figure, the fields required to give 50% ionization are plotted as a function of the binding energy for the ionizing state, i.e. $1 \leq Z \leq 20$. Also shown is a fit proportional to the binding energy to the 3/2 power expected from the simple nonrelativistic $E_{critical}$ treatment. The slight deflection from this value as one approaches binding energies of several hundred atomic units is consistent with our observations from the configuration space distributions where changes of the order 10% to 20% were seen for $Z = 20$ when comparing relativistic to non-relativistic calculations. Above several hundred atomic units of binding energy, a fully relativistic calculation would be suggested for accurate results based on the findings from our work. From Figs. 3 and 4(a) we can see as the intensity is increased by eight orders of magnitude there is little to no difference in $E_{1/2}$ as a function of B_{laser} . The deflection of the results from the 3/2 power scaling as the binding energies exceed 100 a.u. is due primarily to the relativistic change in the electron mass not the influence of B_{laser} . One can conclude the dipole approximation is accurate for calculating classical, one-electron bound state ionization rates and yields up to intensities of 10^7 a.u. (10^{23} W/cm²).

As a test of the quasi-static approximation, we show in Fig. 4(b) the dependence of ${}_{EB} E_{1/2} / {}_E E_{1/2}$ on the carrier frequency of the laser field. For the non-relativistic case ($Z \leq 4$) the ratio is unity as B_{laser} has no impact. For higher Z , relativistic effects begin to contribute and the critical field required to ionize the atom decreases slightly, more so as the frequency is increased. These observations are consistent with calculations of stabilization, which show higher ionization rates when B_{laser} is included [80]. As can be seen with the figure, within a range of 30% the ratio is unity from essentially a d.c. response (i.e. laser frequencies 1/1000 of the Kepler frequency) to 5% of the Kepler orbit frequency. In this range, we find the interactions fall within the quasistatic limit. External field laser frequencies higher than 5% of the Kepler frequency begin to fall into the high frequency limit and are not addressed in the scope of this paper.

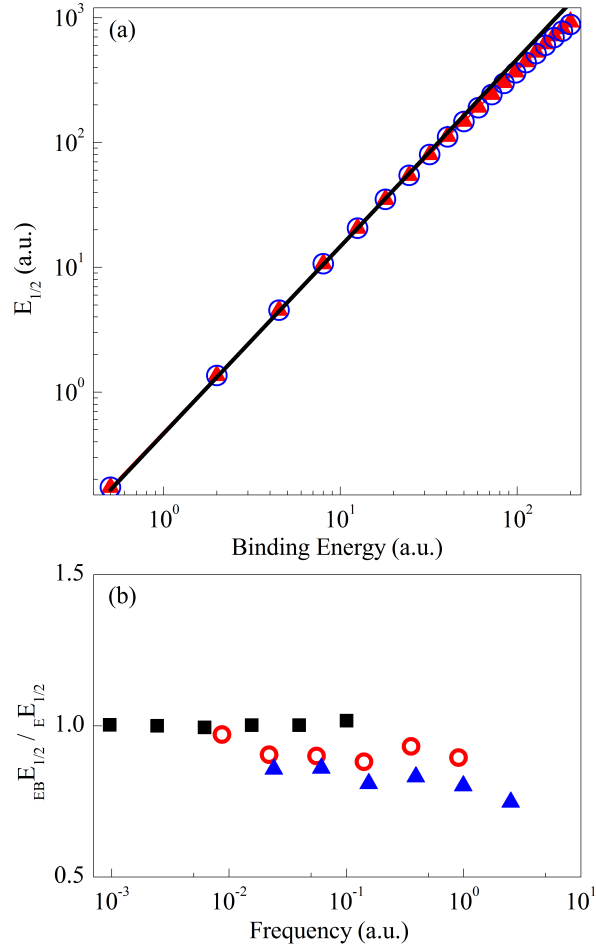


Figure 3.4: $E_{E}E_{1/2}$ (red, solid triangle) and $E_{EB}E_{1/2}$ (blue, open circle) as a function of intensity for multiple Z states (a). A trendline (solid, black) is shown to compare the results expected from a nonrelativistic $E_{critical}$ dependence. Frequency dependence of ionization for $Z=4, 12, 20$ plotted as a ratio of $E_{EB}E_{1/2} / E_{E}E_{1/2}$ (b) from the low frequency limit, i.e. 0.0001 times the Kepler frequency, up to 0.05 times the Kepler frequency for the ionizing state. For reference, the Kepler frequencies (Z state, binding energy) are: 2.5 a.u. (4, 8 a.u.), 23 a.u. (12, 72 a.u.), and 63.6 a.u. (20, 200 a.u.).

3.3.3 Angular distributions

Last, we look in Fig. 5 at the difference in the angular distribution of ionized electrons as they are ‘born into the continuum. The maximum field values for the pulses used in calculating the angular distributions correspond to 50% ionization by the end of the pulse. As the electron is ionized ($r = r_{critical}$) the coordinates are recorded and a polar distribution is calculated based on the electron position at the point of ‘birth’ into the continuum.

As expected in the dipole approximation, the range of angles is narrowly distributed within a few degrees of $-E_{laser}$, set to zero degrees in Fig. 5. The angular distribution at the point of ionization (i.e. $r_{critical}$) is shown in Fig. 5(a) for charge states $1 \leq Z \leq 20$. One can see at the photoelectron birth the angular distribution becomes more peaked as Z increases and the electron moves deeper into, and is more confined by the Coulomb potential. With increasing Z the mean angle also increases as the emission lobe is deflected toward the propagation direction at 90° .

To help shed light on the physics behind this deflection, the mean polar angle deflection can be compared to a gyromagnetic radius, R , for an electron with the classical Bohr velocity in a constant B_{laser} field. The deflection angle can be approximated from this gyromagnetic radius by setting the arc length to the width of the atomic bound state. This estimate of the gyromagnetic radius (deflection angle) changes from $R=800$ a.u. (0.28°) for $Z=1$, to $R=3$ a.u. (3.6°) for $Z=20$ and compares favorably with the inferred radii from the calculation which varies from $R=5000$ a.u. (0.05°) for $Z=1$, to $R=7$ a.u. (1.6°) for $Z=20$. We also quantified the affect of B_{laser} on the momentum distribution at ionization. The mean polar angle deflection in momentum is comparable to that seen for the position deflection. The angular decrease in the spatial distribution range with increasing Z is complemented by an increase in the width for the momentum angular distribution as Z increases.

Figure 5(b) is a difference plot for the emission probability as a function of Z calculated with E_{laser} and B_{laser} minus the E_{laser} only, dipole response result. The deflection by B is seen here as an increase in the probability into angles from $\theta = 10^\circ$

to $\theta = 15^\circ$ for $Z > 10$ and a decrease between $\theta = -20^\circ$ to $\theta = -5^\circ$. This last result on the appearance angles for the electron in the continuum should be distinguished from final state angular distributions [71], which are the result of the acceleration of the free electron after being ‘born’ into the field. In experiments with a tight laser focus, these changes in the emission angle may be small compared to the influence of B_{laser} on the electron momentum once in the continuum. Deflections of this order, however, can be seen in high intensity experiments [81]. In addition to this analysis for the polar angle from E_{laser} into k , we note there is no difference in the normalized azimuthal distributions in the E_{laser} - B_{laser} plane with and without B_{laser} . The emphasis of this study is the interaction of the field with the bound state and the evaluation of how this interaction compares with the strong field dipole treatment for the ultra-intensity tier from 10^{17} W/cm² to 10^{23} W/cm².

The reason behind the increasing influence of the laser magnetic field comes from the larger role B_{laser} in the equations of motion as Z increases. Fig. 6 is a plot of the force on the electron due to the Coulomb, laser electric field and the full Coulomb, laser electric field, and laser magnetic field for a time frame of 200 Kepler orbits. As Z increases from 1 to 20, the force due to the laser magnetic field becomes a larger fraction of the total force on the electron. In each case the magnetic force increases from zero to its full value as the laser field ramps up during the first 50 Kepler orbits. The gaining influence of the force on the electron due to B_{laser} can be seen from a simple Z scaling since the force from $E_{critical}$ scales as Z^3 and the corresponding force from B_{laser} scales as Z^4 with the inclusion of the velocity, which scales as Z for the bound state electron, in the Lorentz force.

3.4 Conclusion

A natural progression is then clear. At optical frequencies, the dipole interaction is valid for all length scales up to intensities of 1 a.u., as the intensity increases the continuum dynamics and rescattering begin to be affected by B_{laser} for intensities beyond 1 a.u. [22]. As the field is further increased, we show in these studies the photoelectron

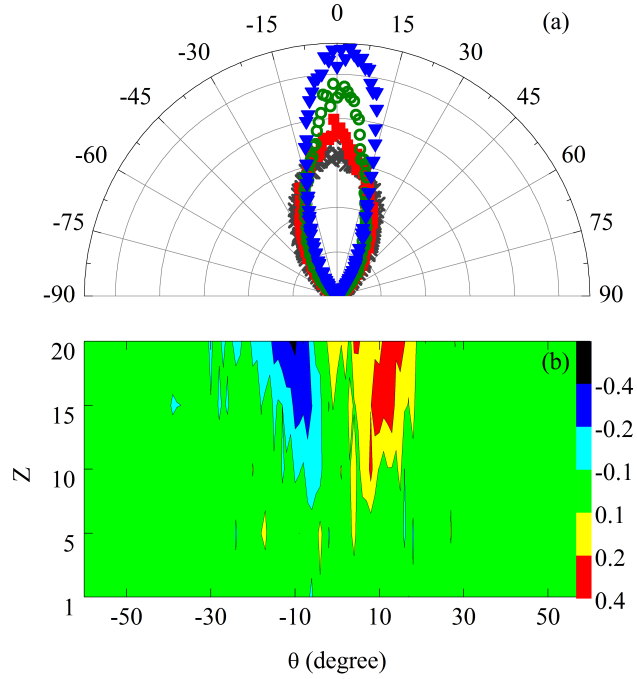


Figure 3.5: Polar plot of the electron position at ‘birth’, i.e. ionization in the full field case E_{laser}, B_{laser} (a). The plot is for $Z=1$ (black, solid x, intensity = 0.16 a.u.), $Z=5$ (red, solid square, intensity = 2200 a.u.), $Z=10$ (green, open circle, intensity = 110,000 a.u.), $Z=20$ (blue, inverted solid triangle, intensity = 4,100,000 a.u.). The difference between this emission and that for the dipole approximation (E_{laser}) is shown in (b) where the distributions with the full field (E_{laser}, B_{laser}) minus dipole case (E_{laser}) only are shown in an angle, Z charge state contour plot.

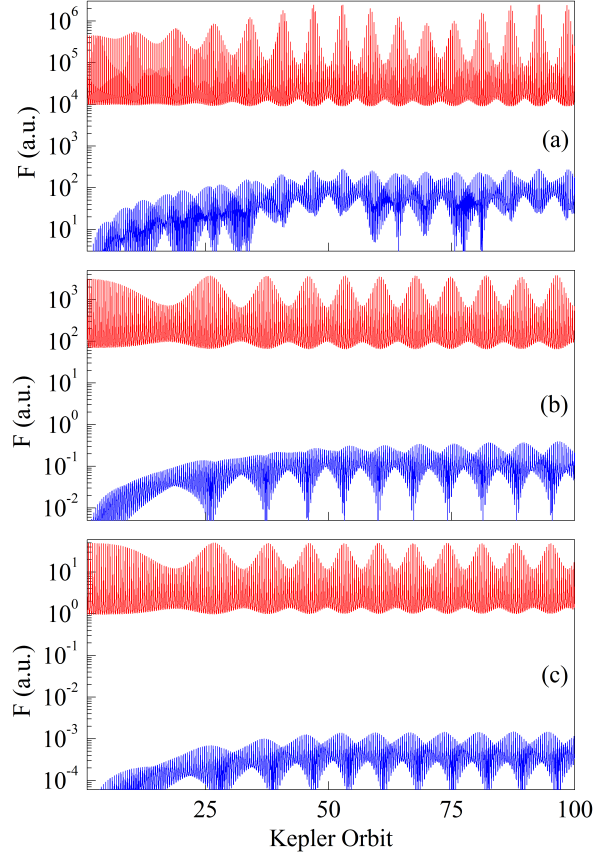


Figure 3.6: Combined Coulomb and Electric field ($F_C + F_{E_{laser}}$, red) and magnetic field ($F_{B_{laser}}$, blue) forces on the electron for (a) $Z = 20, n = 1, l = 0.5$, (b) $Z = 4, n = 1, l = 0.5$ and (c) $Z = 1, n = 1, l = 0.5$. The magnitude of the field in each case is $E_{critical}$: $E_{critical}^{Z=1} = 0.0625a.u.$; $E_{critical}^{Z=4} = 4a.u.$; $E_{critical}^{Z=20} = 500a.u.$

angular distribution are slightly affected for intensities near or exceeding 10^4 a.u. Up to intensities of 10^7 a.u. we do not find B_{laser} significantly affects the ionization rate though some impact at the level of 1% can be seen in population distributions of the bound state.

In conclusion, using classical relativistic Monte Carlo calculations we find the dipole approximation is generally valid with classical ionization for intensities up to 10^{23} W/cm². The laser magnetic field has little influence on bound state dynamics for the electron and slightly shifts the bound state population in the ultrastrong field. We find the angular distributions of ionized electrons are affected by inclusion of the laser magnetic field for fields exceeding 100 a.u. with a result the appearance angles for the photoelectron deflected into the propagation direction. The work is consistent with findings using a relativistic WKB approximation [74] and a semi-classical Dirac theory [82] which show changes to the ionization rate for similar Z and intensities less than 10^{23} W/cm² differ from the non-relativistic rates by 20% or less.

3.5 Afterward

In this section we present briefly the results for the configuration space when increasing the frequency to a value of 3% of the Kepler orbit frequency. Two factors come into play beyond the low-frequency, d.c. case presented in Fig. 2. The first is the increased symmetry introduced to the configuration space due to the oscillating character of E_{laser} that will ‘wash-out’ polarization effects as the electron is forced back and forth across the nucleus. The second is the additional velocity component the electron has as it travels back and forth across the Coulomb potential in the presence of E_{laser} . The results are shown in Fig. 7 in a similar fashion and with the same scale as Fig. 2. The only change is the carrier frequency, which is 0.07 a.u. for $Z=4$ and 1.8 a.u. for $Z=20$, in Fig. 7.

Symmetrization of the bound state appears in Fig 7(a,b) compared to Fig. 2(e,f) where only a dipole shift could be seen. Similar structures, such as aligned orbitals, are still present. Figure 7(c) & (d), where the dipole configuration is subtracted from

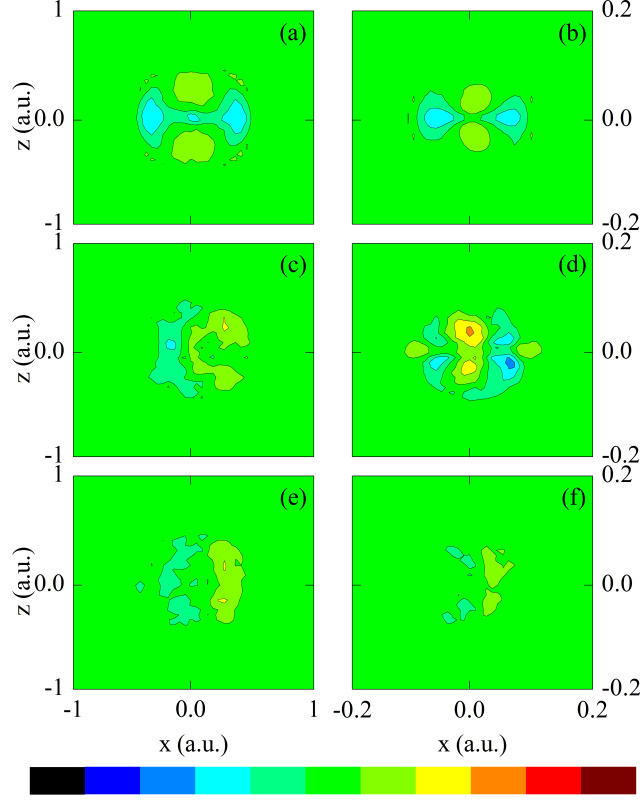


Figure 3.7: Configuration space distributions for $Z = 4$ (a,c,e) and $Z = 20$ (b,d,f). The differences between the configuration space with no external field and an external E_{laser} field with a peak value of $E = 9.1$ a.u. and frequency $f = 0.07$ a.u. for $Z = 4$ and $E = 680$ a.u., $f = 1.8$ a.u. for $Z = 20$ are shown in (a,b). The difference between the configuration space with the full E_{laser}, B_{laser} fields (9.12 a.u. for $Z = 4$, 680 a.u. for $Z = 20$) and the dipole approximation are in (c,d). An estimate of numerical fluctuations within the configuration space plots is shown in (e,f). The color assignment is the same as Fig. 2.(a,b) -0.16(black) to 0.16(red), (c,d,e,f) -0.016(black) to 0.016(red)

the full E_{laser} and B_{laser} do show one small difference from Fig 2(g) & (h). It can be seen that there is an asymmetry in Fig. 7(d). The population of electrons at $z = 0.04$ is larger than that at $z = -0.04$. In the dipole approximation the populations about $z = \pm 0.04$ are similar which leads to an average value of $z = 0$. With full E_{laser} and B_{laser} the asymmetry will lead to an average value of $z \neq 0$. This deflection is similar in character to the general impact of B_{laser} on atomic dynamics through the Lorentz force acting on the electron. In this case, it is the deflection along z due to the Lorentz force from B_{laser} and the velocity the bound state electron has when acted upon by E_{laser} .

This material is based upon work supported by the Army Research Office under Award No. W911NF-09-1-0390 and the National Science Foundation under Award No. 0757953.

BIBLIOGRAPHY

- [1] J. G. Leopold and I. C. Percival. *Phys. Rev. Lett.* **41**, 944–947 (1978).
- [2] Panming Fu, T. J. Scholz, J. M. Hetteema, and T. F. Gallagher. *Phys. Rev. Lett.* **64**, 511–514 (1990).
- [3] David Farrelly and T. Uzer. *Phys. Rev. Lett.* **74**, 1720–1723 (1995).
- [4] J. E. Bayfield and P. M. Koch. *Phys. Rev. Lett.* **33**, 258–261 (1974).
- [5] R. R. Jones, D. You, and P. H. Bucksbaum. *Phys. Rev. Lett.* **70**, 1236–1239 (1993).
- [6] R. Moshhammer, B. Feuerstein, W. Schmitt, A. Dorn, C. D. Schröter, J. Ullrich, H. Rottke, C. Trump, M. Wittmann, G. Korn, K. Hoffmann, and W. Sandner. *Phys. Rev. Lett.* **84**, 447–450 (2000).
- [7] Th. Weber, M. Weckenbrock, A. Staudte, L. Spielberger, O. Jagutzki, V. Mergel, F. Afaneh, G. Urbasch, M. Vollmer, H. Giessen, and R. Dörner. *Phys. Rev. Lett.* **84**, 443–446 (2000).
- [8] J. B. Watson, A. Sanpera, D. G. Lappas, P. L. Knight, and K. Burnett. *Phys. Rev. Lett.* **78**, 1884–1887 (1997).
- [9] S Larochelle, A Talebpour, and S L Chin. *J. Phys. B* **31**(6), 1201 (1998).
- [10] A Becker and F H M Faisal. *J. Phys. B* **38**(3), R1 (2005).
- [11] Gennady L. Yudin and Misha Yu. Ivanov. *Phys. Rev. A* **63**, 033404 (2001).
- [12] B. Sheehy, R. Lafon, M. Widmer, B. Walker, L. F. DiMauro, P. A. Agostini, and K. C. Kulander. *Phys. Rev. A* **58**, 3942–3952 (1998).
- [13] C. Cornaggia and Ph. Hering. *Phys. Rev. A* **62**, 023403 (2000).
- [14] R. Kopold, W. Becker, H. Rottke, and W. Sandner. *Phys. Rev. Lett.* **85**, 3781–3784 (2000).
- [15] Phay J. Ho, R. Panfili, S. L. Haan, and J. H. Eberly. *Phys. Rev. Lett.* **94**, 093002 (2005).
- [16] D. N. Fittinghoff, P. R. Bolton, B. Chang, and K. C. Kulander. *Phys. Rev. Lett.* **69**, 2642–2645 (1992).

- [17] B. Walker, B. Sheehy, L. F. DiMauro, P. Agostini, K. J. Schafer, and K. C. Kulander. *Phys. Rev. Lett.* **73**, 1227–1230 (1994).
- [18] M Protopapas, C H Keitel, and P L Knight. *Reports on Progress in Physics* **60**(4), 389 (1997).
- [19] A DiChiara, S Palaniyappan, A F Falkowski, E L Huskins, and B C Walker. *J. Phys. B* **38**(10), L183 (2005).
- [20] Yousef I. Salamin, S.X. Hu, Karen Z. Hatsagortsyan, and Christoph H. Keitel. *Physics Reports* **427**(23), 41 – 155 (2006).
- [21] Gerard A. Mourou, Toshiki Tajima, and Sergei V. Bulanov. *Rev. Mod. Phys.* **78**, 309–371 (2006).
- [22] Sasi Palaniyappan, Rob Mitchell, Rob Sauer, Isaac Ghebregziabher, Samantha L. White, M. F. Decamp, and B. C. Walker. *Phys. Rev. Lett.* **100**, 183001 (2008).
- [23] H. Wabnitz, L. Bittner, A. R. B. de Castro, R. Dohrmann, P. Gurtler, T. Laarmann, W. Laasch, J. Schulz, A. Swiderski, K. von Haefen, T. Moller, B. Faatz, A. Fateev, J. Feldhaus, C. Gerth, U. Hahn, E. Saldin, E. Schneidmiller, K. Sytchev, K. Tiedtke, R. Treusch, and M. Yurkov. *Nature* **420**(6915), 482–485 (2002).
- [24] P. Emma, R. Akre, J. Arthur, R. Bionta, C. Bostedt, J. Bozek, A. Brachmann, P. Bucksbaum, R. Coffee, F. J. Decker, Y. Ding, D. Dowell, S. Edstrom, A. Fisher, S. Gilevich, J. Hastings, G. Hays, Ph. Hering, Z. Huang, R. Iverson, H. Loos, M. Messerschmidt, A. Miahnahri, S. Moeller, H. D. Nuhn, G. Pile, D. Ratner, J. Rzepiela, D. Schultz, T. Smith, P. Stefan, H. Tompkins, J. Turner, J. Welch, W. White, J. Wu, G. Yocky, and J. Galayda. *Nature Photonics* **4**, 641.
- [25] John N. Galayda, John Arthur, Daniel F. Ratner, and William E. White. *J. Opt. Soc. Am. B* **27**(11), B106–B118 (2010).
- [26] Barry Walker, Csaba Toth, David Fittinghoff, Ting Guo, Dong-Eon Kim, Christoph Rose-Petruck, Jeffrey Squier, Koichi Yamakawa, Kent Wilson, and Christopher Barty. *Opt. Express* **5**(10), 196–202 (1999).
- [27] Thomas Brabec and Ferenc Krausz. *Rev. Mod. Phys.* **72**, 545–591 (2000).
- [28] Anthony DiChiara, Enam A. Chowdhury, George Ongadi, Barry C. Walker, and Robert S. Tamosaitis. *Opt. Lett.* **28**(21), 2106–2108 (2003).
- [29] G. A. Mourou, C. P. J. Barty, and M. D. Perry. *Physics Today* **51**, 22–28 (1998).
- [30] Yutaka Akahane, Jinglong Ma, Yuji Fukuda, Makoto Aoyoma, Hiromitsu Kiriya, Julia V. Sheldakova, Alexis V. Kudryashov, and Koichi Yamakawa. *Review of Scientific Instruments* **77**(2), 023102, 2006.

- [31] Michael D. Perry and Gerard Mourou. *Science* **264**(5161), 917–924, 1994.
- [32] M. D. Perry, D. Pennington, B. C. Stuart, G. Tietbohl, J. A. Britten, C. Brown, S. Herman, B. Golick, M. Kartz, J. Miller, H. T. Powell, M. Vergino, and V. Yanovsky. *Opt. Lett.* **24**(3), 160–162 (1999).
- [33] C Stoeckl, J A Delettrez, J H Kelly, T J Kessler, B E Kruschwitz, S J Loucks, R L Mccrory, D D Meyerhofer, D N Maywar, S F B Morse, J Myatt, A L Rigatti, L J Waxer, J D Zuegel, and R B Stephens. *Fusion Science and Technology* **49**(3), 367–373 (2006).
- [34] Erhard W. Gaul, Mikael Martinez, Joel Blakeney, Axel Jochmann, Martin Ringuette, Doug Hammond, Ted Borger, Ramiro Escamilla, Skylar Douglas, Watson Henderson, Gilliss Dyer, Alvin Erlandson, Rick Cross, John Caird, Christopher Ebbers, and Todd Ditmire. *Appl. Opt.* **49**(9), 1676–1681 (2010).
- [35] L.F. Dimauro and P. Agostini. Ionization dynamics in strong laser fields. Volume 35 of *Advances In Atomic, Molecular, and Optical Physics*, pages 79 – 120, Academic Press, 1995.
- [36] P. B. Corkum. *Phys. Rev. Lett.* **71**, 1994–1997 (1993).
- [37] Jeffrey L. Krause, Kenneth J. Schafer, and Kenneth C. Kulander. *Phys. Rev. A* **45**, 4998–5010 (1992).
- [38] X. M. Tong, Z. X. Zhao, and C. D. Lin. *Phys. Rev. A* **66**, 033402 (2002).
- [39] K Burnett, V C Reed, and P L Knight. *J. Phys. B* **26**(4), 561 (1993).
- [40] A Becker and F H M Faisal. *J. Phys. B* **38**(3), R1 (2005).
- [41] S. Palaniyappan, I. Ghebregziabher, A. DiChiara, J. MacDonald, and B. C. Walker. *Phys. Rev. A* **74**, 033403 (2006).
- [42] V. Popov, B. Karnakov, V. Mur, and S. Pozdnyakov. *Journal of Experimental and Theoretical Physics* **102**, 760–775, 2006.
- [43] V.S. Popov, V.D. Mur, B.M. Karnakov, and S.G. Pozdnyakov. *Physics Letters A* **358**(1), 21 – 26, 2006.
- [44] N Milosevic, V P Krainov, and T Brabec. *J. Phys. B* **35**(16), 3515 (2002).
- [45] H. R. Reiss. *Phys. Rev. Lett.* **101**, 043002 (2008).
- [46] N J Kylstra, A M Ermolaev, and C J Joachain. *J. Phys. B* **30**(13), L449 (1997).
- [47] S. X. Hu and C. H. Keitel. *Phys. Rev. A* **63**, 053402 (2001).

- [48] I. Ghebregziabher, S. Palaniyappan, J. MacDonald, and B. C. Walker. *Phys. Rev. A* **73**, 033419 (2006).
- [49] Heiko Bauke, Henrik G. Hetzheim, Guido R. Mocken, Matthias Ruf, and Christoph H. Keitel. *Phys. Rev. A* **83**, 063414 (2011).
- [50] Enam A. Chowdhury, C. P. J. Barty, and Barry C. Walker. *Phys. Rev. A* **63**, 042712 (2001).
- [51] K. Yamakawa, Y. Akahane, Y. Fukuda, M. Aoyama, N. Inoue, and H. Ueda. *Phys. Rev. A* **68**, 065403 (2003).
- [52] S Palaniyappan, A DiChiara, I Ghebregziabher, E L Huskins, A Falkowski, D Pajerowski, and B C Walker. *J. Phys. B* **39**(13), S357 (2006).
- [53] Enam Chowdhury, Isaac Ghebregziabher, James MacDonald, and Barry Walker. *Opt. Express* **12**(17), 3911–3920 (2004).
- [54] A. D. DiChiara, I. Ghebregziabher, R. Sauer, J. Waesche, S. Palaniyappan, B. L. Wen, and B. C. Walker. *Phys. Rev. Lett.* **101**, 173002 (2008).
- [55] C. I. Moore, J. P. Knauer, and D. D. Meyerhofer. *Phys. Rev. Lett.* **74**, 2439–2442 (1995).
- [56] Matthias Dammasch, Martin Dörr, Ulli Eichmann, Ernst Lenz, and Wolfgang Sandner. *Phys. Rev. A* **64**, 061402 (2001).
- [57] E Gubbini, U Eichmann, M Kalashnikov, and W Sandner. *J. Phys. B* **38**(6), L87 (2005).
- [58] S. Palaniyappan, A. DiChiara, E. Chowdhury, A. Falkowski, G. Ongadi, E. L. Huskins, and B. C. Walker. *Phys. Rev. Lett.* **94**, 243003 (2005).
- [59] A. D. DiChiara, I. Ghebregziabher, J. M. Waesche, T. Stanev, N. Ekanayake, L. R. Barclay, S. J. Wells, A. Watts, M. Videtto, C. A. Mancuso, and B. C. Walker. *Phys. Rev. A* **81**, 043417 (2010).
- [60] M. W. Walser, C. H. Keitel, A. Scrinzi, and T. Brabec. *Phys. Rev. Lett.* **85**, 5082, 2000).
- [61] Michael Klaiber, Karen Z. Hatsagortsyan, and Christoph H. Keitel. *Phys. Rev. A* **75**, 063413 (2007).
- [62] Alejandro Bugacov, Marcel Pont, and Robin Shakeshaft. *Phys. Rev. A* **48**, R4027–R4030 (1993).
- [63] E. Gubbini, U. Eichmann, M. Kalashnikov, and W. Sandner. *Phys. Rev. Lett.* **94**, 053602 (2005).

- [64] R. E. Wagner, Q. Su, and R. Grobe. *Phys. Rev. Lett.* **84**, 3282–3285 (2000).
- [65] P. B. Corkum. *Phys. Rev. Lett.* **71**, 1994 (1993).
- [66] L. F. DiMauro and P. Agostini. *Advances in Atomic Molecular and Optical Physics D* **35**, 79 (1995).
- [67] J. Ho Phay and J. H. Eberly. *Optics Express* **15**, 1845 (2007).
- [68] M. Gavrilu. *Atoms in Intense Laser Fields*. Supplement to *Advances in Atomic, Molecular, and Optical Physics*, Academic Press, 1992.
- [69] S Palaniyappan, A DiChiara, I Ghebregziabher, E L Huskins, A Falkowski, D Pajerowski, and B C Walker. *J. Phys. B* **39**(13), S357 (2006).
- [70] J G Leopold and I C Percival. *Journal of Physics B: Atomic and Molecular Physics* **12**(5), 709 (1979).
- [71] George A. Kyrala. *J. Opt. Soc. Am. B* **4**(5), 731–738 (1987).
- [72] T.F. Gallagher. *Rydberg Atoms*. Cambridge Monographs on Atomic, Molecular and Chemical Physics. Cambridge University Press, 2005.
- [73] L. N. Gaier and C. H. Keitel. *Phys. Rev. A* **65**, 023406 (2002).
- [74] V. Popov, B. Karnakov, V. Mur, and S. Pozdnyakov. *Journal of Experimental and Theoretical Physics* **102**, 760–775 (2006).
- [75] J. Murray-Krezan. *American Journal of Physics* **76**(11), 1007–1011 (2008).
- [76] J. P. Hansen, J. Lu, L. B. Madsen, and H. M. Nilsen. *Phys. Rev. A* **64**, 033418 (2001).
- [77] L. Young, D. A. Arms, E. M. Dufresne, R. W. Dunford, D. L. Ederer, C. Höhr, E. P. Kanter, B. Krässig, E. C. Landahl, E. R. Peterson, J. Rudati, R. Santra, and S. H. Southworth. *Phys. Rev. Lett.* **97**, 083601 (2006).
- [78] M. V. Ammosov, N. B. Delone, and V. P. Krainov. *Zh. Eksp. Teor. Fiz.* **91**, 2008–2013 (1986).
- [79] T. P. Hezel, C. E. Burkhardt, M. Ciocca, and J. J. Leventhal. *American Journal of Physics* **60**(4), 324–328 (1992).
- [80] C. J. Joachain, N. J. Kylstra, and R. M. Potvliege. *Journal of Modern Optics* **50**(3-4), 313–329 (2003).
- [81] S. J. McNaught, J. P. Knauer, and D. D. Meyerhofer. *Phys. Rev. A* **58**, 1399–1411 (1998).
- [82] N. Milosevic, V. P. Krainov, and T. Brabec. *Phys. Rev. Lett.* **89**, 193001 (2002).

Chapter 4

SUBSTITUTION EFFECTS ON STRONG AND ULTRA-STRONG FIELD MOLECULAR IONIZATION

4.1 Introduction

The light-matter interaction is an expansive area of research with topics ranging across atomic physics [1, 2, 3, 4], high harmonic generation (HHG) [5, 6, 7], fusion science [8], controlled reactions [9], and imaging [10]. One such process is ionization, which includes the photoelectric effect [11], multi-photon ionization [12, 13, 14], tunnelling ionization [15, 16], and classical over the barrier ionization [17].

For atoms at optical frequencies many of these ionization processes are well understood. At lower intensities ($<10^{12}$ W/cm²), it is possible to use perturbation techniques to model the interaction. As the intensity increases to strong (10^{13} - 10^{16} W/cm²) and ultra-strong fields (10^{16} - 10^{19} W/cm²), perturbation techniques are no longer accurate and a semi-classical approach is often used. This has led to the quasi-static tunnelling picture of ionization that has accurately determined threshold ionization intensities and ionization rates.

The molecular response to intense light is more complex. Processes that occur include molecular alignment [18], stabilization [19], pendular states [20], dissociative ionization [21], enhanced ionization [22], and Coulomb explosion [23]. Much of the work on molecular systems focuses on diatomic homo- and hetero-nuclear molecules in the strong field [24, 25]. Work has also been carried out on dissociative ionization in polyatomic molecules both experimentally [26, 27] and theoretically [28]. Recent experimental results [29] on highly charged atomic ions C^{m+} , N^{m+} , and O^{m+} for $0 \leq m \leq 4$ from different molecules showed that the production of the $m = 1$ ion was reduced in the case when a hydrogen atom is part of the molecule compared to molecules

with no hydrogen, and that in the ultra high intensity regime the response can approach the atomic ion limit [30].

In this study we investigate the production of highly charged carbon atoms and ions from polyatomic molecules of similar shape but varying composition in the ultrastrong intensity regime. This work will expand the understanding of the role of nearest neighbour charge and separation distance in the ultrastrong field as well as show that at in this intensity regime, the response of individual ions becomes more atomic in nature. We also show that the energy of ion fragments is only driven by Coulomb explosion and the initial dissociation of the molecule, and the influence of the nearest neighbor Coulomb potential on ionization is an adjustment in the ionization potential due to the nearest neighbor Coulomb potential (charge).

While at first these multiple effects could seem to give a complex, if not uninterpretable spectra and interaction, we show there is a clear trending and analytical predictability to their role.

4.2 Experimental Setup

The experiments are carried out using a home built terawatt CPA laser system [31] consisting of a Ti:Sapphire oscillator seeding a ring-type regenerative amplifier passing into a 5 pass bow-tie multipass amplifier with final output of 35 fs pulses with 150 mJ at 790 nm. These laser pulses are passed into a high resolution time-of-flight ion spectrometer where they interact with the sample.

Just before the laser enters the spectrometer, it passes through a zero-order $\lambda/4$ or $\lambda/2$ waveplate to adjust the polarization of the incoming beam. Inside of the spectrometer, the beam is reflected off of a $f/2$ off axis parabolic gold coated mirror focused to a spot size of $\sim 2 \mu\text{m}$. This spot crosses an effusive gas jet of the sample molecular species inside of the extraction region.

The ion spectrometer uses a single stage extraction region with an extraction field varied between 1 and 3 kV/cm. The ions pass through an aperture before entering the drift region of the spectrometer. Two different apertures were used in the

collections. A 0.254 mm circular aperture which resulted in high angular selectivity of the ion emission when the laser polarization was parallel versus perpendicular to the drift region ($E_{laser}^{\perp}/E_{laser}^{\parallel} \ll 1$). For isotropic (no angular selection) collections we make use of an rectangular aperture of 0.254 mm along the laser propagation direction (\hat{k}) and 10 mm perpendicular to the drift region. This rectangular aperture allowed for a large angle since ions ejected perpendicular to the detector pass through the slit and could be collected.

The field free drift region of the spectrometer measures 0.12 m long. The ions are detected by a pair of chevron micro-channel plates (MCPs). Signals from the MCPs are sent to a preamplifier (Ortec VT 120) then through a voltage discriminator (Ortec 9307) and finally to a picosecond time analyzer (Ortec PTA 9308) where the signal is digitized and downloaded to a computer for every laser pulse. From this information, time-of-flight histograms are constructed.

For the gas samples, manifold pressure which feeds the leak valve is kept at roughly 5 psi above atmosphere. The base pressure in our chamber is roughly 9×10^{-10} torr to ensure the least amount of contamination from atmosphere and water vapor. The working pressure inside our ultra-high vacuum chamber ion spectrometer is kept below 10^{-6} torr to avoid space charge and other collective effects.

All the molecules are put under the same experimental conditions (laser intensity, working pressure) so any small differences in ion production can be clearly identified as coming from the molecular response and not a daily fluctuation or systematic error.

To eliminate degeneracy in our TOF spectra (e.g. $^{12}\text{C}^{4+}$, $^{12}\text{CH}_3^{5+}$) the ^{13}C isotope was used for detecting lower charge states $1 \leq m \leq 4$. Degeneracy was not an issue for the highest charge state seen, $m = 5$.

Intensity calibrations for the terawatt laser system are done by comparing calculated ADK ionization rates [16] to experimental values for argon, and the kilohertz system calibrations by comparing ion yields in carbon to previously recorded rates [30].

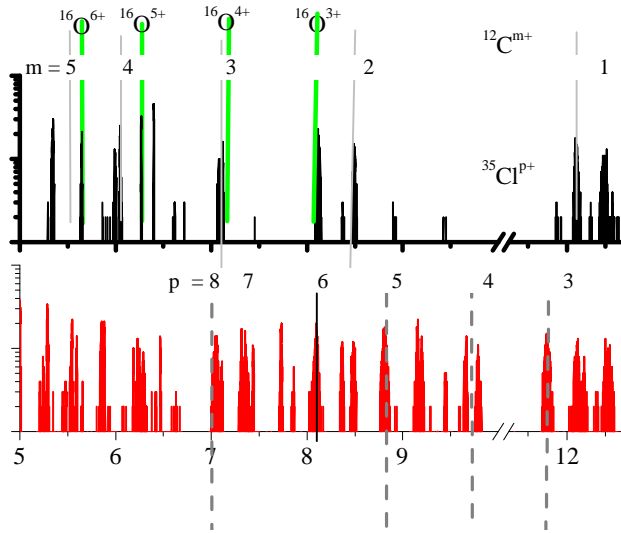


Figure 4.1: Time of flight spectra gathered at 5×10^{18} W/cm² for the molecules methane (black)(CH₄), chloromethane (red)(CH₃Cl) as a function of mass to charge ratio, m/q . Indicated in the figure are some of the relevant ions studied.

4.3 Experimental Results

4.3.1 TOF Spectra

Figure 4.1 shows an example TOF spectra for the species studied. Similarities in the traces can be seen, such as the presence of multiply charged carbon ions, C^{+,2+,3+,4+} and fragmental ions CH⁺, CCl⁺. Below $m/q = 20$, the spectra become more complex, with peak splitting, contaminates, and high charge state fragmental ions.

For chlorinated species, we see the expected 3:1 isotope ratio of ³⁵Cl:³⁷Cl. This also allows the determination of chlorine ion production that could be degenerate with other species (e.g. ³⁵Cl⁵⁺ and ¹²CH₂²⁺, $m/q = 7$). For all the chlorinated molecules studied we clearly see charge states of up to Cl⁷⁺ indicating ionization of the valence shell of a chlorine atom, ending with an ionization potential (IP) of ~ 114 eV. The ionization of M shell electrons from chlorine is more difficult to see, the IP for Cl⁸⁺ and Cl⁹⁺ are ~ 314 eV and ~ 400 eV, respectively, for an isolated chlorine atom. This is comparable to the ~ 392 eV required to see C⁵⁺ of an isolated carbon atom, the

highest charge state seen in this study.

Closer inspection of the TOF spectra for specific ions is shown in Fig. 4.2. Each spectrum is taken at the saturation intensity for that particular ion in methane. For each part ((a)-(d)) the chloromethane spectrum has been offset from the methane spectrum by a set amount only to show the distinction between the two spectra. In each spectrum the time span of the carbon ion produced from methane is only a few nanoseconds (< 10 ns), but from chloromethane the span of time increases to tens of nanoseconds due to the recoil momentum from the C-Cl dissociation.

The coupling of intense laser light to atoms and molecules has been studied at lower intensities and many insights have been brought forth, including molecular field tunneling ionization, dissociative ionization, and enhanced ionization. There is also the process of Coulomb explosion, where a molecule becomes highly charged and the positively charged nuclear ions energetically repel one another [32]. This process is usually produced when the parent ion reaches a doubly charged state.

4.3.2 Ion Fragment Energy

Coulomb explosion can impart a large amount of kinetic energy to exiting ions. Methane has been shown to have little or no initial momentum due to the ionization process. This conclusion is drawn from experiment [33] and theoretical work [34] that suggests that an Enhanced Ionization (EI) process [35] takes place at each of the C-H bonds simultaneously as compared to a bond by bond stepwise process.

For chlorinated species, the carbon charge states $1 \leq m \leq 4$ show a distinct broadening of the peaks in the TOF spectra, indicating that the ions have an initial momentum along the flight tube. Likewise, when the laser polarization is oriented perpendicular to the flight tube, the signal is reduced or may completely disappear. The kinetic energy of release (E_{KER}) [35] of these ions has been calculated from the difference in the times of the corresponding fast and slow peaks using the relationship [36],

$$E_{KER} \cong \frac{1}{8m}(qF\Delta t)^2 \quad (4.1)$$

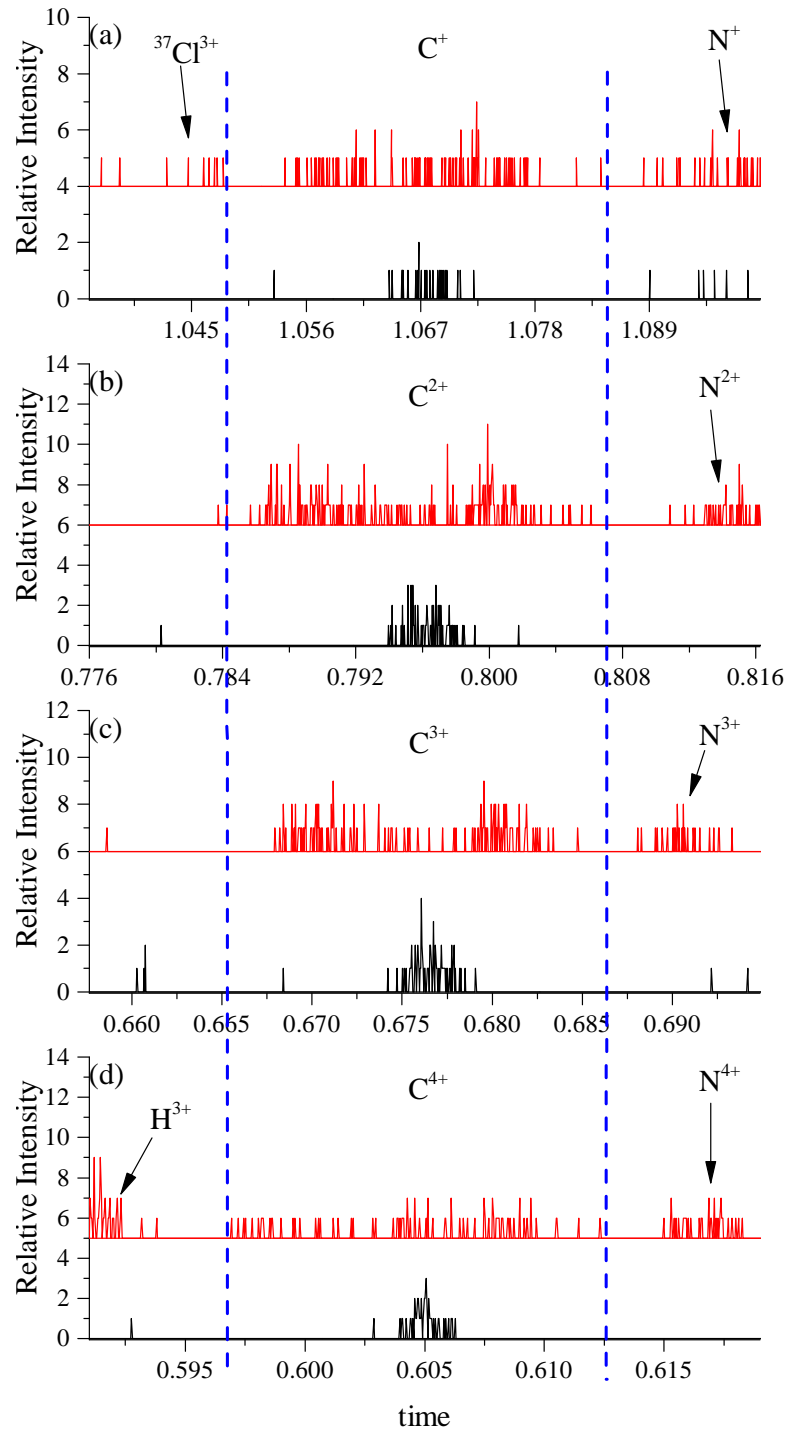


Figure 4.2: Time of flight spectra for carbon ions from methane (black) and chloromethane (red) (a) C^+ , (b) C^{2+} , (c) C^{3+} and (d) C^{4+} gathered at saturation intensities for each ion. The chloromethane spectra have been offset to allow for easier distinction of the spectra. Blue dashed guidelines have been added to show the time span of each ion used in the energy analysis. Contaminates of known ions have also been indicated.

Table 4.1: Kinetic energy of release for carbon and chlorine ions at $I=1 \times 10^{16}$ W/cm² for chloromethane.

Ion	E_{KER} (eV)
C ⁺	5.10
C ²⁺	11.99
C ³⁺	23.34
C ⁴⁺	34.59
Cl ³⁺	10.33
Cl ⁴⁺	16.02

where Δt is the time difference of the fast and slow peaks, q is the charge on the ion, m is the mass and F is the force on the ion due to the extraction field.

Table 4.1 gives a summary of carbon and chlorine ion initial kinetic energies for chloromethane. The splitting of the ion peaks is independent of the laser intensity, indicative of an enhanced ionization mechanism. The values reported in Table 4.1 are for intensities ranging from 5×10^{14} W/cm², but an intensity of 7×10^{15} W/cm² give similar E_{KER} .

From Table 4.1 we can see that as the ion number increases, so to does the E_{KER} . This change in E_{KER} could be the result of several factors. First, the difference in the masses of the respective ions. Other possible explanations include, the critical separation between a carbon and chlorine atom, R_c [35]. We note in these cases, ¹³C was used for the methane and chloromethane collections to avoid degeneracy with H₃⁺, a known $m/q = 3$ contaminant [36].

4.3.3 Coincidence Measurements

Insight into the ionization process that leads to large KER can be gained by determining the correlation between arriving ions. The auto-variance function for a time of flight spectrum is given by [37],

$$C(x, y) = \frac{1}{N} \sum_{i=1}^N TOF_i(x) TOF_i(y) - \left[\frac{1}{N} \sum_{i=1}^N TOF_i(x) \right] \left[\frac{1}{N} \sum_{i=1}^N TOF_i(y) \right] \quad (4.2)$$

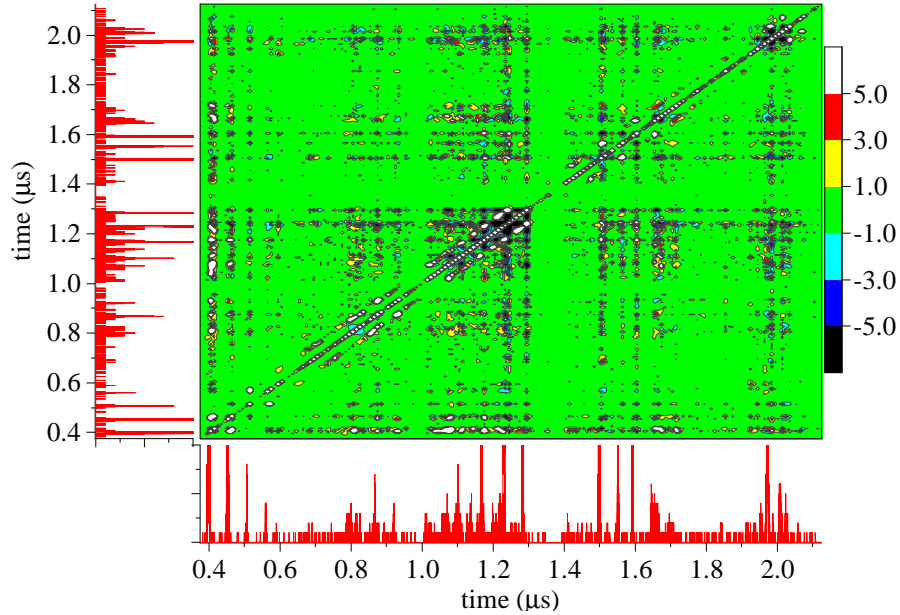


Figure 4.3: Covariance map for chloromethane taken at C^{2+} saturation intensity of $5.7 \times 10^{14} \text{ W/cm}^2$. TOF spectra has a 10 ns bin size. Scale of contours are divided by 10^{-4}

where N is the number of shots, $TOF(x)$ and $TOF(y)$ are the TOF spectra that have been binned. The second part of eq. 4.2 subtracts out the square of the average of the TOF spectrum, which is the statistical, uncorrelated probability of a coincidence.

Figure 4.3 shows the covariance map for chloromethane taken at the C^{2+} saturation intensity of $5.7 \times 10^{14} \text{ W/cm}^2$. The TOF spectra that the map is created from is shown along the side and the bottom of the map. Once a peak is identified, it can be traced along the map to determine any correlated ions.

Based on the the shape of the ion peaks in the TOF spectra, we can be certain that the carbon peaks with the faster arrival times (so-called forward peaks) should be correlated with another ion's longer arrival time (so-called backward peaks). This conclusion is based on conservation of momentum considerations and the covariance map will indicate the particular ion that carbon is associated with.

Knowing the arrival times for each of the individual carbon ions we can take a

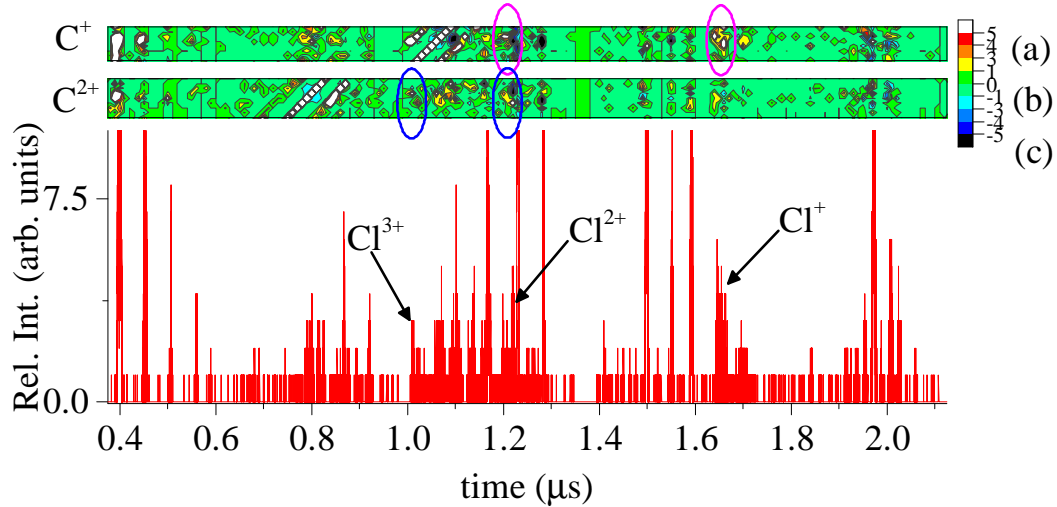


Figure 4.4: Time slices of the covariance map for chloromethane taken at C^{2+} saturation intensity of 5.7×10^{14} W/cm² corresponding to the times around (a) C^+ and (b) C^{2+} arrival times. Plotted below is (c) the normal TOF spectrum used to create the covariance map. Indicated in the figure are peaks for Cl^+ , Cl^{2+} , and Cl^{3+} . Circled in magenta are portions of the map where there is correlation between C^+ and Cl^+ and C^+ and Cl^{2+} . Circled in blue are portions of the map where there is correlation between C^{2+} and Cl^{2+} and C^{2+} and Cl^{3+} .

selection of the map and look for positive auto-variance values. Figure 4.4 shows two portions of the covariance map corresponding to times in which C^+ will fall between as well as one for C^{2+} .

From the figure, we can see that C^+ has a strong correlation with Cl^+ with the characteristic forward carbon peak and backward chlorine peak and vice versa. This is consistent with the idea that the energy of the carbon ions comes from the C-Cl dissociation.

For small correlations, it can be beneficial to sum over a portion of the covariance map. This is done in figure 4.5, where the sum is taken over the C^+ portion of the covariance map in figure 4.4 and plotted as a function of time.

The correlation that we saw in figure 4.4 is now clearly present in the sum. At a time corresponding to $\sim 1.65 \mu s$, we see a rise in the positive correlation that matches

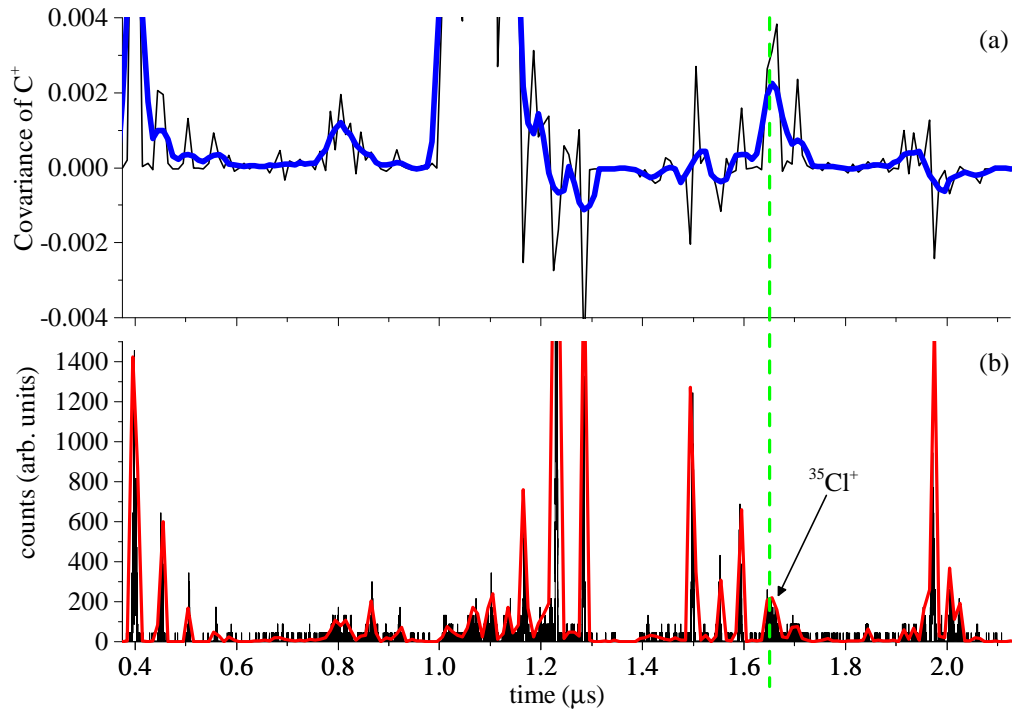


Figure 4.5: (Top) Sum over the C^+ portion of the covariance map versus time. (Black line) is the raw sum over a time range of 0.995 μs - 1.155 μs , (Blue line) a weighted average smoothing function to highlight correlations. (Bottom) time of flight spectrum for the collected coincidence measurement. (Black) TOF data with 39 ps bins, (Red) TOF data with 10 ns bins.

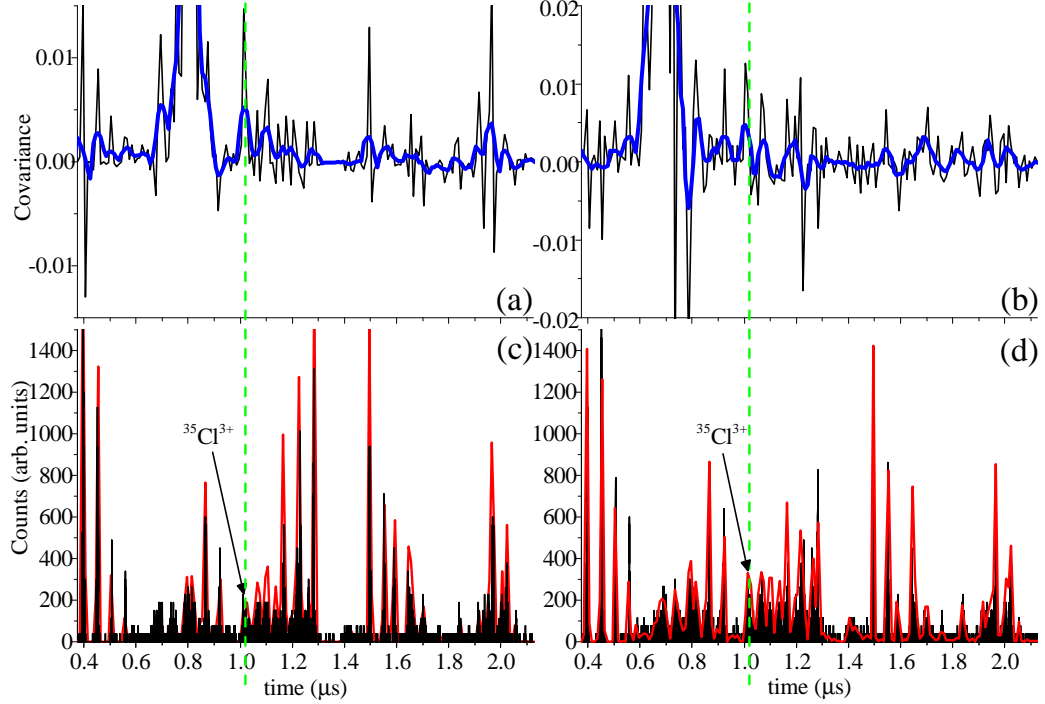


Figure 4.6: (a) Sum over the C^{2+} portion of the covariance map versus time with (c) the corresponding time of flight spectrum for the collected coincidence measurement taken at an intensity of 1.05×10^{16} W/cm². (b) Sum over the C^{3+} portion of the covariance map versus time with (d) the corresponding time of flight spectrum for the collected coincidence measurement taken at an intensity of 2.25×10^{16} W/cm².

with the TOF for a $^{35}\text{Cl}^+$ ion.

A similar process is undertaken for the C^{2+} and C^{3+} ions in figure 4.6. We can see in Fig. 4.6(a) that the $^{35}\text{Cl}^{3+}$ ion has a small correlation with the C^{2+} for which this sum is taken over at an intensity of 1.05×10^{16} W/cm². At a slightly higher intensity of 2.25×10^{16} W/cm² in Fig. 4.6(b) the sum is taken over the C^{3+} , and again we see a small positive correlation at the time of $^{35}\text{Cl}^{3+}$.

Having a correlation of one type of ion, $^{35}\text{Cl}^{3+}$, with two other ions, C^{2+} and C^{3+} at only slight different intensities will be examined later on, and a possible explanation will be presented.

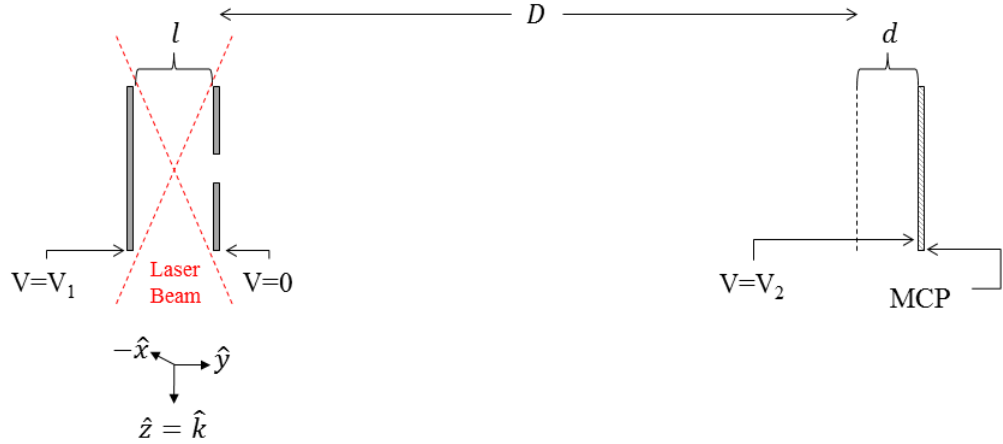


Figure 4.7: Schematic diagram of the spectrometer with parameters to be varied. These include the extraction voltage ΔV_1 , the flight tube length D , the initial ion position y_0 , the length of the interaction with the MCP voltage ΔV_2 , and the time offset t_0 (not indicated).

4.3.4 Energy Spectra

From the energies of the ions seen in Table 4.1, one can come to the conclusion that not all ions of a given species are collected during an experiment. To ensure that we have accurately identified the peaks and the energy spectrum, we have modelled the spectrometer. By varying certain aspects of the spectrometer, such as extraction voltage, flight tube length, and a time offset, we can calculate the time of flight for an ion using the relation,

$$t_{calc} = t_{extraction} + t_{ft} + t_d + t_0 \quad (4.3)$$

Where,

$$t_{extraction} = \left(\frac{m}{q}\right) \left(\frac{l}{\Delta V_1}\right) \left[-v_0 + \sqrt{v_0^2 + \left(\frac{q}{m}\right) \left(\frac{\Delta V_1}{l}\right) (l - 2y_0)}\right] \quad (4.4)$$

is the time the ion with mass m and charge q , starting at position y_0 and initial velocity v_0 spends in the extraction region with potential difference ΔV_1 over a distance of l .

$$t_{ft} = \frac{D}{\sqrt{v_0^2 + \left(\frac{q}{m}\right) \left(\frac{\Delta V_1}{l}\right) (l - 2y_0)}} \quad (4.5)$$

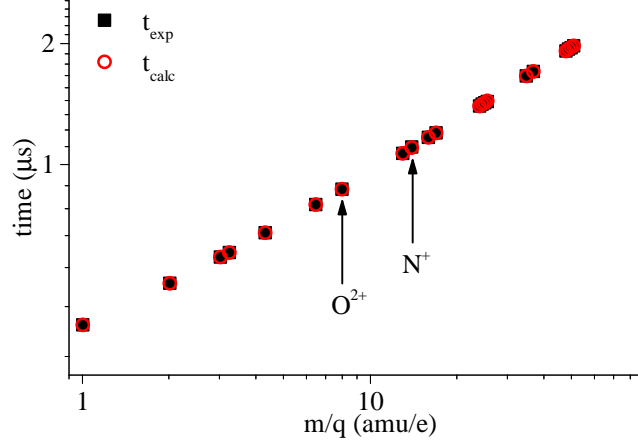


Figure 4.8: Experimental, t_{exp} , and calculated, t_{calc} , times for our TOF spectrometer. The values of the chamber parameters for this particular configuration are: $V_1=2995$ V, $D=0.1195$ m, $y_0=-5\times 10^{-4}$ m, $d=3.25\times 10^{-3}$ m, $t_0=1.425\times 10^{-7}$ s. These values give a residue $S=3.8404\times 10^{-6}$.

is the time in the field free flight tube of length D .

$$t_d = \left(\frac{m}{q}\right) \left(\frac{d}{\Delta V_2}\right) \left(-\sqrt{v_0^2 + \left(\frac{q}{m}\right) \left(\frac{\Delta V_1}{l}\right) (l - 2y_0)} + \sqrt{v_0^2 + \left(\frac{q}{m}\right) \left(\frac{\Delta V_1}{l}\right) (l - 2y_0) + 2\left(\frac{q}{m}\right) \Delta V_2}\right) \quad (4.6)$$

is the time an ion takes to traverse a region of length d , close to the detector where a negative potential, ΔV_2 , is placed on the detector, and t_0 is the time offset for the spectrometer.

By setting the initial velocity, $v_0 = 0$ (thermal energy $\sim \frac{1}{40}$ eV), the time for particular known ions can be calculated and compared to measured times, t_{exp} . Figure 4.8 shows the results for t_{exp} and t_{calc} for a given set of chamber parameters as a function of mass to charge ratio.

Varying the parameters, ΔV_1 , D , d , and t_0 , we calculate and minimize the residual $S = \left(\frac{t_{exp}-t_{calc}}{t_{exp}}\right)^2$. Typical values for these parameters allow for values of the residual on the order of $\sim 10^{-6}$ and give a calculated species TOF that differs from the experimental peak TOF time by ≤ 2 ns. For comparison, the full width at half maximum for a C^{2+} peak from methane is ~ 2.5 ns.

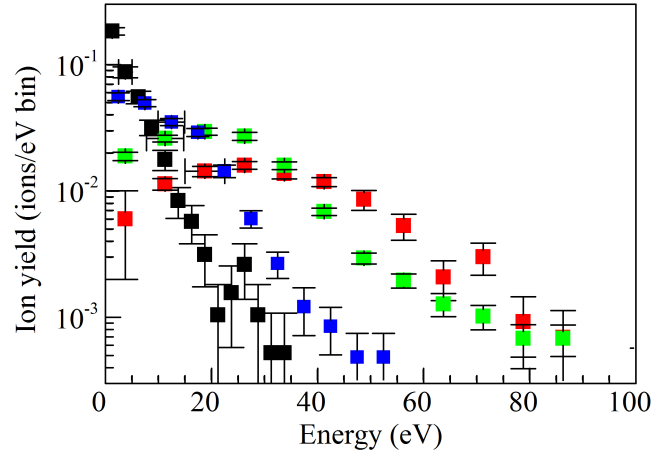


Figure 4.9: Energy spectrum of carbon ions C^+ (black), C^{2+} (blue), C^{3+} (green), C^{4+} (red) from CH_3Cl with laser polarization parallel to the flight tube axis and an intensity in the interaction region at the saturation intensity for the carbon ion yield of each species: 4.4×10^{14} W/cm^2 for C^+ , 5.7×10^{14} W/cm^2 for C^{2+} , 1.3×10^{15} W/cm^2 for C^{3+} , 6.5×10^{15} W/cm^2 for C^{4+} .

Once we determine these chamber parameters we can then use them to determine a relationship between the time of flight and initial velocity and convert the TOF spectrum into an energy spectrum for a given mass to charge ratio. Figure 4.9 shows the energy spectrum results for carbon ions C^+ , C^{2+} , C^{3+} and C^{4+} . As the ion number increases so does the average energy and the distribution of possible energies for the ions.

C^+ has a typical energy spread of 2.5 eV whereas C^{4+} is broad and peaks around 30 eV. These values are consistent with those found from using equation 4.1.

An intensity question one may ask could be: "How does this energy depend on the intensity of the laser pulse?" Figure 4.10 shows the energy spectra for the carbon ions at different intensities. The top spectrum shows the energy of C^+ ions at the saturation intensities for each of the carbon ions. Moving down, each spectrum is for C^{2+} moving all the way to C^{4+} .

For the C^{4+} , even at the lowest saturation intensity for C^+ at 4.4×10^{14} W/cm^2 ,

there are still some ions detected. Surprisingly, these ions still have an energy distribution that is consistent with those collected at the saturation intensity of C^{4+} at 6.5×10^{15} W/cm².

Such an intensity dependent finding indicates the energy of the final fragments comes entirely from the Coulomb explosion, dissociation process and is not a result of acceleration in the laser field.

4.3.5 Ion Count Rates

Ion count rates as a function of laser intensity can be determined by varying laser power and collecting all ions at that intensity. Figures 4.11 and 4.12 show the count rates of carbon ions upto C^{4+} and chlorine up to Cl^{7+} produced from the ionization of chloromethane. Figure 4.12 does not show Cl^{5+} because of the degeneracy of $^{35}Cl^{5+}$ with N^{2+} and a lack of isotope resolution of $^{37}Cl^{5+}$.

The spectra of chloromethane show a doubly charged parent ion, CH_3Cl^{2+} , as well as the partial ion CCl^{2+} . With the determination of the energies of different ions, there is a correlation with the amount of energy of carbon ions and chlorine ions that is in agreement with the conservation of momentum. These data lead us to suspect that the hydrogen atoms have little influence on the production of either carbon or chlorine ions and again confirms the energy is a result of the dissociation process over multiple cycles and not from field acceleration (which would reverse ion energies every half cycle).

We can see from the ion yields that above the saturation intensity, the yield scales as $I^{\frac{3}{2}}$, as expected for a Gaussian spatial distribution. At the saturation intensities we can get an indication of the process in which the parent ion goes through in order to produce the carbon and chlorine ions.

We can see from comparing the ion yields that Cl^+ is the first of the ions to saturate, quickly followed by C^+ and then Cl^{2+} . This helps us to understand why the covariance map showed a correlation between C^+ and Cl^+ as well as C^+ and Cl^{2+} . Each of these ions are being produced at nearly equal intensities. The next ion to

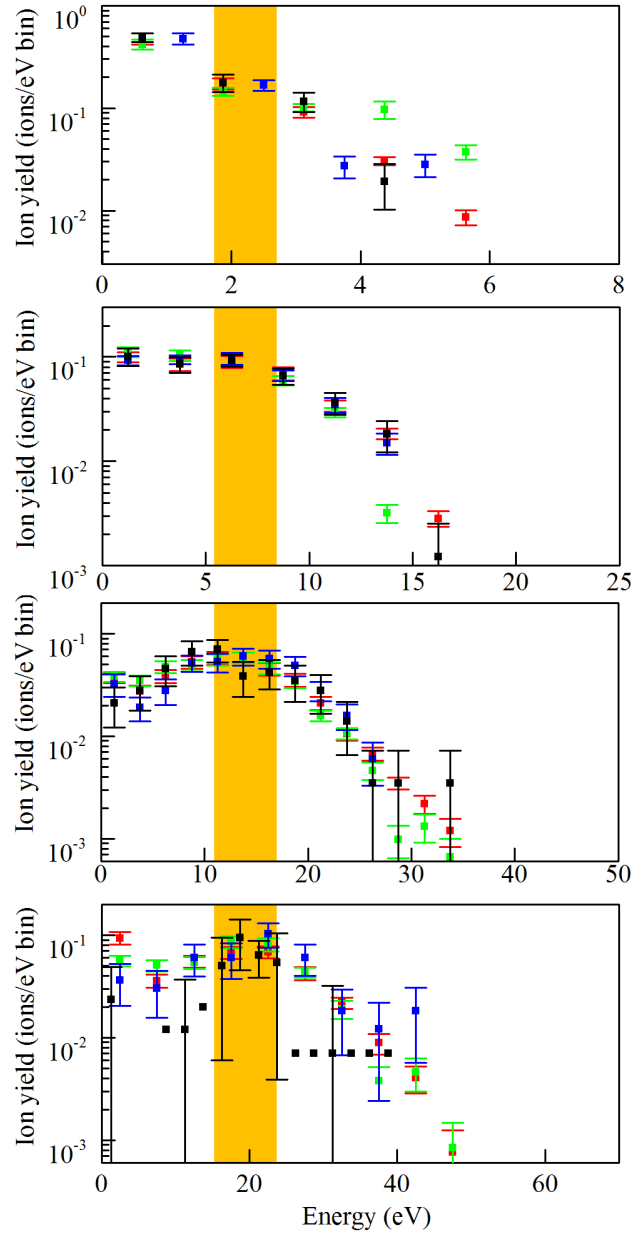


Figure 4.10: Energy spectrum of carbon ions C^+ (top), C^{2+} (second), C^{3+} (third), C^{4+} (bottom) from CH_3Cl with laser polarization parallel to the flight tube axis and rectangular aperture collected at the saturation intensities for each species from C^+ 4.4×10^{14} W/cm^2 (black), C^{2+} 5.7×10^{14} W/cm^2 (blue), C^{3+} 1.3×10^{15} W/cm^2 (green), C^{4+} 6.5×10^{15} W/cm^2 (red). The ion yields have been adjusted to give a normalized (unity) yield when integrated over energy. Half of the maximum energy observed for the fragments is highlighted in the figure.

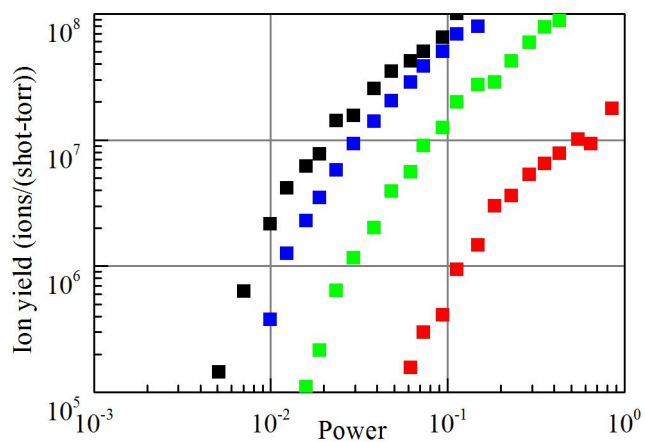


Figure 4.11: (a) Ion count rates for C^+ (black), C^{2+} (blue), C^{3+} (green), C^{4+} (red) as a function of laser power. The calibration to intensity is 10^{-3} in power corresponds to 3.54×10^{13} W/cm².

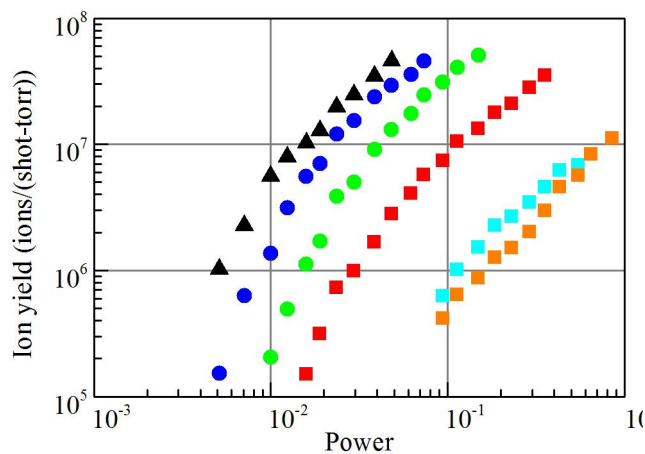


Figure 4.12: (a) Ion count rates for Cl^+ (black triangles), Cl^{2+} (blue circles), Cl^{3+} (green circles), Cl^{4+} (red squares), Cl^{6+} (light blue squares), Cl^{7+} (orange squares) as a function of laser power. The calibration to intensity is 10^{-3} in power corresponds to 3.54×10^{13} W/cm².

reach saturation is C^{2+} and then Cl^{3+} with their saturation intensities being less than a factor of two of one another. The correlation of these two ions was also seen in the covariance map. After the saturation of Cl^{3+} , both C^{3+} and Cl^{4+} reach saturation and after that C^{4+} then Cl^{6+} and Cl^{7+} .

From the covariance map, we know that carbon and chlorine atoms are associated with one another. We now need to understand how a bound C-Cl fragment that is ionizing will give carbon and chlorine ions with specific energies in the same order as the individual saturation intensities.

4.4 Understanding the Interaction

Knowing the energies of individual ions and roughly the order of appearance of each ion from the saturation intensity, we can start to model the interaction. We assume the hydrogen has little influence on the interaction and take a simple 1D classical model of a bound carbon and chlorine ions aligned in the field.

The first step of the ionization process is the production of the parent ion CH_3Cl^+ that has an ionization potential of 11.27 eV [38] as shown in figure 4.13. The saturation of this ion has already occurred at an intensity of $\sim 1.6 \times 10^{14}$ W/cm², the lowest intensity in our study. This leaves a bound CCl^+ ion with the possibility of a positively charged chlorine ion, ionization potential of 16.6 eV [39] and saturation intensity of 2.8×10^{14} W/cm², of then leaving.

The considerations of our model proceeds from the CCl^+ ion and is developed in the following way. Using the order of ion saturation intensities along with the kinetic energies of each ion we determine the critical separation, R_c , between the carbon and chlorine atoms with,

$$R_c = \frac{1}{4\pi\epsilon_0} \frac{q_1 q_2}{E_K^{q_1} + E_K^{q_2}} \quad (4.7)$$

where q_1 and q_2 are the charges on the ions and $E_K^{q_1}$ and $E_K^{q_2}$ are the kinetic energies of each ion.

In the model, chlorine is set to have a position at $x = 0$ and carbon is allowed to move along the \hat{x} axis, its position determined by the calculation of R_c . The potential

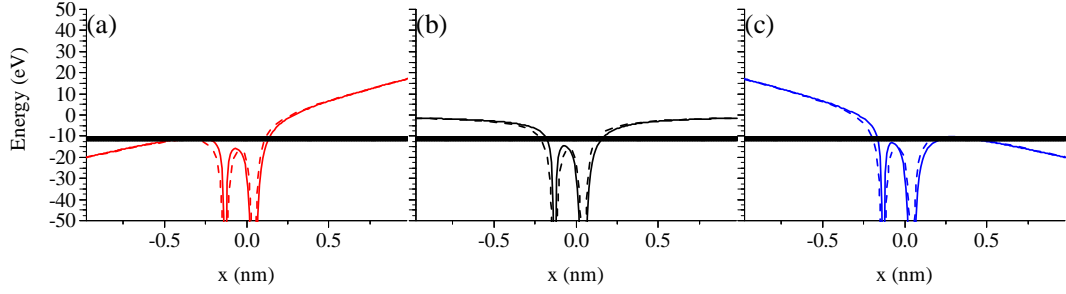


Figure 4.13: (a)-(c) Ionization of parent molecule CH_3Cl at $4.8 \times 10^{13} \text{ W/cm}^2$ where the separation of the carbon and chlorine, $r = 1.0R_{eq}$. Also plotted is the ionization energy of the parent ion CH_3Cl^+ . The zero of the plot is at the center of mass of the system. Solid lines represent the potential where the charge distribution on the carbon and chlorine atoms takes into account the dipole moment and polarizability of the molecule. Dashed lines represent the potential when the charge is evenly distributed.

that an electron will be subject to will be determined by the ionization number of the carbon and chlorine ions. The ionization potential of each electron must be determined to see if the electron has the possibility of ionizing from the C-Cl potential well.

To determine the ionization energies we consider the amount of work required to move an electron from infinity to a position around the carbon or chlorine ion,

$$W = \int_{\infty}^r \vec{E}_{tot} \cdot d\vec{r}' \quad (4.8)$$

The \vec{E}_{tot} is the total electric field of the two ions present, \vec{E}_{carbon} and $\vec{E}_{chlorine}$.

First considering the ionization of the carbon atom, the integral from the carbon portion will just give the IP of the particular ion. The integral over the chlorine portion will be the change in energy for the carbon ion IP

$$W = IP_{carbon} + \int_{\infty}^{R_c} \vec{E}_{chlorine} \cdot d\vec{r}' = IP_{carbon} + \Delta IP \quad (4.9)$$

The change in energy will depend on the charge of the chlorine ion and the separation distance between the carbon and chlorine ions. The result for the change

Table 4.2: Values for IP of carbon and chlorine ions. Starred energies are those determined by electron impact studies on chloromethane, the rest are atomic data.

Ion	IP (eV)
C ⁺	26.3*
C ²⁺	24.3845
C ³⁺	47.88778
C ⁴⁺	64.49351
Cl ⁺	16.6*
Cl ²⁺	23.81364
Cl ³⁺	39.8
Cl ⁴⁺	53.24
Cl ⁵⁺	67.68
Cl ⁶⁺	96.94
Cl ⁷⁺	114.2013

in energy of the carbon IP is,

$$\Delta IP = -\frac{1}{4\pi\epsilon_0} \frac{q_{chlorine}}{R_c} \quad (4.10)$$

This process can also be carried out for the chlorine ion under consideration and the change in ionization potential will come from the carbon ion in a similar manner. Table 4.2 gives a summary of the ionization potentials used before any changes are made due to neighbouring ions.

The changes in the ionization potentials are in the range of 5 to 20 eV's which could be a significant amount of energy. This amount of energy could change a classical over-the-barrier type of ionization to a tunneling type of ionization. Table 4.3 gives a summary of the changes in the ionization potentials that are calculated for our model and gives the ion being considered for ionization, the perturbing ion, the separation between the two ions and the amount of energy change that is produced by the ion.

Once the change in the IP is known, the energy shift due to the external electric field can then be added or subtracted from the new ionization potential. The energy

Table 4.3: Values for ΔIP at varying values of separation between the carbon and chlorine ions.

Changing Ion	Perturbing Ion	Separation Distance (R_{eq})	ΔIP (eV)
C ⁺	Cl ⁺	1.14	7.1
Cl ²⁺	C ⁺	1.4	5.78
C ²⁺	Cl ²⁺	1.75	9.24
Cl ³⁺	C ²⁺	1.94	8.34
C ³⁺	Cl ³⁺	2.0	12.13
Cl ⁴⁺	C ³⁺	2.3	10.55
Cl ⁵⁺	C ³⁺	2.35	10.33
C ⁴⁺	Cl ⁵⁺	2.4	16.85
Cl ⁶⁺	C ⁴⁺	2.65	12.21
Cl ⁷⁺	C ⁴⁺	2.8	11.56

change due to the external field is given by,

$$\Delta E = \pm |\vec{E}_{laser}| x_{carbon} = \pm |\vec{E}_{laser}| R_c \quad (4.11)$$

With the position of the chlorine ion being $x = 0$ there is no change in its IP due to the external field.

Knowing the energy of the electron we can compare it to the potential energy produced by the carbon and chlorine ions,

$$U = -\frac{1}{4\pi\epsilon_0} \left(\frac{q_{carbon}}{|x + R_c|} + \frac{q_{chlorine}}{|x|} \right) \quad (4.12)$$

this will allow us to determine possible or dominant ionization mechanism.

Starting from the CCl⁺ ion, the next step that we consider is its transformation, where the chlorine atom has a larger positive charge, to that of CCl²⁺ where the electron ionizes from the carbon atom. With the energies of C⁺ and Cl⁺ we determine the critical separation of $\sim 2.03 \times 10^{-10}$ m which is $1.14 R_{eq}$, where $R_{eq} = 1.781 \times 10^{-10}$ m is the equilibrium separation of carbon-chlorine bond in chloromethane.

In figure 4.14(a)-(c) we show the potential of a neutral carbon atom in the $1s^2 2s^2 2p^2$ state along with the potential of a Cl⁺ ion in the $[\text{Ne}] 3s^2 3p^4$ state with an

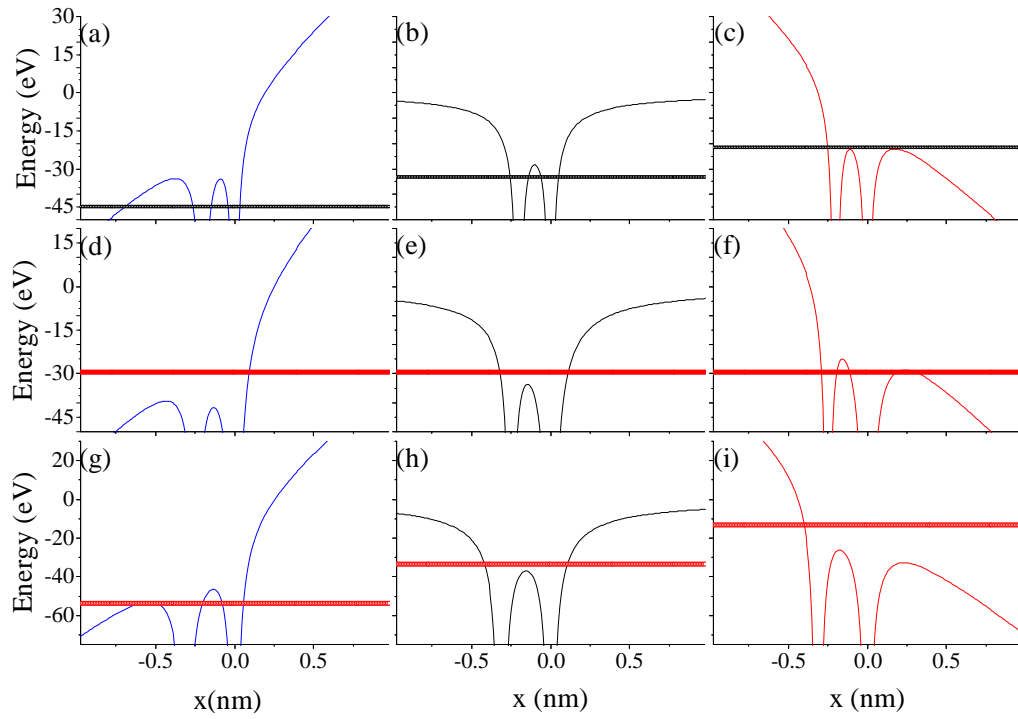


Figure 4.14: (a)-(c) Ionization of C neutral at 4.4×10^{14} W/cm² where the separation of the carbon and chlorine, $r = 1.14R_{eq}$. (d)-(f) Ionization of Cl⁺ at 4.4×10^{14} W/cm² where $r = 1.4R_{eq}$. (g)-(i) Ionization of C⁺ at 5.6×10^{14} W/cm² where $r = 1.75R_{eq}$.

electric field oscillating from one direction, $\pm\hat{x}$, to the other with a maximum value corresponding to an intensity of 4.4×10^{14} W/cm². The results of the energy shifts of the carbon ions IP are also shown in Fig. 4.14(a)-(c). With the presence of Cl⁺ amount of change in C⁺ IP is 7.1 eV and the amount of change due to the electric field is ± 11.7 eV. We can see in the figure that for a particular electric field direction, tunneling ionization will occur, but the opposite field direction will allow enhanced ionization (EI) [40] to occur.

In Fig. 4.14(d)-(f) we consider the ionization of Cl²⁺. With this particular ion, we will have a change in IP due to the presence of C⁺ but there will be no shift in energy due to the external field since the position of the chlorine atom is at the origin. We can see from the figure that once the carbon atom transitions to C⁺ we can easily obtain the Cl²⁺ ion without a change in the intensity of the beam due to enhanced ionization that is provided by the carbon ion. The presence of enhanced ionization (EI) was also apparent in the production of C⁺ where tunneling is required for one field direction, but a reversal allows the Cl⁺ ion to suppress the middle barrier enough for an electron to escape without the need for tunneling.

For the production of C²⁺ shown in Fig. 4.14(g)-(i), EI is still a factor in its production as can be seen in Fig. 4.12(i), but because of the charge on the chlorine ion, the barrier suppression is greater than that as seen in the production of C⁺.

Figure 4.15 gives the details of production for Cl³⁺ and Cl⁴⁺ as well as C³⁺. A similar process as seen in Fig. 4.14 takes place here. Enhanced ionization, due to a more positively charged partner, allows the escape of an electron when the electric field is oriented toward the ionizing atom, whereas tunneling would have occurred if the electric field were oriented in the opposite direction.

One observation that can be made between Fig. 4.14(d) and Fig. 4.15(a) in the enhanced ionization from Cl⁺ to Cl²⁺ and Cl²⁺ to Cl³⁺ respectively is that the barrier suppression between the two atoms is less for Fig. 4.15(a). Even though the amount of charge on the carbon atom is more than in the previous ionization step, the separation distance between the two ions is greater. In figure 4.14(d) the difference between the

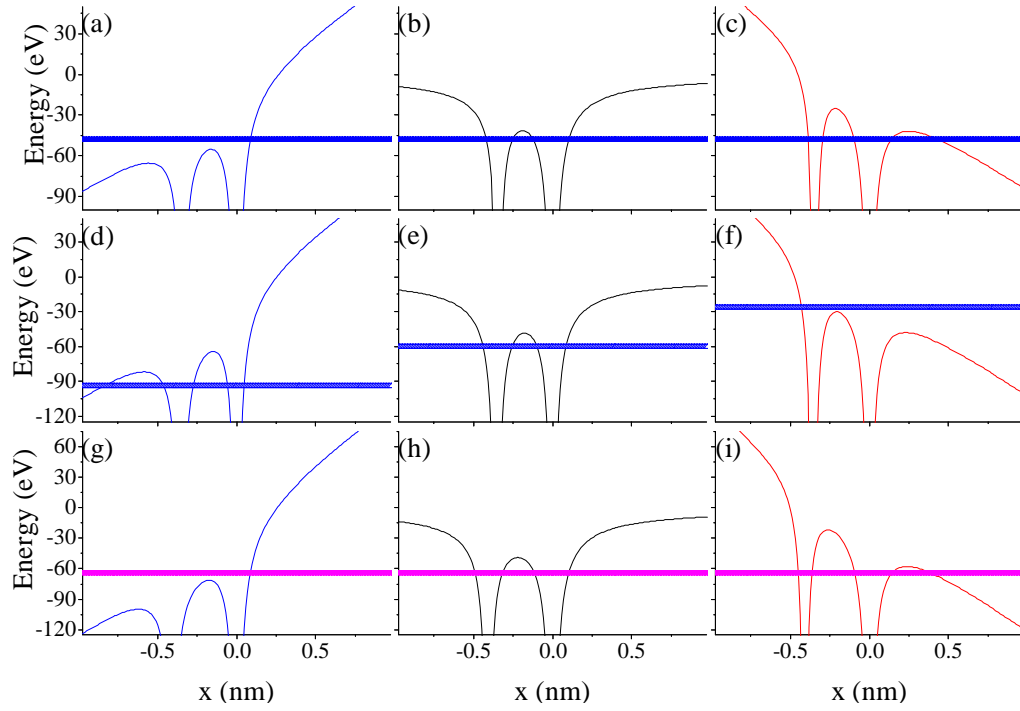


Figure 4.15: (a)-(c) Ionization of Cl^{2+} at $8.3 \times 10^{14} \text{ W/cm}^2$ where $r = 1.94R_{eq}$. (d)-(f) Ionization of C^{2+} at $1.2 \times 10^{15} \text{ W/cm}^2$ where $r = 2.0R_{eq}$. (g)-(i) Ionization of Cl^{3+} at $1.7 \times 10^{15} \text{ W/cm}^2$ where $r = 2.3R_{eq}$.

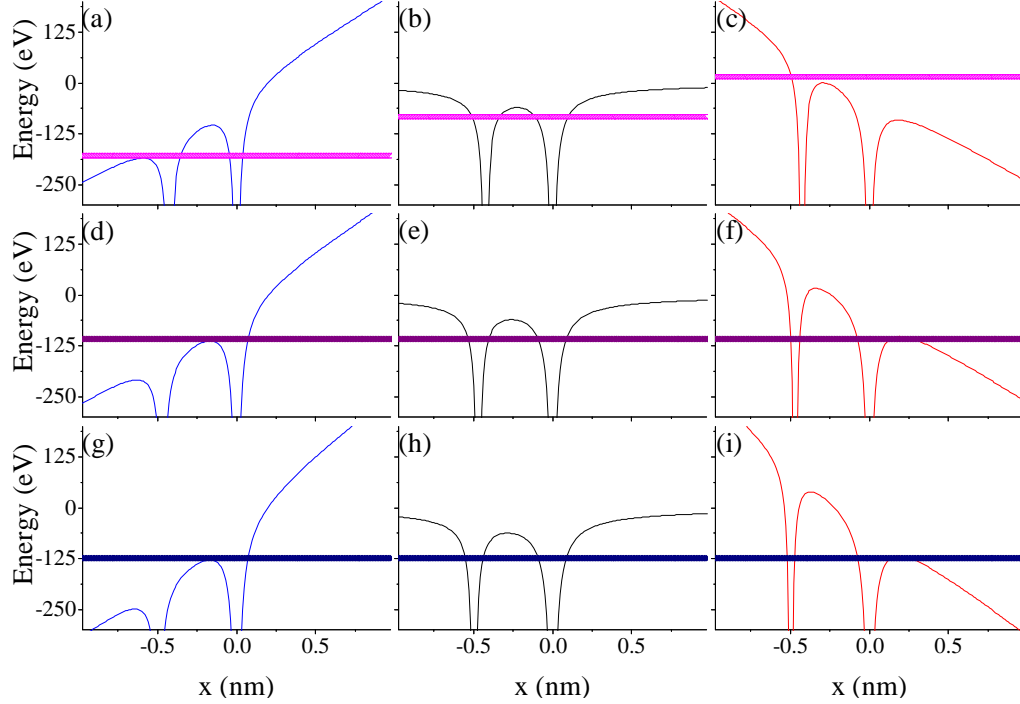


Figure 4.16: (a)-(c) Ionization of C^{3+} at $7.12 \times 10^{15} \text{ W/cm}^2$ where $r = 2.4R_{eq}$. (d)-(f) Ionization of Cl^{5+} at $8.4 \times 10^{15} \text{ W/cm}^2$ where $r = 2.65R_{eq}$. (g)-(i) Ionization of Cl^{6+} at $1.2 \times 10^{16} \text{ W/cm}^2$ where $r = 2.8R_{eq}$.

ionization potential and the maximum of the central barrier is $\sim 12 \text{ eV}$ as compared to Fig. 4.15(a) where the difference is $\sim 7 \text{ eV}$.

In figure 4.16 we see the final stages of ionization, the production of C^{4+} , Cl^{6+} and Cl^{7+} . From Fig 4.14(a)-(c), we can see that EI is still occurring for the carbon ion, but for chlorine the influence of the carbon ion for EI is almost non-existent and the ionization of chlorine is approaching an atomic-like response.

4.5 Conclusion

In conclusion, we have investigated how the substitution of a chlorine atom for a hydrogen atom in methane influences the ionization process in the production of the highest charge state of carbon. We have shown that lower charge states of carbon have a molecular type response and KER's have been measured. The energy of the

fragments is independent of the laser intensity, indicating that the energy come from the dissociation of a CCl ion. From our simple model, we have seen that enhanced ionization plays a large role in the production of C^+ through C^{4+} as well as for Cl^{2+} through Cl^{4+} . As we get to the highest charge states of chlorine the response of the chlorine ion becomes more atomic with the role of enhanced ionization playing a minimal role.

BIBLIOGRAPHY

- [1] J. G. Leopold and I. C. Percival. *Phys. Rev. Lett.* **41**, 944–947 (1978).
- [2] R. Moshhammer, B. Feuerstein, W. Schmitt, A. Dorn, C. D. Schröter, J. Ullrich, H. Rottke, C. Trump, M. Wittmann, G. Korn, K. Hoffmann, and W. Sandner. *Phys. Rev. Lett.* **84**, 447–450 (2000).
- [3] B. Walker, B. Sheehy, L. F. DiMauro, P. Agostini, K. J. Schafer, and K. C. Kulander. *Phys. Rev. Lett.* **73**, 1227–1230 (1994).
- [4] M Protopapas, C H Keitel, and P L Knight. *Reports on Progress in Physics* **60**(4), 389 (1997).
- [5] Jeffrey L. Krause, Kenneth J. Schafer, and Kenneth C. Kulander. *Phys. Rev. Lett.* **68**, 3535–3538 (1992).
- [6] M. Lewenstein, Ph. Balcou, M. Yu. Ivanov, Anne L’Huillier, and P. B. Corkum. *Phys. Rev. A* **49**, 2117–2132 (1994).
- [7] B. A. Reagan, T. Popmintchev, M. E. Grisham, D. M. Gaudiosi, M. Berrill, O. Cohen, B. C. Walker, M. M. Murnane, J. J. Rocca, and H. C. Kapteyn. *Phys. Rev. A* **76**, 013816 (2007).
- [8] J. Nuckolls, A. Thiessen, L. Wood, and G. Zimmerma. *Nature* **239**(5368), 139 (1972).
- [9] Robert J. Levis, Getahun M. Menkir, and Herschel Rabitz. *Science* **292**(5517), 709–713 (2001).
- [10] S. Baker, J. S. Robinson, C. A. Haworth, H. Teng, R. A. Smith, C. C. Chirila, M. Lein, J. W. G. Tisch, and J. P. Marangos. *Science* **312**(5772), 424–427 (2006).
- [11] A. Einstein. *Ann. Phys. LPZ* **17**, 132 (1905).
- [12] P. Agostini, G. Barjot, J. Bonnal, G. Mainfray, C. Manus, and J. Morellec. *IEEE Journal of Quantum Electronics* **4**(10), 667–669 (1968).
- [13] L.V. Keldysh. *Sov. Phys. JETP* **20**(5), 1307 (1965).
- [14] G.S. Voronov and N.B. Delone. *Sov. Phys. JETP* **23**(1), 54 (1966).

- [15] A.M. Perelomov, V.S. Popov, and M.V. Terent'ev. *Sov. Phys. JETP* **23**(5), 926 (1966).
- [16] M.V. Ammosov, N.B. Delone, and V.P. Krainov. *Zh. Eksp. Teor. Fiz.* **91**, 2008 (1986).
- [17] I.Yu. Kiyan and V.P. Krainov. *Zh. Eksp. Teor. Fiz.* **100**, 776 (1991).
- [18] Bretislav Friedrich and Dudley Herschbach. *Phys. Rev. Lett.* **74**, 4623–4626 (1995).
- [19] Eric E. Aubanel, Jean-Marc Gauthier, and André D. Bandrauk. *Phys. Rev. A* **48**, 2145–2152 (1993).
- [20] Bretislav Friedrich and Dudley Herschbach. *The Journal of Physical Chemistry* **99**(42), 15686–15693 (1995).
- [21] P A Hatherly, M Stankiewicz, K Codling, L J Frasinski, and G M Cross. *J. Phys. B* **27**(14), 2993 (1994).
- [22] K Codling, L J Frasinski, and P A Hatherly. *J. Phys. B* **22**(12), L321 (1989).
- [23] Chengyin Wu, Haizhen Ren, Tingting Liu, Ri Ma, Hong Yang, Hongbing Jiang, and Qihuang Gong. *J. Phys. B* **35**(11), 2575 (2002).
- [24] K. Boyer, T. S. Luk, J. C. Solem, and C. K. Rhodes. *Phys. Rev. A* **39**, 1186–1192 (1989).
- [25] K. Zhao and W. T. Hill. *Phys. Rev. A* **71**, 013412 (2005).
- [26] V. R. Bhardwaj, F. A. Rajgara, K. Vijayalakshmi, V. Kumarappan, D. Mathur, and A. K. Sinha. *Phys. Rev. A* **58**, 3849–3855 (1998).
- [27] Xiaofeng Tang, Xiaoguo Zhou, Manman Wu, Shilin Liu, Fuyi Liu, Xiaobin Shan, and Liusi Sheng. *The Journal of Chemical Physics* **136**(3), 034304 (2012).
- [28] Hong-Wei Xi, Ming-Bao Huang, Bo-Zhen Chen, and Wen-Zuo Li. *The Journal of Physical Chemistry A* **109**(19), 4381–4387 (2005).
- [29] Ph. Hering and C. Cornaggia. *Phys. Rev. A* **57**, 4572–4580 (1998).
- [30] Sasi Palaniyappan, Rob Mitchell, Rob Sauer, Isaac Ghebregziabher, Samantha L. White, M. F. Decamp, and B. C. Walker. *Phys. Rev. Lett.* **100**, 183001 (2008).
- [31] Anthony DiChiara, Enam A. Chowdhury, George Ongadi, Barry C. Walker, and Robert S. Tamosaitis. *Opt. Lett.* **28**(21), 2106–2108 (2003).
- [32] K. Boyer, T. S. Luk, J. C. Solem, and C. K. Rhodes. *Phys. Rev. A* **39**, 1186–1192 (1989).

- [33] Stefan Roither, Xinhua Xie, Daniil Kartashov, Li Zhang, Markus Schöffler, Huailiang Xu, Atsushi Iwasaki, Tomoya Okino, Kaoru Yamanouchi, Andrius Baltuska, and Markus Kitzler. *Phys. Rev. Lett.* **106**, 163001 (2011).
- [34] Sergiy Bubin, Mackenzie Atkinson, Kálmán Varga, Xinhua Xie, Stefan Roither, Daniil Kartashov, Andrius Baltuška, and Markus Kitzler. *Phys. Rev. A* **86**, 043407 (2012).
- [35] J H Posthumus, L J Frasinski, A J Giles, and K Codling. *J. Phys. B* **28**(10), L349 (1995).
- [36] Kenosuke Hoshina, Yusuke Furukawa, Tomoya Okino, and Kaoru Yamanouchi. *The Journal of Chemical Physics* **129**(10), – (2008).
- [37] L. J. Frasinski, K. Codling, and P. A. Hatherly. *Science* **246**(4933), 1029–1031 (1989).
- [38] F.P. Lossing. *Bull. Soc. Chim. Belg.* **81**, 125 (1972).
- [39] C.E.; Hamill W.H. Tsuda, S.; Melton. *J. Chem. Phys.* **41**, 689 (1964).
- [40] D. M. Villeneuve, M. Yu. Ivanov, and P. B. Corkum. *Phys. Rev. A* **54**, 736–741 (1996).

Chapter 5

LIMITS OF STRONG FIELD RESCATTERING IN THE RELATIVISTIC REGIME

5.1 Introduction

Rescattering [1, 2] between a photoelectron and parent ion is an essential physical process underpinning twenty years of advances in coherent x-ray radiation generation [3, 4], insight into multielectron dynamics [5, 6], and the launch of attosecond science [7, 8]. The highest energy for a laser driven rescattering collision between a photoelectron and the ionizing parent ion is described by a ‘ $3.2U_p$ ’ rule [9], where $U_p = e^2 E_0^2 / (4m\omega^2)$ is the kinetic quiver energy, or ponderomotive energy, of a free electron charge e mass m in an oscillating electric field amplitude E_0 frequency ω . Elastic scattering of the photoelectron when it ‘re’-encounters the parent ion at this energy is responsible for the high energy plateau in the above-threshold ionization (ATI) [10] and has been used to image electron wave functions of molecules [11, 12]. Inelastic scattering, including multielectron nonsequential (e,ne) ionization (NSI) [13], is a mechanism to further excite the parent ion and can photoinitiate inner-shell excitation (ISE) processes [14]. Recombination with the parent ion during recollision gives rise to coherent high-order harmonic generation (HHG) and can produce soft x-ray, attosecond radiation [15]. As the strong field science frontier expands to higher intensities, relativistic effects enter into play. For atomic systems a Lorentz deflection parameter [16] was proposed as a way to gauge their impact,

$$\Gamma_R = \frac{\sqrt{2I_p mc^2 a_0^3}}{16\hbar\omega}, \quad (5.1)$$

where $a_0 = eE_0 / (mc\omega)$ is the Lorentz invariant field parameter [17]. For $\Gamma_R > 1$ the Lorentz force due to the laser magnetic field can deflect the photoelectron position

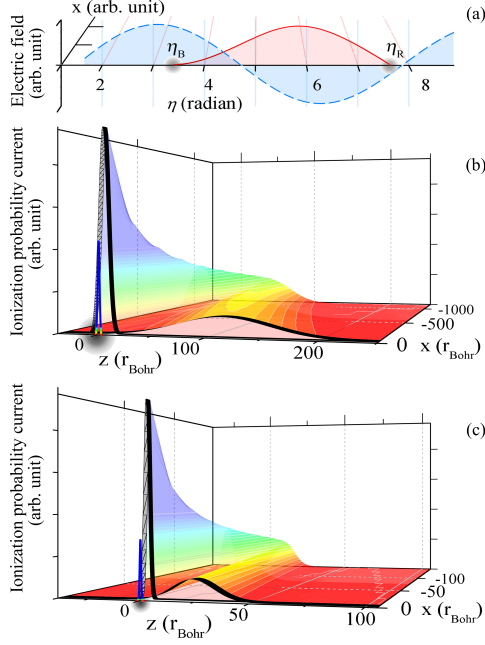


Figure 5.1: (a) Trajectory (solid-red) for photoelectron born (η_B) and returning to the parent ion (η_R) in an oscillating electric field (dashed-blue) for the peak “ $3.2U_p$ ” recollision. Corresponding ionization probability current $\mathbf{j}(\mathbf{r}, \eta_B)$ for Ar^{4+} ionization at $4.6 \times 10^{15} \text{ W/cm}^2$, 2400 nm (b); and Ar^{9+} , $1.6 \times 10^{18} \text{ W/cm}^2$, 200 nm (c). In (b,c) the initial localized $\mathbf{j}(0, \eta_B)$ magnitude is divided by ten.

by more than the electron wave packet extent in space at the recollision moment, significantly reducing the recollision probability and related phenomena [18, 19, 20, 21, 22, 23, 24]. The attenuation is especially large at higher recollision energies, which effectively constrains the HHG cutoff in the relativistic regime [23, 24, 25, 26]. Changes to HHG in the relativistic regime have been recognized theoretically for more than ten years; shaped or counter propagating laser pulses and additional fields have been proposed to counteract this Lorentz drift and realize HHG in the relativistic domain [25, 26, 27, 28, 29, 30, 31, 32, 33, 34, 35, 36, 37, 38]. For ultrahigh intensities ($\Gamma_R \gg 1$), the Lorentz deflection is very large and there is no observed interaction between the photoelectron and parent ion [39, 40].

What has remained elusive is a general quantitative description for the relativistic rescattering cutoff and yield at the limits of rescattering. For example, how the recollision energy and the recollision flux scale with laser or atomic parameters at large Γ_R and what ultimate recollision energy is achievable. The answers to these questions are vital to set the boundary for attosecond physics based on the recollision concept. In particular, for the generation of hard x-ray attosecond radiation [41] and laser induced electron diffraction imaging used to investigate dynamics with sub-angstrom, attosecond precision [42, 43].

In this chapter we investigate the rescattering process in the relativistic regime and describe quantitatively its limits in terms of recollision flux and recollision energy. The recollision photoelectron flux is calculated quantum mechanically using the relativistic Coulomb-corrected strong field approximation (RCCSFA) and semi-classically with a Monte-Carlo trajectory ensemble (SCMC) method. For a broad range of species in different laser fields, we find the rescattering flux can be non-negligible in the relativistic regime, $\Gamma_R > 1$, yielding recollision cutoff energies with a scaling different from the well-known $3.2U_p$ -rule. The scaling laws for the ultimate energy cutoff and corresponding flux are derived via intuitive estimations. We show the ultimate energy cutoff at $\Gamma_R \gg 1$ is practically limited by the available intensities of the short wavelength lasers and cannot exceed a few thousand Hartree.

5.2 Theoretical Considerations

We begin by discussing the rescattering photoelectron before ensuing elastic, inelastic and recombination processes. We study intensities from 10^{13} W/cm² to 10^{21} W/cm² with wavelengths from 80 nm to 8 μ m. Across this span we use highly charged ion (HCI) states for argon (Ar^{Z+} , $1 \leq Z \leq 17$) in external fields with amplitudes $E_0 \leq 0.95E_{\text{OBI}}$, where $E_{\text{OBI}} = I_p^2/(4e^3Z)$ is the classical over-barrier-ionization (OBI) field [44]. The tunneling regime of ionization is considered since $\hbar\omega \ll I_p$ and the Keldysh adiabaticity $\gamma = \omega\sqrt{2mI_p}/(eE_0)$ is much less than one [45]. The calculated tunneling ionization probability per laser cycle W_0 is kept below 50%. Depletion of the

tunneling ion ground state in the rising edge of the laser pulse is not substantial; the results are comparable to experiments near saturation with few cycle pulses. Changing to other atomic species does not alter our findings.

Once in the continuum a tunneling photoelectron current density \mathbf{j} is used to describe the electron, including the rescattering portion \mathbf{j}_R that revisits the parent ion. The rate for a rescattering process ($\frac{dw_R}{dt}$) can be estimated via the photoelectron rescattering current density and the cross-section of the process (σ_R): $\frac{dw_R}{dt} = \sigma_R j_R$. A more relevant physical quantity in rescattering is the probability per unit energy during one laser cycle $\frac{dw_R}{d\varepsilon} = \sigma_R \frac{dF_R}{d\varepsilon}$, which is determined by the flux per unit energy

$$\frac{dF_R}{d\varepsilon} = j_R \frac{dt}{d\varepsilon}. \quad (5.2)$$

5.2.1 Quantum Mechanical Treatment

In our quantum mechanical treatment the rescattering flux is calculated via RCCSFA based on the Dirac equation [46, 47, 48]. The wave function of the electron ionized from a hydrogen-like atomic bound state $|\phi_0(\eta)\rangle$ in a strong laser field $\mathbf{E}(\eta) = -\mathbf{A}'(\eta)$, with the vector-potential $\mathbf{A}(\eta) = (E_0/\omega) \sin(\eta)\hat{x}$, and the laser phase $\eta = \omega(t - z/c)$, is given by [48]:

$$\begin{aligned} \psi(\mathbf{r}, \eta) &= - \int d^3\mathbf{q} \int \frac{d\eta'}{\omega} \langle \mathbf{r} | \mathbf{q}(\eta) \rangle \langle \mathbf{q}(\eta') | \mathbf{r} \cdot \mathbf{E}(\eta') Q | \phi_0(\eta') \rangle \\ &\times \exp[-iS(\mathbf{q}, \eta, \eta')], \end{aligned} \quad (5.3)$$

where $|\mathbf{q}(\eta)\rangle$ is the relativistic momentum state of the photoelectron before recollision, $Q = (-4I_p/(\mathbf{r} \cdot \mathbf{E}(\eta')))^{Z/(2I_p)^{1/2}}$ is the Coulomb correction factor, $S(\mathbf{q}, \eta, \eta') = \int_{\eta'}^{\eta} d\eta'' [\varepsilon_{\mathbf{q}}(\eta'') - mc^2 + I_p]/\omega$, with the electron energy and momentum in the laser field $\varepsilon_{\mathbf{q}}(\eta) = \varepsilon_{\mathbf{q}} + c^2[\mathbf{q} \cdot \mathbf{A}(\eta) + \mathbf{A}(\eta)^2/(2\Lambda)]$, $\mathbf{q}(\eta) = \mathbf{q} + \mathbf{A}(\eta) + c^2[\mathbf{q} \cdot \mathbf{A}(\eta) + \mathbf{A}(\eta)^2/(2\Lambda)]$, respectively, $\varepsilon_{\mathbf{q}} = c^2\sqrt{m^2c^2 + \mathbf{q}^2}$, and $\Lambda = \varepsilon_{\mathbf{q}}(\eta) - c\hat{z} \cdot \mathbf{q}(\eta)$ is the integral of motion in the plane laser field; unit vectors \hat{x}, \hat{y} , and \hat{z} point in the laser electric, magnetic field, and propagation directions, respectively.

The quantum wave function allows us to obtain the rescattering probability current density at the atomic core, by inserting the $\mathbf{r} = 0$ condition into the current

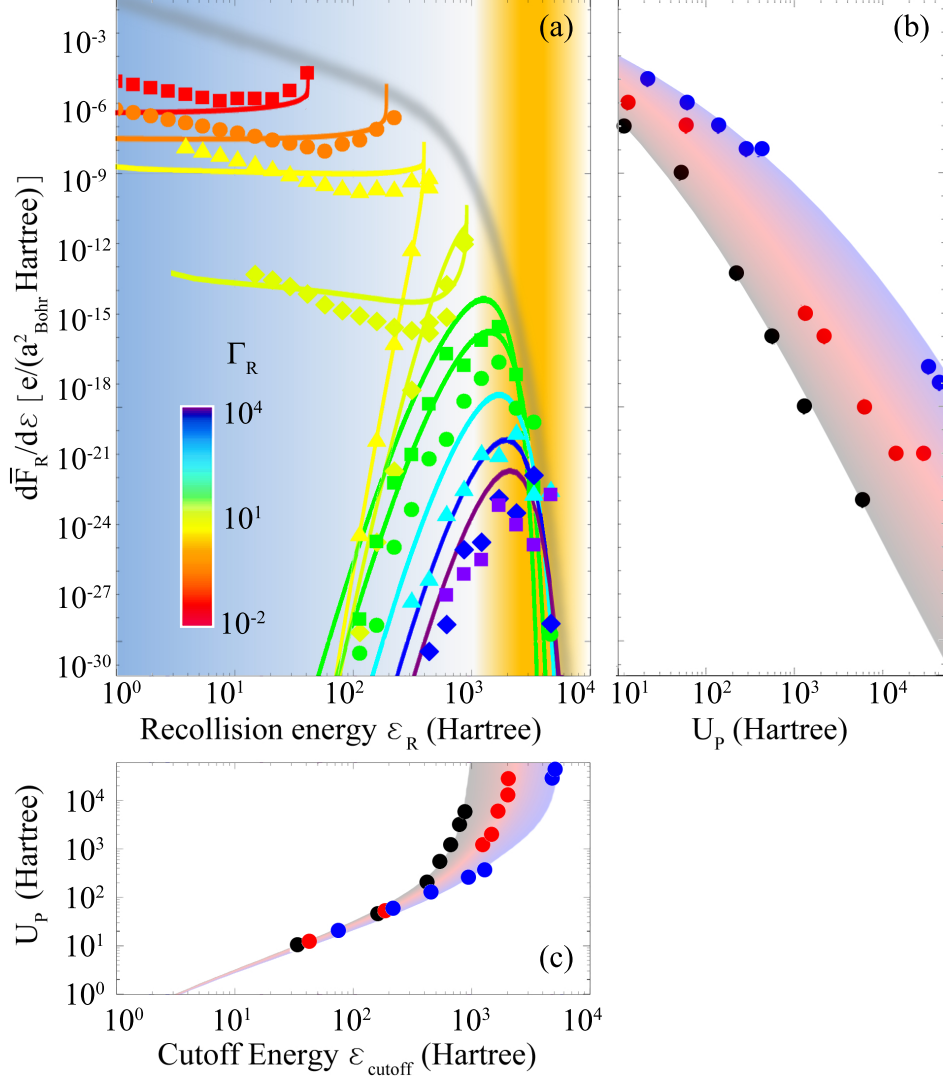


Figure 5.2: Normalized differential rescattering flux (a) via RCCSFA (line) and SMC (symbol) for the laser wavelength $\lambda = 800$ nm. Line color scales with Γ_R : Ar^{5+} at 5.8×10^{15} W/cm 2 ($\Gamma_R = 0.06$, square); Ar^{7+} 2.7×10^{16} W/cm 2 ($\Gamma_R = 0.7$, circle); Ar^{8+} 5.6×10^{16} W/cm 2 ($\Gamma_R = 3.8$, triangle); Ar^{8+} 1.3×10^{17} W/cm 2 ($\Gamma_R = 13$, diamond); Ar^{8+} at 6×10^{17} W/cm 2 ($\Gamma_R = 140$, square); Ar^{9+} at 1×10^{18} W/cm 2 ($\Gamma_R = 320$, circle); Ar^{11+} at 2.8×10^{18} W/cm 2 ($\Gamma_R = 1,700$, triangle); Ar^{13+} at 6.3×10^{18} W/cm 2 ($\Gamma_R = 6,100$, diamond); Ar^{14+} at 1.3×10^{19} W/cm 2 ($\Gamma_R = 20,000$, square). In (a) the change from traditional rescattering (blue) to the relativistic cutoff region (orange) is highlighted in the background and a shadow line gives the typical highest possible $d\bar{F}_R/d\varepsilon$ at optical frequencies. For clarity, long and short contributions to $d\bar{F}_R/d\varepsilon$ are summed in the non-relativistic limit $\Gamma_R < 1$. For RCCSFA with argon HCI (see Afterward), $d\bar{F}_R/d\varepsilon$ at cutoff as a function of U_p is shown in (b) and the relationship between U_p and the recollision cutoff energy is given (c) for laser wavelengths 80 nm (blue), 800 nm (red), and 8000 nm (black) with shading to aid the eye.

density expression ($\mathbf{j}_R(0, \eta_R) = \mathbf{q}(\eta_R)|\psi(0, \eta_R)|^2/(2\pi)^3$) and calculating the differential flux from Eq. (5.2). The four-dimensional integral for $\mathbf{j}_R(0, \eta_R)$ is solved with the saddle point method, which also yields for each recollision η_R an initial ‘birth’ phase η_B (Fig. 5.1). The RCCSFA accounts for the Coulomb field effects in the tunneling step of ionization, yielding a tunneling rate that coincides with the relativistic extension of the Perelomov-Popov-Terent’ev (PPT) theory [49, 50, 51, 52]. For our purposes and to a high degree of accuracy, PPT is the same as the nonrelativistic Ammosov, Delone, and Krainov (ADK) tunneling rate [53] shown to describe ionization up to intensities of 10^{19} W/cm² [54].

5.2.2 Semi-Classical Treatment

Our semi-classical SCMC calculation follows the quantum calculation. Briefly, for each time in the optical cycle the ADK ionization rate is used to quantify the initial current density $\mathbf{j}(\mathbf{r}, \eta_B)$ at the tunneling barrier, which is then represented by an ensemble of trajectories given an initial spatial width (and corresponding momentum uncertainty) perpendicular to the electric field. The ensemble current density propagates relativistically in the fields of the laser and the atomic core, providing the SCMC $\mathbf{j}_R(0, \eta_R)$ recollision flux and $\frac{\partial F_R}{\partial \varepsilon}$ [55]. We note that in both quantum and semi-classical treatments, contributions from multiple returns are not considered.

5.3 Results

In Fig. 5.2 the differential rescattering flux normalized to W_0 , (i.e. $\frac{d\bar{F}_R}{d\varepsilon} \equiv \frac{1}{W_0} \frac{dF_R}{d\varepsilon}$), is shown for argon HCl. Nonrelativistic rescattering flux ($\Gamma_R \lesssim 1$) show the well-known characteristic plateau extending up to $3.2U_p$, where the flux peaks and then drops to zero [1]. As rescattering moves into the relativistic domain ($\Gamma_R \gtrsim 1$), a change occurs in the form of the flux distribution from a plateau to a ‘looping bow’. The peak of the loop is the maximum return energy, approximately $3.2U_p$, and the two ends of the bow are the energetically degenerate collisions in the field commonly described as

long and short trajectories. As Γ_R increases, the normally dominant long trajectory contribution to $d\bar{F}_R/d\varepsilon$ is suppressed by the extended time in the Lorentz force.

Proceeding to the ultrarelativistic recollision regime ($\Gamma_R \sim 100$) long trajectories are deflected by many times the spatial width of $\mathbf{j}_R(0, \eta_R)$. Only a diminishing $d\bar{F}_R/d\varepsilon$ ‘peak’ remains from a narrow range of short trajectories able to return to the parent ion (similar features are shown in HHG spectra [23, 24, 25]). A characteristic feature of relativistic recollision is, regardless of increasing Γ_R or U_p , the ultimate cut-off energy does not change. The recollision flux has been calculated for a broad range of wavelengths and HCIs (see Afterward). Our conclusion and the extreme limits of possible strong field interactions (far ultraviolet, optical, far infrared) are presented in Fig. 5.2(b,c). We see in Fig. 5.2(b) that, while decreasing with the growth of Γ_R , the flux is not negligible at large Γ_R . In Fig. 5.2(a,c) we show the cutoff energy scaling begins to deviate from the $3.2U_p$ rule beyond ponderomotive energies of a few hundred Hartree ($\Gamma_R > 1$), with the cutoff ε_{cutoff} saturating and reaching an ultimate limit of a few thousand Hartree even as U_p exceeds 10^4 Hartree ($\Gamma_R > 100$).

In Fig. 5.1 we can inspect the ionization probability current \mathbf{j} corresponding to a peak rescattering energy. Two species are shown in juxtaposition; Ar^{4+} at 4.6×10^{15} W/cm², 2400 nm, and Ar^{9+} at 1.6×10^{18} W/cm², 200 nm. On first inspection these two cases seem very different by laser intensity, wavelength, and ionization potentials. Fig. 5.1 follows the ionization current \mathbf{j} from birth (η_B) at the parent ion (origin) to recollision (η_R). Initially, $\mathbf{j}(0, \eta_B)$ is highly localized at the parent ion with an initial spatial width χ_i of the order of the Bohr radius, $\chi_i \sim r_{Bohr}$. After moving only a few percent of the single cycle displacement from the parent ion (black outline at $x = -44 r_{Bohr}$ and $-5 r_{Bohr}$ in Fig. 5.1(b,c), respectively), the spatial width of \mathbf{j} is overwhelmed by spreading from momentum uncertainty. The continuum electron for Ar^{4+} extends 1200 Bohr in x and is deflected by > 100 Bohr in z , while Ar^{9+} extends to 100 Bohr and is deflected by ~ 25 Bohr. Nevertheless, near the recollision point there is a clearly observable consistency in the deflection with respect to the electron wave packet size.

To better understand rescattering, we estimate the rescattering current density

using the rescattering velocity v_R , the electron wave packet spatial extent at recollision along $\hat{x}, \hat{y}, \hat{z}$ -directions $(\chi_{x,y,z})$, and the Lorentz deflection parameter Γ_R :

$$j_R \sim \frac{W_0 v_R}{\chi_x \chi_y \chi_z} \exp(-\Gamma_R), \quad (5.4)$$

where the exponential factor stems from the fact rescattering in the relativistic regime is attained by the electron tunneled out from the atom with an initial momentum compensating the drift momentum in the laser propagation direction $p_z \sim -U_p/c$, the probability of the latter being $\exp(-p_z^2/\Delta p_z^2) = \exp(-\Gamma_R)$, with $\Delta p_z = (eE\hbar)^{1/2}/(2I_p/m)^{1/4}$ [56]. We tested our estimation in the nonrelativistic regime (see Afterward) and focus our discussion here on dynamics in the relativistic regime $\Gamma_R \gg 1$. As the Lorentz force increases, photoionization must be ‘launched’ closer to the laser field zero-crossing at a field $E(\eta_B) \approx E_0\eta_B$ to avoid being deflected. In this cutoff region we estimate the laser phase η_B for the most probable ionization of the short rescattering trajectories, using the scaling of the tunneling ionization probability: $\propto \exp[-2E_a/(3E_0\eta_B) - \Gamma_R\eta_B^3]$, where the rescattering from fields near zero-crossing rather than the peak field is incorporated by replacing E_0 with $E(\eta_B)$ in the Γ_R expression of Eq. (5.1) and we have used the atomic field $E_a \equiv (2I_p)^{3/2}\sqrt{m}/e\hbar$. From the exponent above, the short rescattering trajectories within the cutoff are most probably launched at the laser phase $\eta_{cutoff} \approx (1.37/a_0)(2I_p/mc^2)^{1/4}$ near the laser zero-crossing and correspond to a recollision energy of $\varepsilon_{cutoff} \approx 3.2mc^2 a_0^2 \eta_{cutoff}^2/4$, which reads

$$\varepsilon_{cutoff} \approx 1.5\sqrt{2I_p mc^2}. \quad (5.5)$$

Thus, the well-known 3.2 U_p rule for the recollision cutoff energy is replaced in the relativistic regime $\Gamma_R \gg 1$ by Eq. (5.5), which indicates a cutoff for the corresponding peak of the bell-shape flux distribution that tends to the constant value in the relativistic domain, see Fig. 5.2(c) (also see Afterward).

5.4 Further Considerations

A reasonable prediction for the relativistic rescattering flux at $\Gamma_R \gg 1$ (Fig. 5.2(b)) can be obtained in the cutoff region from Eq. (5.4), with $\eta_B = \eta_{cutoff}$, and the electron

wave packet extensions $\chi_x \sim \lambda a_0$, $\chi_y \sim \lambda a_0^2$, and $\chi_z = \Delta p_z / (m\omega)$:

$$\frac{d\bar{F}_R(\varepsilon_R)}{d\varepsilon} \sim \frac{\sqrt{2\varepsilon_R/m} e^{-\Gamma_R \eta_{cutoff}^3}}{\chi_x \chi_y \chi_z \omega \varepsilon_R} \sim \frac{e^{-\frac{1}{16} \frac{mc^2}{\hbar\omega} \left(\frac{2I_p}{mc^2}\right)^{5/4}}}{\lambda^2 a_0^3 \sqrt{a_0 \hbar \omega m c^2}}. \quad (5.6)$$

The region of the non-negligible flux (up to $\Gamma_R \sim 100$ in Afterward) can be estimated from the exponential factor of Eq. (5.6): $\hbar\omega \sim (mc^2/16)(2I_p/mc^2)^{5/4}$. To extend the relativistic cutoff a large I_p is required, which calls for a large laser intensity as well as a short laser wavelength. For instance with infrared lasers ($\lambda = 800$ nm, $I \sim 10^{17}$ W/cm²) one can achieve an ultimate recollision energy of $\varepsilon_R \sim 1000$ Hartree, while with ultraviolet lasers ($\lambda = 200$ nm, $I \sim 10^{19}$ W/cm²) $\varepsilon_R \sim 2000$ Hartree.

Considering the laser field as an ‘optical scale’ laser accelerator, the ultimate cutoff represents the acceleration energy where the electron from an atom (atomic radius $r_a \sim \hbar/\sqrt{2I_p m}$) will be deflected by its width and miss the parent ion at rescattering. Returning to the Lorentz deflection parameter expressed as $\Gamma_R \approx U_p^2 \chi_i^2 / (\hbar^2 c^2)$ and setting $\Gamma_R = 1$, one can see for any system with an initial extent $\chi_i = r_a$ an electron accelerated in a radiation field will have an ultimate cutoff of $U_p = c\sqrt{2I_p m}$, i.e., a $3.2 U_p$ rescattering energy limit of 10^3 Hartree.

5.5 Influence on Above Threshold Ionization

The significance of an ultimate cutoff is clear as rescattering is the mechanism for high energy ATI, NSI, HHG, and ISE. We briefly here show the impact on ATI. The angle resolved differential ATI rate is calculated quantum mechanically using RCCSFA:

$\frac{dw_{\text{ATI}}}{d\Omega} = \frac{\omega^2 p_{\mathbf{p}}}{c^2} |M_{\mathbf{p}}|^2$, with

$$M_{\mathbf{p}} = - \int d\eta \int d\eta' \int d^3\mathbf{q} \langle \mathbf{p}(\eta) | V | \mathbf{q}(\eta) \rangle \langle \mathbf{q}(\eta') | \mathbf{r} \cdot \mathbf{E}(\eta') Q | \phi_0(\eta') \rangle \times \exp[-iS(\mathbf{p}, \infty, \eta)] - iS(\mathbf{q}, \eta, \eta')] \quad (5.7)$$

where $\mathbf{p}(\eta) = \mathbf{p} + \mathbf{A}(\eta) + \mathbf{T}(\eta, \mathbf{p})$, $\mathbf{q}(\eta) = \mathbf{q} + \mathbf{A}(\eta) + \mathbf{T}(\eta, \mathbf{q})$ are the relativistic kinetic momentum after the recollision and during excursion, respectively, the drift momentum $\mathbf{T}(\eta, \mathbf{p}) = \hat{z}[\mathbf{p} \cdot \mathbf{A}(\eta) + \mathbf{A}^2(\eta)/2]/c$, and $V(r)$ is the Coulomb-potential of the atomic

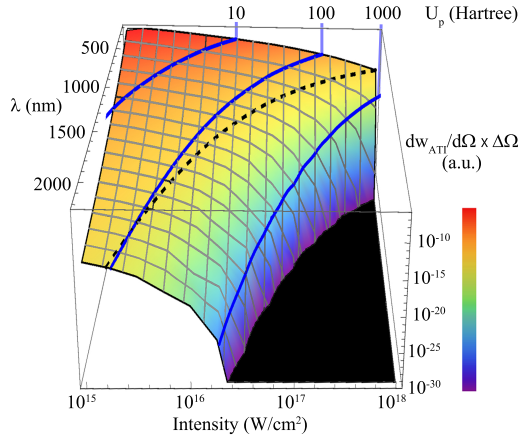


Figure 5.3: ATI as a function of laser intensity and wavelength for photoelectron energies near $10U_p$. Blue lines indicate $U_p = 10, 100, 1000$ a.u. The dashed line corresponds to $\Gamma_R = 1$. The color scale for ATI spans from 10^{-30} to 10^{-6} a.u.

core [57]. The findings presented here are not changed for CTMC calculations with more accurate potentials using numerical Dirac–Fock electron densities [58].

The energy resolved ionization is evaluated by integrating the outgoing photoelectron over an effective solid angle of $\Delta\Omega = \pi/8$. In Fig. 5.3, high-order ATI as function of the laser intensity and wavelength is shown plotted for electrons with a final energy (at the detector) of $10U_p \pm U_p/2$. We see the probability of elastic scattering with recollision energies beyond the ultimate cutoff of ~ 1000 a.u. is precipitously suppressed with the drop in ATI after one crosses the $\Gamma_R = 1$ threshold. For the same recollision energy the probability of elastic scattering is larger when using short wavelength lasers, consistent with a $\lambda^{-4/3}$ scaling that can be obtained from Eq. (5.4). Elastic scattering with a recollision energy of 30 Hartree ($U_p = 10$) can be achieved with $\lambda = 1700$ nm (at 10^{15} W/cm²) as well as with $\lambda = 200$ nm (at 4×10^{16} W/cm²); however, in the shorter wavelength case the ATI rate is larger by four orders of magnitude.

Our calculations so far have involved single electron dynamics. Clearly, as rescattering energies increase many electrons are excited [59, 60]. For a recollision of several

hundred Hartree, the new possibility of exciting all bound states in high Z atoms becomes possible. Further clarification of multielectron physics [61] will be required to better understand such highly excited species. We have extended our analysis to consider ionization at any phase η_B , rather than limited by tunneling. These results indicate that electrons ionized at any time during the laser cycle, e.g. by inner shell thermalization, will still be limited by the ultimate cutoff.

5.6 Conclusion

In conclusion, we have calculated the ultimate limit of rescattering in laser fields. The presented relativistic quantum and semi-classical calculations show for a broad range of species in different laser fields that rescattering continues to be important in the relativistic regime ($\Gamma_R \geq 1$) and has an ultimate energy cutoff for $\Gamma_R \gg 1$. Scaling laws for the ultimate energy cutoff and flux are derived. The cutoff energy changes from a strong field $3.2U_p$ -rule to a relativistic limit of $\varepsilon_{cutoff} \approx 1.5\sqrt{2I_p mc^2}$, beyond which the recollision process in a given species will cease to contribute to ATI, HHG, and ISE. We show the ultimate energy cutoff and highest rescattering flux is best realized by intense, short wavelength lasers and cannot exceed a few thousand Hartree, indicating hard x-rays via recollision induced HHG [62, 37] can be extended to photon energies of 60 keV.

5.7 Afterward

Here we provide information about our analytical estimate of the nonrelativistic recollision flux. We also apply the derived relativistic rescattering energy cutoff ε_{cutoff} and relativistic rescattering current density at cutoff (Eqs. (5.5) and (5.6) of the chapter, respectively) to our RCCSFA and SCMC calculations.

5.7.1 Analytic estimate of nonrelativistic recollision flux

We analytically estimate the rescattering current density for ionization with a rescattering velocity v_R using the wave packet extent and Lorentz deflection:

$$j_R \sim \frac{W_0 v_R}{\chi_x \chi_y \chi_z} \exp(-\Gamma_R), \quad (5.8)$$

where $\chi_{x,y,z}$ are the electron wave packet extensions at recollision along \hat{x} , \hat{y} , and \hat{z} . For a nonrelativistic recollision ($\Gamma_R \ll 1$), the electron wave packet extensions are: $\chi_x \sim \lambda a_0 / (2\pi)$ along the electric field and $\chi_y = \chi_z \approx \chi_i + \Delta p_\perp / (m\omega) \approx \Delta p_\perp / (m\omega) \equiv \chi_\perp$ in the transverse direction. Using these, we can estimate the normalized rescattering flux,

$$\frac{d\bar{F}_R(\varepsilon)}{d\varepsilon} \sim \left(\frac{E_a}{E}\right)^{1/3} \left(\frac{eEr_{Bohr}}{mc^2\alpha^2}\right)^{4/3} \frac{\alpha^2}{mc^2 a_0^4 r_{Bohr}^2}. \quad (5.9)$$

where α is the fine structure constant and we approximate $\partial\varepsilon/\partial t \sim \omega U_p$. Since $U_p = mc^2 a_0^2 / 4$, Eq. (5.9) indicates the flux dependence on the recollision energy is $\propto U_p^{-2}$ for a given species. Furthermore, when the recollision energy and ionization probability are fixed ($a_0 = const$ and $E/E_a = const$) the rescattering flux scales with intensity as $\propto I^{2/3}$ or with wavelength as $\propto \lambda^{-4/3}$. These scalings are important as they impact the amount rescattering observed prior to the cutoff.

5.7.2 Relativistic recollision cutoff and flux

The normalized differential recollision flux ($d\bar{F}_R/d\varepsilon$) at the cutoff and the cutoff energy for the laser wavelengths of 80 nm, 800 nm and 8000 nm are presented in Fig.5.2. For 800 nm, the actual $d\bar{F}_R/d\varepsilon$ distributions from which the Figs. 5.4(b,c) values originate are in Fig. 5.2(a). In Figs. 5.4 and 5.5 we provide $d\bar{F}_R/d\varepsilon$ for the 8000 nm and 80 nm laser wavelengths.

We begin with the 8000 nm, far-IR case in Fig. 5.4. Rescattering departs from a nonrelativistic limit (Ar^+ and Ar^{2+}) beginning with Ar^{3+} at 1×10^{15} W/cm² where the signature relativistic onset ‘looping-bow’ in $d\bar{F}_R/d\varepsilon$ is seen. To demonstrate the accuracy of our estimations for the cutoff energy and relativistic recollision flux, we compare Eqs. (5.5) and (5.6) with the RCCSFA calculation, which is in agreement with the SCMC results. The $3.2U_p$ nonrelativistic and $\varepsilon_{cutoff} \approx 1.5\sqrt{2I_p mc^2}$ relativistic cutoffs are shown in Fig. 5.4 (b). In the figure, both cutoff energy rules provide an accurate description for the nonrelativistic and relativistic regions where they apply. The estimation for the recollision flux, given by Eq. (5.6), describes the RCCSFA calculation satisfactory in the physically relevant region $\Gamma_R \lesssim 100$ (see Fig. 5.4 (c)).

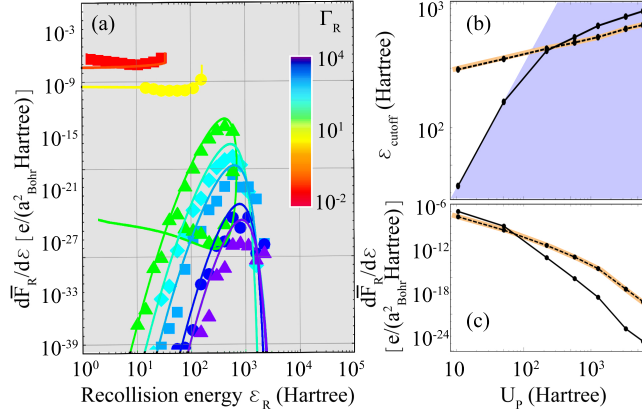


Figure 5.4: Normalized differential rescattering flux (a) via RCCSFA (line) and SMC (symbol) with a 8000 nm laser wavelength for: Ar^+ at 4.8×10^{13} W/cm^2 ($\Gamma_R = 0.25$, square); Ar^{2+} 2.3×10^{14} W/cm^2 ($\Gamma_R = 3.0$, circle); Ar^{3+} 1×10^{15} W/cm^2 ($\Gamma_R = 37$, triangle); Ar^{4+} 2.6×10^{15} W/cm^2 ($\Gamma_R = 160$, diamond); Ar^{5+} 5.8×10^{15} W/cm^2 ($\Gamma_R = 590$, square); Ar^{6+} 1.5×10^{16} W/cm^2 ($\Gamma_R = 2900$, circle); Ar^{7+} 2.7×10^{16} W/cm^2 ($\Gamma_R = 7400$, triangle). The cutoff energy (b) and flux at cutoff (c) are summarized from RCCSFA (a) and plotted as a function of U_p . The points in (b,c) from low to high U_p correspond to the Ar^+ to Ar^{7+} charge state progression. The Eq. (5) cutoff (b) and Eq. (6) flux are shown by highlighted orange dashed lines. Energies possible with a $3.2 U_p$ rule are indicated by shading in (b).

We note that beyond $\Gamma_R \sim 100$, the flux is damped with respect to the nonrelativistic case by more than $\sim 10^6$.

We next move to the short-wavelength limit of the relativistic strong field by using a far-UV, 80 nm external field. The high binding energy of the interacting bound states results in the Keldysh definition of tunneling ($\gamma = \omega \sqrt{2mI_p}/(eE_0) < 1$) being satisfied for the calculations shown in Fig. 5.5. Despite the two order of magnitude change in wavelength for the external field, when comparing between Figs. 5.4(b,c) and Figs. 5.5(b,c) one sees a similar level of agreement with the RCCSFA comparison to $\varepsilon_{cutoff} \approx 1.5\sqrt{2I_p mc^2}$ cutoff and $d\bar{F}_R/d\varepsilon$ of Eq. (6). For completeness, we include in Fig. 5.6 the cutoff and flux comparisons for $d\bar{F}_R/d\varepsilon$ at 800 nm shown in Fig. 5.2(a).

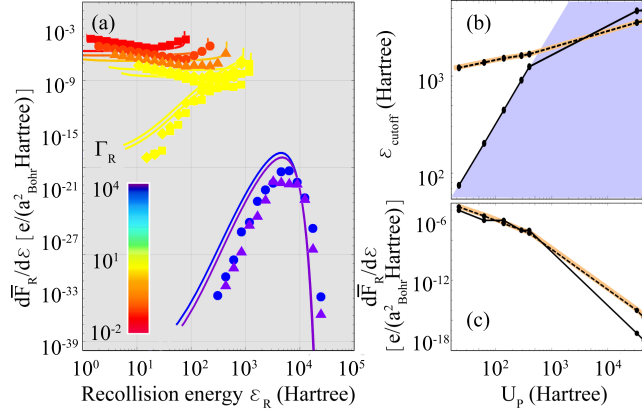


Figure 5.5: Normalized differential rescattering flux (a) via RCCSFA (line) and SCMC (symbol) with a laser wavelength of 80 nm for: Ar⁹⁺ at 1×10^{18} W/cm² ($\Gamma_R=0.03$, square); Ar¹¹⁺ 2.8×10^{18} W/cm² ($\Gamma_R=0.17$, circle); Ar¹³⁺ 6.3×10^{18} W/cm² ($\Gamma_R=0.61$, triangle); Ar¹⁴⁺ 1.3×10^{19} W/cm² ($\Gamma_R=2.1$, diamond); Ar¹⁵⁺ 1.8×10^{19} W/cm² ($\Gamma_R=3.3$, square); Ar¹⁶⁺ 1.5×10^{21} W/cm² ($\Gamma_R=5300$, circle); Ar¹⁷⁺ 2×10^{21} W/cm² ($\Gamma_R=7700$, triangle). The cutoff energy (b) and flux at cutoff (c) are summarized from RCCSFA (a) and plotted as a function of U_p . The points in (b,c) from low to high U_p have a correspond to the Ar⁹⁺ to Ar¹⁷⁺ charge state progression. The Eq. (5) cutoff (b) and Eq. (6) flux are shown by highlighted orange dashed lines. Energies possible with a $3.2 U_p$ rule are indicated by shading in (b).

To further test the robustness of our analytic description, we calculated the recollision flux for a given argon ion (Ar⁸⁺) at different laser wavelengths. The respective cutoff energies and recollision flux at cutoff are shown in Fig. 4. Since one charge state is involved, Eq. (5) has a single value. The saturation of the maximum RCCSFA ε_{cutoff} can be seen in Fig. 4 to agree with the flux and cutoff estimates.

Finally we add that RCCSFA does not include the Coulomb field during the electron excursion in the laser field. To evaluate the impact of this omission we carried out SCMC calculations including the Coulomb field. These SCMC results show including the Coulomb interactions after tunneling does not affect the presented results. When dealing with ultrastrong fields, the quick and large excursion of the photoelectron away from the parent ion after tunneling limits the effect of the ion core on the

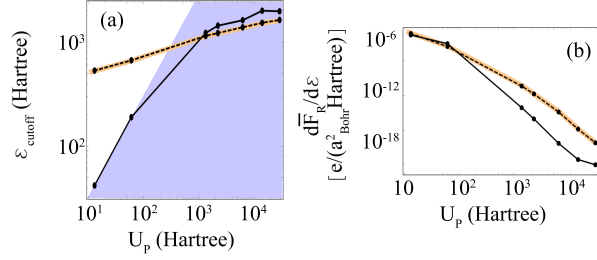


Figure 5.6: The cutoff energy (a) and flux at cutoff (b) are summarized from Fig. 5.2(a) and plotted as a function of U_p . The points in (a,b) from low to high U_p (also Ar^{5+} to Ar^{14+}) have a corresponding $\Gamma_R=0.058, 0.74, 140, 319, 1674, 6091$. The Eq. (5) cutoff (b) and Eq. (6) flux are shown by highlighted orange dashed lines. Energies possible with a $3.2 U_p$ rule are indicated by shading in (a).

continuum dynamics.

This material is based upon work supported by the National Science Foundation under Grant No. 1607321 and No. 1307042.

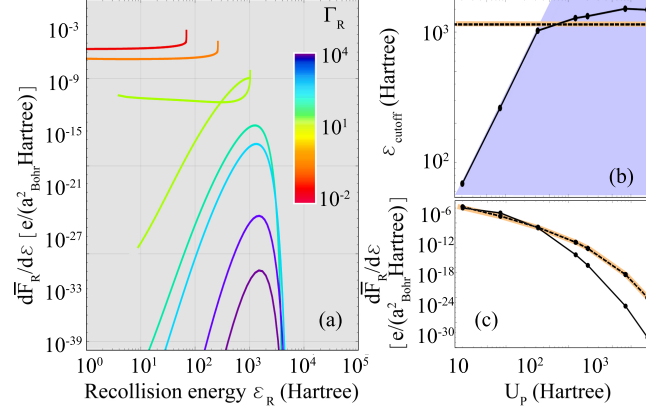


Figure 5.7: Normalized differential rescattering flux (a) via RCCSFA with Ar^{8+} at $5.9 \times 10^{17} \text{ W/cm}^2$ for the laser wavelengths: 100 nm ($\Gamma_R = 0.034$), 200 nm ($\Gamma_R = 0.55$), 400 nm ($\Gamma_R = 8.8$), 800 nm ($\Gamma_R = 140$), 1000 nm ($\Gamma_R = 341$), 2000 nm ($\Gamma_R = 5000$), 3000 nm ($\Gamma_R = 3 \times 10^4$). The cutoff energy (b) and flux at cutoff (c) are summarized from (a) and plotted as a function of U_p . The points in (b,c) from low to high U_p (also short 100 nm to long 3000 nm wavelength) have a corresponding $\Gamma_R=0.034, 0.55, 8.8, 140, 341, 5000,$ and 3×10^4 . The Eq. (5) cutoff (b) and Eq. (6) flux are shown by highlighted orange dashed lines. Energies possible with a $3.2 U_p$ rule are indicated by shading in (b).

BIBLIOGRAPHY

- [1] P. B. Corkum. *Phys. Rev. Lett.* **71**, 1994 (1993).
- [2] W. Becker, F. Grasbon, R. Kopold, D. Milošević, G. G. Paulus, and H. Walther. *Adv. Atom. Mol. Opt. Phys.* **48**, 35 (2002).
- [3] M Ferray, A L’Huillier, XF Li, LA Lompre, G Mainfray, and C Manus. *J. Phys. B* **21**(3), L31–L35 (1988).
- [4] Michael Chini, Kun Zhao, and Zenghu Chang. *Nat. Photon.* **8**(3), 178–186 (2014).
- [5] B Walker, B Sheehy, LF Dimauro, P Agostini, KJ Schafer, and KC Kulander. *Phys. Rev. Lett.* **73**(9), 1227–1230 (1994).
- [6] Wilhelm Becker, XiaoJun Liu, Phay Jo Ho, and Joseph H. Eberly. *Rev. Mod. Phys.* **84**(3), 1011–1043 (2012).
- [7] PM Paul, ES Toma, P Breger, G Mullot, F Auge, P Balcou, HG Muller, and P Agostini. *Science* **292**(5522), 1689–1692 (2001).
- [8] F. Krausz and M. Ivanov. *Rev. Mod. Phys.* **81**, 163 (2009).
- [9] KJ Schafer, B Yang, LF Dimauro, and KC Kulander. *Phys. Rev. Lett.* **70**(11), 1599–1602 (1993).
- [10] Baorui Yang, K. J. Schafer, B. Walker, K. C. Kulander, P. Agostini, and L. F. DiMauro. *Phys. Rev. Lett.* **71**, 3770–3773 (1993).
- [11] J Itatani, J Levesque, D Zeidler, Hiromichi Niikura, H Pépin, J C Kieffer, P B Corkum, and D M Villeneuve. *Nature* **432**(7019), 867–71 (2004).
- [12] Y Huismans, A Rouzée, A Gijsbertsen, J H Jungmann, A S Smolkowska, P S W M Logman, F Lépine, C Cauchy, S Zamith, T Marchenko, J M Bakker, G Berden, B Redlich, A F G van der Meer, H G Muller, W Vermin, K J Schafer, M Spanner, M Yu Ivanov, O Smirnova, D Bauer, S V Popruzhenko, and M J J Vrakking. *Science* **331**(6013), 61–4 (2011).
- [13] R Moshhammer, B Feuerstein, W Schmitt, A Dorn, CD Schroter, J Ullrich, H Rotke, C Trump, M Wittmann, G Korn, K Hoffmann, and W Sandner. *Phys. Rev. Lett.* **84**(3), 447–450 (2000).

- [14] Yunpei Deng, Zhinan Zeng, Zhengmao Jia, Pavel Komm, Yinhui Zheng, Xiaochun Ge, Ruxin Li, and Gilad Marcus. *Phys. Rev. Lett.* **116**, 073901 (2016).
- [15] D Popmintchev, C Hernández-García, F. Dollar, C Mancuso, J. A. Perez-Hernandez, M.-C. Chen, A. Hankla, X. Gao, B. Shim, A. L. Gaeta, M. Tarazkar, D. A. Romanov, R. J. Levis, J. A. Gaffney, M. Foord, S. B. Libby, A. Jaron-Becker, A. Becker, L. Plaja, M M Murnane, H C Kapteyn, and T Popmintchev. *Science* **350**(6265), 1225–1231 (2015).
- [16] S. Palaniyappan, I. Ghebregziabher, A. DiChiara, J. MacDonald, and B. C. Walker. *Phys. Rev. A* **74**, 033403 (2006).
- [17] A. Di Piazza, C. Müller, K. Z. Hatsagortsyan, and C. H. Keitel. *Rev. Mod. Phys.* **84**, 1177 (2012).
- [18] C. H. Keitel and P. L. Knight. *Phys. Rev. A* **51**, 1420–1430 (1995).
- [19] M. W. Walser, C. H. Keitel, A. Scrinzi, and T. Brabec. *Phys. Rev. Lett.* **85**(24), 5082–5085, 2000.
- [20] Matthias Dammasch, Martin Dörr, Ulli Eichmann, Ernst Lenz, and Wolfgang Sandner. *Phys. Rev. A* **64**, 061402 (2001).
- [21] N J Kylstra, R M Potvliege, and C J Joachain. *J. Phys. B* **34**(3), L55 (2001).
- [22] J. Prager and C. H. Keitel. *J. Phys. B* **35**, L167 (2002).
- [23] D. B. Milošević, Suxing Hu, and Wilhelm Becker. *Phys. Rev. A* **63**(1), 011403(R) (2000).
- [24] D. B. Milošević, S. X. Hu, and W. Becker. *Laser Phys.* **12**, 389–397 (2002).
- [25] C. C. Chirilă, C. J. Joachain, N. J. Kylstra, and R. M. Potvliege. *Phys. Rev. Lett.* **93**, 243603 (2004).
- [26] H. K. Avetissian, A. G. Markossian, and G. F. Mkrtchian. *Physics Letters A* **375**(42), 3699–3703 (2011).
- [27] C. C. Chirilă, N. J. Kylstra, R. M. Potvliege, and C. J. Joachain. *Phys. Rev. A* **66**, 063411 (2002).
- [28] G. R Mocken and C. H. Keitel. *J. Phys. B* **37**, L275 (2004).
- [29] Nenad Milosevic, Paul B. Corkum, and Thomas Brabec. *Phys. Rev. Lett.* **92**, 013002 (2004).
- [30] Michael Klaiber, Karen Z. Hatsagortsyan, and Christoph H. Keitel. *Phys. Rev. A* **74**, 051803 (2006).

- [31] Q. Lin, S. Li, and W. Becker. *Opt. Lett.* **31**, 2163 (2006).
- [32] R. Fischer, M. Lein, and C. H. Keitel. *Phys. Rev. Lett.* **97**, 143901 (2006).
- [33] M. Verschl and C. H. Keitel. *Euro Phys. Lett.* **77**, 64004 (2007).
- [34] Michael Klaiber, Karen Z. Hatsagortsyan, Carsten Müller, and Christoph H. Keitel. *Opt. Lett.* **33**, 411 (2008).
- [35] M. Verschl. *Laser Phys.* **18**, 598–607 (2008).
- [36] M. C. Kohler, M. Klaiber, K. Z. Hatsagortsyan, and C. H. Keitel. *Euro Phys. Lett.* **94**, 14002 (2011).
- [37] Benjamin R. Galloway, D Popmintchev, Emilio Pisanty, Daniel D. Hickstein, Margaret M. Murnane, Henry C. Kapteyn, and Tenio Popmintchev. *Opt. Expr.* **24**(19), 21818 (2016).
- [38] Emilio Pisanty, Daniel D. Hickstein, Benjamin R. Galloway, Charles G. Durfee, Henry C. Kapteyn, Margaret M. Murnane, and Misha Ivanov. *arXiv:1606.01931*[physics.atom-ph]
- [39] A. D. DiChiara, I. Ghebregziabher, R. Sauer, J. Waesche, S. Palaniyappan, B. L. Wen, and B. C. Walker. *Phys. Rev. Lett.* **101**(17), 173002 (2008).
- [40] N. Ekanayake, S. Luo, P. D. Grugan, W. B. Crosby, A. D. Camilo, C. V. McCowan, R. Scalzi, A. Tramontozzi, L. E. Howard, S. J. Wells, C. Mancuso, T. Stanev, M. F. Decamp, and B. C. Walker. *Phys. Rev. Lett.* **110**(20), 2013.
- [41] C. Hernandez-Garcia, J. A. Perez-Hernandez, T. Popmintchev, M. M. Murnane, H. C. Kapteyn, A. Jaron-Becker, A. Becker, and L. Plaja. *Phys. Rev. Lett.* **111**(3), 033002 (2013).
- [42] M. Meckel, D. Comtois, D. Zeidler, A. Staudte, D. Pavicic, H. C. Bandulet, H. Pepin, J. C. Kieffer, R. Doerner, D. M. Villeneuve, and P. B. Corkum. *Science* **320**(5882), 1478–1482 (2008).
- [43] Cosmin I. Baga, Junliang Xu, Anthony D. DiChiara, Emily Sistrunk, Kaikai Zhang, Pierre Agostini, Terry A. Miller, Louis F. DiMauro, and C. D. Lin. *Nature* **483**(7388), 194–197 (2012).
- [44] S. Augst, D. Strickland, D. D. Meyerhofer, S. L. Chin, and J. H. Eberly. *Phys. Rev. Lett.* **63**, 2212–2215 (1989).
- [45] L V Keldysh. *Sov. Phys. JETP* **20**, 1307 (1965).
- [46] H. R. Reiss. *Phys. Rev. A* **42**, 1476 (1990).

- [47] Michael Klaiber, Karen Z. Hatsagortsyan, and Christoph H. Keitel. *Phys. Rev. A* **75**, 063413 (2007).
- [48] Michael Klaiber, Enderalp Yakaboylu, and Karen Z. Hatsagortsyan. *Phys. Rev. A* **87**, 023418 (2013).
- [49] V. Popov, V. Mur, and B. Karnakov. *JETP Letters* **66**, 229 (1997).
- [50] V. Mur, B. Karnakov, and V. Popov. *JETP Letters* **87**, 433 (1998).
- [51] N. Milosevic, V. P. Krainov, and T. Brabec. *Phys. Rev. Lett.* **89**, 193001 (2002).
- [52] N Milosevic, V P Krainov, and T Brabec. *J. Phys. B* **35**(16), 3515 (2002).
- [53] M. V. Ammosov, N. B. Delone, and V. P. Krainov. *Zh. Eksp. Teor. Fiz.* **91**, 2008 (1986).
- [54] Enam A. Chowdhury, C. P. J. Barty, and Barry C. Walker. *Phys. Rev. A* **63**, 042712 (2001).
- [55] S. Palaniyappan, A. DiChiara, E. Chowdhury, A. Falkowski, G. Ongadi, E. L. Huskins, and B. C. Walker. *Phys. Rev. Lett.* **94**, 243003 (2005).
- [56] Vladimir S Popov. *Phys. Usp.* **47**, 855 (2004).
- [57] Michael Klaiber, Enderalp Yakaboylu, and Karen Z. Hatsagortsyan. *Phys. Rev. A* **87**, 023417 (2013).
- [58] F Salvat, A Jablonski, and CJ Powell. *Computer Physics Communications* **165**(2), 157–190 (2005).
- [59] A DiChiara, S Palaniyappan, AF Falkowski, EL Huskins, and BC Walker. *J. Phys. B* **38**(10), L183–L190 (2005).
- [60] A. D. DiChiara, E. Sistrunk, C. I. Blaga, U. B. Szafruga, P. Agostini, and L. F. DiMauro. *Phys. Rev. Lett.* **108**(3), 033002 (2012).
- [61] M. Kuebel, C. Burger, Nora G. Kling, T. Pischke, L. Beaufore, I. Ben-Itzhak, G. G. Paulus, J. Ullrich, T. Pfeifer, R. Moshhammer, M. F. Kling, and B. Bergues. *Phys. Rev. A* **93**(5), 053422 (2016).
- [62] T Popmintchev, M C Chen, D Popmintchev, P Arpin, S Brown, S Alisauskas, G Andriukaitis, T Balciunas, O D Mucke, A Pugzlys, A Baltuska, B Shim, S E Schrauth, A Gaeta, C Hernández-García, L Plaja, A Becker, A Jaron-Becker, M M Murnane, and H C Kapteyn. *Science* **336**(6086), 1287–1291 (2012).

Chapter 6

CONCLUSIONS

In this thesis, we try to better understand the role of ionization dynamics as the external light fields transition to the ultrastrong field and thus the response of the atom or molecule transitions from a dipole to a relativistic response. Here we briefly summarize the results and implications of each chapter as well as look to how this work could be extended to encompass future work in this interesting and growing field.

6.1 Bound State Dynamics: Validity of the Dipole Approximation

The dipole approximation has been used to describe the interaction of light with matter for many years. With the advent of new laser technology, further pushing the intensity of light to ever increasing scales, the validity of this approximation must be questioned. At what point does the dipole approximation no longer describe the interaction of atoms and molecules with light? When must the effects of the laser magnetic field also be included in this description?

To address these questions we studied the interaction of one-electron atoms, with increasing atomic number, Z , with ultrastrong light fields and by looking at the differences in the electron dynamics when the dipole approximation is made and when the laser magnetic field is included.

To understand this interaction we employ a classical relativistic Monte Carlo simulation and specifically study the ionization rate of electrons from these ions, the population distributions around the nucleus, and the angular distribution of the electron as it ionizes.

We find that the dipole approximation is generally valid for classical relativistic ionization for intensities up to 10^{23} W/cm². The small differences that we do see are a

roughly 1% change in the ionization rate due to the inclusion of the magnetic field for intensities above 10^3 a.u. We also see a slight shift in the distribution of bound electrons towards more stable orbits, corresponding to the magnetic quantum mechanical states of $m = \pm 1$, but these shifts are only a few percent at an intensity of 10^{23} W/cm². Finally we do see a shift in the ionizing electron's angular distribution (i.e., its position at the point of ionization), but only a few degrees (on the order of 5°) for intensities of 10^4 a.u.

These results are consistent with work done using a relativistic WKB approximation [1] as well as a semi-classical Dirac theory [2] and show that the dipole approximation is valid for intensities up to 10^4 a.u.

6.2 Molecular Ionization in the Strong and Ultrastrong field

The interaction of molecules with intense light is complex and spans many different processes. These include molecular alignment, stabilization, dissociative ionization, enhanced ionization, and Coulomb explosion. How these proceed and influence other processes into the strong field is a needed avenue of exploration.

In this study we experimentally investigate the strong field ionization of chloromethane (CH₃Cl) and show that the carbon and chlorine ion fragments can come away from the interaction with kinetic energies ranging from almost zero to close to 100 eV. We show that the energy distribution of these ions is independent of the intensity of the external laser light, which indicates the energy is dependant only on the initial dissociation between the carbon and chlorine ions of the molecule, the hydrogen atoms have little or no effect.

To understand the interaction, we employ a simple one dimensional classical model of a carbon and chlorine ion fragment aligned with the external field. From the model we show that the appearance of a particular ion is governed by its ionization potential and the separation distance between the carbon and chlorine ions. We also show that in the strong field ($\sim 10^{14}$ W/cm²), the enhanced ionization [3] process plays a major role in production of ions. As the field strength increases towards the

ultrastrong regime ($\sim 10^{16}$ W/cm²), the role of enhanced ionization decreases and the production of particular ions becomes more atomic in nature.

6.3 Limits of Strong Field Rescattering

Rescattering is an important process in the ionization of atoms and molecules. The so-called three-step model [4] has shown that once an electron tunnel ionizes it has a chance to revisit the parent ion due to a change in the direction of the external field.

This can result in many different outcomes such as non-sequential ionization, high harmonic generation (HHG), and above threshold ionization (ATI). These processes depend heavily on the amount of energy the rescattering electron may have. It has been show that in the strong field, the highest amount of energy for a rescattering electron scales as $3.2U_p$ [5], where U_p is the ponderomotive energy of the electron.

How does this relationship change as the intensity of light is pushed into the relativistic regime? The study we conducted tried to expressly answer this question by investigating the rescattering process in the relativistic regime and describe quantitatively its limits in terms of recollision flux and recollision energy. This is done using two different methods. One method relies on a relativistic Coulomb-corrected strong field approximation (RCCSFA) and the other a semiclassically with a Monte Carlo trajectory ensemble (SCMC) method.

Both models show similar results that indicate a scaling law for the energy cutoff of rescattering electrons different than that of the strong field $3.2U_p$. Using intuitive estimations, the scaling law in the relativistic regime is show to be,

$$\epsilon_{cutoff} \approx 1.5\sqrt{2I_p mc^2} \tag{6.1}$$

beyond this energy the recollision process will cease to contribute to processes such as ATI and HHG.

6.4 Outlook for Future Work

As the next generation of light sources, including high peak power petawatt lasers, 4th generation free-electron lasers, and attosecond pulse duration lasers, come online the response of atoms and molecules to ultra intense light will need to be understood.

Specifically, we need to extend our understanding of ionization processes such as tunneling ionization, rescattering dynamics, dissociative ionization and enhanced ionization to the relativistic regime, where the magnetic field of the laser light can no longer be ignored.

Chapter 4 of this work explored the response of molecules to strong and the beginnings of ultrastrong light, but this work could be extended to intensities that go above 10^{16} W/cm² to explore the role of enhanced ionization to the highest charge states of carbon and chlorine. Work on methane [6] has shown that the production of C⁵⁺ is possible with intensities near 10^{19} W/cm². The ionization of carbon to the K shell is something that was not seen in the present work and only the ionization of the M shell of chlorine was achieved. To see the influence on enhanced ionization due to these very high charge states would be an interesting extension to this work.

Another possibility is to use other molecules in the chloromethane series, such as dichloromethane or carbon tetrachloride, or even other halomethanes, to compare the results of the interaction of those molecules with intense light to that of chloromethane.

Chapter 5 presented the theoretical extension of the rescattering process to the relativistic regime and saw the emergence of an ultimate cutoff to the rescattering energy. Extending this work to include an experimental component would be an interesting project to consider. This experimental work would necessarily include the use of XUV and x-ray types of lasers

BIBLIOGRAPHY

- [1] V. Popov, B. Karnakov, V. Mur, and S. Pozdnyakov. *Journal of Experimental and Theoretical Physics* **102**, 760–775 (2006).
- [2] N Milosevic, V P Krainov, and T Brabec. *J. Phys. B* **35**(16), 3515 (2002).
- [3] D. M. Villeneuve, M. Yu. Ivanov, and P. B. Corkum. *Phys. Rev. A* **54**, 736–741 (1996).
- [4] P. B. Corkum. *Phys. Rev. Lett.* **71**, 1994–1997 (1993).
- [5] K. J. Schafer, Baorui Yang, L. F. DiMauro, and K. C. Kulander. *Phys. Rev. Lett.* **70**, 1599–1602 (1993).
- [6] Sasi Palaniyappan, Rob Mitchell, Rob Sauer, Isaac Ghebregziabher, Samantha L. White, M. F. Decamp, and B. C. Walker. *Phys. Rev. Lett.* **100**, 183001 (2008).

Appendix A
SOURCE CODE FOR CLASSICAL IONIZATION STUDY

```
C ***CLASSICAL IONIZATION CODE***
C
C THIS PROGRAM SIMULATES THE INTERACTION OF A SINGLE ELECTRON & A LASER
C PULSE.
C
C SOLUTIONS ARE GENERATED FOR ELECTRIC FIELD ONLY INTERACTION AND
C FOR ELECTRIC AND MAGNETIC FIELD INTERACTION SO THAT COMPARISONS BETWEEN
C THE TWO MAY BE MADE.
C
C RELATIVISTIC EQUATIONS OF MOTION ARE ALSO SOLVED, ALLOWING LARGER Z AND
C INTENSITY VALUES TO BE EXPLORED AND COMPARISON WITH CLASSICAL EQUATIONS
C OF MOTION TO BE MADE
C
C INTEGRATION IS CARRIED OUT WITH A 4-5TH ORDER
C RUNGE-KUTTA VARIABLE STEP SIZE INTEGRATION CODE (rksuite.f).
C
C RELEVANT INFORMATION IS COMPUTED IN 2 DIFFERENT WAYS, A LINEAR INCREASE
C IN THE FIELD STRENGTH AND A PULSE WITH SINE SQUARED ENVELOPE.
C
C MANY SITUATIONS ARE CONSIDERED. LAUNCH CONDITIONS ARE GENERATED EITHER
C RANDOMLY (GIVING KEPLER ORBITS IN 2 OR 3 DIMENSIONS) OR LINEARLY (STARTING
C THE ELECTRON AT THE ORIGIN AND GIVING IT MOMENTUM IN A SPECIFIC DIRECTION).
C
C A SOFT CORE POTENTIAL IS USED WITH A VALUE OF THE SOFT CORE PARAMETER
C CHOSEN TO KEEP THE ELECTRON IN THE CLASSICAL REGIME
C
C
C DESCRIPTION OF SEVERAL PARAMETERS
C     N          --> PRINCIPLE QUANTUM #
C     Z          --> ATOMIC NUMBER
C     TAU        --> HALF OF PULSE DURATION
C     FREQ       --> FREQUENCY OF LIGHT (ATOMIC UNITS)
C     INT        --> INTENSITY OF PULSE (ATOMIC UNITS)
C     ALPHA     --> SOFT CORE PARAMETER
```

```

C     DIMSN      -->  PARAMETER TO DETERMINE 2D OR 3D
C
C                    -->  0= random initial conditions (IC's)
C                    -->  1= x-y plane IC's
C                    -->  2= x-z plane IC's
C                    -->  3= y-z plane IC's
C     conditions -->  DETERMINES SINE SQUARED PULSE OR LINEAR RAMP
C                    -->  0= linear ramp
C                    -->  1= pulse
C     totaln     -->  TOTAL # OF ELECTRONS LAUNCHED
C     indicator1 -->  DETERMINES LINEAR OR RANDOM LAUNCH CONDITIONS
C                    -->  0= linear
C                    -->  1= random
C     indicator2 -->  DETERMINESE WHAT TYPE OF FILES WE WILL GET
C                    -->  0= trajectories
C                    -->  1= fraction of e-'s ionized vs. E field strength
C                    -->  2= configuration space distributions
C

```

PROGRAM CLASSICAL_IONIZATION

C***DECLARATIONS***

C ***RKSUITE***

```

      INTEGER      NEQ,METHOD,LENWRK,CFLAG,CFLAG3,L,TOTF,STPCST,
&                STPSOK,UFLAG
      PARAMETER    (NEQ=6,METHOD=2,LENWRK=32*NEQ)
      DOUBLE PRECISION HSTART,TNOW,TNOWB,RTNOW,RTNOWB,TOL,WASTE,HNEXT,
&                TWANT,TWANTB,RTWANT,RTWANTB,TGOT,TGOTB,RTGOT,
&                RTGOTB
      DOUBLE PRECISION THRES(NEQ),WORK(LENWRK),WORKB(LENWRK),
&                RWORK(LENWRK),RWORKB(LENWRK),
&                YMAX(NEQ),YNOW(NEQ),YPNOW(NEQ),YNOWB(NEQ),
&                YPNOWB(NEQ),RYNOW(NEQ),RYPNOW(NEQ),RYNOWB(NEQ),
&                RYPNOWB(NEQ),YGOT(NEQ),YGOTB(NEQ),RYGOT(NEQ),
&                RYGOTB(NEQ),YPGOT(NEQ),YPGOTB(NEQ),RYPGOT(NEQ),
&                RYPGOTB(NEQ)
      LOGICAL      ERRASS,MESAGE

```

C ***COUNTERS***

```

      INTEGER      i,j,k,m,ii,jj,kk,ll,mm,nn,pp

```

C ***PULSE AND ATOM PARAMETERS***

```

      DOUBLE PRECISION N,Z,TAU,FREQ,INT
      COMMON /params1/ N,Z,TAU,FREQ,INT

```

```

C      ***CONSTANT PARAMETERS***
      DOUBLE PRECISION PI,CLIGHT,ALPHA
      COMMON /params2/ PI,CLIGHT,ALPHA

C      ***MISC PARAMETERS***
      INTEGER          totaln,a,indicator1,bins,type,indicator2,gridnum,
&                    numorbs,numints
      PARAMETER        (totaln=100000,a=50,indicator1=1,bins=100,
&                    type=0,indicator2=2,gridnum=967,numorbs=201,
&                    numints=29) !39
      DOUBLE PRECISION radmax,radmin,theta,phi,rmax
      PARAMETER        (radmax=1.0D0,radmin=1.0D-6)

      INTEGER          conditions,binnum,NRnumionE,NRnumionB,
&                    NRnumoriginE,NRnumoriginB,RnumionE,RnumionB,
&                    RnumoriginE,RnumoriginB,dimsn,
&                    NRnumionEtot,NRnumionBtot,
&                    RnumionEtot,RnumionBtot

C ***COMMON DATA***
      DOUBLE PRECISION YSTART(NEQ),TSTART,TEND,TEND1,TEND2,
&                    NRRADE,NRKEE,NRPEE,NRETOTE,
&                    NRRADB,NRKEB,NRPEB,NRETOTB,
&                    RRADE,RKEE,RPEE,RETOTE,
&                    RRADB,RKEB,RPEB,RETOTB,
&                    tlookc,deltatcheck,EF,tlast

      INTEGER          cutnum,run,check,NRskipE,NRskipB,RskipE,RskipB,
&                    NRnumE,NRnumB,RnumE,RnumB,NRcheckcountE,
&                    NRcheckcountB,RcheckcountE,RcheckcountB,
&                    NRchecknumE,NRchecknumB,RchecknumE,RchecknumB

      DOUBLE PRECISION NREfieldvec(totaln),NRBfieldvec(totaln),
&                    NRtvecE(totaln),NRtvecB(totaln),
&                    NREfieldbin(bins),NRBfieldbin(bins),
&                    NRtbinE(bins),NRtbinB(bins),
&                    REfieldvec(totaln),RBfieldvec(totaln),
&                    RtvecE(totaln),RtvecB(totaln),
&                    REfieldbin(bins),RBfieldbin(bins),
&                    RtbinE(bins),RtbinB(bins),
&                    NRfracE(bins),NRfracB(bins),
&                    RfracE(bins),RfracB(bins),

```

```

& NRsumE(3),NRaveE(3),NRsumB(3),NRaveB(3),
& RsumE(3),RaveE(3),RsumB(3),RaveB(3),
& xmax(3),xmin(3),deltax(4),
& NRcheckE(numorbs,2),NRcheckB(numorbs,2),
& RcheckE(numorbs,2),RcheckB(numorbs,2),
& NRcheckaveE(numorbs,2),NRcheckaveB(numorbs,2),
& RcheckaveE(numorbs,2),RcheckaveB(numorbs,2),
& NRchecksumE(2),NRchecksumB(2),
& RchecksumE(2),RchecksumB(2),
& Efieldvec(numints),
& NRprobE(numints),NRprobB(numints),
& RprobE(numints),RprobB(numints)

INTEGER NREfieldcount(bins),NRBfieldcount(bins),
& NRtcountE(bins),NRtcountB(bins),
& REfieldcount(bins),RBfieldcount(bins),
& RtcountE(bins),RtcountB(bins),
& NRcountE(3),NRcountB(3),RcountE(3),RcountB(3)

DOUBLE PRECISION NRgridExc(gridnum,gridnum),
& NRgridExi(gridnum,gridnum),
& NRgridBxc(gridnum,gridnum),
& NRgridBxi(gridnum,gridnum),
& NRgridEyc(gridnum,gridnum),
& NRgridEyi(gridnum,gridnum),
& NRgridByc(gridnum,gridnum),
& NRgridByi(gridnum,gridnum),
& NRgridEzc(gridnum,gridnum),
& NRgridEzi(gridnum,gridnum),
& NRgridBzc(gridnum,gridnum),
& NRgridBzi(gridnum,gridnum),
& RgridExc(gridnum,gridnum),
& RgridExi(gridnum,gridnum),
& RgridBxc(gridnum,gridnum),
& RgridBxi(gridnum,gridnum),
& RgridEyc(gridnum,gridnum),
& RgridEyi(gridnum,gridnum),
& RgridByc(gridnum,gridnum),
& RgridByi(gridnum,gridnum),
& RgridEzc(gridnum,gridnum),
& RgridEzi(gridnum,gridnum),
& RgridBzc(gridnum,gridnum),
& RgridBzi(gridnum,gridnum)

```

```

DOUBLE PRECISION tstar,tprime
COMMON /params3/ tstar,tprime,conditions,dimsn

DOUBLE PRECISION frac,NRmaxE,NRmaxB,RmaxE,RmaxB,tlook,deltat,
&          delta,f1,f2

DOUBLE PRECISION SEED
INTEGER*4      NOW(3),TODAY(3),time(3)

C      ***DATA FILES***
CHARACTER*50   fname1,fname2,fname3,fname4,fname5,fname6,
&             fname7,fname8,fname9,fname10,fname11,fname12,
&             fname13,fname14,fname15,fname16

C ***FUNCTIONS & SUBROUTINES***
EXTERNAL  DERIVS,DERIVSNB,DERIVSB,RDERIVS,RDERIVSNB,RDERIVSB,
&         CT,SETUP,RESET,EFIELD,BFIELD,STATE1,STATE2,STATE3,
&         LinearIC,INITIAL,INIELEM,EKEPL1,RAND,sort,
&         GridIncrement,CheckValues,Initialize1,Initialize2,
&         Initialize3,FILENAME1,FILENAME2,FILENAME3,PRINTMTRX,
&         ITIME,IDATE,STAT,UT

INTRINSIC  ABS,MAX,SQRT,SIN,COS,TAN,ATAN,ASIN,ACOS,IFIX,ALOG10

C      ***DEFINITIONS***
PI=4.0*ATAN(1.0)
CLIGHT=137.03545
ALPHA=1.0D-8
binnum=IFIX(REAL(SQRT(DBLE(totaln)))+0.5)

C  SET PARAMETERS
Z=4.0D0
N=1.0D0
FREQ=0.0 !0.07257
c  !0.7257 !0.3368 !0.1564 !0.07257 !0.03368 !0.01564 !0.007257
TAU=((numorbs-1.0)/2.0)*2.0*PI*(N**3)/(Z**2)
INT=((7.0225*CLIGHT)/(2048.0*PI))*((Z**6)/(N**8)) !865.634
c 2.955 Ec for Z=4 -> 80% ionization, 1.775 Ec for Z=4 -> 10% ionization
c 2.5 Ec for Z=20 -> 80% ionization, 1.42 Ec for Z=20 -> 40% ionization

```

```

c 1.075 Ec for Z=20 -> 10% ionization
  conditions=0
  dims=0
  run=23
  check=10 !1=<ENERGY>&<RADIUS>

  f1=500.0
  f2=1.0
  cutnum=(gridnum+1)/2
  rmax=4.0*((N**2)/Z)
  xmax(1)=rmax
  xmax(2)=rmax
  xmax(3)=rmax
  xmin(1)=-rmax
  xmin(2)=-rmax
  xmin(3)=-rmax

  deltax(1)=(xmax(1)-xmin(1))/gridnum
  deltax(2)=(xmax(2)-xmin(2))/gridnum
  deltax(3)=(xmax(3)-xmin(3))/gridnum
  deltax(4)=deltax(1)*deltax(2)*deltax(3)

  CALL ITIME(NOW)
  CALL IDATE(TODAY)
  SEED=TODAY(3)-(TODAY(1)+NOW(2)*60+NOW(3))
  CALL RAND(SEED)

C  DETERMINE IF WE HAVE LINEAR OR PULSE CONDITIONS
C  *****LINEAR CONDITIONS*****
  IF(indicator2.EQ.0 .OR. indicator2.EQ.1 .OR. indicator2.EQ.2) THEN

C  INITIALIZE VECTORS
  IF(indicator2.EQ.1) THEN
    CALL Initialize1(totaln,NREfieldvec)
    CALL Initialize1(totaln,NRBfieldvec)
    CALL Initialize1(totaln,REfieldvec)
    CALL Initialize1(totaln,RBfieldvec)
    CALL Initialize1(totaln,NRtvecE)
    CALL Initialize1(totaln,NRtvecB)
    CALL Initialize1(totaln,RtvecE)
    CALL Initialize1(totaln,RtvecB)
    CALL Initialize1(binnum,NREfieldbin)

```

```

CALL Initialize1(binnum,NRfieldbin)
CALL Initialize1(binnum,REfieldbin)
CALL Initialize1(binnum,RBfieldbin)
CALL Initialize1(binnum,NRfracE)
CALL Initialize1(binnum,NRfracB)
CALL Initialize1(binnum,RfracE)
CALL Initialize1(binnum,RfracB)
CALL Initialize2(binnum,NREfieldcount)
CALL Initialize2(binnum,NRBfieldcount)
CALL Initialize2(binnum,REfieldcount)
CALL Initialize2(binnum,RBfieldcount)
ELSE IF(indicator2.EQ.2) THEN
  CALL Initialize3(gridnum,gridnum,NRgridExc)
  CALL Initialize3(gridnum,gridnum,NRgridExi)
  CALL Initialize3(gridnum,gridnum,NRgridEyc)
  CALL Initialize3(gridnum,gridnum,NRgridEyi)
  CALL Initialize3(gridnum,gridnum,NRgridEzc)
  CALL Initialize3(gridnum,gridnum,NRgridEzi)
  CALL Initialize3(gridnum,gridnum,NRgridBxc)
  CALL Initialize3(gridnum,gridnum,NRgridBxi)
  CALL Initialize3(gridnum,gridnum,NRgridByc)
  CALL Initialize3(gridnum,gridnum,NRgridByi)
  CALL Initialize3(gridnum,gridnum,NRgridBzc)
  CALL Initialize3(gridnum,gridnum,NRgridBzi)
  CALL Initialize3(gridnum,gridnum,RgridExc)
  CALL Initialize3(gridnum,gridnum,RgridExi)
  CALL Initialize3(gridnum,gridnum,RgridEyc)
  CALL Initialize3(gridnum,gridnum,RgridEyi)
  CALL Initialize3(gridnum,gridnum,RgridEzc)
  CALL Initialize3(gridnum,gridnum,RgridEzi)
  CALL Initialize3(gridnum,gridnum,RgridBxc)
  CALL Initialize3(gridnum,gridnum,RgridBxi)
  CALL Initialize3(gridnum,gridnum,RgridByc)
  CALL Initialize3(gridnum,gridnum,RgridByi)
  CALL Initialize3(gridnum,gridnum,RgridBzc)
  CALL Initialize3(gridnum,gridnum,RgridBzi)
END IF
IF(check.EQ.1) THEN
  CALL Initialize3(numorbs,2,NRcheckaveE)
  CALL Initialize3(numorbs,2,NRcheckaveB)
  CALL Initialize3(numorbs,2,RcheckaveE)
  CALL Initialize3(numorbs,2,RcheckaveB)
  CALL Initialize3(numorbs,2,NRcheckE)

```

```

        CALL Initialize3(numorbs,2,NRcheckB)
        CALL Initialize3(numorbs,2,RcheckE)
        CALL Initialize3(numorbs,2,RcheckB)
    END IF
    NRnumoriginE=0
    NRnumoriginB=0
    NRnumionE=0
    NRnumionB=0
    RnumoriginE=0
    RnumoriginB=0
    RnumionE=0
    RnumionB=0

C   SET TOLERANCE & THRESHOLD, STARTING STEP SIZE AND TIME INCREMENTS
    TOL=1.0D-10
    DO 1 L=1,NEQ
        THRES(L)=1.0D-10
1    END DO

    MESSAGE=.FALSE.
    ERRASS=.FALSE.
    HSTART=0.0D0
    delta=(1.0/1000.0)*2.0*PI*(N**3)/(Z**2)
    deltat=(1.0/f1)*2.0*PI*(N**3)/(Z**2)
    deltatcheck=(1.0/f2)*2.0*PI*(N**3)/(Z**2)

C   DETERMINE RAMP UP TIME
    frac=a*FREQ*2.0*PI*(N**3)/(Z**2)
    IF(FREQ.EQ.0.0D0) THEN
        tstar=DBLE(a)*(2.0*PI*(N**3)/(Z**2))
    ELSE
        tstar=(1/FREQ)*frac
    END IF
    tprime=2.0*PI*(N**3)/(Z**2)

    jj=60

    CALL ITIME(time)
    WRITE(*,*) time(1),time(2),time(3)

C   LOOP OVER NUMBER OF ELECTRONS
    DO 26 j=1,totaln

```

```

C      CHECK WHICH INITIAL CONDITIONS I WANT
      tstart=0.0
      tend1=tstart+tprime
      tend2=tend1+2.0*TAU

      theta=PI/2.0
      phi=0.0

      IF(indicator1.EQ.0) THEN
        CALL LinearIC(YSTART,theta,phi)
      ELSE
        CALL INITIAL(YSTART(1),YSTART(2),YSTART(3),YSTART(4),
&                YSTART(5),YSTART(6))
      END IF

C      INITIALIZE VALUES FOR DISTRIBUTION CALCULATIONS/CHECK VALUES
      IF(indicator2.EQ.2) THEN
        CALL Initialize1(3,NRsumE)
        CALL Initialize1(3,NRsumB)
        CALL Initialize1(3,NRaveE)
        CALL Initialize1(3,NRaveB)
        CALL Initialize1(3,RsumE)
        CALL Initialize1(3,RsumB)
        CALL Initialize1(3,RaveE)
        CALL Initialize1(3,RaveB)
        CALL Initialize2(3,NRcountE)
        CALL Initialize2(3,NRcountB)
        CALL Initialize2(3,RcountE)
        CALL Initialize2(3,RcountB)
      END IF
      IF(check.EQ.1) THEN
        CALL Initialize1(2,NRchecksumE)
        CALL Initialize1(2,NRchecksumB)
        CALL Initialize1(2,RchecksumE)
        CALL Initialize1(2,RchecksumB)
        NRcheckcountE=0
        NRcheckcountB=0
        RcheckcountE=0
        RcheckcountB=0
      END IF

C      OPEN FILES IF NEEDED
      kk=jj+1

```

```
ll=jj+2
mm=jj+3
nn=jj+4
```

```
IF(indicator2.EQ.0) THEN
```

```
  IF(j.LE.10) THEN
```

```
    CALL FILENAME1(j,Z,N,FREQ,type,0,fname1,fname2,'N')
```

```
    CALL FILENAME1(j,Z,N,FREQ,type,1,fname3,fname4,'N')
```

```
    CALL FILENAME1(j,Z,N,FREQ,type,0,fname5,fname6,'R')
```

```
    CALL FILENAME1(j,Z,N,FREQ,type,1,fname7,fname8,'R')
```

```
    OPEN(UNIT=jj,FILE=fname1)
```

```
    OPEN(UNIT=ll,FILE=fname3)
```

```
    OPEN(UNIT=mm,FILE=fname5)
```

```
    OPEN(UNIT=nn,FILE=fname7)
```

```
    WRITE(jj,1000)
```

```
    WRITE(ll,1000)
```

```
    WRITE(mm,1000)
```

```
    WRITE(nn,1000)
```

```
    IF(j.EQ.1) THEN
```

```
      OPEN(UNIT=kk,FILE=fname2)
```

```
      WRITE(kk,3000)
```

```
    END IF
```

```
    CALL STATE1(TSTART,YSTART,NRRADE,NRKEE,NRPEE,NRETOTE,  
&              'N')
```

```
    CALL STATE1(TSTART,YSTART,NRRADB,NRKEB,NRPEB,NRETOTB,  
&              'N')
```

```
    CALL STATE1(TSTART,YSTART,RRADE,RKEE,RPEE,RETOTE,  
&              'R')
```

```
    CALL STATE1(TSTART,YSTART,RRADB,RKEB,RPEB,RETOTB,  
&              'R')
```

```
    WRITE(jj,2000) TSTART,YSTART(1),YSTART(2),YSTART(3),  
&                YSTART(4),YSTART(5),YSTART(6),NRRADE,NRKEE,  
&                NRPEE,NRETOTE
```

```
    WRITE(ll,2000) TSTART,YSTART(1),YSTART(2),YSTART(3),  
&                YSTART(4),YSTART(5),YSTART(6),NRRADB,NRKEB,  
&                NRPEB,NRETOTB
```

```
    WRITE(mm,2000) TSTART,YSTART(1),YSTART(2),YSTART(3),  
&                YSTART(4),YSTART(5),YSTART(6),RRADE,RKEE,  
&                RPEE,RETOTE
```

```
    WRITE(nn,2000) TSTART,YSTART(1),YSTART(2),YSTART(3),  
&                YSTART(4),YSTART(5),YSTART(6),RRADB,RKEB,  
&                RPEB,RETOTB
```

```
  END IF
```

```

                END IF

C *****NON-RELATIVISTIC*****
C *****E FIELD INTEGRATION*****
C SET ERROR AND OTHER PARAMETERS NEEDED BY CT & UT
      DO 2 L=1,NEQ
          YMAX(L)=ABS(YSTART(L))
2          END DO

          TEND=(1.0/1000.0)*2.0*PI*(N**3)/(Z**2)
          tlook=tstart+deltat
          tlookc=tstart+deltatcheck
          ii=1

C INTEGRATE EQUATIONS FOR SHORT TIME WITHOUT LASER PULSE
      CALL SETUP(NEQ,TSTART,YSTART,TEND,TOL,THRES,METHOD,
&              'Complex Task',ERRASS,HSTART,WORK,LENWRK,MESSAGE)

          CFLAG3=0

3          CONTINUE
          CALL CT(DERIVS,TNOW,YNOW,YPNOW,WORK,CFLAG)

C UPDATE AVERAGE CHECK VALUES
      IF(check.EQ.1) THEN
          CALL CheckValues(YNOW,TNOW,tlookc,deltatcheck,
&              NRchecksumE,NRcheckcountE,NRcheckaveE,ii,NRRADE,
&              NRKEE,NRPEE,NRETOTE,numorbs,'N',0)
          END IF
C UPDATE ERROR
      DO 4 L=1,NEQ
          YMAX(L)=MAX(YMAX(L),ABS(YNOW(L)))
4          END DO

C INCREMENT AVERAGE/CALCULATE AVERAGE
      IF(indicator2.EQ.2) THEN
          CALL GridIncrement(YNOW,TNOW,tlook,deltat,totaln,cutnum,
&              NRsumE,NRcountE,NRaveE,xmin,deltax,
&              NRgridExc,NRgridEyc,NRgridEzc,NRgridExi,NRgridEyi,
&              NRgridEzi,gridnum)
          END IF

```

```

C   RECORD VALUES AND UPDATE NEXT INTEGRATION STEP
      IF(CFLAG.LE.5) THEN
        IF(indicator2.EQ.0) THEN
          IF(j.LE.10) THEN
            CALL STATE1(TNOW,YNOW,NRRADE,NRKEE,NRPEE,NRETOTE,
&              'N')
            WRITE(jj,2000) TNOW,YNOW(1),YNOW(2),YNOW(3),
&              YPNOW(1),YPNOW(2),YPNOW(3),NRRADE,NRKEE,NRPEE,
&              NRETOTE
          END IF
        END IF
      IF(CFLAG.EQ.4) CFLAG3=CFLAG3+1
      IF(TEND.LE.TEND1 .AND. CFLAG3.LT.5) THEN
        TEND=TEND+delta
        CALL RESET(TEND)
        GO TO 3
      END IF
    END IF
C   SEPARATE OUT END TIMES OF INTEGRATION FOR SPECIFIC SITUATION
      IF(indicator2.EQ.1) THEN ! .AND. FREQ.NE.0.0) THEN
        TEND=TEND+2.0*TAU
      ELSE
        TEND=TEND+delta
      END IF
C   INTEGRATE EQUATIONS WITH PULSE PRESENT
      CALL RESET(TEND)

      CFLAG3=0

5     CONTINUE
      CALL CT(DERIVSNB,TNOW,YNOW,YPNOW,WORK,CFLAG)
C   UPDATE AVERAGE CHECK VALUES
      IF(check.EQ.1) THEN
        CALL CheckValues(YNOW,TNOW,tlookc,deltatcheck,
&          NRchecksumE,NRcheckcountE,NRcheckaveE,ii,NRRADE,
&          NRKEE,NRPEE,NRETOTE,numorbs,'N',1)
      END IF
C   CHECK FOR CROSSING OF ORIGIN
      IF(indicator1.NE.0) THEN
        CALL STATE2(TNOW,YNOW,NRRADE,NRKEE,NRPEE,NRETOTE,'N')
        IF(NRRADE.LE.Radmin) THEN

```

```

        NRnumoriginE=NRnumoriginE+1
        GO TO 7
    END IF
END IF
C   INCREMENT AVERAGE/CALCULATE AVERAGE
    IF(indicator2.EQ.2) THEN
        NRnumE=totaln-NRnumionE-NRnumoriginE
        CALL GridIncrement(YNOW,TNOW,tlook,deltat,NRnumE,
&           cutnum,NRsumE,NRcountE,NRaveE,xmin,deltax,
&           NRgridExc,NRgridEyc,NRgridEzc,NRgridExi,NRgridEyi,
&           NRgridEzi,gridnum)
    END IF
C   CHECK FOR IONIZATION
    CALL STATE2(TNOW,YNOW,NRRADE,NRKEE,NRPEE,NRETOTE,'N')
    IF(NRRADE.GT.radmax) THEN
        NRnumionE=NRnumionE+1
        IF(FREQ.EQ.0.0) THEN
            NREfieldvec(j)=EFIELD(TNOW,YNOW)
        ELSE
            NREfieldvec(j)=ABS(EFIELD(TNOW,YNOW))
        END IF
        NRTvecE(j)=TNOW
        IF(indicator2.EQ.0) THEN
            IF(j.LE.10) THEN
                CALL STATE2(TNOW,YNOW,NRRADE,NRKEE,NRPEE,NRETOTE,
&                 'N')
                WRITE(jj,2000) TNOW,YNOW(1),YNOW(2),YNOW(3),
&                 YPNOW(1),YPNOW(2),YPNOW(3),NRRADE,NRKEE,NRPEE,
&                 NRETOTE
                IF(j.EQ.1) WRITE(kk,4000) TNOW,EFIELD(TNOW,YNOW),
&                 BFIELD(TNOW,YNOW)
            END IF
        END IF
        GO TO 7
    END IF
C   UPDATE ERROR
    DO 6 L=1,NEQ
        YMAX(L)=MAX(YMAX(L),ABS(YNOW(L)))
6    END DO
C   RECORD VALUES AND UPDATE NEXT INTEGRATION STEP
    IF(CFLAG.LE.5) THEN
        IF(indicator2.EQ.0) THEN

```

```

        IF(j.LE.10) THEN
            CALL STATE2(TNOW,YNOW,NRRADE,NRKEE,NRPEE,NRETOTE,
&                'N')
            WRITE(jj,2000) TNOW,YNOW(1),YNOW(2),YNOW(3),
&                YPNOW(1),YPNOW(2),YPNOW(3),NRRADE,NRKEE,NRPEE,
&                NRETOTE
            IF(j.EQ.1) WRITE(kk,4000) TNOW,EFIELD(TNOW,YNOW),
&                BFIELD(TNOW,YNOW)
            END IF
        END IF
        IF(CFLAG.EQ.4) CFLAG3=CFLAG3+1
        IF(indicator2.EQ.1) THEN ! .AND. FREQ.NE.0.0) THEN
            IF(TNOW.LT.TEND .AND. CFLAG3.LT.5) GO TO 5
        ELSE
            IF(TEND.LE.TEND2 .AND. CFLAG3.LT.5) THEN
                TEND=TEND+delta
                CALL RESET(TEND)
                GO TO 5
            END IF
        END IF
    END IF
END IF

7          CONTINUE
C          *****END E FIELD INTEGRATION*****

C          *****E&B-FIELD INTEGRATION*****
C          SET ERROR AND OTHER PARAMETERS NEEDED BY CT & UT
            DO 8 L=1,NEQ
                YMAX(L)=ABS(YSTART(L))
8          END DO

            TEND=(1.0/1000.0)*2.0*PI*(N**3)/(Z**2)
            tlook=tstart+deltat
            tlookc=tstart+deltatcheck
            ii=1

C          INTEGRATE EQUATIONS FOR SHORT TIME WITHOUT LASER PULSE
            CALL SETUP(NEQ,TSTART,YSTART,TEND,TOL,THRES,METHOD,
&                'Complex Task',ERRASS,HSTART,WORKB,LENWRK,MESAGE)

            CFLAG3=0

9          CONTINUE

```

```

        CALL CT(DERIVS, TNOWB, YNOWB, YPNOWB, WORKB, CFLAG)

C      UPDATE AVERAGE CHECK VALUES
        IF(check.EQ.1) THEN
            CALL CheckValues(YNOWB, TNOWB, tlookc, deltatcheck,
&                NRchecksumB, NRcheckcountB, NRcheckaveB, ii, NRRADB,
&                NRKEB, NRPEB, NRETOTB, numorbs, 'N', 0)
        END IF

C      UPDATE ERROR
        DO 10 L=1, NEQ
            YMAX(L)=MAX(YMAX(L), ABS(YNOWB(L)))
10      END DO

C      INCREMENT AVERAGE/CALCULATE AVERAGE
        IF(indicator2.EQ.2) THEN
            CALL GridIncrement(YNOWB, TNOWB, tlook, deltata, totaln,
&                cutnum, NRsumB, NRcountB, NRaveB, xmin, deltax,
&                NRgridBxc, NRgridByc, NRgridBzc, NRgridBxi, NRgridByi,
&                NRgridBzi, gridnum)
        END IF

C      RECORD VALUES AND UPDATE NEXT INTEGRATION STEP
        IF(CFLAG.LE.5) THEN
            IF(indicator2.EQ.0) THEN
                IF(j.LE.10) THEN
                    CALL STATE1(TNOWB, YNOWB, NRRADB, NRKEB, NRPEB, NRETOTB,
&                'N')
                    WRITE(11, 2000) TNOWB, YNOWB(1), YNOWB(2), YNOWB(3),
&                YPNOWB(1), YPNOWB(2), YPNOWB(3), NRRADB, NRKEB,
&                NRPEB, NRETOTB
                END IF
            END IF
            IF(CFLAG.EQ.4) CFLAG3=CFLAG3+1
            IF(TEND.LE.TEND1 .AND. CFLAG3.LT.5) THEN
                TEND=TEND+delta
                CALL RESET(TEND)
                GO TO 9
            END IF
        END IF

C      SEPARATE OUT END TIMES OF INTEGRATION FOR SPECIFIC SITUATION
        IF(indicator2.EQ.1) THEN ! .AND. FREQ.NE.0.0) THEN
            TEND=TEND+2.0*TAU

```

```

        ELSE
            TEND=TEND+delta
        END IF

C      INTEGRATE EQUATIONS WITH PULSE PRESENT
        CALL RESET(TEND)

        CFLAG3=0

11     CONTINUE
        CALL CT(DERIVSB,TNOWB,YNOWB,YPNOWB,WORKB,CFLAG)
C      UPDATE AVERAGE CHECK VALUES
        IF(check.EQ.1) THEN
            CALL CheckValues(YNOWB,TNOWB,tlookc,deltatcheck,
&                NRchecksumB,NRcheckcountB,NRcheckaveB,ii,NRRADB,
&                NRKEB,NRPEB,NRETOTB,numorbs,'N',2)
        END IF

C      CHECK FOR CROSSING OF ORIGIN
        IF(indicator1.NE.0) THEN
            CALL STATE3(TNOWB,YNOWB,NRRADB,NRKEB,NRPEB,NRETOTB,'N')
            IF(NRRADB.LE.Radmin) THEN
                NRnumoriginB=NRnumoriginB+1
                GO TO 13
            END IF
        END IF

C      INCREMENT AVERAGE/CALCULATE AVERAGE
        IF(indicator2.EQ.2) THEN
            NRnumB=totaln-NRnumionB-NRnumoriginB
            CALL GridIncrement(YNOWB,TNOWB,tlook,deltat,NRnumB,
&                cutnum,NRsumB,NRcountB,NRaveB,xmin,deltax,
&                NRgridBxc,NRgridByc,NRgridBzc,NRgridBxi,NRgridByi,
&                NRgridBzi,gridnum)
        END IF

C      CHECK FOR IONIZATION
        CALL STATE3(TNOWB,YNOWB,NRRADB,NRKEB,NRPEB,NRETOTB,'N')
        IF(NRRADB.GT.radmax) THEN
            NRnumionB=NRnumionB+1
            IF(FREQ.EQ.0.0) THEN
                NRBfieldvec(j)=EFIELD(TNOWB,YNOWB)
            ELSE
                NRBfieldvec(j)=ABS(EFIELD(TNOWB,YNOWB))
            END IF
        END IF

```

```

      NRtvecB(j)=TNOWB
      IF(indicator2.EQ.0) THEN
        IF(j.LE.10) THEN
          CALL STATE3(TNOWB,YNOWB,NRRADB,NRKEB,NRPEB,NRETOTB,
&                'N')
          WRITE(11,2000) TNOWB,YNOWB(1),YNOWB(2),YNOWB(3),
&                YPNOWB(1),YPNOWB(2),YPNOWB(3),NRRADB,NRKEB,
&                NRPEB,NRETOTB
          END IF
        END IF
        GO TO 13
      END IF
C    UPDATE ERROR
      DO 12 L=1,NEQ
        YMAX(L)=MAX(YMAX(L),ABS(YNOWB(L)))
12    END DO

C    RECORD VALUES AND UPDATE NEXT INTEGRATION STEP
      IF(CFLAG.LE.5) THEN
        IF(indicator2.EQ.0) THEN
          IF(j.LE.10) THEN
            CALL STATE3(TNOWB,YNOWB,NRRADB,NRKEB,NRPEB,NRETOTB,
&                'N')
            WRITE(11,2000) TNOWB,YNOWB(1),YNOWB(2),YNOWB(3),
&                YPNOWB(1),YPNOWB(2),YPNOWB(3),NRRADB,NRKEB,
&                NRPEB,NRETOTB
            END IF
          END IF
          IF(CFLAG.EQ.4) CFLAG3=CFLAG3+1
          IF(indicator2.EQ.1) THEN ! .AND. FREQ.NE.0.0) THEN
            IF(TNOWB.LT.TEND .AND. CFLAG3.LT.5) GO TO 11
          ELSE
            IF(TEND.LE.TEND2 .AND. CFLAG3.LT.5) THEN
              TEND=TEND+delta
              CALL RESET(TEND)
              GO TO 11
            END IF
          END IF
        END IF
      END IF

13    CONTINUE

C    *****END E&B-FIELD INTEGRATION*****

```

```

C *****END NON-RELATIVISTIC*****
C *****RELATIVISTIC*****
C *****E FIELD INTEGRATION*****
C SET ERROR AND OTHER PARAMETERS NEEDED BY CT & UT
      DO 14 L=1,NEQ
          YMAX(L)=ABS(YSTART(L))
14      END DO

      TEND=(1.0/1000.0)*2.0*PI*(N**3)/(Z**2)
      tlook=tstart+deltat
      tlookc=tstart+deltatcheck
      ii=1

C INTEGRATE EQUATIONS FOR SHORT TIME WITHOUT LASER PULSE
      CALL SETUP(NEQ,TSTART,YSTART,TEND,TOL,THRES,METHOD,
&              'Complex Task',ERRASS,HSTART,RWORK,LENWRK,MESAGE)

      CFLAG3=0

15      CONTINUE
      CALL CT(RDERIVS,RTNOW,RYNOW,RYPNOW,RWORK,CFLAG)

C UPDATE AVERAGE CHECK VALUES
      IF(check.EQ.1) THEN
          CALL CheckValues(RYNOW,RTNOW,tlookc,deltatcheck,
&              RchecksumE,RcheckcountE,RcheckaveE,ii,RRADE,
&              RKEE,RPEE,RETOTE,numorbs,'R',0)
      END IF

C UPDATE ERROR
      DO 16 L=1,NEQ
          YMAX(L)=MAX(YMAX(L),ABS(RYNOW(L)))
16      END DO

C INCREMENT AVERAGE/CALCULATE AVERAGE
      IF(indicator2.EQ.2) THEN
          CALL GridIncrement(RYNOW,RTNOW,tlook,deltat,totaln,
&              cutnum,RsumE,RcountE,RaveE,xmin,deltax,
&              RgridExc,RgridEyc,RgridEzc,RgridExi,RgridEyi,

```

```

&          RgridEzi,gridnum)
      END IF

C   RECORD VALUES AND UPDATE NEXT INTEGRATION STEP
      IF(CFLAG.LE.5) THEN
        IF(indicator2.EQ.0) THEN
          IF(j.LE.10) THEN
            CALL STATE1(RTNOW,RYNOW,RRADE,RKEE,RPEE,RETOTE,
&              'R')
            WRITE(mm,2000) RTNOW,RYNOW(1),RYNOW(2),RYNOW(3),
&              RYPNOW(1),RYPNOW(2),RYPNOW(3),RRADE,RKEE,RPEE,
&              RETOTE
          END IF
        END IF
        IF(CFLAG.EQ.4) CFLAG3=CFLAG3+1
        IF(TEND.LE.TEND1 .AND. CFLAG3.LT.5) THEN
          TEND=TEND+delta
          CALL RESET(TEND)
          GO TO 15
        END IF
      END IF

C   SEPARATE OUT END TIMES OF INTEGRATION FOR SPECIFIC SITUATION
      IF(indicator2.EQ.1) THEN ! .AND. FREQ.NE.0.0) THEN
        TEND=TEND+2.0*TAU
      ELSE
        TEND=TEND+delta
      END IF

C   INTEGRATE EQUATIONS WITH PULSE PRESENT
      CALL RESET(TEND)

      CFLAG3=0

17   CONTINUE
      CALL CT(RDERIVSNB,RTNOW,RYNOW,RYPNOW,RWORK,CFLAG)

C   UPDATE AVERAGE CHECK VALUES
      IF(check.EQ.1) THEN
        CALL CheckValues(RYNOW,RTNOW,tlookc,deltatcheck,
&          RchecksumE,RcheckcountE,RcheckaveE,ii,RRADE,
&          RKEE,RPEE,RETOTE,numorbs,'R',1)
      END IF

C   CHECK FOR CROSSING OF ORIGIN

```

```

        IF(indicator1.NE.0) THEN
            CALL STATE2(RTNOW,RYNOW,RRADE,RKEE,RPEE,RETOTE,'R')
            IF(RRADE.LE.Radmin) THEN
                RnumoriginE=RnumoriginE+1
                GO TO 19
            END IF
        END IF
C   INCREMENT AVERAGE/CALCULATE AVERAGE
        IF(indicator2.EQ.2) THEN
            RnumE=totaln-RnumionE-RnumoriginE
            CALL GridIncrement(RYNOW,RTNOW,tlook,deltat,RnumE,
&                cutnum,RsumE,RcountE,RaveE,xmin,deltax,
&                RgridExc,RgridEyc,RgridEzc,RgridExi,RgridEyi,
&                RgridEzi,gridnum)
        END IF
C   CHECK FOR IONIZATION
        CALL STATE2(RTNOW,RYNOW,RRADE,RKEE,RPEE,RETOTE,'R')
        IF(RRADE.GT.radmax) THEN
            RnumionE=RnumionE+1
            IF(FREQ.EQ.0.0) THEN
                REfieldvec(j)=EFIELD(RTNOW,RYNOW)
            ELSE
                REfieldvec(j)=ABS(EFIELD(RTNOW,RYNOW))
            END IF
            RtvecE(j)=RTNOW
            IF(indicator2.EQ.0) THEN
                IF(j.LE.10) THEN
                    CALL STATE2(RTNOW,RYNOW,RRADE,RKEE,RPEE,RETOTE,
&                        'R')
                    WRITE(mm,2000) RTNOW,RYNOW(1),RYNOW(2),RYNOW(3),
&                        RYPNOW(1),RYPNOW(2),RYPNOW(3),RRADE,RKEE,RPEE,
&                        NRETOTE
                END IF
            END IF
            GO TO 19
        END IF
C   UPDATE ERROR
        DO 18 L=1,NEQ
            YMAX(L)=MAX(YMAX(L),ABS(RYNOW(L)))
18      END DO
C   RECORD VALUES AND UPDATE NEXT INTEGRATION STEP
        IF(CFLAG.LE.5) THEN

```



```

C      UPDATE AVERAGE CHECK VALUES
          IF(check.EQ.1) THEN
              CALL CheckValues(RYNOWB,RTNOWB,tlookc,deltatcheck,
&                  RchecksumB,RcheckcountB,RcheckaveB,ii,RRADB,
&                  RKEB,RPEB,RETOTB,numorbs,'R',0)
          END IF

C      UPDATE ERROR
          DO 22 L=1,NEQ
              YMAX(L)=MAX(YMAX(L),ABS(RYNOWB(L)))
22      END DO

C      INCREMENT AVERAGE/CALCULATE AVERAGE
          IF(indicator2.EQ.2) THEN
              CALL GridIncrement(RYNOWB,RTNOWB,tlook,deltat,totaln,
&                  cutnum,RsumB,RcountB,RaveB,xmin,deltax,
&                  RgridBxc,RgridByc,RgridBzc,RgridBxi,RgridByi,
&                  RgridBzi,gridnum)
          END IF

C      RECORD VALUES AND UPDATE NEXT INTEGRATION STEP
          IF(CFLAG.LE.5) THEN
              IF(indicator2.EQ.0) THEN
                  IF(j.LE.10) THEN
                      CALL STATE1(RTNOWB,RYNOWB,RRADB,RKEB,RPEB,RETOTB,
&                          'R')
                      WRITE(nn,2000) RTNOWB,RYNOWB(1),RYNOWB(2),
&                          RYNOWB(3),RYPNOWB(1),RYPNOWB(2),RYPNOWB(3),
&                          RRADB,RKEB,RPEB,RETOTB
                  END IF
              END IF
              IF(CFLAG.EQ.4) CFLAG3=CFLAG3+1
              IF(TEND.LE.TEND1 .AND. CFLAG3.LT.5) THEN
                  TEND=TEND+delta
                  CALL RESET(TEND)
                  GO TO 21
              END IF
          END IF

C      SEPARATE OUT END TIMES OF INTEGRATION FOR SPECIFIC SITUATION
          IF(indicator2.EQ.1) THEN ! .AND. FREQ.NE.0.0) THEN
              TEND=TEND+2.0*TAU
          ELSE

```

```

        TEND=TEND+delta
    END IF

C    INTEGRATE EQUATIONS WITH PULSE PRESENT
    CALL RESET(TEND)

    CFLAG3=0

23    CONTINUE
    CALL CT(RDERIVSB,RTNOWB,RYNOWB,RYPNOWB,RWORKB,CFLAG)
C    UPDATE AVERAGE CHECK VALUES
    IF(check.EQ.1) THEN
        CALL CheckValues(RYNOWB,RTNOWB,tlookc,deltatcheck,
&            RchecksumB,RcheckcountB,RcheckaveB,ii,RRADB,
&            RKEB,RPEB,RETOTB,numorbs,'R',2)
    END IF

C    CHECK FOR CROSSING OF ORIGIN
    IF(indicator1.NE.0) THEN
        CALL STATE3(RTNOWB,RYNOWB,RRADB,RKEB,RPEB,RETOTB,'R')
        IF(RRADB.LE.Radmin) THEN
            RnumoriginB=RnumoriginB+1
            GO TO 25
        END IF
    END IF

C    INCREMENT AVERAGE/CALCULATE AVERAGE
    IF(indicator2.EQ.2) THEN
        RnumB=totaln-RnumionB-RnumoriginB
        CALL GridIncrement(RYNOWB,RTNOWB,tlook,deltat,RnumB,
&            cutnum,RsumB,RcountB,RaveB,xmin,deltax,
&            RgridBxc,RgridByc,RgridBzc,RgridBxi,RgridByi,
&            RgridBzi,gridnum)
    END IF

C    CHECK FOR IONIZATION
    CALL STATE3(RTNOWB,RYNOWB,RRADB,RKEB,RPEB,RETOTB,'R')
    IF(RRADB.GT.radmax) THEN
        RnumionB=RnumionB+1
        IF(FREQ.EQ.0.0) THEN
            RBfieldvec(j)=EFIELD(RTNOWB,RYNOWB)
        ELSE
            RBfieldvec(j)=ABS(EFIELD(RTNOWB,RYNOWB))
        END IF
        RtvecB(j)=RTNOWB
    
```

```

        IF(indicator2.EQ.0) THEN
            IF(j.LE.10) THEN
                CALL STATE3(RTNOWB,RYNOWB,RRADB,RKEB,RPEB,RETOTB,
&                'R')
                WRITE(nn,2000) RTNOWB,RYNOWB(1),RYNOWB(2),
&                RYNOWB(3),RYPNOWB(1),RYPNOWB(2),RYPNOWB(3),
&                RRADB,RKEB,RPEB,RETOTB
            END IF
        END IF
        GO TO 25
    END IF
C   UPDATE ERROR
    DO 24 L=1,NEQ
        YMAX(L)=MAX(YMAX(L),ABS(YNOWB(L)))
24   END DO

C   RECORD VALUES AND UPDATE NEXT INTEGRATION STEP
    IF(CFLAG.LE.5) THEN
        IF(indicator2.EQ.0) THEN
            IF(j.LE.10) THEN
                CALL STATE3(RTNOWB,RYNOWB,RRADB,RKEB,RPEB,RETOTB,
&                'R')
                WRITE(nn,2000) RTNOWB,RYNOWB(1),RYNOWB(2),
&                RYNOWB(3),RYPNOWB(1),RYPNOWB(2),RYPNOWB(3),
&                RRADB,RKEB,RPEB,RETOTB
            END IF
        END IF
        IF(CFLAG.EQ.4) CFLAG3=CFLAG3+1
        IF(indicator2.EQ.1) THEN ! .AND. FREQ.NE.0.0) THEN
            IF(RTNOWB.LT.TEND .AND. CFLAG3.LT.5) GO TO 23
        ELSE
            IF(TEND.LE.TEND2 .AND. CFLAG3.LT.5) THEN
                TEND=TEND+delta
                CALL RESET(TEND)
                GO TO 23
            END IF
        END IF
    END IF

25   CONTINUE

C   *****END E&B-FIELD INTEGRATION*****
C   *****END RELATIVISTIC*****

```

```

C      CLOSE ANY FILES THAT HAVE BEEN OPENED FOR PARTICULAR ELECTRONS
      IF(indicator2.EQ.0) THEN
          IF(j.LE.10) THEN
              CLOSE(UNIT=jj)
              IF(j.EQ.1) CLOSE(UNIT=kk)
              CLOSE(UNIT=ll)
              CLOSE(UNIT=mm)
              CLOSE(UNIT=nn)
          END IF
      END IF
      jj=jj+5

c          CALL ITIME(time)
c          WRITE(*,*) j,time(1),time(2),time(3)

26      CONTINUE

      CALL ITIME(time)
      WRITE(*,*) time(1),time(2),time(3)

c          IF(check.EQ.0) THEN
c              WRITE(*,*) 'N:E',NRnumionE,NRnumoriginE
c              WRITE(*,*) 'N:B',NRnumionB,NRnumoriginB
c              WRITE(*,*) 'R:E',RnumionE,RnumoriginE
c              WRITE(*,*) 'R:B',RnumionB,RnumoriginB
c          END IF

C      SORT VECTORS
      IF(indicator2.EQ.1) THEN
          CALL sort(totaln,NREfieldvec,NRtvecE)
          CALL sort(totaln,NRBfieldvec,NRtvecB)
          CALL sort(totaln,REfieldvec,RtvecE)
          CALL sort(totaln,RBfieldvec,RtvecB)

C      OPEN FILES FOR BINNED DATA
      CALL FILENAME2(Z,N,FREQ,type,fname9,fname10,'N',run)
      CALL FILENAME2(Z,N,FREQ,type,fname11,fname12,'R',run)
      OPEN(UNIT=95,FILE=fname9)
      OPEN(UNIT=96,FILE=fname10)
      OPEN(UNIT=97,FILE=fname11)
      OPEN(UNIT=98,FILE=fname12)

```

```

C   WRITE RESULTS TO OUTFILE
      WRITE(95,5500)
      WRITE(96,5500)
      WRITE(97,5500)
      WRITE(98,5500)
      DO 27 j=1,totaln
          WRITE(95,6500) NREfieldvec(j),NRtvecE(j)
          WRITE(96,6500) NRBfieldvec(j),NRtvecB(j)
          WRITE(97,6500) REfieldvec(j),RtvecE(j)
          WRITE(98,6500) RBfieldvec(j),RtvecB(j)
27  END DO

      WRITE(*,*) 'N:E',NRnumionE,NRnumoriginE
      WRITE(*,*) 'N:B',NRnumionB,NRnumoriginB
      WRITE(*,*) 'R:E',RnumionE,RnumoriginE
      WRITE(*,*) 'R:B',RnumionB,RnumoriginB

C   CLOSE FILES THAT ARE OPENED
      CLOSE(UNIT=95)
      CLOSE(UNIT=96)
      CLOSE(UNIT=97)
      CLOSE(UNIT=98)
      END IF

C   PRINT OUT DISTRIBUTIONS
      IF(indicator2.EQ.2) THEN
          CALL PRINTMTRX(Z,N,gridnum,NRgridExc,NRgridBxc,1,1,run,'N')
          CALL PRINTMTRX(Z,N,gridnum,NRgridExi,NRgridBxi,1,2,run,'N')
          CALL PRINTMTRX(Z,N,gridnum,NRgridEyc,NRgridByc,2,1,run,'N')
          CALL PRINTMTRX(Z,N,gridnum,NRgridEyi,NRgridByi,2,2,run,'N')
          CALL PRINTMTRX(Z,N,gridnum,NRgridEzc,NRgridBzc,3,1,run,'N')
          CALL PRINTMTRX(Z,N,gridnum,NRgridEzi,NRgridBzi,3,2,run,'N')

          CALL PRINTMTRX(Z,N,gridnum,RgridExc,RgridBxc,1,1,run,'R')
          CALL PRINTMTRX(Z,N,gridnum,RgridExi,RgridBxi,1,2,run,'R')
          CALL PRINTMTRX(Z,N,gridnum,RgridEyc,RgridByc,2,1,run,'R')
          CALL PRINTMTRX(Z,N,gridnum,RgridEyi,RgridByi,2,2,run,'R')
          CALL PRINTMTRX(Z,N,gridnum,RgridEzc,RgridBzc,3,1,run,'R')
          CALL PRINTMTRX(Z,N,gridnum,RgridEzi,RgridBzi,3,2,run,'R')

          WRITE(*,*) 'N:E',NRnumionE,NRnumoriginE
          WRITE(*,*) 'N:B',NRnumionB,NRnumoriginB

```

```

WRITE(*,*) 'R:E',RnumionE,RnumoriginE
WRITE(*,*) 'R:B',RnumionB,RnumoriginB
END IF

```

```

IF(check.EQ.1) THEN
  CALL FILENAME3(Z,N,fname13,fname14,run,'N')
  CALL FILENAME3(Z,N,fname15,fname16,run,'R')
  OPEN(UNIT=26,FILE=fname13)
  OPEN(UNIT=27,FILE=fname14)
  OPEN(UNIT=28,FILE=fname15)
  OPEN(UNIT=29,FILE=fname16)
  WRITE(26,7000)
  WRITE(27,7000)
  WRITE(28,7000)
  WRITE(29,7000)
  NRchecknumE=totaln-NRnumionE-NRnumoriginE
  NRchecknumB=totaln-NRnumionB-NRnumoriginB
  RchecknumE=totaln-RnumionE-RnumoriginE
  RchecknumB=totaln-RnumionB-RnumoriginB
  DO 28 j=1,numorbs
    NRcheckE(j,1)=NRcheckaveE(j,1)/DBLE(NRchecknumE)
    NRcheckE(j,2)=NRcheckaveE(j,2)/DBLE(NRchecknumE)
    NRcheckB(j,1)=NRcheckaveB(j,1)/DBLE(NRchecknumB)
    NRcheckB(j,2)=NRcheckaveB(j,2)/DBLE(NRchecknumB)
    RcheckE(j,1)=RcheckaveE(j,1)/DBLE(RchecknumE)
    RcheckE(j,2)=RcheckaveE(j,2)/DBLE(RchecknumE)
    RcheckB(j,1)=RcheckaveB(j,1)/DBLE(RchecknumB)
    RcheckB(j,2)=RcheckaveB(j,2)/DBLE(RchecknumB)
    WRITE(26,8000) NRcheckE(j,1),NRcheckE(j,2)
    WRITE(27,8000) NRcheckB(j,1),NRcheckB(j,2)
    WRITE(28,8000) RcheckE(j,1),RcheckE(j,2)
    WRITE(29,8000) RcheckB(j,1),RcheckB(j,2)

```

```

28 CONTINUE

```

```

CLOSE(UNIT=26)
CLOSE(UNIT=27)
CLOSE(UNIT=28)
CLOSE(UNIT=29)
END IF

```

```

ELSE IF(indicator2.EQ.3) THEN
C  DETERMINE RAMP UP TIME
    frac=a*FREQ*2.0*PI*(N**3)/(Z**2)
    IF(FREQ.EQ.0.0D0) THEN
        tstar=DBLE(a)*(2.0*PI*(N**3)/(Z**2))
    ELSE
        tstar=(1/FREQ)*frac
    END IF

    tprime=2.0*PI*(N**3)/(Z**2)
    tstart=0.0
    TEND=TSTART+tprime+2.0*TAU
    TEND1=tstart+tprime
    TEND2=TEND1+2.0*TAU
    HSTART=0.0

    NRnumionEtot=0
    NRnumionBtot=0
    RnumionEtot=0
    RnumionBtot=0

    NRnumionE=0
    NRnumionB=0
    RnumionE=0
    RnumionB=0

    CALL Initialize1(numints,NRprobE)
    CALL Initialize1(numints,NRprobB)
    CALL Initialize1(numints,RprobE)
    CALL Initialize1(numints,RprobB)
    CALL Initialize1(numints,Efieldvec)

    CALL ITIME(NOW)
    CALL IDATE(TODAY)
    SEED=TODAY(3)-(TODAY(1)+NOW(2)*60+NOW(3))
    CALL RAND(SEED)

    TOL=1.0D-10

```

```

DO 29 L=1,NEQ
  THRES(L)=1.0D-10
29  END DO

MESSAGE=.FALSE.
ERRASS=.FALSE.

CALL ITIME(time)
WRITE(*,*) time(1),time(2),time(3)

C  LOOP OVER INTENSITIES
DO 56 i=1,numints
  INT=(1.1**(2.0*i))*((0.0625*CLIGHT)/(2048.0*PI))*
&    ((Z**6)/(N**8))
  Efieldvec(i)=SQRT(8.0*PI*INT/CLIGHT)
c((6.25*CLIGHT)/(2048.0*PI))*((Z**6)/(N**8))

C  LOOP OVER ELECTRONS
DO 55 j=1,totaln

  theta=PI/2.0
  phi=0.0

  IF(indicator1.EQ.0) THEN
    CALL LinearIC(YSTART,theta,phi)
  ELSE
    CALL INITIAL(YSTART(1),YSTART(2),YSTART(3),YSTART(4),
&    YSTART(5),YSTART(6))
  END IF

  DO 30 L=1,NEQ
    YMAX(L)=ABS(YSTART(L))
30  END DO

C  *****NON-RELATIVISTIC*****
C  *****E FIELD INTEGRATION*****
C  SET ERROR AND OTHER PARAMETERS NEEDED BY CT & UT
DO 31 L=1,NEQ
  YMAX(L)=ABS(YSTART(L))
31  END DO

C  INTEGRATE EQUATIONS FOR SHORT TIME WITHOUT LASER PULSE
CALL SETUP(NEQ,TSTART,YSTART,TEND1,TOL,THRES,METHOD,

```

```

&          'Complex Task',ERRASS,HSTART,WORK,LENWRK,MESAGE)

          CFLAG3=0

32          CONTINUE
          CALL CT(DERIVS,TNOW,YNOW,YPNOW,WORK,CFLAG)

c          EF=EFIELD(TNOW,YNOW)
c          write(*,*) TNOW,YNOW(3),EF

C          UPDATE ERROR
          DO 33 L=1,NEQ
              YMAX(L)=MAX(YMAX(L),ABS(YNOW(L)))
33          END DO

C          RECORD VALUES AND UPDATE NEXT INTEGRATION STEP
          IF(CFLAG.LE.5) THEN
              IF(CFLAG.EQ.4) CFLAG3=CFLAG3+1
              IF(TNOW.LT.TEND1 .AND. CFLAG3.LT.5) GO TO 32
          END IF

C          INTEGRATE EQUATIONS WITH PULSE PRESENT
          CALL RESET(TEND)

          CFLAG3=0
34          CONTINUE
          CALL CT(DERIVSNB,TNOW,YNOW,YPNOW,WORK,CFLAG)

c          EF=EFIELD(TNOW,YNOW)
c          write(*,*) TNOW,YNOW(3),EF

C          CHECK FOR CROSSING OF ORIGIN
          IF(indicator1.NE.0) THEN
              CALL STATE2(TNOW,YNOW,NRRADE,NRKEE,NRPEE,NRETOTE,'N')
              IF(NRRADE.LE.Radmin) THEN
                  NRnumoriginE=NRnumoriginE+1
                  GO TO 36
              END IF
          END IF

C          CHECK FOR IONIZATION
          CALL STATE2(TNOW,YNOW,NRRADE,NRKEE,NRPEE,NRETOTE,'N')
          IF(NRRADE.GT.radmax) THEN

```

```

        NRnumionE=NRnumionE+1
        GO TO 36
    END IF

C    UPDATE ERROR
        DO 35 L=1,NEQ
            YMAX(L)=MAX(YMAX(L),ABS(YNOW(L)))
35    END DO

C    RECORD VALUES AND UPDATE NEXT INTEGRATION STEP
        IF(CFLAG.LE.5) THEN
            IF(CFLAG.EQ.4) CFLAG3=CFLAG3+1
            IF(TNOW.LT.TEND .AND. CFLAG3.LT.5) GO TO 34
        END IF

36    CONTINUE
C    *****END E FIELD INTEGRATION*****
c        write(*,*)
c        CALL ITIME(time)
c        WRITE(*,*) time(1),time(2),time(3)
c        write(*,*)
C    *****E&B-FIELD INTEGRATION*****
C    SET ERROR AND OTHER PARAMETERS NEEDED BY CT & UT
        DO 37 L=1,NEQ
            YMAX(L)=ABS(YSTART(L))
37    END DO

C    INTEGRATE EQUATIONS FOR SHORT TIME WITHOUT LASER PULSE
        CALL SETUP(NEQ,TSTART,YSTART,TEND1,TOL,THRES,METHOD,
&                'Complex Task',ERRASS,HSTART,WORKB,LENWRK,MESSAGE)

        CFLAG3=0

38    CONTINUE
        CALL CT(DERIVS,TNOWB,YNOWB,YPNOWB,WORKB,CFLAG)

c        EF=EFIELD(TNOWB,YNOWB)
c        write(*,*) TNOWB,YNOWB(3),EF

C    UPDATE ERROR
        DO 39 L=1,NEQ
            YMAX(L)=MAX(YMAX(L),ABS(YNOWB(L)))
39    END DO

```

```

C   RECORD VALUES AND UPDATE NEXT INTEGRATION STEP
      IF(CFLAG.LE.5) THEN
          IF(CFLAG.EQ.4) CFLAG3=CFLAG3+1
          IF(TNOWB.LT.TEND1 .AND. CFLAG3.LT.5) GO TO 38
      END IF

C   INTEGRATE EQUATIONS WITH PULSE PRESENT
      CALL RESET(TEND)

      CFLAG3=0
40    CONTINUE
      CALL CT(DERIVSB,TNOWB,YNOWB,YPNOWB,WORKB,CFLAG)

c      EF=EFIELD(TNOWB,YNOWB)
c      write(*,*) TNOWB,YNOWB(3),EF

C   CHECK FOR CROSSING OF ORIGIN
      IF(indicator1.NE.0) THEN
          CALL STATE3(TNOWB,YNOWB,NRRADB,NRKEB,NRPEB,NRETOTB,
&              'N')
          IF(NRRADB.LE.Radmin) THEN
              NRnumoriginB=NRnumoriginB+1
              GO TO 42
          END IF
      END IF

C   CHECK FOR IONIZATION
      CALL STATE3(TNOWB,YNOWB,NRRADB,NRKEB,NRPEB,NRETOTB,'N')
      IF(NRRADB.GT.radmax) THEN
          NRnumionB=NRnumionB+1
          GO TO 42
      END IF

C   UPDATE ERROR
      DO 41 L=1,NEQ
          YMAX(L)=MAX(YMAX(L),ABS(YNOWB(L)))
41    END DO

C   RECORD VALUES AND UPDATE NEXT INTEGRATION STEP
      IF(CFLAG.LE.5) THEN
          IF(CFLAG.EQ.4) CFLAG3=CFLAG3+1
          IF(TNOWB.LT.TEND .AND. CFLAG3.LT.5) GO TO 40

```

```

                END IF

42             CONTINUE
C             *****END E&B-FIELD INTEGRATION*****
C             *****END NON-RELATIVISTIC*****
c             write(*,*)
c             CALL ITIME(time)
c             WRITE(*,*) time(1),time(2),time(3)
c             write(*,*)
C             *****RELATIVISTIC*****
C             *****E FIELD INTEGRATION*****
C             SET ERROR AND OTHER PARAMETERS NEEDED BY CT & UT
                DO 43 L=1,NEQ
                    YMAX(L)=ABS(YSTART(L))
43             END DO

C             INTEGRATE EQUATIONS FOR SHORT TIME WITHOUT LASER PULSE
                CALL SETUP(NEQ,TSTART,YSTART,TEND1,TOL,THRES,METHOD,
&                    'Complex Task',ERRASS,HSTART,RWORK,LENWRK,MESAGE)

                CFLAG3=0

44             CONTINUE
                CALL CT(RDERIVS,RTNOW,RYNOW,RYPNOW,RWORK,CFLAG)

c             EF=EFIELD(RTNOW,RYNOW)
c             write(*,*) RTNOW,RYNOW(3),EF

C             UPDATE ERROR
                DO 45 L=1,NEQ
                    YMAX(L)=MAX(YMAX(L),ABS(RYNOW(L)))
45             END DO

C             RECORD VALUES AND UPDATE NEXT INTEGRATION STEP
                IF(CFLAG.LE.5) THEN
                    IF(CFLAG.EQ.4) CFLAG3=CFLAG3+1
                    IF(RTNOW.LT.TEND1 .AND. CFLAG3.LT.5) GO TO 44
                END IF

C             INTEGRATE EQUATIONS WITH PULSE PRESENT
                CALL RESET(TEND)

                CFLAG3=0

```

```

46          CONTINUE
          CALL CT(RDERIVSNB,RTNOW,RYNOW,RYPNOW,RWORK,CFLAG)

c          EF=EFIELD(RTNOW,RYNOW)
c          write(*,*) RTNOW,RYNOW(3),EF

C          CHECK FOR CROSSING OF ORIGIN
          IF(indicator1.NE.0) THEN
              CALL STATE2(RTNOW,RYNOW,RRADE,RKEE,RPEE,RETOTE,'R')
              IF(RRADE.LE.Radmin) THEN
                  RnumoriginE=RnumoriginE+1
                  GO TO 48
              END IF
          END IF

C          CHECK FOR IONIZATION
          CALL STATE2(RTNOW,RYNOW,RRADE,RKEE,RPEE,RETOTE,'R')
          IF(RRADE.GT.radmax) THEN
              RnumionE=RnumionE+1
              GO TO 48
          END IF

C          UPDATE ERROR
          DO 47 L=1,NEQ
              YMAX(L)=MAX(YMAX(L),ABS(RYNOW(L)))
47          END DO

C          RECORD VALUES AND UPDATE NEXT INTEGRATION STEP
          IF(CFLAG.LE.5) THEN
              IF(CFLAG.EQ.4) CFLAG3=CFLAG3+1
              IF(RTNOW.LT.TEND .AND. CFLAG3.LT.5) GO TO 46
          END IF

48          CONTINUE
C          *****END E FIELD INTEGRATION*****
c          write(*,*)
c          CALL ITIME(time)
c          WRITE(*,*) time(1),time(2),time(3)
c          write(*,*)
C          *****E&B-FIELD INTEGRATION*****
C          SET ERROR AND OTHER PARAMETERS NEEDED BY CT & UT
          DO 49 L=1,NEQ

```

```

          YMAX(L)=ABS(YSTART(L))
49          END DO

C      INTEGRATE EQUATIONS FOR SHORT TIME WITHOUT LASER PULSE
          CALL SETUP(NEQ,TSTART,YSTART,TEND1,TOL,THRES,METHOD,
&          'Complex Task',ERRASS,HSTART,RWORKB,LENWRK,MESSAGE)

          CFLAG3=0

50          CONTINUE
          CALL CT(RDERIVS,RTNOWB,RYNOWB,RYPNOWB,RWORKB,CFLAG)

c          EF=EFIELD(RTNOWB,RYNOWB)
c          write(*,*) RTNOWB,RYNOWB(3),EF

C      UPDATE ERROR
          DO 51 L=1,NEQ
              YMAX(L)=MAX(YMAX(L),ABS(RYNOWB(L)))
51          END DO

C      RECORD VALUES AND UPDATE NEXT INTEGRATION STEP
          IF(CFLAG.LE.5) THEN
              IF(CFLAG.EQ.4) CFLAG3=CFLAG3+1
              IF(RTNOWB.LT.TEND1 .AND. CFLAG3.LT.5) GO TO 50
          END IF

C      INTEGRATE EQUATIONS WITH PULSE PRESENT
          CALL RESET(TEND)

          CFLAG3=0

52          CONTINUE
          CALL CT(RDERIVSB,RTNOWB,RYNOWB,RYPNOWB,RWORKB,CFLAG)

c          EF=EFIELD(RTNOWB,RYNOWB)
c          write(*,*) RTNOWB,RYNOWB(3),EF

C      CHECK FOR CROSSING OF ORIGIN
          IF(indicator1.NE.0) THEN
              CALL STATE3(RTNOWB,RYNOWB,RRADB,RKEB,RPEB,RETOTB,'R')
              IF(RRADB.LE.Radmin) THEN
                  RnumoriginB=RnumoriginB+1
                  GO TO 54

```

```

                END IF
            END IF

C      CHECK FOR IONIZATION
          CALL STATE3(RTNOWB,RYNOWB,RRADB,RKEB,RPEB,RETOTB,'R')
          IF(RRADB.GT.radmax) THEN
              RnumionB=RnumionB+1
              GO TO 54
          END IF

C      UPDATE ERROR
          DO 53 L=1,NEQ
              YMAX(L)=MAX(YMAX(L),ABS(YNOWB(L)))
53      END DO

C      RECORD VALUES AND UPDATE NEXT INTEGRATION STEP
          IF(CFLAG.LE.5) THEN
              IF(CFLAG.EQ.4) CFLAG3=CFLAG3+1
              IF(RTNOWB.LT.TEND .AND. CFLAG3.LT.5) GO TO 52
          END IF

54      CONTINUE
C      *****END E&B-FIELD INTEGRATION*****
C      *****END RELATIVISTIC*****

c          WRITE(*,*)

55      CONTINUE

          NRprobeE(i)=(1.0*NRnumionE)/(1.0*totaln)
          NRprobB(i)=(1.0*NRnumionB)/(1.0*totaln)
          RprobeE(i)=(1.0*RnumionE)/(1.0*totaln)
          RprobB(i)=(1.0*RnumionB)/(1.0*totaln)

c          WRITE(*,*) 'N:E',NRnumionE
c          WRITE(*,*) 'N:B',NRnumionB
c          WRITE(*,*) 'R:E',RnumionE
c          WRITE(*,*) 'R:B',RnumionB

          NRnumionEtot=NRnumionEtot+NRnumionE
          NRnumionBtot=NRnumionBtot+NRnumionB
          RnumionEtot=RnumionEtot+RnumionE
          RnumionBtot=RnumionBtot+RnumionB

```

```

        NRnumionE=0
        NRnumionB=0
        RnumionE=0
        RnumionB=0

c        WRITE(*,*)
c        WRITE(*,*)

56      CONTINUE

c        WRITE(*,*)
c        WRITE(*,*)
c        WRITE(*,*)
c        WRITE(*,*)

        CALL ITIME(time)
        WRITE(*,*) time(1),time(2),time(3)

        CALL FILENAME2(Z,N,FREQ,type,fname9,fname10,'N',run)
        CALL FILENAME2(Z,N,FREQ,type,fname11,fname12,'R',run)
        OPEN(UNIT=95,FILE=fname9)
        OPEN(UNIT=96,FILE=fname10)
        OPEN(UNIT=97,FILE=fname11)
        OPEN(UNIT=98,FILE=fname12)

        WRITE(95,5700)
        WRITE(96,5700)
        WRITE(97,5700)
        WRITE(98,5700)

        DO 57 i=1,numints
            WRITE(95,6500) Efieldvec(i),NRprobE(i)
            WRITE(96,6500) Efieldvec(i),NRprobB(i)
            WRITE(97,6500) Efieldvec(i),RprobE(i)
            WRITE(98,6500) Efieldvec(i),RprobB(i)
57      CONTINUE

        WRITE(*,*) 'N:E',NRnumionEtot
        WRITE(*,*) 'N:B',NRnumionBtot
        WRITE(*,*) 'R:E',RnumionEtot
        WRITE(*,*) 'R:B',RnumionBtot

```

```
CLOSE(UNIT=95)
CLOSE(UNIT=96)
CLOSE(UNIT=97)
CLOSE(UNIT=98)
```

```
END IF
```

```
C ***FORMAT STATEMENTS***
```

```
C *****MY FORMATS*****
```

```
C TRAJECTORIES
```

```
1000 FORMAT(' ', 't', 3X, 'x', 3X, 'y', 3X, 'z', 3X, 'px', 3X,
&          'py', 3X, 'pz', 3X, 'R', 3X, 'KE', 3X, 'PE', 3X, 'Etot')
2000 FORMAT(' ', D16.8, 3X, D16.8, 3X, D16.8, 3X, D16.8, 3X, D16.8, 3X, D16.8, 3X,
&          D16.8, 3X, D16.8, 3X, D16.8, 3X, D16.8, 3X, D16.8)
```

```
C FIELDS
```

```
3000 FORMAT(' ', 't', 3X, 'Efield', 3X, 'Bfield')
4000 FORMAT(' ', D16.8, 3X, D16.8, 3X, D16.8)
```

```
C BINNED DATA
```

```
5000 FORMAT(' ', 'BinAve', 3X, 'BinCount', 3X, 'Prcnt')
6000 FORMAT(' ', D16.8, 3X, I16, 3X, D16.8)
```

```
5500 FORMAT(' ', 'Efield', 3X, 'time')
5700 FORMAT(' ', 'Efield', 3X, 'Probability')
6500 FORMAT(' ', D16.8, 3X, D16.8)
```

```
7000 FORMAT(' ', 'Eave', 3X, 'Rave')
8000 FORMAT(' ', 2(D16.8, 3X))
```

```
9000 FORMAT(' ', 12(D16.8, 3X))
9500 FORMAT(' ', D16.8, 3X, D16.8, 3X)
```

```
END
```

```
C END OF MAIN PROGRAM
```

```
C////////////////////////////////////////////////////////////////////////////////////////////////////////////////////////////////
```

```
***SUBROUTINES***
```

C ***COMMON SUBROUTINES***

C THIS SUBROUTINE GIVES THE RHS OF THE DERIVATIVES OF OUR
C SYSTEM OF 1ST ORDER ODE'S. NO E OR B FIELDS ARE PRESENT
SUBROUTINE DERIVS(T,Y,YP)

```
DOUBLE PRECISION rsq,magr,PI,ALPHA,CLIGHT,FREQ,TAU,Z,N,INT,  
&                tstar,tprime  
INTEGER          conditions  
COMMON /params1/ N,Z,TAU,FREQ,INT  
COMMON /params2/ PI,CLIGHT,ALPHA  
COMMON /params3/ tstar,tprime,conditions,dimsn
```

```
DOUBLE PRECISION T  
DOUBLE PRECISION YP(*),Y(*)
```

```
INTRINSIC SQRT
```

```
rsq=((Y(1))**2+(Y(2))**2+(Y(3))**2)  
magr=SQRT(rsq+ALPHA)
```

```
YP(1)=Y(4)  
YP(2)=Y(5)  
YP(3)=Y(6)  
YP(4)=-((Z*Y(1))/(magr**3))  
YP(5)=-((Z*Y(2))/(magr**3))  
YP(6)=-((Z*Y(3))/(magr**3))
```

```
RETURN  
END
```

C
C END OF DERIVATIVES WITHOUT E OR B

C

C//

C THIS SUBROUTINE GIVES THE RHS OF THE DERIVATIVES OF OUR
C SYSTEM OF 1ST ORDER ODE'S. E-FIELD ONLY IS PRESENT
SUBROUTINE DERIVSNB(T,Y,YP)

```
DOUBLE PRECISION rsq,magr,PI,ALPHA,CLIGHT,FREQ,TAU,Z,N,INT,
```

```

&          tstar,E,tprime
INTEGER    conditions
COMMON /params1/ N,Z,TAU,FREQ,INT
COMMON /params2/ PI,CLIGHT,ALPHA
COMMON /params3/ tstar,tprime,conditions,dimsn

DOUBLE PRECISION T
DOUBLE PRECISION YP(*),Y(*)

INTRINSIC SQRT,SIN,COS

E=SQRT(8.0D0*PI*INT/CLIGHT)
rsq=((Y(1))**2+(Y(2))**2+(Y(3))**2)
magr=SQRT(rsq+ALPHA)

YP(1)=Y(4)
YP(2)=Y(5)
YP(3)=Y(6)

C  DETERMINE INDICATOR (MY OR YOUR CONDITIONS)
  IF(conditions.EQ.0) THEN

    IF(T.LE.tstar) THEN
      YP(4)=-((Z*Y(1))/(magr**3))-((T-tprime)/(tstar-tprime))*E*
&          COS((2.0*PI*FREQ/CLIGHT)*Y(3)-2.0*PI*FREQ*T)
    ELSE
      YP(4)=-((Z*Y(1))/(magr**3))-E*
&          COS((2.0*PI*FREQ/CLIGHT)*Y(3)-2.0*PI*FREQ*T)
    END IF
  ELSE
    YP(4)=-((Z*Y(1))/(magr**3))-E*((SIN((PI/2.0)*((T-Y(3))/CLIGHT)
&          /TAU)))**2)*COS((2.0*PI*FREQ/CLIGHT)*Y(3)-2.0*PI*FREQ*T)

  END IF

  YP(5)=-((Z*Y(2))/(magr**3))
  YP(6)=-((Z*Y(3))/(magr**3))
  RETURN
  END

C
C  END OF DERIVATIVES WITH E-FIELD ONLY
C
C////////////////////////////////////

```

```

C   THIS SUBROUTINE GIVES THE RHS OF THE DERIVATIVES OF OUR
C   SYSTEM OF 1ST ORDER ODE'S.  E&B FIELDS ARE PRESENT
      SUBROUTINE DERIVSB(T,Y,YP)

```

```

      DOUBLE PRECISION  rsq,magr,PI,ALPHA,CLIGHT,FREQ,TAU,Z,N,INT,
&                      tstar,E,B,tprime
      INTEGER           conditions
      COMMON /params1/  N,Z,TAU,FREQ,INT
      COMMON /params2/  PI,CLIGHT,ALPHA
      COMMON /params3/  tstar,tprime,conditions,dimsn

```

```

      DOUBLE PRECISION T
      DOUBLE PRECISION YP(*),Y(*)

```

```

      INTRINSIC SQRT,SIN,COS

```

```

      E=SQRT(8.0D0*PI*INT/CLIGHT)
      B=E/CLIGHT
      rsq=((Y(1))**2+(Y(2))**2+(Y(3))**2)
      magr=SQRT(rsq+ALPHA)

```

```

      YP(1)=Y(4)
      YP(2)=Y(5)
      YP(3)=Y(6)

```

```

C   DETERMINE INDICATOR (MY OR YOUR CONDITIONS)
      IF(conditions.EQ.0) THEN

```

```

          IF(T.LE.tstar) THEN
              YP(4)=-((Z*Y(1))/(magr**3))-E*((T-tprime)/(tstar-tprime))*
&                  COS((2.0*PI*FREQ/CLIGHT)*Y(3)-2.0*PI*FREQ*T)
&                  +Y(6)*B*((T-tprime)/(tstar-tprime))*
&                  COS((2.0*PI*FREQ/CLIGHT)*Y(3)-2.0*PI*FREQ*T)
              YP(5)=-((Z*Y(2))/(magr**3))
              YP(6)=-((Z*Y(3))/(magr**3))-Y(4)*B*((T-tprime)/(tstar-tprime)
&                  ))*COS((2.0*PI*FREQ/CLIGHT)*Y(3)-2.0*PI*FREQ*T)
&
          ELSE
              YP(4)=-((Z*Y(1))/(magr**3))-E*COS((2.0*PI*FREQ/CLIGHT)*Y(3)-
&                  2.0*PI*FREQ*T)+Y(6)*B*COS((2.0*PI*FREQ/CLIGHT)*Y(3)-
&                  2.0*PI*FREQ*T)
              YP(5)=-((Z*Y(2))/(magr**3))

```

```

        YP(6)=-((Z*Y(3))/(magr**3))-Y(4)*B*COS((2.0*PI*FREQ/CLIGHT)*
&          Y(3)-2.0*PI*FREQ*T)
      END IF
    ELSE
      YP(4)=-((Z*Y(1))/(magr**3))-E*((SIN((PI/2.0)*((T-Y(3)/
&          CLIGHT)/TAU)))**2)*COS((2.0*PI*FREQ/CLIGHT)*Y(3)-
&          2.0*PI*FREQ*T)+Y(6)*B*((SIN((PI/2.0)*((T-Y(3)/CLIGHT)
&          /TAU)))**2)*COS((2.0*PI*FREQ/CLIGHT)*Y(3)-
&          2.0*PI*FREQ*T)
      YP(5)=-((Z*Y(2))/(magr**3))
      YP(6)=-((Z*Y(3))/(magr**3))-Y(4)*B*((SIN((PI/2.0)*((T-Y(3)
&          /CLIGHT)/TAU)))**2)*COS((2.0*PI*FREQ/CLIGHT)*Y(3)-
&          2.0*PI*FREQ*T)

      END IF

      RETURN
    END

C
C  END OF DERIVATIVES WITH E&B FIELDS
C
C ///////////////////////////////////////////////////////////////////

C  THIS SUBROUTINE GIVES THE RHS OF THE DERIVATIVES OF OUR
C  SYSTEM OF 1ST ORDER ODE'S.  NO E OR B FIELDS ARE PRESENT
C  SUBROUTINE RDERIVS(T,Y,YP)

      DOUBLE PRECISION  rsq,magr,PI,ALPHA,CLIGHT,FREQ,TAU,Z,N,INT,
&          tstar,tprime,gamsqrt
      INTEGER           conditions
      COMMON /params1/  N,Z,TAU,FREQ,INT
      COMMON /params2/  PI,CLIGHT,ALPHA
      COMMON /params3/  tstar,tprime,conditions,dimsn

      DOUBLE PRECISION T
      DOUBLE PRECISION YP(*),Y(*)

      INTRINSIC SQRT

      rsq=((Y(1))**2+(Y(2))**2+(Y(3))**2)
      magr=SQRT(rsq+ALPHA)

```

```

gamsqrt=SQRT((Y(4))**2+(Y(5))**2+(Y(6))**2+CLIGHT**2)

YP(1)=Y(4)*CLIGHT/gamsqrt
YP(2)=Y(5)*CLIGHT/gamsqrt
YP(3)=Y(6)*CLIGHT/gamsqrt
YP(4)=-((Z*Y(1))/(magr**3))
YP(5)=-((Z*Y(2))/(magr**3))
YP(6)=-((Z*Y(3))/(magr**3))

RETURN
END

C
C END OF DERIVATIVES WITHOUT E OR B
C
C ///////////////////////////////////////////////////////////////////

C THIS SUBROUTINE GIVES THE RHS OF THE DERIVATIVES OF OUR
C SYSTEM OF 1ST ORDER ODE'S. E-FIELD ONLY IS PRESENT
C SUBROUTINE RDERIVSNB(T,Y,YP)

DOUBLE PRECISION rsq,magr,PI,ALPHA,CLIGHT,FREQ,TAU,Z,N,INT,
& tstar,E,tprime,gamsqrt
INTEGER conditions
COMMON /params1/ N,Z,TAU,FREQ,INT
COMMON /params2/ PI,CLIGHT,ALPHA
COMMON /params3/ tstar,tprime,conditions,dimsn

DOUBLE PRECISION T
DOUBLE PRECISION YP(*),Y(*)

INTRINSIC SQRT,SIN,COS

E=SQRT(8.000*PI*INT/CLIGHT)
rsq=((Y(1))**2+(Y(2))**2+(Y(3))**2)
magr=SQRT(rsq+ALPHA)
gamsqrt=SQRT((Y(4))**2+(Y(5))**2+(Y(6))**2+CLIGHT**2)

YP(1)=Y(4)*CLIGHT/gamsqrt
YP(2)=Y(5)*CLIGHT/gamsqrt
YP(3)=Y(6)*CLIGHT/gamsqrt

C DETERMINE INDICATOR (MY OR YOUR CONDITIONS)

```

```

IF(conditions.EQ.0) THEN

    IF(T.LE.tstar) THEN
        YP(4)=-((Z*Y(1))/(magr**3))-((T-tprime)/(tstar-tprime))*E*
&          COS((2.0*PI*FREQ/CLIGHT)*Y(3)-2.0*PI*FREQ*T)
    ELSE
        YP(4)=-((Z*Y(1))/(magr**3))-E*
&          COS((2.0*PI*FREQ/CLIGHT)*Y(3)-2.0*PI*FREQ*T)
    END IF
ELSE
    YP(4)=-((Z*Y(1))/(magr**3))-E*((SIN((PI/2.0)*((T-Y(3)/CLIGHT)
&    /TAU)))**2)*COS((2.0*PI*FREQ/CLIGHT)*Y(3)-2.0*PI*FREQ*T)

END IF

YP(5)=-((Z*Y(2))/(magr**3))
YP(6)=-((Z*Y(3))/(magr**3))
RETURN
END

C
C  END OF DERIVATIVES WITH E-FIELD ONLY
C
C ////////////////////////////////////////////////////////////////////

C  THIS SUBROUTINE GIVES THE RHS OF THE DERIVATIVES OF OUR
C  SYSTEM OF 1ST ORDER ODE'S.  E&B FIELDS ARE PRESENT
    SUBROUTINE RDERIVSB(T,Y,YP)

    DOUBLE PRECISION  rsq,magr,PI,ALPHA,CLIGHT,FREQ,TAU,Z,N,INT,
&                    tstar,E,B,tprime,gamsqrt
    INTEGER           conditions
    COMMON /params1/  N,Z,TAU,FREQ,INT
    COMMON /params2/  PI,CLIGHT,ALPHA
    COMMON /params3/  tstar,tprime,conditions,dimsn

    DOUBLE PRECISION T
    DOUBLE PRECISION YP(*),Y(*)

    INTRINSIC SQRT,SIN,COS

    E=SQRT(8.0D0*PI*INT/CLIGHT)
    B=E/CLIGHT

```

```

rsq=((Y(1))**2+(Y(2))**2+(Y(3))**2)
magr=SQRT(rsq+ALPHA)
gamsqrt=SQRT((Y(4))**2+(Y(5))**2+(Y(6))**2+CLIGHT**2)

```

```

YP(1)=Y(4)*CLIGHT/gamsqrt
YP(2)=Y(5)*CLIGHT/gamsqrt
YP(3)=Y(6)*CLIGHT/gamsqrt

```

```

C DETERMINE INDICATOR (MY OR YOUR CONDITIONS)
  IF(conditions.EQ.0) THEN

```

```

    IF(T.LE.tstar) THEN
      YP(4)=-((Z*Y(1))/(magr**3))-E*((T-tprime)/(tstar-tprime))*
&      COS((2.0*PI*FREQ/CLIGHT)*Y(3)-2.0*PI*FREQ*T)+
&      (Y(6)/gamsqrt)*E*((T-tprime)/(tstar-tprime))*
&      COS((2.0*PI*FREQ/CLIGHT)*Y(3)-2.0*PI*FREQ*T)
      YP(5)=-((Z*Y(2))/(magr**3))
      YP(6)=-((Z*Y(3))/(magr**3))-(Y(4)/gamsqrt)*E*
&      ((T-tprime)/(tstar-tprime))*COS((2.0*PI*FREQ/CLIGHT)*
&      Y(3)-2.0*PI*FREQ*T)
    ELSE
      YP(4)=-((Z*Y(1))/(magr**3))-E*COS((2.0*PI*FREQ/CLIGHT)*Y(3)-
&      2.0*PI*FREQ*T)+(Y(6)/gamsqrt)*E*
&      COS((2.0*PI*FREQ/CLIGHT)*Y(3)-
&      2.0*PI*FREQ*T)
      YP(5)=-((Z*Y(2))/(magr**3))
      YP(6)=-((Z*Y(3))/(magr**3))-(Y(4)/gamsqrt)*E*
&      COS((2.0*PI*FREQ/CLIGHT)*
&      Y(3)-2.0*PI*FREQ*T)
    END IF
  ELSE
    YP(4)=-((Z*Y(1))/(magr**3))-E*((SIN((PI/2.0)*((T-Y(3)/
&      CLIGHT)/TAU)))**2)*COS((2.0*PI*FREQ/CLIGHT)*Y(3)-
&      2.0*PI*FREQ*T)+(Y(6)/gamsqrt)*E*((SIN((PI/2.0)*((T-Y(3)
&      /CLIGHT)/TAU)))**2)*COS((2.0*PI*FREQ/CLIGHT)*Y(3)-
&      2.0*PI*FREQ*T)
    YP(5)=-((Z*Y(2))/(magr**3))
    YP(6)=-((Z*Y(3))/(magr**3))-(Y(4)/gamsqrt)*E*((SIN((PI/2.0)*
&      ((T-Y(3)/CLIGHT)/TAU)))**2)*COS((2.0*PI*FREQ/CLIGHT)*
&      Y(3)-2.0*PI*FREQ*T)
  END IF

RETURN

```

```

        END
C
C   END OF DERIVATIVES WITH E&B FIELDS
C
C///////////////////////////////////////////////////////////////////

C   THIS FUNCTION GIVES THE VALUE OF THE E-FIELD AT A GIVEN TIME
    FUNCTION EFIELD(T,Y)
    DOUBLE PRECISION Y(*)
    DOUBLE PRECISION T

    DOUBLE PRECISION PI,ALPHA,CLIGHT,FREQ,TAU,Z,N,INT,
&          tstar,E,B,tprime
    INTEGER          conditions
    COMMON /params1/ N,Z,TAU,FREQ,INT
    COMMON /params2/ PI,CLIGHT,ALPHA
    COMMON /params3/ tstar,tprime,conditions,dimsn

    INTRINSIC SIN,COS,SQRT

    E=SQRT(8.0D0*PI*INT/CLIGHT)
    B=E/CLIGHT

C   DETERMINE INDICATOR (MY OR YOUR CONDITIONS)

    IF(conditions.EQ.0) THEN
        IF(T.LE.tstar) THEN
            EFIELD=((T-tprime)/(tstar-tprime))*E*(COS((2.0*PI*
&          FREQ/CLIGHT)*Y(3)-2.0*PI*T*FREQ))
            ELSE
            EFIELD=E*(COS((2.0*PI*FREQ/CLIGHT)*Y(3)-2.0*PI*T*FREQ))
            END IF
        ELSE
            EFIELD=E*((SIN((PI/2.0)*((T-Y(3)/CLIGHT)/TAU)))**2)*
&          (COS((2.0*PI*FREQ/CLIGHT)*Y(3)-2.0*PI*T*FREQ))

            END IF

        RETURN
    END

C
C   END OF E-FIELD CALCULATION

```

```

C
C/////////////////////////////////////////////////////////////////

C THIS FUNCTION GIVES THE VALUE OF THE B-FIELD AT A GIVEN TIME
  FUNCTION BFIELD(T,Y)
    DOUBLE PRECISION Y(*)
    DOUBLE PRECISION T

    DOUBLE PRECISION PI,ALPHA,CLIGHT,FREQ,TAU,Z,N,INT,
&          tstar,E,B,tprime
    INTEGER          conditions
    COMMON /params1/ N,Z,TAU,FREQ,INT
    COMMON /params2/ PI,CLIGHT,ALPHA
    COMMON /params3/ tstar,tprime,conditions,dimsn

    INTRINSIC SIN,COS,SQRT

    E=SQRT(8.0DO*PI*INT/CLIGHT)
    B=E/CLIGHT

C DETERMINE INDICATOR (MY OR YOUR CONDITIONS)

    IF(conditions.EQ.0) THEN
      IF(T.LE.tstar) THEN
        BFIELD=((T-tprime)/(tstar-tprime))*B*(COS((2.0*PI*
&          FREQ/CLIGHT)*Y(3)-2.0*PI*T*FREQ))
        ELSE
          BFIELD=B*(COS((2.0*PI*
&          FREQ/CLIGHT)*Y(3)-2.0*PI*T*FREQ))
        END IF
      ELSE
        BFIELD=B*((SIN((PI/2.0)*((T-Y(3)/CLIGHT)/TAU)))**2)
&          *(COS((2.0*PI*FREQ/CLIGHT)*Y(3)-2.0*PI*T*FREQ))

        END IF

      RETURN
    END

C
C END OF B-FIELD CALCULATION
C
C/////////////////////////////////////////////////////////////////

```

```

C THIS SUBROUTINE GIVES THE "STATE" OF THE SYSTEM. GIVES THE RADIUS,
C KINETIC ENERGY, POTENTIAL ENERGY AND THE TOTAL ENERGY, NO FIELDS PRESENT
C INPUTS:
C T --> CURRENT TIME
C Y --> VECTOR WITH X,Y,Z,PX,PY,PZ VALUES
C RADIUS --> VALUE OF THE DISTANCE AWAY FROM NUCLEUS
C KE --> KINETIC ENERGY OF ELECTRON
C PE --> POTENTIAL ENERGY OF ELECTRON
C ETOT --> TOTAL ENERGY OF ELECTRON
C ID --> DETERMINES IF WE HAVE RELATIVISTIC OR NON-RELATIVISTIC
SUBROUTINE STATE1(T,Y,RADIUS,KE,PE,ETOT,id)
DOUBLE PRECISION rsq,magr,RADIUS,KE,PE,ETOT,E,B
DOUBLE PRECISION Y(*)
DOUBLE PRECISION T
CHARACTER id*1
DOUBLE PRECISION PI,ALPHA,CLIGHT,FREQ,TAU,Z,N,INT,
& tstar,tprime,gamma
INTEGER conditions
COMMON /params1/ N,Z,TAU,FREQ,INT
COMMON /params2/ PI,CLIGHT,ALPHA
COMMON /params3/ tstar,tprime,conditions,dimsn

INTRINSIC SIN,COS,SQRT

rsq=Y(1)**2+Y(2)**2+Y(3)**2
magr=SQRT(rsq+ALPHA)
gamma=1/SQRT(1-((Y(4)**2+Y(5)**2+Y(6)**2)/(CLIGHT**2)))

RADIUS=SQRT(rsq)
IF(id.EQ.'N') THEN
  KE=(Y(4)**2+Y(5)**2+Y(6)**2)/2.0
ELSE
  KE=(CLIGHT**2)*(gamma-1)
END IF
PE=(-1.0*Z)/magr
ETOT=KE+PE

RETURN
END
C
C END OF STATE1 SUBROUTINE

```

C//

C THIS SUBROUTINE GIVES THE "STATE" OF THE SYSTEM. GIVES THE RADIUS,
C KINETIC ENERGY, POTENTIAL ENERGY AND THE TOTAL ENERGY, E FIELD PRESENT

C INPUTS:

C T --> CURRENT TIME
C Y --> VECTOR WITH X,Y,Z,PX,PY,PZ VALUES
C RADIUS --> VALUE OF THE DISTANCE AWAY FROM NUCLEUS
C KE --> KINETIC ENERGY OF ELECTRON
C PE --> POTENTIAL ENERGY OF ELECTRON
C ETOT --> TOTAL ENERGY OF ELECTRON
C ID --> DETERMINES IF WE HAVE RELATIVISTIC OR NON-RELATIVISTIC

SUBROUTINE STATE2(T,Y,RADIUS,KE,PE,ETOT,id)

DOUBLE PRECISION rsq,magr,RADIUS,KE,PE,ETOT,E,B

DOUBLE PRECISION Y(*)

DOUBLE PRECISION T

CHARACTER id*1

DOUBLE PRECISION PI,ALPHA,CLIGHT,FREQ,TAU,Z,N,INT,

& tstar,tprime,gamma

INTEGER conditions

COMMON /params1/ N,Z,TAU,FREQ,INT

COMMON /params2/ PI,CLIGHT,ALPHA

COMMON /params3/ tstar,tprime,conditions,dimsn

INTRINSIC SQRT,SIN,COS

rsq=Y(1)**2+Y(2)**2+Y(3)**2

magr=SQRT(rsq+ALPHA)

gamma=1/SQRT(1-((Y(4)**2+Y(5)**2+Y(6)**2)/(CLIGHT**2)))

E=SQRT(8.000*PI*INT/CLIGHT)

RADIUS=SQRT(rsq)

IF(id.EQ.'N') THEN

KE=(Y(4)**2+Y(5)**2+Y(6)**2)/2.0

ELSE

KE=(CLIGHT**2)*(gamma-1)

END IF

IF(conditions.EQ.0) THEN

IF(T.LE.tstar) THEN

PE=(-1.0*Z)/magr+((T-tprime)/(tstar-tprime))*E*Y(1)*

& (COS((2.0*PI*FREQ/CLIGHT)*Y(3)-2.0*PI*T*FREQ))

```

        ELSE
            PE=((-1.0*Z)/magr)+E*(COS((2.0*PI*FREQ/CLIGHT)*Y(3)-
&                2.0*PI*T*FREQ))*Y(1)
        END IF
    ELSE
        PE=((-1.0*Z)/magr)+E*((SIN((PI/2.0)*((T-Y(3)/CLIGHT)/TAU))
&                )**2)*(COS((2.0*PI*FREQ/CLIGHT)*Y(3)-2.0*PI*T*FREQ))
&                *Y(1)

    END IF

    ETOT=KE+PE

    RETURN
    END

C
C  END OF STATE2 SUBROUTINE
C //////////////////////////////////////

C  THIS SUBROUTINE GIVES THE "STATE" OF THE SYSTEM.  GIVES THE RADIUS,
C  KINETIC ENERGY, POTENTIAL ENERGY AND THE TOTAL ENERGY, E&B FIELDS PRESENT
C  INPUTS:
C  T      --> CURRENT TIME
C  Y      --> VECTOR WITH X,Y,Z,PX,PY,PZ VALUES
C  RADIUS --> VALUE OF THE DISTANCE AWAY FROM NUCLEUS
C  KE     --> KINETIC ENERGY OF ELECTRON
C  PE     --> POTENTIAL ENERGY OF ELECTRON
C  ETOT  --> TOTAL ENERGY OF ELECTRON
C  ID     --> DETERMINES IF WE HAVE RELATIVISTIC OR NON-RELATIVISTIC
SUBROUTINE STATE3(T,Y,RADIUS,KE,PE,ETOT,id)
DOUBLE PRECISION rsq,magr,RADIUS,KE,PE,ETOT,E,B
DOUBLE PRECISION Y(*)
DOUBLE PRECISION T
CHARACTER          id*1
DOUBLE PRECISION PI,ALPHA,CLIGHT,FREQ,TAU,Z,N,INT,
&                tstar,tprime,gamma,gamsqrt
INTEGER           conditions
COMMON /params1/  N,Z,TAU,FREQ,INT
COMMON /params2/  PI,CLIGHT,ALPHA
COMMON /params3/  tstar,tprime,conditions,dimsn

    INTRINSIC SQRT,SIN,COS

```

```

rsq=Y(1)**2+Y(2)**2+Y(3)**2
magr=SQRT(rsq+ALPHA)
gamsqrt=SQRT((Y(4))**2+(Y(5))**2+(Y(6))**2+CLIGHT**2)
gamma=1/SQRT(1-((Y(4)**2+Y(5)**2+Y(6)**2)/(CLIGHT**2)))
E=SQRT(8.0D0*PI*INT/CLIGHT)
B=E/CLIGHT

RADIUS=SQRT(rsq)
IF(id.EQ.'N') THEN
  KE=(Y(4)**2+Y(5)**2+Y(6)**2)/2.0
  IF(conditions.EQ.0) THEN
    IF(T.LE.tstar) THEN
      PE=(-1.0*Z)/magr+E*((T-tprime)/(tstar-tprime))*
      &      (COS((2.0*PI*FREQ/CLIGHT)*Y(3)-2.0*PI*T*FREQ))*Y(1)-
      &      (Y(4)*B*((T-tprime)/(tstar-tprime))*
      &      (COS((2.0*PI*FREQ/CLIGHT)*Y(3)-2.0*PI*T*FREQ))*Y(3)-
      &      Y(6)*B*((T-tprime)/(tstar-tprime))*
      &      (COS((2.0*PI*FREQ/CLIGHT)*Y(3)-2.0*PI*T*FREQ))*Y(1)) !+
      c &      (1.0/4.0)*(((B*((T-tprime)/(tstar-tprime))*
      c &      (COS((2.0*PI*FREQ/CLIGHT)*Y(3)-2.0*PI*T*FREQ)))**2)*
      c &      (Y(3)**2)+((B*((T-tprime)/(tstar-tprime))*
      c &      (COS((2.0*PI*FREQ/CLIGHT)*Y(3)-2.0*PI*T*FREQ)))**2)*
      c &      (Y(1)**2))
    ELSE
      PE=(-1.0*Z)/magr+E*(COS((2.0*PI*FREQ/CLIGHT)*Y(3)-
      &      2.0*PI*T*FREQ))*Y(1)-
      &      (Y(4)*B*(COS((2.0*PI*FREQ/CLIGHT)*Y(3)-2.0*PI*T*FREQ
      &      ))*Y(3)-
      &      Y(6)*B*(COS((2.0*PI*FREQ/CLIGHT)*Y(3)-2.0*PI*T*FREQ
      &      ))*Y(1)) !+
      c &      (1.0/4.0)*(((B*(COS((2.0*PI*FREQ/CLIGHT)*Y(3)-
      c &      2.0*PI*T*FREQ)))**2)*Y(3)**2)+
      c &      (((B*(COS((2.0*PI*FREQ/CLIGHT)*Y(3)-2.0*PI*T*FREQ)))**2)
      c &      )*Y(1)**2))
    END IF
  ELSE
    PE=(-1.0*Z)/magr+E*((SIN((PI/2.0)*((T-Y(3)/CLIGHT)/TAU))
    &      )**2)*(COS((2.0*PI*FREQ/CLIGHT)*Y(3)-2.0*PI*T*FREQ))*
    &      Y(1)-(Y(4)*B*((SIN((PI/2.0)*((T-Y(3)/CLIGHT)/TAU)))**2)
    &      *(COS((2.0*PI*FREQ/CLIGHT)*Y(3)-2.0*PI*T*FREQ))*Y(3)-
    &      Y(6)*B*((SIN((PI/2.0)*((T-Y(3)/CLIGHT)/TAU)))**2)
    &      *(COS((2.0*PI*FREQ/CLIGHT)*Y(3)-2.0*PI*T*FREQ))

```

```

&          *Y(1)) !+(1.0/4.0)*(((B*((SIN((PI/2.0)*((T-Y(3)/CLIGHT)
C  &          /TAU)))**2)*(COS((2.0*PI*FREQ/CLIGHT)*Y(3)-2.0*PI*T*
C  &          FREQ)))**2)*(Y(3)**2)+((B*((SIN((PI/2.0)*((T-Y(3)/
C  &          CLIGHT)/TAU)))**2)*(COS((2.0*PI*FREQ/CLIGHT)*Y(3)-
C  &          2.0*PI*T*FREQ)))**2)*(Y(1)**2))

      END IF
    ELSE
      KE=(CLIGHT**2)*(gamma-1)
      IF(conditions.EQ.0) THEN
        IF(T.LE.tstar) THEN
          PE=(-1.0*Z)/magr+E*((T-tprime)/(tstar-tprime))*
&          (COS((2.0*PI*FREQ/CLIGHT)*Y(3)-2.0*PI*T*FREQ))*Y(1)-
&          (Y(4)/gamsqrt*E*((T-tprime)/(tstar-tprime))*
&          (COS((2.0*PI*FREQ/CLIGHT)*Y(3)-2.0*PI*T*FREQ))*Y(3)-
&          Y(6)/gamsqrt*E*((T-tprime)/(tstar-tprime))*
&          (COS((2.0*PI*FREQ/CLIGHT)*Y(3)-2.0*PI*T*FREQ))*Y(1)) !+
C  &          (1.0/4.0)*(((E*((T-tprime)/(tstar-tprime))*
C  &          (COS((2.0*PI*FREQ/CLIGHT)*Y(3)-2.0*PI*T*FREQ)))**2)*
C  &          ((Y(3)/gamsqrt)**2)+((E*((T-tprime)/(tstar-tprime))*
C  &          (COS((2.0*PI*FREQ/CLIGHT)*Y(3)-2.0*PI*T*FREQ)))**2)*
C  &          ((Y(1)/gamsqrt)**2))
        ELSE
          PE=(-1.0*Z)/magr+E*(COS((2.0*PI*FREQ/CLIGHT)*Y(3)-
&          2.0*PI*T*FREQ))*Y(1)-
&          (Y(4)/gamsqrt*E*(COS((2.0*PI*FREQ/CLIGHT)*Y(3)-
&          2.0*PI*T*FREQ))*Y(3)-
&          Y(6)/gamsqrt*E*(COS((2.0*PI*FREQ/CLIGHT)*Y(3)-
&          2.0*PI*T*FREQ))*Y(1)) !+
C  &          (1.0/4.0)*(((E*(COS((2.0*PI*FREQ/CLIGHT)*Y(3)-
C  &          2.0*PI*T*FREQ)))**2)*(Y(3)/gamsqrt)**2)+
C  &          ((E*(COS((2.0*PI*FREQ/CLIGHT)*Y(3)-2.0*PI*T*FREQ)))**2
C  &          )*(Y(1)/gamsqrt)**2))
        END IF
      ELSE
        PE=(-1.0*Z)/magr+E*((SIN((PI/2.0)*((T-Y(3)/CLIGHT)/TAU))
&          )**2)*(COS((2.0*PI*FREQ/CLIGHT)*Y(3)-2.0*PI*T*FREQ))*
&          Y(1)-(Y(4)/gamsqrt*E*((SIN((PI/2.0)*((T-Y(3)/CLIGHT)/
&          TAU)))**2)*(COS((2.0*PI*FREQ/CLIGHT)*Y(3)-2.0*PI*T*
&          FREQ))*Y(3)-Y(6)/gamsqrt*E*((SIN((PI/2.0)*((T-Y(3)/
&          CLIGHT)/TAU)))**2)*(COS((2.0*PI*FREQ/CLIGHT)*Y(3)-
&          2.0*PI*T*FREQ))*Y(1)) !+(1.0/4.0)*(((B*((SIN((PI/2.0)*
C  &          (T-Y(3)/CLIGHT)/TAU)))**2)*(COS((2.0*PI*FREQ/CLIGHT)*

```

```

c      &          Y(3)-2.0*PI*T*FREQ)))**2)*(Y(3)**2)+((B*((SIN((PI/2.0)*
c      &          ((T-Y(3)/CLIGHT)/TAU)))**2)*(COS((2.0*PI*FREQ/CLIGHT)*
c      &          Y(3)-2.0*PI*T*FREQ)))**2)*(Y(1)**2))

      END IF
END IF

ETOT=KE+PE

RETURN
END

C
C  END OF STATE3 SUBROUTINE
C //////////////////////////////////////

C  THIS SUBROUTINE GIVES THE INITIAL CONDITIONS FOR STARTING AT THE ORIGIN
      SUBROUTINE LinearIC(ystart,theta,phi)
      DOUBLE PRECISION ystart(*)
      DOUBLE PRECISION theta,phi,beta,gamma,momentum

      DOUBLE PRECISION PI,ALPHA,CLIGHT,FREQ,TAU,Z,N,INT,
&          tstar,tprime
      INTEGER          conditions
      COMMON /params1/ N,Z,TAU,FREQ,INT
      COMMON /params2/ PI,CLIGHT,ALPHA
      COMMON /params3/ tstar,tprime,conditions,dimsn

      INTRINSIC SQRT,SIN,COS

      YSTART(1)=0.0D0
      YSTART(2)=0.0D0
      YSTART(3)=0.0D0

      beta=(Z*1.0D0)/SQRT((YSTART(1)**2+YSTART(2)**2+YSTART(3)**2)
& +ALPHA)
      gamma=(Z**2)/(2.0D0*(N**2))
      momentum=SQRT(2.0D0*(beta-gamma))

      YSTART(4)=momentum*SIN(theta)*COS(phi)
      YSTART(5)=momentum*SIN(theta)*SIN(phi)
      YSTART(6)=momentum*COS(theta)

```

```

        RETURN
        END
C
C   END OF LINEAR INITIAL CONDITIONS SUBROUTINE
C ///////////////////////////////////////////////////////////////////

C   THIS SUBROUTINE RETURNS THE INITIAL DISPLACEMENT AND VELOCITY
C   COMPONENTS
      SUBROUTINE INITIAL(RX0,RYO,RZO,VX0,VYO,VZO)
      DOUBLE PRECISION IE,MA,EO,IO,LA,AP,EA,TA,
&
&           ANGMOM,RADDIS,LINMOM,RX0,RYO,RZO,VX0,VYO,VZO

      DOUBLE PRECISION PI,ALPHA,CLIGHT,FREQ,TAU,Z,N,INT,
&
&           tstar,tprime
      INTEGER           conditions
      COMMON /params1/  N,Z,TAU,FREQ,INT
      COMMON /params2/  PI,CLIGHT,ALPHA
      COMMON /params3/  tstar,tprime,conditions,dimsn

C   *****
C   IE = IONIZATION ENERGY
C   MA = MEAN ANOMALY
C   EO = ECCENTRICITY OF ORBIT
C   IO = INCLINATION OF ORBIT
C   LA = LONGITUDE OF ASCENDING NODE
C   AP = ARGUMENT OF PERIHELION
C   EA = ECCENTRIC ANOMALY
C   TA = TRUE ANOMALY
C   ANGMOM = ANGULAR MOMENTUM
C   RADDIS = RADIAL DISTANCE
C   LINMOM = LINEAR MOMENTUM
C   RX0 = INITIAL DISPLACEMENT IN X-DIRECTION
C   RYO = INITIAL DISPLACEMENT IN Y-DIRECTION
C   RZO = INITIAL DISPLACEMENT IN Z-DIRECTION
C   VX0 = INITIAL VELOCITY IN X-DIRECTION
C   VYO = INITIAL VELOCITY IN Y-DIRECTION
C   VZO = INITIAL VELOCITY IN Z-DIRECTION
C   *****
      CALL INIELEM(MA,EO,IO,LA,AP)
      IE=-(Z**2)/(2.0*N**2)
      EA=EKEPL1(MA,EO)
      TA=2D0*ATAN(SQRT((1D0+SQRT(EO))/(1D0-SQRT(EO)))*TAN(EA/2D0))
      ANGMOM=SQRT((Z**2)*(EO-1D0)/(2D0*IE))

```

```

RADDIS=Z*(SQRT(E0)*COS(EA)-1D0)/(2D0*IE)
LINMOM=SQRT(2D0*(Z/RADDIS+
&((Z**2)*(1D0-E0))/(4D0*IE*(RADDIS**2))+IE))
RXO=RADDIS*(COS(LA)*COS(AP+TA)-SIN(LA)*IO*SIN(AP+TA))
RYO=RADDIS*(SIN(LA)*COS(AP+TA)+COS(LA)*IO*SIN(AP+TA))
RZO=RADDIS*(SQRT(1.0-(IO**2))*SIN(AP+TA))
VXO=(1D0/RADDIS)*(LINMOM*RXO-ANGMOM*(COS(LA)*
&SIN(AP+TA)+SIN(LA)*IO*COS(AP+TA)))
VYO=(1D0/RADDIS)*(LINMOM*RYO-ANGMOM*(SIN(LA)*
&SIN(AP+TA)-COS(LA)*IO*COS(AP+TA)))
VZO=(1D0/RADDIS)*(LINMOM*RZO+ANGMOM*(SQRT(1.0-(IO**2))*
&COS(AP+TA)))

```

```

RETURN
END

```

```

C END OF INITIAL COMPONENTS

```

```

C////////////////////////////////////////////////////////////////////////////////////////////////////////////////////////////////

```

```

C THIS SUBROUTINE RETURNS THE RANDOM VALUES FOR THE FIVE ORBITING
C ELEMENTS

```

```

C INDICATOR --> DETERMINES WHICH PLANE WE ARE IN
C indicator=0 --> random
C indicator=1 --> x-y plane
C indicator=2 --> x-z plane
C indicator=3 --> y-z plane

```

```

SUBROUTINE INIELEM(MAS,EOS,IOS,LAS,APS)
DOUBLE PRECISION MAS,EOS,IOS,LAS,APS,r1,r2

```

```

DOUBLE PRECISION PI,ALPHA,CLIGHT,FREQ,TAU,Z,N,INT,
& tstar,tprime
INTEGER conditions,dimsn
COMMON /params1/ N,Z,TAU,FREQ,INT
COMMON /params2/ PI,CLIGHT,ALPHA
COMMON /params3/ tstar,tprime,conditions,dimsn

```

```

EXTERNAL RAND

```

```

CALL RAND(LAS)
LAS=LAS*2.0*PI

```

```

CALL RAND(APS)
APS=APS*2.0*PI

CALL RAND(MAS)
MAS=MAS*2.0*PI
CALL RAND(EOS)
EOS=EOS*1.0

IF(dimsn.EQ.0) THEN
  CALL RAND(r1)
  CALL RAND(r2)
  IF(r1.LE.0.5) THEN
    CALL RAND(IOS)
    IOS=-IOS
  ELSE
    CALL RAND(IOS)
    IOS=IOS
  END IF
ELSE IF(dimsn.EQ.1) THEN
  CALL RAND(r1)
  IF(r1.LE.0.5) THEN
    IOS=-1.0
  ELSE
    IOS=1.0
  END IF
ELSE IF(dimsn.EQ.2) THEN
  IOS=0.0
  CALL RAND(r1)
  IF(r1.LT.0.5) THEN
    LAS=PI
  ELSE
    LAS=0
  END IF
ELSE IF(dimsn.EQ.3) THEN
  IOS=0.0
  CALL RAND(r1)
  IF(r1.LT.0.5) THEN
    LAS=PI/2.0
  ELSE
    LAS=3.0*PI/2.0
  END IF
END IF

```

```

CALL RAND(APS)
APS=APS*2.0*PI

RETURN
END
C SPECIFIC CASES
C x-y plane: IOS=0 (PI)
C x-z plane: IOS=PI/2, LAS=PI (0)
C y-z plane: IOS=PI/2, LAS=PI/2 (3PI/2)
C END OF ORBITING ELEMENTS
C ///////////////////////////////////////////////////////////////////

C THIS FUNCTION RETURNS THE ECCENTRIC ANOMALY
C REFERENCE - A.W.ODELL AND R.H.GOODING(1986)
FUNCTION EKEPL1 (EM,EE)
DOUBLE PRECISION EM,EE,TESTSQ,C,S,PSI,XI,ETA,FD,FDD,
& F
DATA TESTSQ /1D-10/
C=EE*COS(EM)
S=EE*SIN(EM)
PSI=S/SQRT(1D0-C-C+EE*EE)
1 XI=COS(PSI)
ETA=SIN(PSI)
FD=(1D0-C*XI)+S*ETA
FDD=C*ETA+S*XI
F=PSI-FDD
PSI=PSI-F*FD/(FD*FD-5D-1*F*FDD)
IF(F*F.GE.TESTSQ) GO TO 1
EKEPL1=EM+PSI
RETURN
END
C END OF KEPLER EQUATION
C ///////////////////////////////////////////////////////////////////

C THIS SUBROUTINE GENERATES A RANDOM NUMBER IN THE RANGE [0,1]. FROM
C FORTRAN 77 FOR ENGINEERS AND SCIENTISTS 4TH ED., BY NYHOFF AND LEESTMA
C PAGE 420
C INPUTS:
C RANDNUM --> NUMBER THAT WILL BE RANDOM
SUBROUTINE RAND(randnum)

```

```

    INTEGER M,CONST1
    DOUBLE PRECISION randnum,CONST2
    PARAMETER (CONST1=2147483647,CONST2=0.4656613D-9)
    SAVE
    DATA M /0/

    IF(M.EQ.0) M=INT(randnum)
    M=M*65539
    IF(M.LT.0) M=(M+1)+CONST1
    randnum=M*CONST2

    END

C   END OF SUBROUTINE RAND
C
C////////////////////////////////////
C
C   THIS SUBROUTINE SORTS A VECTOR IN ASCENDING ORDER
C   THIS IS A SUBROUTINE THAT IS FROM "NUMERICAL RECIPES: FORTRAN 77"
C   INPUTS:
C   N    --> SIZE OF ARRAYS TO BE SORTED
C   ARR  --> FIRST ARRAY TO BE SORTED
C   BRR  --> COMPLEMENTARY ARRAY TO BE SORTED
C   SUBROUTINE sort(n,arr,brr)

    INTEGER n,M,NSTACK
    DOUBLE PRECISION arr(n),brr(n)
    PARAMETER (M=7,NSTACK=50)
C   Sorts an array arr(1:n) into ascending numerical order using the Quicksort
C   algorithm. n is input; arr is replaced on output by its sorted
C   rearrangement.
C   Parameters: M is the size of subarrays sorted by straight insertion and
C   NSTACK is the required auxiliary storage.
    INTEGER i,ir,j,jstack,k,l,istack(NSTACK)
    REAL a,b,temp
    jstack=0
    l=1
    ir=n
1   if(ir-l.lt.M)then !Insertion sort when subarray small enough.
    do 12 j=l+1,ir
        a=arr(j)

```

```

        b=brr(j)
        do 11 i=j-1,l,-1
            if(arr(i).le.a)goto 2
            arr(i+1)=arr(i)
            brr(i+1)=brr(i)
11        enddo
        i=l-1
2        arr(i+1)=a
        brr(i+1)=b
12    enddo
    if(jstack.eq.0)return
    ir=istack(jstack) !Pop stack and begin a new round of partitioning.
    l=istack(jstack-1)
    jstack=jstack-2
    else
        k=(l+ir)/2 !Choose median of left, center, and right elements as
                !partitioning element a. Also rearrange so that
                ! a(l).le.a(l+1).le.a(ir).
        temp=arr(k)
        arr(k)=arr(l+1)
        arr(l+1)=temp
        temp=brr(k)
        brr(k)=brr(k+1)
        brr(l+1)=temp
        if(arr(l).gt.arr(ir))then
            temp=arr(l)
            arr(l)=arr(ir)
            arr(ir)=temp
            temp=brr(l)
            brr(l)=brr(ir)
            brr(ir)=temp
        endif
        if(arr(l+1).gt.arr(ir))then
            temp=arr(l+1)
            arr(l+1)=arr(ir)
            arr(ir)=temp
            temp=brr(l+1)
            brr(l+1)=brr(ir)
            brr(ir)=temp
        endif
        if(arr(l).gt.arr(l+1))then
            temp=arr(l)
            arr(l)=arr(l+1)

```

```

        arr(l+1)=temp
        temp=brr(l)
        brr(l)=brr(l+1)
        brr(l+1)=temp
    endif
    i=l+1          !Initialize pointers for partitioning.
    j=ir
    a=arr(l+1)     !Partitioning element.
    b=brr(l+1)
3    continue     !Beginning of innermost loop.
    i=i+1         !Scan up to
nd element > a.
    if(arr(i).lt.a)goto 3
4    continue
    j=j-1         !Scan down to
nd element < a.
    if(arr(j).gt.a)goto 4
    if(j.lt.i)goto 5 !Pointers crossed. Exit with partitioning complete.
    temp=arr(i)    !Exchange elements.
    arr(i)=arr(j)
    arr(j)=temp
    temp=brr(i)
    brr(i)=brr(j)
    brr(j)=temp
    goto 3        !End of innermost loop.
5    arr(l+1)=arr(j) !Insert partitioning element.
    arr(j)=a
    brr(l+1)=brr(j)
    brr(j)=b
    jstack=jstack+2
                    !Push pointers to larger subarray on stack, process
                    !smaller subarray immediately.
    if(jstack.gt.NSTACK)pause 'NSTACK too small in sort'
    if(ir-i+1.ge.j-1)then
        istack(jstack)=ir
        istack(jstack-1)=i
        ir=j-1
    else
        istack(jstack)=j-1
        istack(jstack-1)=l
        l=i
    endif
endif
endif

```

```

        goto 1
        END

C   END OF SUBROUTINE SORT
C
C///////////////////////////////////////////////////////////////////

C   function to give updated grid
c   receives as arguments:
c       DOUBLE PRECISION vector with present x,y,z
c       DOUBLE PRECISION value of present time
c       DOUBLE PRECISION value of time to average over
c       DOUBLE PRECISION value to increment time by
c       INTEGER total number of paraticles
c       INTEGER number in x,y,z direction to "cut" along
c       DOUBLE PRECISION vector of sum to go into average x,y,z calculation
c       INTEGER vector of number of x,y,z have in average calculation
c       DOUBLE PRECISION vector of average x,y,z position
c       DOUBLE PRECISION vector holding min x,y,z values
c       DOUBLE PRECISION vector holding deltax,deltay,deltz & deltaV values
c       DOUBLE PRECISION x6 arrays that will give us distributions

        SUBROUTINE GridIncrement(YNOW,TNOW,tlook,deltat,totalsn,cutnum,sum,
&          count,ave,xmin,deltax,grid1,grid2,grid3,grid4,grid5,grid6,
&          gnum)

        INTEGER          totalsn,cutnum,count(*),nx,ny,nz,gnum

        DOUBLE PRECISION YNOW(*),TNOW,tlook,sum(*),ave(*),xmin(*),
&          deltax(*),grid1(gnum,gnum),grid2(gnum,gnum),
&          grid3(gnum,gnum),grid4(gnum,gnum),
&          grid5(gnum,gnum),grid6(gnum,gnum),deltat

        IF(TNOW.LE.tlook) THEN
            sum(1)=sum(1)+YNOW(1)           !x direction sum
            sum(2)=sum(2)+YNOW(2)           !y direction sum
            sum(3)=sum(3)+YNOW(3)           !z direction sum
            count(1)=count(1)+1             !x direction count
            count(2)=count(2)+1             !y direction count
            count(3)=count(3)+1             !z direction count
        ELSE

```

```

IF(count(1).EQ.0) THEN
  ave(1)=YNOW(1)/1.0
ELSE
  ave(1)=sum(1)/DBLE(count(1))      !x direction average
END IF
IF(count(2).EQ.0) THEN
  ave(2)=YNOW(2)/1.0
ELSE
  ave(2)=sum(2)/DBLE(count(2))      !y direction average
END IF
IF(count(3).EQ.0) THEN
  ave(3)=YNOW(3)/1.0
ELSE
  ave(3)=sum(3)/DBLE(count(3))      !z direction average
END IF
tlook=TNOW+deltat
nx=IFIX(REAL((ave(1)-xmin(1))/deltax(1))+0.99)
ny=IFIX(REAL((ave(2)-xmin(2))/deltax(2))+0.99)
nz=IFIX(REAL((ave(3)-xmin(3))/deltax(3))+0.99)
IF(nx.EQ.cutnum) THEN
  grid1(ny,nz)=grid1(ny,nz)+      !cut along x
&      (1.0/(totaln*deltax(4)))
END IF
IF(ny.EQ.cutnum) THEN
  grid2(nx,nz)=grid2(nx,nz)+      !cut along y
&      (1.0/(totaln*deltax(4)))
END IF
IF(nz.EQ.cutnum) THEN
  grid3(nx,ny)=grid3(nx,ny)+      !cut along z
&      (1.0/(totaln*deltax(4)))
END IF
grid4(ny,nz)=grid4(ny,nz)+      !integration along x
&      (1.0*deltax(2)/(totaln*deltax(4)))
grid5(nx,nz)=grid5(nx,nz)+      !integration along y
&      (1.0*deltax(2)/(totaln*deltax(4)))
grid6(nx,ny)=grid6(nx,ny)+      !integration along z
&      (1.0*deltax(2)/(totaln*deltax(4)))

sum(1)=YNOW(1)
sum(2)=YNOW(2)
sum(3)=YNOW(3)
count(1)=1
count(2)=1

```

```

        count(3)=1
    END IF

    END

C
C  END OF SUBROUTINE GRIDINCREMENT
C
C ///////////////////////////////////////////////////////////////////

C  SUBROUTINE TO CHECK VALUES OF RADIUS AND ENERGY OF ENSEMBLE
c  RECEIVES AS ARGUMENTS:
c    DOUBLE PRECISION vector representing x,y,z present values
c    DOUBLE PRECISION value representing present time
c    DOUBLE PRECISION vector representing ensemble sum of energy and radius
c    INTEGER value representing count for average calculation
c    DOUBLE PRECISION array of ensemble average energy and radius
c    INTEGER value that is the current orbit #
c    DOUBLE PRECISION value of when to average over
c    DOUBLE PRECISION value of how much to increment time by
c    INTEGER value representing if relativistic or non-relativistic
c    INTEGER value representing what type of energy should be called
c    calls subroutine to check the energy and radius
    SUBROUTINE CheckValues(YNOW,TNOW,tlook,deltat,sum,count,ave,i,
&      RAD,KE,PE,ETOT,numorbs,id1,id2)

    INTEGER          i,count,id2,numorbs
    CHARACTER        id1*1
    DOUBLE PRECISION YNOW(*),TNOW,sum(2),ave(numorbs,2),tlook,
&      deltat,RAD,KE,PE,ETOT

    EXTERNAL        STATE1,STATE2,STATE3

    IF(TNOW.LE.tlook) THEN
        IF(id2.EQ.0) THEN
            CALL STATE1(TNOW,YNOW,RAD,KE,PE,ETOT,id1)
            sum(1)=sum(1)+ETOT
            sum(2)=sum(2)+RAD
            count=count+1
        ELSE IF(id2.EQ.1) THEN
            CALL STATE2(TNOW,YNOW,RAD,KE,PE,ETOT,id1)
            sum(1)=sum(1)+ETOT
            sum(2)=sum(2)+RAD

```

```

        count=count+1
    ELSE
        CALL STATE3(TNOW,YNOW,RAD,KE,PE,ETOT,id1)
        sum(1)=sum(1)+ETOT
        sum(2)=sum(2)+RAD
        count=count+1
    END IF
ELSE
    IF(id2.EQ.0) THEN
        CALL STATE1(TNOW,YNOW,RAD,KE,PE,ETOT,id1)
    ELSE IF(id2.EQ.1) THEN
        CALL STATE2(TNOW,YNOW,RAD,KE,PE,ETOT,id1)
    ELSE
        CALL STATE3(TNOW,YNOW,RAD,KE,PE,ETOT,id1)
    END IF
    ave(i,1)=ave(i,1)+sum(1)/DBLE(count)
    ave(i,2)=ave(i,2)+sum(2)/DBLE(count)
    i=i+1
    sum(1)=ETOT
    sum(2)=RAD
    count=1
    tlook=TNOW+deltat
END IF

END

C
C   END OF SUBROUTINE CHECKVALUES
C
C////////////////////////////////////
```

Appendix B

SOURCE CODE FOR COINCIDENCE MAPPING

```
/*PROGRAM TO PRINT OUT COINCIDENCE MAP CONTAINING SPECTRA FROM EXPERIMENT*/

#include <stdio.h>
#include <stdlib.h>
#include <math.h>
#include <string.h>
#include <stdint.h>
#include <time.h>

#define N 27000          /*NUMBER OF ENTRIES IN *.lst FILE*/
#define M 512 /*65536*/ /*NUMBER OF BINS*/

int main(){

    FILE *infile,*outfile1,*outfile2;
    int i,j,k,l,m,n,ii,jj,kk,ll,mm,nn,pp,qq,n1,n2;
    float *C0;
    int *C1,*C2,*C3;
    int p1,p2;
    int count[M]={0};
    float time[M],ave[M];
    float deltat,span,offset;
    int shots=0;

    span=2.56;
    deltat=span/M;
    offset=span/(2.0*M);

    /*OPEN DATA FILE, MAKE SURE COMMAND LINE IS CORRECT*/
    if((infile=fopen("35.lst","r"))==NULL){
        printf("InFile could not be opened...\n");
        exit(0);
    }
    else{
```

```

/*READ IN DATA COLUMN BY COLUMN*/
C0=(float *) malloc(N*sizeof(*C0));
if(C0==NULL){
    printf("Could not allocate memory for C0\n");
    return 0;
}
C1=(int *) malloc(N*sizeof(*C1));
if(C1==NULL){
    printf("Could not allocate memory for C1\n");
    return 0;
}
C2=(int *) malloc(N*sizeof(*C2));
if(C2==NULL){
    printf("Could not allocate memory for C2\n");
    return 0;
}
C3=(int *) malloc(N*sizeof(*C3));
if(C3==NULL){
    printf("Could not allocate memory for C3\n");
    return 0;
}
kk=0;
while(!feof(infile)){
    fscanf(infile,"%f %d %d %d",&C0[kk],&C1[kk],&C2[kk],&C3[kk]);
    kk++;
}
printf("%d\n",kk);
free(C2);
free(C3);

/*DIVIDE VALUES BY 1000 TO GET TO MICROSECONDS FROM NANO*/
for(i=0;i<=(kk-1);i++){
    C0[i]=C0[i]/1000.0;
}

/*SET TIME ARRAY*/
time[0]=offset;
for(i=1;i<=(M-1);i++){
    time[i]=time[i-1]+deltat;
}

for(i=0;i<=(M-1);i++){

```

```

    ave[i]=0.0;
}

/*CREATE MATRIX OF MxM ELEMENTS*/
float CM1[M][M],CM2[M][M];

for(i=0;i<=(M-1);i++){
    for(j=0;j<=(M-1);j++){
CM1[i][j]=0.0;
CM2[i][j]=0.0;
    }
}

/*DETERMINE NUMBER OF SHOTS THAT PASSED*/
for(i=0;i<=(kk-1);i++){
    shots+=C1[i];
}
printf("\n\nTotal number of shots:%d\n\n",shots);

p1=0;
p2=0;

/*SWEEP THROUGH DATA ARRAY TO CREATE TOF TRACES FOR EACH SHOT*/
for(i=0;i<=(kk-1);i++){
    if(C1[i]==1){
p1=i;                                /*determine where shot starts*/
for(j=(i+1);j<=kk;j++){
    if(C1[j]==1){
p2=j;                                /*determine where shot stops*/
break;
    }
else{
p2=kk;
    }
}
}

/*CLEAN COUNT VECTOR FOR SHOT*/
for(m=0;m<=(M-1);m++){
    count[m]=0;
}

/*SWEEP THROUGH SHOT TO CHECK FOR TIME MATCHING & BIN SHOT*/
for(ii=(p1+1);ii<=(p2-1);ii++){

```

```

for(l=0;l<=(M-1);l++){
    if(CO[ii]<=(time[l]+deltat/2.0) && CO[ii]>=(time[l]-deltat/2.0)){
        count[l]+=1;
        ave[l]+=1.0;                /*create vector of binned average*/
    }
}

/*SWEEP THROUGH COUNT ARRAY & BUILD TOF WEIGHTED MATRIX*/
for(m=0;m<=(M-1);m++){
    for(n=0;n<=(M-1);n++){
        CM1[m][n]+=count[m]*count[n];
    }
}

for(m=0;m<=(M-1);m++){
    for(n=0;n<=(M-1);n++){
CM1[m][n]=(1.0/shots)*CM1[m][n];
    }
}

for(m=0;m<=(M-1);m++){
    for(n=0;n<=(M-1);n++){
CM2[m][n]=(1.0/shots)*(1.0/shots)*ave[m]*ave[n];
    }
}

/*PRINT OUT NEW FILE COINCIDENCE MAP*/
if((outfile1=fopen("35_cmap_4096.dat","w"))==NULL){
    printf("File could not be opened...\n");
    exit(0);
}
else{
    for(i=0;i<=(M-1);i++){
for(j=0;j<=(M-1);j++){
        fprintf(outfile1,"%f\t",CM1[i][j]-CM2[i][j]);
    }
    fprintf(outfile1,"\n");
}
}

```

```
/*PRINT OUT NEW FILE OF TIME OF FLIGHT*/
if((outfile2=fopen("35_tof_4096.dat","w"))==NULL){
printf("File could not be opened...\n");
exit(0);
}
else{
for(i=0;i<=(M-1);i++){
fprintf(outfile2,"%f\t%f\n",time[i],ave[i]);
}
}

free(C0);
free(C1);

fclose(outfile1);
fclose(outfile2);

}
}
```

Appendix C

SOURCE CODE SPECTROMETER CHARACTERIZATION

```
/*PROGRAM TO BIN ENERGY SPECTRUM DATA*/

#include <stdio.h>
#include <stdlib.h>
#include <math.h>
#include <string.h>
#include <stdint.h>
#include <time.h>

/*GLOBAL VARIABLES*/
#define mp 1.6726E-27 /*MASS OF THE PROTON IN kg's*/
#define e 1.6022e-19 /*CHARGE OF THE ELECTRON IN coulombs*/
#define l 0.01778 /*SEPARATION BETWEEN FIELD PLATES*/

#define N 20 /*NUMBER OF EXPERIMENTAL VALUES OF TIME OF FLIGHT*/

int main(){
    /*COUNTERS*/
    int i,j,k,m,ii,jj,kk,mm;

    /*VARIABLES THAT WE ARE TRYING TO FIT*/
    /*V1 --> VOLTAGE ACROSS INTERACTION REGION
    *V2 --> VOLTAGE ACROSS MCP
    *D --> FLIGHT TUBE DISTANCE
    *d --> DISTANCE FOR THE MCP VOLTAGE
    *y0 --> INITIAL STARTING POSITION OF THE ION */
    double V1,V2,D,d,y0,t0,V1opt,V2opt,Dopt,dopt,y0opt;

    /*EXPERIMENTAL TIME OF FLIGHTS FOR IONS*/
    double texp[N],tcalc[N],topt[N];

    /*MASS TO CHARGE RATIOS*/
    double mtc[N];
```

```

/*CALCULATED TIMES*/
double tmod[N];

/*RESIDUE SUMS (THE THING WE ARE TRYING TO MINIMIZE)*/
double Sold,Snew,S,Smin;

/*FILE *outfile*/

V2=1750.0;

/*VALUES FOR EXPERIMENTAL TIME OF FLIGHTS*/
texp[0]=0.6051E-6; /*13C4+*/
texp[1]=0.6768E-6; /*13C3+*/
texp[2]=0.7966E-6; /*13C2+*/
texp[3]=1.0670E-6; /*13C1+*/
texp[4]=1.1683E-6; /*O1+*/
texp[5]=1.2001E-6; /*OH1+*/
texp[6]=0.3997E-6; /*H1+*/
texp[7]=0.5064E-6; /*(H_2)1+*/
texp[8]=0.5888E-6; /*(H_3)1+*/
texp[9]=1.2250E-6; /*H2O+*/
texp[10]=1.4963E-6; /*N2+*/
texp[11]=1.5896E-6; /*O2+*/
texp[12]=1.8398E-6; /*CO2+*/
/* texp[9]=1.3991E-6;*/ /*13CC12+*/
/* texp[10]=1.4118E-6;*/ /*13CHC12+*/
/* texp[11]=1.4247E-6;*/ /*13CH2C12+*/
/* texp[12]=1.4373E-6;*/ /*13CH3C12+*/
texp[13]=1.6585E-6; /*35C11+*/
texp[14]=1.7038E-6; /*37C11+*/
texp[15]=1.9729E-6; /*1.9187E-6;*/ /*13CC11+*/
texp[16]=1.9909E-6; /*1.9370E-6;*/ /*13CHC11+*/
texp[17]=2.0083E-6; /*1.9552E-6;*/ /*13CH2C11+*/
texp[18]=2.0257E-6; /*1.9721E-6;*/ /*13CH3C11+*/
texp[19]=2.0616E-6; /*13CH337C1+*/

/*VALUES FOR MASS TO CHARGE RATIOS*/
mtc[0]=13.003*mp/(4.0*e); /*13C4+*/
mtc[1]=13.003*mp/(3.0*e); /*13C3+*/
mtc[2]=13.003*mp/(2.0*e); /*13C2+*/
mtc[3]=13.003*mp/(1.0*e); /*13C1+*/
mtc[4]=15.995*mp/(1.0*e); /*O1+*/
mtc[5]=17.003*mp/(1.0*e); /*OH1+*/

```

```

mtc[6]=1.008*mp/(1.0*e) ; /*H1+*/
mtc[7]=2.016*mp/(1.0*e); /*(H_2)1+*/
mtc[8]=3.024*mp/(1.0*e); /*(H_3)1+*/
mtc[9]=18.011*mp/(1.0*e); /*H20+*/
mtc[10]=28.006*mp/(1.0*e); /*N2+*/
mtc[11]=31.99*mp/(1.0*e); /*O2+*/
mtc[12]=43.99*mp/(1.0*e); /*CO2+*/
/* mtc[9]=47.972*mp/(2.0*e);*/ /*13CC12+*/
/* mtc[10]=48.98*mp/(2.0*e);*/ /*13CHC12+*/
/* mtc[11]=49.988*mp/(2.0*e);*/ /*13CH2C12+*/
/* mtc[12]=50.996*mp/(2.0*e);*/ /*13CH3C12+*/
mtc[13]=34.969*mp/(1.0*e); /*35C11+*/
mtc[14]=36.966*mp/(1.0*e); /*37C11+*/
mtc[15]=47.972*mp/(1.0*e); /*13CC11+*/
mtc[16]=48.98*mp/(1.0*e); /*13CHC11+*/
mtc[17]=49.988*mp/(1.0*e); /*13CH2C11+*/
mtc[18]=50.966*mp/(1.0*e); /*13CH3C11+*/
mtc[19]=52.993*mp/(1.0*e); /*13CH337C11+*/

/*SET INITIAL VALUE OF RESIDUE TO LARGE VALUE*/
Sold=100.0;

for(V1=2990.0;V1<=3040.0;V1+=1.0){
  for(D=0.1175;D<=0.1225;D+=0.000125){
    for(y0=-0.001;y0<=0.001;y0+=0.000125){
for(d=0.003;d<=0.004;d+=0.000125){
  for(t0=0.0;t0<=(250.0E-9);t0+=1.25E-9){
    S=0.0;
    for(i=0;i<=(N-1);i++){
      tcalc[i]=mtc[i]*l/V1*sqrt((1.0/mtc[i])*V1/l*(1-2*y0))+D/sqrt((1.0/mtc[i])*V1/

      S+=((texp[i]-tcalc[i])/texp[i])*((texp[i]-tcalc[i])/texp[i]);
    }
    if(S<=Sold){
      Sold=S;
      /*Smin=Sold;
V1opt=V1;
V2opt=V2;
Dopt=D;
dopt=d;
y0opt=y0;*/
    printf("%E\t%f\t%f\t%f\t%f\t%f\t%E\n",Sold,V1,D,y0,d,t0);
    for(j=0;j<=(N-1);j++){

```

```
printf("%E\t%E\t%E\n",mtc[j],tcalc[j],texp[j]);  
    }  
  }  
}  
  }  
}  
}
```